![U.S. NRC logo — United States Nuclear Regulatory Commission — Protecting People and the Environment]

Jet Impingement in High-Energy Piping Systems

Office of Nuclear Regulatory Research

AVAILABILITY OF REFERENCE MATERIALS
IN NRC PUBLICATIONS

NRC Reference Material

As of November 1999, you may electronically access NUREG-series publications and other NRC records at the NRC's Library at www.nrc.gov/reading-rm.html. Publicly released records include, to name a few, NUREG-series publications; *Federal Register* notices; applicant, licensee, and vendor documents and correspondence; NRC correspondence and internal memoranda; bulletins and information notices; inspection and investigative reports; licensee event reports; and Commission papers and their attachments.

NRC publications in the NUREG series, NRC regulations, and Title 10, "Energy," in the *Code of Federal Regulations* may also be purchased from one of these two sources:

1. The Superintendent of Documents
U.S. Government Publishing Office
Washington, DC 20402-0001
Internet: www.bookstore.gpo.gov
Telephone: (202) 512-1800
Fax: (202) 512-2104

2. The National Technical Information Service
5301 Shawnee Road
Alexandria, VA 22312-0002
Internet: www.ntis.gov
1-800-553-6847 or, locally, (703) 605-6000

A single copy of each NRC draft report for comment is available free, to the extent of supply, upon written request as follows:

Address: **U.S. Nuclear Regulatory Commission**
Office of Administration
Division of Resource Management & Analysis
Washington, DC 20555-0001
E-mail: distribution.resource@nrc.gov
Facsimile: (301) 415-2289

Some publications in the NUREG series that are posted at the NRC's Web site address www.nrc.gov/reading-rm/doc-collections/nuregs are updated periodically and may differ from the last printed version. Although references to material found on a Web site bear the date the material was accessed, the material available on the date cited may subsequently be removed from the site.

Non-NRC Reference Material

Documents available from public and special technical libraries include all open literature items, such as books, journal articles, transactions, *Federal Register* notices, Federal and State legislation, and congressional reports. Such documents as theses, dissertations, foreign reports and translations, and non-NRC conference proceedings may be purchased from their sponsoring organization.

Copies of industry codes and standards used in a substantive manner in the NRC regulatory process are maintained at—

The NRC Technical Library
Two White Flint North
11545 Rockville Pike
Rockville, MD 20852-2738

These standards are available in the library for reference use by the public. Codes and standards are usually copyrighted and may be purchased from the originating organization or, if they are American National Standards, from—

American National Standards Institute
11 West 42nd Street
New York, NY 10036-8002
Internet: www.ansi.org
(212) 642-4900

Jet Impingement in High-Energy Piping Systems

Manuscript Completed: September 2020
Date Published: March 2021

Prepared by: S. Kim, M. Ishii, and R. Kong

Thermal-hydraulics and Reactor Safety Laboratory
School of Nuclear Engineering
Purdue University
West Lafayette, IN 47907-2017

Andrew Ireland, NRC Project Manager

Office of Nuclear Regulatory Research

ABSTRACT

Appendix A of the Standard Review Plan (U.S. Nuclear Regulatory Commission, 2015) identified several potential non-conservatisms in the existing models for jet impingement in high-energy piping systems as in nuclear power plants, with respect to (a) blast wave formation, (b) jet plume expansion and zone of influence, (c) distribution of pressure within the jet plume, and (d) jet dynamic loading. The current work performs a comprehensive literature review and model evaluation to aid in addressing these potential non-conservatisms. Based on the results, the model is revised and model guidance is developed.

The literature review covers important jet impingement phenomena, experimental studies, as well as important models and CFD simulations of jet impingement. It is found that key phenomena including jet expansion, jet impingement, and critical flow are reflected in the existing models, but the potential blast waves and jet dynamic loading are not considered in modeling jet impingement in nuclear power plants. The publicly available experimental studies are reviewed and an experimental database is established for data analysis and model evaluation. The parameters including pressure, break size, and axial distance are non-dimensionalized such that the effects of the initial fluid condition and break size can be investigated. Using this database, correlations are developed to predict the static and stagnation pressures at the center of jets with different initial fluid conditions and break sizes.

Important jet impingement models including the Standard model (ANSI/ANS-58.2, American Nuclear Society, 1988) and the two-phase jet load model (NUREG/CR-2913, Weigand, 1983) are evaluated. It is found that the stagnation pressure for saturated steam jets can generally be predicted well by the Standard model. The stagnation pressure for saturated water/two-phase jets can also be predicted well using the Standard model for the large-scale test data ($D > 0.28$ m), but are underestimated for medium- and small-scale test data ($D < 0.15$ m). Significant overestimation in stagnation pressure is observed for subcooled water jets in Region 1 with a high degree of subcooling ($\Delta T > 40$ °C), which is because the critical mass flux is significantly overestimated using the Homogeneous Equilibrium Model (HEM). In addition, the distance between the break plane and the asymptotic plane is also investigated. It is found that the Standard model can predict this distance well for saturated steam jets, but overpredicts that with 100% difference for saturated water/two-phase and subcooled water jets. Although this will predict a larger zone of influence, the pressure within the jets is still predicted conservatively in Regions 2 and 3.

Based on the results of the literature review and model evaluation, the Standard model is revised and model guidance is developed to address the potential non-conservatisms. The revised model shows improved predictions for stagnation pressure. For the potential blast wave effect, approaches based on the equivalent weight of TNT are developed to quantify the static overpressure and the reflected pressure. For jet geometry, it is found that the jet spreading angle for saturated steam jets in the Standard model generally agrees with the dynamic model (Morita et al., 2016) in literature for a wide range of initial stagnation pressure conditions. Regarding the pressure distribution within jets, it is confirmed that edge-peaking pressure profiles are observed for saturated steam jets at far distances from the break plane ($z > 3.3D$); however, the dimensionless pressures at these locations are generally less than 0.07. On the potential jet dynamic loading effect, the justifications provided in Kauffman et al. (2019) are reviewed and it indicates that this effect might not occur for jet impingement in nuclear power plants.

TABLE OF CONTENTS

LIST OF FIGURES

LIST OF TABLES

EXECUTIVE SUMMARY

The jet impingement due to postulated pipe rupture is of significant interest in the design and safety analysis of nuclear power plants. The fluid within the high-energy piping systems is discharged into the surrounding environment as a high-energy jet, leading to an extreme load that can cause malfunction and significant damage to the surrounding structures, systems, and components (SSCs). While models of jet impingement have been developed to assist to design protective systems to mitigate the damage, several potential non-conservatisms in these models have been specified following the interaction with the Advisory Committee on Reactor Safeguards (ACRS) (Standard Review Plan, U.S. Nuclear Regulatory Commission, 2015). To address these potential non-conservatisms, the current work performs a comprehensive literature review and model evaluation. Based on the results, model guidance is developed to address the potential non-conservatisms.

The current work starts with a comprehensive literature review. Key phenomena and governing flow parameters are first identified. Pipe whip, jet expansion, jet impingement, and critical flow are identified as the important phenomena that should be investigated. Corresponding parameters including thrust force, jet geometry, pressure distribution, jet impingement force, dynamic load factor, and critical flow rate should be modeled. It is found that most of the phenomena and parameters are considered in the existing models such as the Standard model ANSI/ANS-58.2 (American Nuclear Society, 1988) and the two-phase jet load model (NUREG/CR-2913). However, the potential jet dynamic loading and blast waves are usually not considered. Therefore, they are also reviewed to understand their effects on structures. Special attention needs to be paid when extending the current studies of blast waves and jet dynamic loading in modeling jet impingement.

The reviewed experimental studies on jet impingement cover a wide range of test facility geometries in different scale levels. It is found that most of the experimental studies on jet impingement were performed in the 1980s. An experimental database is established for data analysis and model evaluation. The parameters including pressure, break size, and axial distance are non-dimensionalized such that the effects of initial fluid condition (initial vessel stagnation pressure, temperature, and quality) and break size on stagnation pressure can be investigated. It is found that the initial stagnation pressure and break size have negligible effects on the non-dimensional pressure within the jets for saturated steam ($x \geq 0.7$) and saturated water/two-phase jets ($0 \leq x < 0.7$), but the initial quality for two-phase jets has significant effects. For subcooled water jets, the degree of subcooling and the break size have significant effects on pressure distribution. To systematically investigate these effects, additional experimental data need to be obtained. Meanwhile, correlations are developed to predict the static and stagnation pressures. It is found that a power law can be used to correlate the dimensionless static and stagnation pressures at the center of the free jets, while either a power law or an exponential function can be used to correlate the dimensionless stagnation pressure at the center of the targets in impinging jets.

From model evaluations, the stagnation pressure within the saturated steam jets can generally be predicted well by the Standard model. Although stagnation pressures at far distances ($z > 3.3\,D$) can be underestimated, the dimensionless pressures at these axial locations are less than 0.07. For saturated water jets, the stagnation pressure can be predicted well using the Standard model for the large-scale test data ($D > 0.28$ m), but calculations using the Standard model underestimate the medium- and small-scale ($D < 0.15$ m) experimental data. Significant overestimation in stagnation pressure is observed for subcooled water jets with a high degree of

subcooling ($\Delta T > 40$ °C), which is because the critical mass flux is overestimated using Homogeneous Equilibrium Model (HEM). For subcooled water jets with a low degree of subcooling ($\Delta T < 20$ °C), HEM underestimates the data. Unlike HEM, Henry-Fauske model always overpredicts the experimental data, but the degree of overestimation increases as the degree of subcooling decreases. The critical mass flux for saturated steam jets and saturated water/two-phase jets can be predicted well by isentropic expansion model and HEM, respectively. In addition to critical mass flux, the jet core length and the distance between the break plane and the asymptotic plane are also investigated, which are important parameters to define the zone of influence for jets. It is found that the Standard model can predict the jet core length well for conditions with a low degree of subcooling ($\Delta T < 30$ °C), but underestimates it for conditions with a high degree of subcooling ($\Delta T > 30$ °C). The distance between the break plane and the asymptotic plane can be predicted well for saturated steam jets. However, it is overpredicted with 100% difference for saturated-water/two-phase and subcooled water jets, which indicates that a larger zone of influence is predicted. Despite this, the pressure within the jets is still predicted conservatively by the Standard model in Regions 2 and 3. In addition, the thrust coefficients employed in the Standard model agree well with the experimental data for different jet regimes.

Based on the results of the literature review and model evaluation, the Standard model is revised and the model guidance is developed to address the potential non-conservatisms, with respect to (a) blast waves, (b) jet plume expansion and zone of influence, (c) distribution of pressure within the jet plume, and (d) jet dynamic loading. Newly developed correlations for core length and pressure distributions are implemented to revise the Standard model. It is shown that the revised code can provide improved predictions for stagnation pressure for the conditions investigated in saturated water/two-phase jets and subcooled water jets. On the potential blast wave effect, the transcript of the Advisory Committee on Reactor Safeguards (ACRS) subcommittee meeting is first reviewed. However, technical basis that can provide one to assess the conditions whether the blast wave is or is not significant could not be established. To quantify the potential blast wave effect, the TNT approach in the detonation research is employed. Two methods are developed to calculate the released energy or the equivalent weight of TNT based on conservative assumptions. As such, the static overpressure and the reflected pressure can be calculated. For jet geometry, dynamic models to predict the jet spreading angle for saturated steam and flashing jets are reviewed. It is found that the jet spreading angle for saturated steam jets in the Standard generally agrees with the dynamic model in literature (Morita et al., 2016) for a wide range of initial stagnation pressure conditions. Regarding the pressure distribution within jets, it is confirmed that edge-peaking pressure profiles can be observed for saturated steam jets at far distances from the break plane ($z > 3.3$ D); however, the dimensionless pressures at these locations are generally less than 0.07. On the jet dynamic loading effect, the justifications provided in Kauffman et al. (2019) are reviewed and it indicates that dynamic amplification and resonance of impinged downstream structures and components might not occur for jet impingement in nuclear power plants.

ACKNOWLEDGMENTS

ABBREVIATIONS

ACRONYMS

ACRS	Advisory Committee on Reactor Safeguards
ANSI/ANS	American National Standard Institute/American Nuclear Society
BWR	Boiling Water Reactor
CFD	Computational Fluid Dynamics
CHARTD	Coupled Hydrodynamics And Radiation Transport Diffusion
CRIEPI	Central Research Institute of Electric Power Industry
CSQ	CHARTD Squared
DLF	Dynamic Loading Factor
ENEA	Energia Nucleare ed Energie Alternative
EPRI	Electric Power Research Institute
GSI	Generis Safety Issues
HEM	Homogeneous Equilibrium Model
HF	Henry-Fauske
ID	Inner Diameter
JAERI	Japan Atomic Energy Research Institute
KWU	Kraftwerk Union
LOCA	Loss of Coolant Accident
LU-SGS	Lower-Upper Symmetric-Gauss-Seidel
MDOF	Multi-Degree of Freedom
MUSCL	Monotone Upstream-centered Schemes for Conservation Law
NEI	Nuclear Energy Institute
NRC	Nuclear Regulatory Commission
PIV	Particle Image Velocimetry
SDOF	Single Degree of Freedom
SFM	Separated Flow Model
SLAU	Simple Low-dissipation Advection Upstream Splitting Method
SSC	Sturctures, Systems and Components
TNT	Trinitrotoluene

VARIABLES

a_{jet}	Jet speed of sound [m/s]
aamb	Ambient speed of sound [m/s]
$\overline{A}_{pipe}$	Pipe external surface area [m^2]
A	Area [m^2]
A_a	Jet area at the asymptotic plane [m^2]
A_e	Break area [m^2]
$A_{f,a}$	Asymptotic plane area occupied by liquid [m^2]
$A_{g,a}$	Asymptotic plane area occupied by gas [m^2]
A_j	Jet area [m^2]
A_{je}	Jet area at the break plane [m^2]
C_D	Discharge coefficient [-]
C_T	Thrust coefficient [-]
D	Break size [m]
D_{eff}	Effective break diameter [m]
D_{je}	Jet diameter at the break plane [m]

D_{jet}	Jet diameter [m]
D_{nozzle}	Nozzle diameter [m]
D_P	Pipe diameter [m]
f	Frequency [Hz]
f_{min}	Minimum axisymmetric mode resonance frequency for supersonic jet [Hz]
f_P	Pipe Darcy friction factor [-]
F_b	Jet blowdown force [N]
F_j	Impinging force [N]
$\vec{F}$	Vector sum of external forces [N]
g_c	Gravitational constant [ft/s^2]
G	Mass flux [kg/(m^{2}s)]
G_{cr}	Critical mass flux [kg/(m^{2}s)]
h	Enthalpy [kJ/kg]
h_0	Specific stagnation enthalpy [J/kg]
h_{fg}	Latent heat of vaporization [J/kg]
H_a	Width of the asymptotic plane [m]
k	Ratio of specific heats [-]
L	Distance between measurement point and break [m]
L_a	Distance from the break plane to the asymptotic plane [m]
L_c	Jet core length [m]
L_P	Pipe or nozzle length [m]
m	Fluid mass [kg]
$\dot{m}$	Mass flow rate [kg/s]
M	Mach number [-]
p	Static pressure [Pa]
p_{amb}	Ambient pressure [Pa]
p_e	Static pressure at the exit plane [Pa]
p^*	Dimensionless static pressure [-]
P	Stagnation pressure [Pa]
P^*	Dimensionless stagnation pressure [-]
P_0	Initial stagnation pressure [Pa]
P_c	Stagnation pressure at the center of jets [Pa]
P_{cr}	Exit pressure for isentropic flow [Pa]
P_e	Fluid static pressure at the break plane [Pa]
P_{Fg}	Fraction of channel's perimeter covered with gas [-]
P_{Ff}	Fraction of channel's perimeter covered with liquid [-]
P_i	Interfacial perimeter [m]
P_r	Reflected pressure [Pa]
P_s	Static overpressure [Pa]
r	Radial distance from the center of jets [m]
R	Universal gas constant [J/(K·mol)]
$\vec{R}$	Pipe reaction force acting on the fluid [N]
s	Entropy [J/K]
s_{fg}	Entropy difference between saturated vapor and saturated liquid [J/K]
S	Slip ratio [-]
St	Strouhal number [-]
$St_{cut-off}$	The minimum Strouhal number for helical modes in supersonic [-]
t	Time [s]
t'	Time required to reach the stagnation pressure [s]
t^*	Time at which pressure changes from positive to negative [s]

ΔT	Degree of subcooling [°C]
T	Thrust force [N]
T_e	The thrust force acting on pipe in the jet direction [N]
$\overrightarrow{T}$	Fluid thrust force vector on pipe [N]
u	Velocity [m/s]
u_a	Jet velocity at the asymptotic plane [m/s]
u_e	Jet velocity at the break plane [m/s]
u_f	Liquid phase velocity [m/s]
u_g	Gas phase velocity [m/s]
U_{jet}	Jet velocity [m/s]
U_S	Blast wavefront velocity [m/s]
U_{cr}	Critical flow velocity for isentropic flow [m/s]
$\overrightarrow{u}$	Fluid velocity vector [m/s]
$v_{M,a}$	Momentum specific volume at asymptotic plane [kg·m/s]
v_f	Specific volume of liquid [m³/kg]
v_g	Specific volume of gas [m³/kg]
V	Fluid control volume [m³]
W	Equivalent weight of TNT [kg]
W_a	Jet width at asymptotic plane [m]
W_f	Separation distance [m]
W_j	Jet width [m]
W_{jf}	Jet width corresponding to Ajf [m]
x	Steam quality [-]
Y	One half of the smaller of the object front's height or base width [m]
z	Axial distance downstream of the break plane [m]
z_a	Distance between the break plane and the asymptotic plane [m]
z_c	Jet core length [m]
z^*	Dimensionless axial distance [-]
Z	Scaled distance or Hopkinson-Cranz scaling law [m/kg$^{1/3}$]

GREEK SYMBOLS

α	Void fraction [-]
β	Frequency of damping [1/s]
θ	Angle [rad]
ρ_e	Density at the exit plane [kg/m³]
ρ	Momentum density [kg/m³]
σ_i	First positive zero of the order 1 Bessel Function
τ_{Fg} τ_{Ff}	Shear stress between the gas layer and the wall [Pa]
τ_i	Shear stress between the liquid layer and the wall [Pa]
Γ_{fg}	Interfacial shear stress [Pa]
φ	Rate of mass transfer due to evaporation at gas-liquid interface [kg/(m²·s)]
ω	Subcooling parameter [-]
Ω	Frequency of the structure [1/s]
	Frequency of load [1/s]

SUBSCRIPTS

0	Stagnant condition
a	Asymptotic plane

amb	Ambient condition
c	Center
cr	Critical condition
e	Break plane
eff	Effective nozzle diameter
exp	Experimental values
f	Liquid
g	Gas
i	Interface
in	Into the control volume
j	Jet
out	Out of the control volume

1 INTRODUCTION

The jet impingement due to postulated pipe rupture is of significant interest in the design and safety analysis of nuclear power plants. In nuclear power plants, most of the pipes are defined as a high-energy piping system (the maximum operating pressure exceeds 1.9 MPa or the maximum operating temperature exceeds 93.3°C during normal plant operating conditions) as in ANSI/ANS-58.2 (1988). When pipe rupture occurs, the fluid within the high-energy piping systems is discharged into the surrounding environment as a high-energy jet. Extreme load due to jet impingement after the pipe break can cause malfunction and significant damage to the surrounding structures, systems, and components (SSCs). In order to design protective systems to mitigate the damage from jet impingement, the consequences of a pipe break need to be well understood and properly modeled.

Three major phenomena are of interest for jet impingement in high-energy pipe rupture events, namely; jet impingement on the SSCs, jet expansion, and pipe whip. Jet impingement on the SSCs is the force exerted by the jet on the target and it directly determines the impact on the target, which in turn determines the integrity of the target component. To quantify the effect of jet impingement on the target, the impingement force needs to be calculated. For jet expansion, parameters of interest include jet geometry and pressure distribution within the jet. These two parameters govern the decay and evolution of the jet, which determine the zone of influence and the development of the jet in the spatial domain. Depending on the initial conditions of the fluid in the pipe before the break, the jet may expand due to the compressibility of gas, which determines the jet geometry. On the other hand, the stagnation pressure distribution in radial and axial direction within the jet characterizes the strength of jet. As such, the impingement force can be calculated by integrating the local pressure over the target. When jet impingement occurs, the fluid jet from a break in the high-energy piping system could significantly change the flow characteristics within the piping system, creating reaction forces on the piping system. If no protective device is installed such as pipe restraints, pipe whip can occur and cause rapid motion of the ruptured pipe. This reaction force on the piping system is the thrust force. Apart from these phenomena, the critical flow is also an important phenomenon of incompressible jets. While impingement force, jet geometry, pressure distribution, and thrust force are first-order parameters of interest, the critical flow rate is the second-order parameter of interest. This is because the flow rate is often involved in modeling the first-order parameters. The accuracy of predicting the critical flow rate determines the calculation accuracy for some of the first-order parameters.

In fact, the jet impingement is a complicated phenomenon that is affected by various factors. The factors that play important roles on jet impingement are identified as follows: (a) initial flow conditions (e.g., system pressure, temperature, and flow regime); (b) break conditions (e.g., direction, shape, edge treatment, and break size); and (c) target conditions (e.g., impingement distance and target geometry). In literature, experimental studies have been performed to investigate the jet impingement phenomena and most of the experimental studies were performed in the 1980s. Those include large-scale Marviken test (Marklund, 1985a, 1985b), medium-scale JAERI test (Isozaki et al., 1984; Yano, 1984; Yano et al., 1984, 1983) and Ontario-Hydro test (Forrest et al., 1987), and small-scale Mitsubishi test (Kawanishi et al., 1986; Kitade et al., 1979; Masuda et al., 1981), ENEA test (Celata et al., 1986), KWU test (Kastner and Rippel, 1988), and CRIEPI-Hitachi test (Morita et al., 2016; Takahashi et al., 2016; Xu et al., 2016). Most of the work has investigated the pressure distribution, thrust force, and impingement force.

Due to the importance of the jet impingement in nuclear power plants, both theoretical and empirical models have been developed to predict the important parameters. The models presented in ANSI/ANS-58.2 (1988) appendices and NUREG/CR-2913 (Weigand et al., 1983) are among the most widely used models for jet impingement, which have been employed in the design and safety analysis in nuclear power plants. In this document, the ANSI/ANS-58.2 (1988) model is referred to as the Standard model. The Standard model is a series of formulas while the two-phase jet load model in NUREG/CR-2913 (Weigand et al., 1983) is a series of look-up tables.

However, the Advisory Committee on Reactor Safeguards (ACRS) has identified several potential non-conservatisms in the existing models (Standard Review Plan, 2015: ML14230A035). The potential non-conservatisms are identified in the following phenomena: blast waves, jet plume expansion and zone of influence, distribution of pressure within the jet plume, and jet dynamic loading.

A blast wave is the first significant fluid load on surrounding SSCs in the event of a high-pressure pipe rupture. The way blast wave expands, reflects and amplifies needs to be accounted for in the model (Standard Review Plan, 2015: ML14230A035). However, blast waves are not considered in the Standard model.

For jet geometry, the standard assumes that a jet originating from a high-pressure pipe break will always spread with a fixed 45-degree angle up to an asymptotic plane and subsequently spread at a constant 10-degree angle. However, the jet spreading is highly dependent on the condition of the jet to the ambient condition (Standard Review Plan, 2015; Morita et al., 2016, 2018). Additionally, it has been shown that supersonic jet behavior can persist over far longer distances from the break than those calculated by the models in ANSI/ANS-58.2 (1988) (Standard Review Plan, 2015).

As for the pressure distribution within a jet plume, the standard assumes variable pressure over the jet cross-section for expanding jets. To calculate the spatial distribution of pressure, the standard assumes that the pressure within the jet is maximum at the jet centerline. However, this assumption can be invalid far from the break, where peaking near the edges of the jet is observed (Kitade et al., 1979; Masuda et al., 1981).

Another effect that is not considered in the existing models is jet dynamic loading. The unsteadiness in supersonic jets tends to propagate in the shear layer and induce time-varying oscillatory loads on obstacles in the flow path. Synchronization of the transient waves with the shear layer vortices emanating from the jet break can lead to significant amplification of the jet pressures and forces (Standard Review Plan, 2015). Moreover, the jet loading time scales can synchronize with the response of the neighboring structure, leading to further amplification of the loading. However, this resonance is not considered in the Standard model. In addition, the backward-propagating transient shock and expansion waves, generated by the interaction between jet and obstructions, are not considered in the Standard model.

In view of this, the objective of the current study is to address the identified potential non-conservatisms (Standard Review Plan, 2015) through a comprehensive literature review and model evaluation. Model guidance regarding the potential non-conservatisms will be developed based on the results of the literature review and model evaluation.

2   LITERATURE REVIEW

2.1   Review of Jet Impingement Phenomena

To perform an effective and comprehensive literature review, key phenomena and governing flow parameters are first identified in this section. Pipe whip, jet expansion, jet impingement and critical flow are the key phenomena that should be investigated.

2.1.1   Pipe Whip

The fluid jet from a break in high-energy piping system could significantly change the flow characteristics within the piping system, creating reaction forces on the piping system. This force acting on the ruptured pipe is a function of time and space, and depends upon the fluid state within the pipe prior to rupture, break flow area, frictional losses, plant system characteristics, piping system geometric design, and other factors (ANSI/ANS-58.2, 1988). The derivation of thrust force is presented in the Appendix A of ANSI/ANS-58.2 (1988). The derivation starts with Newton's second law of motion:

$$\sum \vec{F} = \sum \frac{d}{dt}\left(m\vec{u}\right) \tag{2-1}$$

where $\sum \vec{F}$ is vector sum of all external forces acting on the control volume (c.v.), m is the fluid mass in control volume and $\vec{u}$ is the fluid velocity vector. A generalized control volume is shown in Figure 2-1. The momentum time rate of change can be expressed as:

$$\frac{d}{dt}\left(m\vec{u}\right) = \int\limits_{C.V.} \frac{d}{dt}\left(\rho\vec{u}\right) dV + \int\limits_{C.S.} \rho\vec{u}\left(\vec{u} \cdot d\vec{A}\right) \tag{2-2}$$

which is the rate of change of momentum within the control volume and the difference between outgoing and incoming flux across its surfaces (control surface or c.s.). The sum of external forces is:

$$\sum \vec{F} = \int\limits_{c.s.} Pd\,\vec{S} = \vec{R} - \int\limits_{A_{in}} Pd\,\vec{A}_{in} - \int\limits_{A_{out}} Pd\,\vec{A}_{out} \tag{2-3}$$

Therefore, the pipe reaction force acting on the fluid, $\vec{R}$, minus the ambient pressure force is equal to the reaction thrust force acting on the pipe, but in the opposite direction. Combining Equations (2-2) and (2-3), the thrust force is:

$$\vec{T} = -\left(\vec{R} - \int\limits_{A_{pipe}} p_{amb}\,dA_{pipe}^{\rightarrow}\right)$$

$$= -\left[\int\limits_{C.V.} \frac{d}{dt}\left(\rho\vec{u}\right)dV + \int\limits_{C.S.} \rho\vec{u}\left(\vec{u} \cdot d\vec{A}\right) + \int\limits_{A_{in}} Pd\vec{A}_{in} + \int\limits_{A_{out}} Pd\vec{A}_{out} - \int\limits_{A_{pipe}} p_{amb}\,dA_{pipe}^{\rightarrow}\right] \tag{2-4}$$

where P is the fluid pressure within the pipe, p_{amb} is the ambient pressure and A is the pipe cross sectional area. For steady-state flow conditions, assuming uniform flow at any cross-section area and a constant flow area denoted as A_e, the thrust force becomes:

$$T = -\left[\rho u_e^2 A_e + p_e A_e - p_{amb} A_e \right]$$

(2-5)

where T is the thrust force acting on pipe in the flow direction, A_e is the break area, and p_e is the fluid static pressure at the break plane. In literature, a thrust coefficient is usually defined to calculate thrust force:

$$C_T = \frac{T}{\left(p_e - p_{amb} \right) A_e}$$

(2-6)

This thrust coefficient can be predicted by measuring the thrust force T or by theoretical derivation, which will be discussed in Section 2.2.2.1.
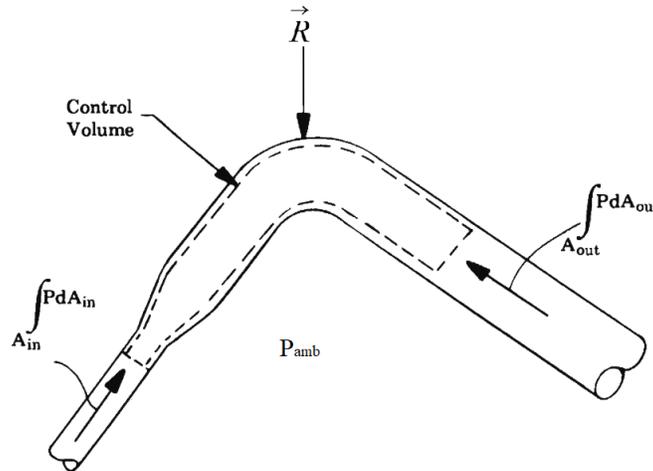
Figure 2-1 Generalized Control Volume (Image from ANSI/ANS-58.2, 1988)

2.1.2 Jet Expansion

The jet geometry and pressure distribution are greatly affected by the initial conditions of the jet including initial flow conditions and break conditions. The initial flow conditions are system pressure, temperature and quality, while the break conditions are the direction, shape, edge treatment, and size of the break.

For high-energy piping systems as in nuclear power plants, the high pressure and high-temperature fluid inside the pipe is discharged into the atmosphere and expands with supersonic velocities downstream of the break. For jet geometry, the jet extension can be investigated by visualization studies using a high-speed camera (Celata et al., 1986), particle image velocimetry (PIV) (Morita et al., 2016; Takahashi et al., 2016; Xu et al., 2016), X-rays (Celata et al., 1986), or through pressure and temperature measurements (Kawanishi et al., 1986; Masuda et al., 1981). Due to the simplicity of jet visualization, the high-speed camera has been often employed in the literature. The obtained images can be analyzed to acquire jet geometry information. Particularly, the photographic images and PIV images can be employed

to define the jet boundary, and X-ray images can be used to investigate the high-density jet core for steam-water mixture jets. The pressure and temperature measurements can generate local-point results, and usually require some interpolation or extrapolation. Meanwhile, a threshold for pressure is needed to determine the jet boundary. Due to the measurement inaccuracies and errors, ambient pressure may not be a good criterion.

The pressure distribution also depends on the target condition. When supersonic jets encounter a target, a shock wave forms in the flow field at a short distance from the target. The thermodynamic properties downstream of this shock determine the pressure field and load on the target. The shock exists because the fluid needs to deaccelerate rapidly in a very short distance. This shock wave can be characterized as an instantaneous, irreversible compression of the fluid. The energy for performing this irreversible compression comes from the kinetic energy of the upstream fluid. Since this process is irreversible, the kinetic energy decreases and the entropy increases across the shock. As a result, stagnation pressure decreases.

2.1.3 Jet Impingement

Jet impingement on the SSCs directly determines the impact on the target, which in turn determines the integrity of the target component. Therefore, it is important to investigate jet impingement. This can be done by predicting a static jet impingement force, in addition to accounting for the effects of jet dynamic loading and blast wave.

2.1.3.1 Jet Impingement Force

In jet impingement, the force exerted by the jet on targets is of particular importance. Unlike the thrust force and jet geometry, this force depends not only on the initial conditions of the jet, but also the target conditions (ANSI/ANS-58.2, 1988). Target conditions such as target axial distance, target radial location, target shape, area, and orientation greatly affect the jet load on targets. If the target is large enough and the entire jet is intercepted, then the entire jet force is applied to the target. If the target intercepts a fraction of the jet, then the jet pressure distribution over the target must be integrated over the target area to obtain the jet force.

2.1.3.2 Jet Dynamic Loading

For high-speed jets, especially supersonic jets, the unsteadiness in the jets tend to propagate in the shear layer, which can induce time-varying oscillatory loads on the targets. When interacting with obstructions, the typical supersonic jet will generate backward-propagating transient shock and expansion waves. This will enhance the unsteadiness in the downstream shear layers. Once the dynamic jet loading on the target synchronizes with the dynamic response of the neighboring structure, resonance can occur and cause further amplification of the loading. This jet dynamic loading effect has not been considered in the existing jet impingement models.

An Areva report (Areva NP Inc., 2013) discusses this dynamic loading effect on surrounding SSCs and provided a modeling approach for jet dynamic loading in nuclear power plants. The approach is to first calculate the resonance frequency of the jet and then compare with that of surrounding structures to determine the dynamic loading factor. However, it needs to be noted that this approach was developed for applications in Aerospace Engineering and may not be directly applicable to the current work. Additional assessments using experimental data may need to be made to evaluate this modeling approach, such that it can be adopted for jet impingement in nuclear power plants.

2.1.3.2.1 Jet Resonant Frequency

The jet resonant frequency has been investigated for single-phase gas in the literature. Nosseir and Ho (1979) and Ho and Nosseir (1981) presented air-jet data and analysis used in calculating the resonant frequency of high-speed subsonic jets ($0.7 < M < 1.0$) at target distances (z/D) less than 7.5. Tam and Ahuya (1990) presented theoretical background and experimental data to calculate the minimum jet resonant frequencies for supersonic jets ($M > 1.0$). Both axisymmetric and helical mode shapes jets are considered. It was also demonstrated that this approach can be employed to predict the minimum resonance frequency for subsonic jets. The study by Henderson (2002) has shown that when NPR (nozzle pressure ratio) is greater than 3.38 and the target distance (z/D) exceeds 5, the resonance in the jet is unlikely to occur.

For supersonic axisymmetric modes jet, the minimum frequencies can be calculated based on the study by Tam and Ahuya (1990):

$$f_{min} = \frac{\sigma_i U_{jet}}{\pi D_{jet} M \left(a_{jet} / a_{amb} \right) \left\{ \left[\left(a_{amb} / a_{jet} \right) + M \right]^2 - 1 \right\}^{0.5}} \tag{2-7}$$

where f_{min} is the minimum axisymmetric mode resonance frequency for supersonic jet, σ_i is the first positive zero of the order 1 Bessel Function, U_{jet} is the jet velocity, D_{jet} is the jet diameter, M is the jet Mach number, a_{jet} is the jet speed of sound and a_{amb} is the ambient speed of sound.

For subsonic axisymmetric modes and supersonic helical modes, the frequencies of the jets (f_{jet}) can be calculated using the Strouhal number, where Strouhal number is defined as:

$$St = \frac{f_{jet} D_{nozzle}}{U_{jet}} \tag{2-8}$$

where f_{jet} is the jet frequency, D_{nozzle} is the characteristic length (nozzle diameter), and U_{jet} is jet velocity. Tam and Ahuya (1990) plotted a relation between Strouhal number and Mach number for axisymmetric modes in subsonic jet and helical modes in supersonic jet as shown in Figure 2-3. For high subsonic jets, the instability waves can only be axisymmetric, while for supersonic jets, they can be either axisymmetric or helical. For the wave mode (n,m) in Figure 2-2, the first number in the bracket (n) is the azimuthal wave number and the second one (m) is the radial wave number. $St_{cut,off}$ is the minimum Strouhal number for supersonic helical modes. When n is 0 it is the axisymmetric wave mode and when n is 1 it is the helical wave mode. For both subsonic and supersonic jets, the least dispersive model ($m = 1$) is the only possible mode of resonance. It needs to be noted that the approaches provided by Tam and Ahuya (1990) are only to calculate the minimum frequencies for jet resonance. The natural frequencies of surrounding SSCs need to be determined to evaluate the dynamic loading effect.
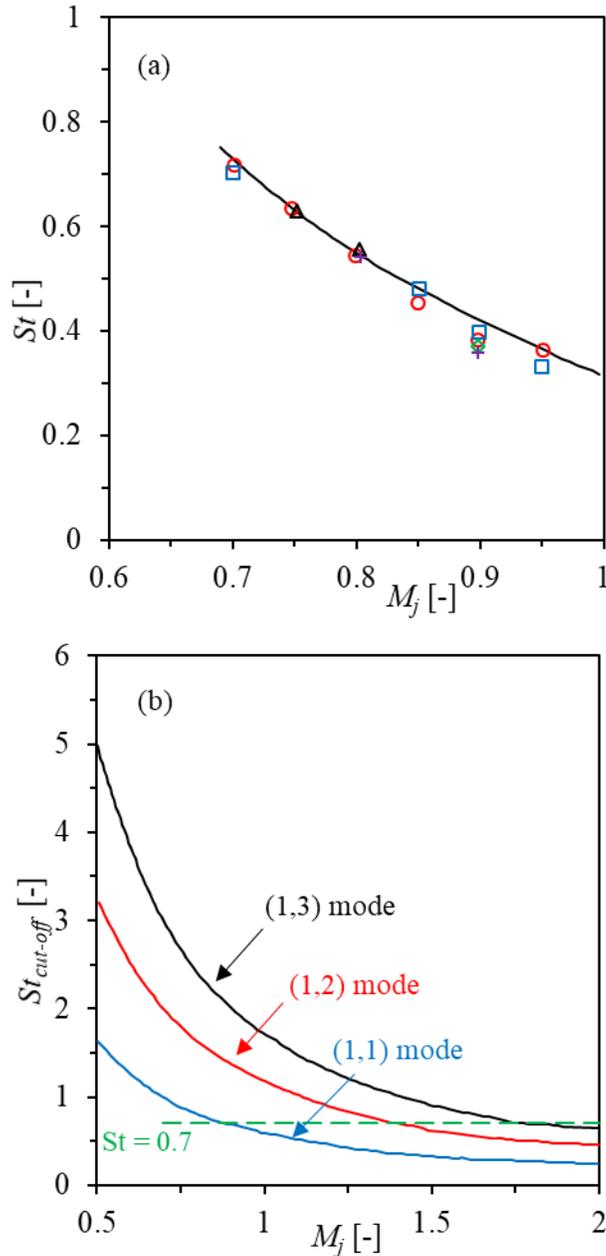
Figure 2-2 Relation between Strouhal Number and Mach Number for (a) Subsonic Axisymmetric Modes (0,1) Mode and (b) Supersonic Helical Modes (Tam and Ahuya, 1990)

2.1.3.2.2 Dynamic Loading Factor (DLF)

The Areva report ANP-10318NP (Areva NP Inc., 2013) discussed the dynamic load factor for idealized single degree of freedom (SDOF) structures and multi-degree of freedom (MDOF) structures. The DLF with a sinusoidally varying load from Biggs (1964) was employed to calculate the DLF for SDOF structures. The relation between DLF, Ω/ω (frequency of load to the frequency of the structure), and β/ω (frequency of damping to the frequency of the structure) is shown in Figure 2-3. As shown in the plot, the damping significantly reduces the DLF. Meanwhile, when the Ω/ω is greater than 1.4, the DLF is always less than 1, independent on the

damping effect. This indicates the dynamic loading effect does not need to be evaluated when the minimum jet frequency is at least 40% greater than the frequency of target structures.
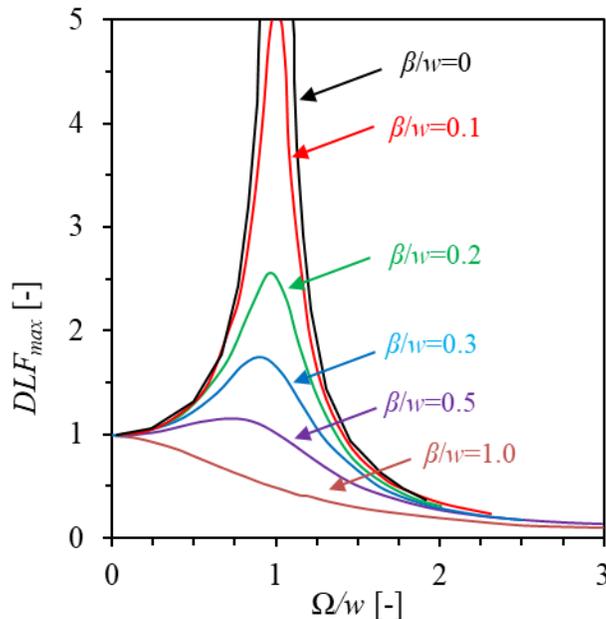
Figure 2-3 Dynamic Load Factor (DLF) with a Sinusoidally Varying Load (Biggs, 1964)

2.1.3.3 Blast Wave

In high-energy pipe rupture events, the first significant fluid load on surrounding SSCs may be induced by a blast wave. This blast wave may create an extreme load on the SSCs within a short time period. While there have been limited studies in investigating the impact of blast wave in jet impingement, extensive studies have been performed in weapon design or building design to understand the impact of blast waves in detonation.

The blast wave is characterized by increased pressure and flow due to the release of a large amount of energy in a small volume. It is an area of compressed air expanding supersonically outward from an explosive core, which has a leading shock at the front of the compressed gases. As the wave propagates away from the explosive core, the pressure of the compressed air at the blast wave front reduces. Meanwhile, the pressure at the explosive core falls below ambient atmospheric levels as cooling and expansion continues. This occurs because the velocity of the gas particles causes them to over-expand slightly before the momentum is lost (Neff, 1998). As a result, the negative pressure draws items back in towards the center.

2.1.3.3.1 Blast Wave Form

The simplest form of a blast wave is described as the Friedlander waveform (Friedlander, 1946). This is when the blast wave is in the free field and there is no surface nearby to interact with the blast wave. The following equation describes the pressure as a function of time for blast waves:

$$P(t) = P_s e^{-\frac{t}{t^*}}\left(1 - \frac{t}{t^*}\right)$$

(2-9)

where $P(t)$ is the pressure as a function of time at the explosive core, P_s is the peak static overpressure and t^* is the time at which the pressure changes from positive value to negative value. At time equals to $2t^*$, the pressure reaches minimum value where P_{min} = -0.135P_s. A schematic drawing of the pressure profile for Friedlander waveform is shown in Figure 2-4.
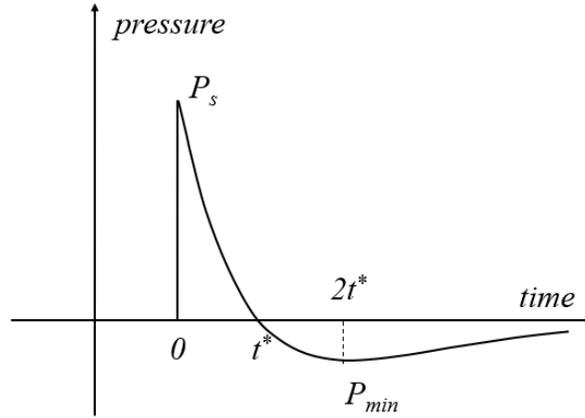
Figure 2-4 Typical Blast Wave Pressure Profile as a Function of Time (Friedlander, 1946)

Apart from the peak static overpressure P_s, there are several more important wavefront parameters, including static density ρ_s, maximum dynamic pressure Q_s, and the blast wavefront velocity U_s. The following equations presented by Rankine and Hugoniot in 1870 (Smith and Hetherington, 1994) can be used to calculate the above parameters for normal reflections based on P_s:

$$U_s = \sqrt{\frac{6P_s + 7p_{amb}}{7p_{amb}}} a_{amb} \tag{2-10}$$

$$\rho_s = \frac{6P_s + 7p_{amb}}{P_s + 7p_{amb}} \rho_{amb} \tag{2-11}$$

$$Q_s = \frac{5P_s^2}{2(P_s + 7p_{amb})} \tag{2-12}$$

where p_{amb}, a_{amb}, and ρ_{amb} are the pressure, speed of sound and density of air in ambient conditions ahead of the blast wave. Therefore, the determination of overpressure P_s is the key to calculate other parameters. There have been two approaches to calculate P_s based on the scaled parameter Z:

$$Z = \frac{r}{W^{\frac{1}{3}}} \tag{2-13}$$

where Z is the scaled distance or Hopkinson-Cranz scaling law, r is the radius from the center of the explosion given in meters and W is the equivalent weight of TNT given in kilograms. For jet impingement, this equivalent weight of TNT can be obtained by measuring the initial energy

released from the sudden break. The first approach to calculate P_s is developed by Brode (1955):

$$P_s = \left(\frac{6.7}{Z^3} + 1\right) \times 10^5 [Pa] \qquad \text{for } P_s > 10^6 \text{ pa} \tag{2-14}$$

$$P_s = \left(\frac{0.975}{Z} + \frac{1.455}{Z^2} + \frac{5.85}{Z^3} - 0.019\right) \times 10^5 [Pa] \qquad \text{for } 10^5 < P_s < 10^6 \text{ pa} \tag{2-15}$$

The equations presented by Henrych (Smith and Hetherington, 1994) divide the analysis into three fields: a near, middle and far field.

$$P_s = \left(\frac{14.072}{Z} + \frac{5.540}{Z^2} - \frac{0.357}{Z^3} + \frac{0.00625}{Z^4}\right) \times 10^5 [Pa] \qquad \text{for } 0.05 < Z < 0.3 \tag{2-16}$$

$$P_s = \left(\frac{6.194}{Z} - \frac{0.326}{Z^2} + \frac{2.132}{Z^3}\right) \times 10^5 [Pa] \qquad \text{for } 0.3 < Z < 1 \tag{2-17}$$

$$P_s = \left(\frac{0.662}{Z} + \frac{4.05}{Z^2} + \frac{3.288}{Z^3}\right) \times 10^5 [Pa] \qquad \text{for } 1 < Z < 10 \tag{2-18}$$

Weggel (2010) also presented a correlation between P_s and Z, which is from US Department of the Army (2008). As shown in Figure 2-5, the approaches by Henrych (Smith and Hetherington, 1994) and Weggel (2010) can also predict the experimental data relatively better than Brode (1995).
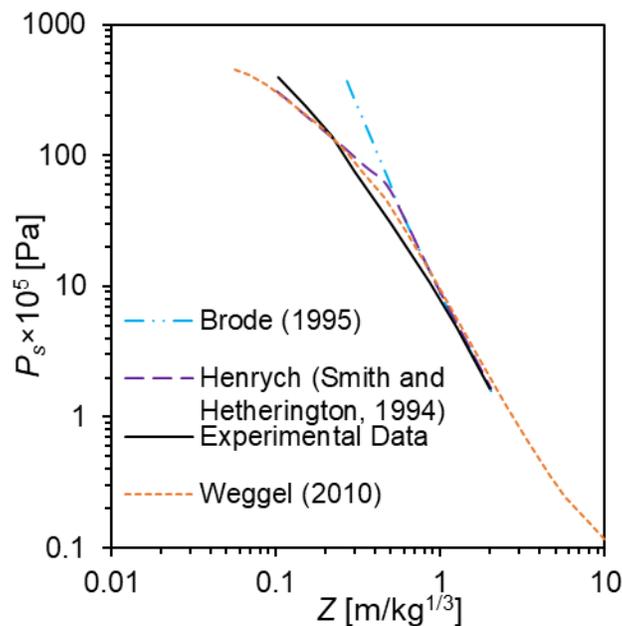
Figure 2-5 Comparison between Brode Equations, Henrych Equations, and Weggel Correlation with Experimental Data (Baker et al., 1983)

2.1.3.3.2 Reflections

In general, it is considered to be reasonable to assume a spherical blast wave, and this assumption can simplify the analysis of the wave transport and wave effects. However, in nuclear power plants, the expansion of the potential blast wave may happen in an enclosed space. The blast wave can diffract through a narrow opening and refract as they pass through materials. When a blast wave reaches the boundary between two different materials, it can be transmitted, absorbed, and reflected. The reflection/deflection of blast waves from walls and neighboring structures may create complex behavior of the wave and increase the wave duration (Neff, 1998).

The reflections of blast wave are divided into three categories based on the incident angle: normal reflections, oblique reflections and Mach stem formation. Normal reflections occur when the incident angle is zero and oblique reflections occur when the incident angle is small, less than approximately 40° in air. Mach stem formation occurs for large angles of incidence. When a blast wave reflects off the ground and the reflection reaches the original shock front, this creates a high-pressure zone that extends from the ground up to a certain point called the triple point at the edge of the blast wave (Neff, 1998).

The total pressure experienced by the object is the peak reflected pressure P_r, which is a combination of static (P_s) and dynamic (Q_s) pressure. For normal reflections, P_r is given by:

$$P_r = 2P_s + (\gamma + 1) Q_s \tag{2-19}$$

The following relation is obtained for air ($\gamma = 1.4$):

$$P_r = 2P_s \frac{7 p_{amb} + 4 P_s}{7 p_{amb} + P_s} \tag{2-20}$$

These relations are derived from the Rankine-Hugoniot relation (Smith and Hetherington, 1994). Although these correlations are derived to model the blast wave in detonation, they are independent of the energy source (e.g., explosion). Therefore, they are used to quantify the potential blast wave in Section 4.2.1.

2.1.3.3.3 Dynamic Loading of Blast Wave

The first load on the target will be the reflected pressure. Since this reflected pressure is much higher than the surrounding medium, this will generate a flow from high pressure region to lower pressure air surrounding the object. A rarefaction wave is developed to dissipate the excess pressure. The pressure drops to the stagnation pressure (P):

$$P(t) = P_s(t) + Q_s(t) \tag{2-21}$$

The time required to reach the stagnation pressure from the initial reflected pressure load is approximately:

$$t' = \frac{3Y}{U_s} \tag{2-22}$$

where *Y* is one half of the smaller of the object front's height or base width. This parameter represents the minimum distance the dissipation wave must travel. Once the stagnation pressure is reached, the load will follow the stagnation pressure curve for the remaining load. More detailed discussion can be found in Smith and Hetherington (1994).

2.1.4   Critical Flow

Critical flow, also referred to as choked flow, is encountered in many engineering devices such as nozzles and throttling valves. The critical flow rate is the maximum flow rate that can be attained by a compressible fluid as it flows from a high-pressure region to a low-pressure region. For incompressible flow, the flow rate can be increased by reducing the receiving region pressure. For compressible flow, the decrease in downstream pressure causes an increase in the flow rate, but choking flow is achieved when further reduction of the downstream pressure no longer affects the flow rate. This situation occurs for both single gas flow as well as two-phase gas-liquid mixture flows.

2.1.4.1   Compressible Gas Flow

For compressible flow, the ideal gas law is employed in calculating the critical flow conditions. The critical flow is identical to the mass flow at the sonic speed for isentropic conditions. The critical flow velocity (U_{cr}), mass flow rate ($\dot{m}$), and exit pressure (P_{cr}) for isentropic flow have been discussed extensively in the literatures (Shapiro, 1953; Webb, 1976; Todreas and Kazimi, 2011) and are summarized as follows:

$$U_{cr} = \left(\frac{2k}{k+1} RT_0 \right)^{1/2} \tag{2-23}$$

$$\dot{m} = A \sqrt{ \frac{k}{R} \left(\frac{2}{k+1} \right)^{(k+1)/(k-1)} } \frac{P_0}{\sqrt{T_0}} \tag{2-24}$$

$$P_{cr} = P_0 \left(\frac{2}{k+1} \right)^{k/(k-1)} \tag{2-25}$$

where *k* is the ratio of specific heats (C_p/C_v), *R* is the universal gas constant, T_0 is the stagnation temperature (°R) and P_0 is the stagnation pressure (psia).

2.1.4.2   Two-phase Gas-liquid Mixture Flow

For two-phase mixture flow, there are critical flow models based on the Homogeneous Equilibrium Model (HEM) and the Separated Flow Model (SFM). The HEM treats a two-phase mixture as a pseudo fluid with uniform properties across the flow area. The model also assumes equal phase velocities and uniform velocity across the flow area. The SFM treats the two phases with their individual properties and velocities. The simplest SFM is the Slip Flow Model, which assumes uniform velocities within each phase and allows for velocity differences between two phases. The critical flow rate can be derived from the momentum equations for two-phase flow in a pipe based on the Slip Flow Model (Kim and Mudawar, 2015):

$$\frac{d}{dz}\left(\rho_g u_g^2 A_g\right) - \Gamma_{fg} u_i = -\alpha A \frac{dP}{dz} - \tau_{F_g} P_{F_g} - \tau_i P_i - \rho_g g \alpha A \sin\theta \qquad (2\text{-}26)$$

$$\frac{d}{dz}\left(\rho_f u_f^2 A_f\right) + \Gamma_{fg} u_i = -(1-\alpha) A \frac{dP}{dz} - \tau_{F_f} P_{F_f} + \tau_i P_i - \rho_f g (1-\alpha) A \sin\theta \qquad (2\text{-}27)$$

where Γ_{fg}, u_i, τ_{Fg}, τ_{Ff}, τ_i, P_{Fg}, P_{Ff}, and P_i are rate of mass transfer due to evaporation at the gas-liquid interface, interfacial axial velocity, shear stress between the gas layer and the wall, shear stress between the liquid layer and the wall, interfacial shear stress, fraction of channel's perimeter covered with gas, fraction of channel's perimeter covered with liquid, and interfacial perimeter. It can be shown that the critical mass flux (G_{cr}) is:

$$G_{cr} = \left[-\frac{d}{dP}\left(\frac{1}{\rho'}\right)\right]^{-1/2} = \left\{-\frac{d}{dP}\left[\frac{v_g x^2}{\alpha} + \frac{v_f (1-x)^2}{(1-\alpha)}\right]\right\}^{-1/2} \qquad (2\text{-}28)$$

Or

$$G_{cr} = \left\{-\left[\frac{x^2}{\alpha}\frac{dv_g}{dP} + \frac{(1-x)^2}{(1-\alpha)}\frac{dv_f}{dP} + \left(\frac{2v_g x}{\alpha} - \frac{2v_f(1-x)}{(1-\alpha)}\right)\frac{dx}{dP} - \left(\frac{v_g x^2}{\alpha^2} - \frac{v_f(1-x)^2}{(1-\alpha)^2}\right)\frac{d\alpha}{dP}\right]\right\}^{-1/2} \qquad (2\text{-}29)$$

where x is flow quality, α is void fraction, v_f and v_g are specific volume of liquid and gas, and ρ' is the momentum density:

$$\frac{1}{\rho'} = \frac{x^2}{\rho_g \alpha} + \frac{(1-x)^2}{\rho_f (1-\alpha)} \qquad (2\text{-}30)$$

By introducing the slip ratio, S, which is defined as the ratio of gas velocity to liquid velocity:

$$S = \frac{u_g}{u_f} \qquad (2\text{-}31)$$

the critical mass flux becomes:

$$G_{cr} = \left\{-\left[\begin{array}{l}\left(x^2 + \frac{x(1-x)}{S}\right)\frac{dv_g}{dP} + \left[(1-x)^2 + Sx(1-x)\right]\frac{dv_f}{dP} + \\[2mm] \left[2v_g x - \frac{v_g(1-2x)}{S} + v_f S(1-2x) - 2v_f(1-x)\right]\frac{dx}{dP} - x(1-x)\left(v_f - \frac{v_g}{S^2}\right)\frac{dS}{dP}\end{array}\right]\right\}^{-1/2} \qquad (2\text{-}32)$$

There have been different models developed for slip ratio. In HEM, the slip ratio is set to be 1. In Fauske model (Fauske, 1962), the slip ratio of $(v_g/v_f)^{1/2}$ was obtained by minimizing the momentum density:

$$\frac{\partial}{\partial S}\left[xu_g+\left(1-x\right)u_f\right]=0 \tag{2-33}$$

Moody (1965) developed a model for slip ratio based on the assumption of isentropic two-phase annular flow through a nozzle. The slip ratio of $(v_g/v_f)^{1/3}$ was obtained by maximizing the two-phase flow rate:

$$\frac{\partial}{\partial S}\left[\frac{xu_g^2}{2}+\frac{\left(1-x\right)u_f^2}{2}\right]=0 \tag{2-34}$$

where h_0, h_f, h_g and h_{fg} is the specific stagnation enthalpy, liquid enthalpy, gas enthalpy, and latent heat of vaporization, respectively. s_0, s_g, s_f and s_{fg} is the stagnation entropy, entropy of saturated vapor, entropy of saturated liquid, and entropy difference between saturated vapor and saturated liquid, respectively. This slip ratio obtained by Moody (1965) is identical to that by Zivi (1964). Based on the experimental study by D'Auria and Vigni (1981) (as cited in Cumo, 1983), the homogeneous assumption at the break exit is more appropriate than the slip correlations such as $(v_g/v_f)^{1/3}$ by Moody (1965), and $(v_g/v_f)^{1/2}$ by Fauske (1962).

In a recent work by Petrovic and Stevanovic (2016), a new model for two-phase critical flow is developed by considering the effects of void fraction and two-phase mixture density on slip ratio. The two-phase mixture critical velocity is calculated using the frozen sonic velocity:

$$c=\left[\frac{\partial\rho}{\partial p}\right]^{-\frac{1}{2}} \tag{2-35}$$

where ρ is the mixture density:

$$\rho=\frac{\alpha}{v_g}+\frac{\left(1-\alpha\right)}{v_f} \tag{2-36}$$

and α is void fraction of gas phase:

$$\alpha=\frac{1}{1+\frac{1-x}{x}S\frac{v_f}{v_g}} \tag{2-37}$$

In Equation (2-37), the slip ratio is calculated by the following equation:

$$S=\min\left(\left[1+x\left(\frac{v_g}{v_f}-1\right)\right]^{0.5}\quad,\quad\left(\frac{v_g}{v_f}\right)^{1/3}\right) \tag{2-38}$$

2.2 Review of Jet Impingement Experiments

This section performs a comprehensive literature review on the experimental studies of jet impingement.

2.2.1 Overview of Experimental Studies

After a literature review, it is found that most of the experimental studies were performed in 1980s. Some of studies including large-scale Marviken test (Marklund, 1985a, 1985b) and small-scale ENEA test (Celata et al., 1986) have been discussed in the workshop on jet impingement and pipe whip in Genova (1981). Since then, additional tests including medium-scale JAERI test (Isozaki et al., 1984; Yano, 1984; Yano et al., 1983, 1984) and Ontario-Hydro test (Forrest et al., 1987), and small-scale Mitsubishi test (Kawanishi et al., 1986; Kitade et al., 1979; Masuda et al., 1981), KWU test (Kastner and Rippel, 1988), and CRIEPI-Hitachi test (Morita et al., 2016; Takahashi et al., 2016; Xu et al., 2016) were performed. A summary of these experimental tests including initial fluid conditions, break conditions, target conditions, and investigated parameters is shown in Table 2-1. As shown in the table, most of the work has investigated the pressure distribution, thrust force, and impingement force. In general, the local static or stagnation pressure was measured by pressure transducers and thrust force or impingement force was measured by load cells. Figure 2-6 through Figure 2-8 show the experimental setup for small-scale (Masuda et al., 1981), medium-scale (Yano et al., 1984) and large-scale (Marklund, 1985b).

2.2.2 Discussion on Experimental Results

This section presents the discussion on results for the experimental tests reviewed. Discussion will be divided based on the jet impingement parameters.

2.2.2.1 Thrust Coefficient

The thrust coefficient can be calculated based on Equation (2-6), once thrust force is measured experimentally. The values of thrust coefficients depend on the initial fluid condition prior to the break. Therefore, the thrust coefficients for different types of jet are discussed.

2.2.2.1.1 Saturated and Superheated Steam Jets

The thrust coefficient for steady-state saturated steam jet was investigated in the Mitsubishi test (Kitade et al., 1979; Masuda et al., 1981). In Kitade et al. (1979), the steam was ejected into the atmospheric condition through a pipe of inner diameter of 9.4 mm. The thrust coefficient was found to be 1.12 based on experimental results. In Masuda et al. (1981), the effects of nozzle geometry and edge treatment on the thrust coefficient are investigated. The results are found as follows:

C_T = 1.21, circular nozzle with round edge;
C_T = 1.12, circular nozzle with sharp edge;
C_T = 1.14, elliptical nozzle with round edge;
C_T = 1.08, elliptical nozzle with sharp edge.

This indicates that the circular nozzle has a larger thrust coefficient than the elliptical nozzle, and round edge break has a larger C_T than the sharp edge break.

Table 2-1 A Summary of Experimental Tests on Jet Impingement

Test Name	Literature	Initial Fluid Conditions Flow Regime	P_0 (MPa)	Free or Impinging	Break Conditions Type	Geometry	ID (mm)	L_P/D [-]	Direction	Edge treatment	Target Conditions Type	z/D [-]	Time Domain	Parameters Measured
	Kitade et al. (1979)	Saturated Steam	0.98 ~ 4.02	Imp	Nozzle	Circular	9.4	12.8	Circumferential	Sharp	Flat Plate	0.59 ~ 6.60	Steady State	Thrust force, impinging force, pressure
	Kitade et al. (1979)	Water (ΔT: 13 ~ 41 °C)	6.86, 14.71	Imp	Nozzle Rupture Disk	Circular	10.5 ~ 43.1	–	Circumferential	Sharp	Flat Plate	3.93 ~ 27.6	Transient	Thrust force, impinging force, pressure
Mitsubishi Test	Masuda et al. (1981)	Steam	4.56	Imp / Free	Nozzle	Circular	10	12	Longitudinal	Sharp / Round	Flat Plate	0.5 ~ 62.5	Steady State	Thrust force, impinging force, pressure
					Nozzle	Elliptical	19.9 x 5 (H_d = 10)	0	Longitudinal	Sharp / Round				
	Kawanishi et al. (1986)	All regimes	2.05, 4.02	Imp / Free	Nozzle	Circular	5	–	Circumferential	Sharp / Round	Flat Plate	1 ~ 11	Steady State	Thrust force, pressure
					Nozzle	Elliptical	10 x 2.5 (H_d = 5)	–	Circumferential	Round			Steady State	Thrust force, pressure
	Yano et al. (1983)	Water (ΔT: 25 °C)	15.6	Imp	Rupture Disk	Irregular	101.6	–	Circumferential	Sharp	–	~100	Transient	Thrust force
JAERI Test	Isozaki et al. (1984)						101.6	–	Circumferential	Sharp	Flat Plate	5	Transient	Thrust force, pressure
	Yano et al. (1984) Yano (1984)	Saturated Water	6.86	Imp	Rupture Disk	Irregular	152.4	60 with 3 elbows	Circumferential	Sharp	Flat Steel Disk	2, 5	Transient	Thrust force, impinging force, pressure
Marviken Test	Marklund (1985a, 1985b)	Water (ΔT: 0, 30, 50 °C)	5	Imp / Free	Rupture Disk	Circular	200, 299, 509	–	Circumferential	Not Specified	Flat Plate / Cavity / Pipe	0.25 ~ 5.24	Transient	Impinging force, pressure

Table 2-1 A Summary of Experimental Tests on Jet Impingement (cont.)

Test Name	Literature	Initial Fluid Conditions		Free or Impinging	Break Conditions						Target Conditions		Time Domain	Parameters Measured
		Flow Regime	P_0 (MPa)		Type	Geometry	ID (mm)	L_P/D [-]	Direction	Edge treatment	Type	z/D [-]		
ENEA Test	Celata et al. (1986)	Water (ΔT: 0 ~ 110 °C)	0.8 ~ 25	Free	Nozzle	Circular	4.6	10, 100, 300	Circumferential	Not Specified	–	2	Transient	Jet geometry
Ontario-Hydro Test	Forrest et al. (1987)	Water (ΔT: 20 ~ 60 °C)	0.7 ~ 7	Imp / Free	Nozzle Air-actuated valve	Circular	25, 76, 102	–	Circumferential	Not Specified	Flat plate / Pipe	1, 3, 9	Transient	Impinging force, pressure
KWU Test	Kastner and Rippel (1988)	Subcooled Water	0.5 ~ 10.2	Imp	Nozzle	Circular	10 - 65	–	Circumferential / Longitudinal	Not Specified	Flat plate / H-Beams / Pipe	–	Quasi-Steady State	Impinging force, pressure
						Rectangular	132 x 10.4							
CRIEPI-Hitachi Test	Morita et al. (2016); Takahashi et al. (2016); Xu et al. (2016)	Steam	0.23, 0.4, 0.58, 0.82	Free	Nozzle	Circular	8, 12	25	Circumferential	Not Specified	–	–	Steady State	Jet Geometry, velocity

2-15
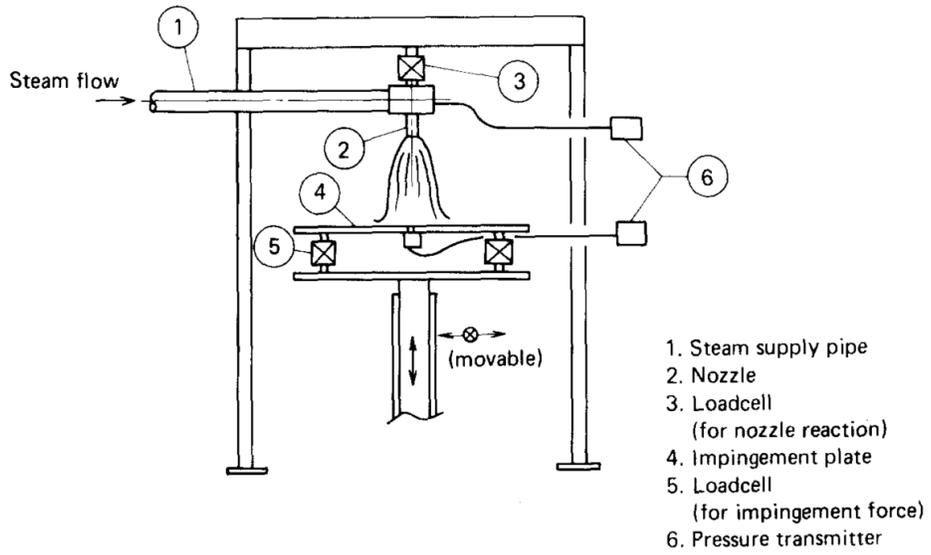
Figure 2-6 Experimental Setup for Jet Impingement in Small-scale Test (Masuda et al., 1981)

1. Steam supply pipe
2. Nozzle
3. Loadcell
   (for nozzle reaction)
4. Impingement plate
5. Loadcell
   (for impingement force)
6. Pressure transmitter
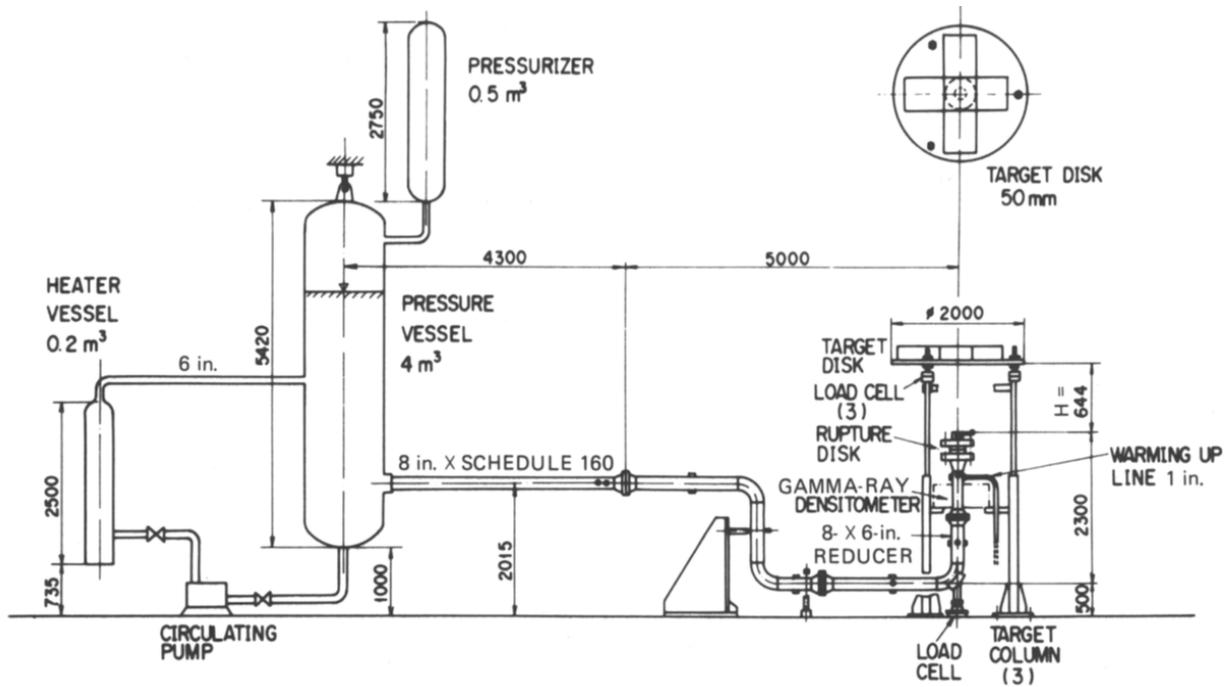
Figure 2-7 Experimental Setup for Jet Impingement in Medium-scale Test (Yano et al., 1984)
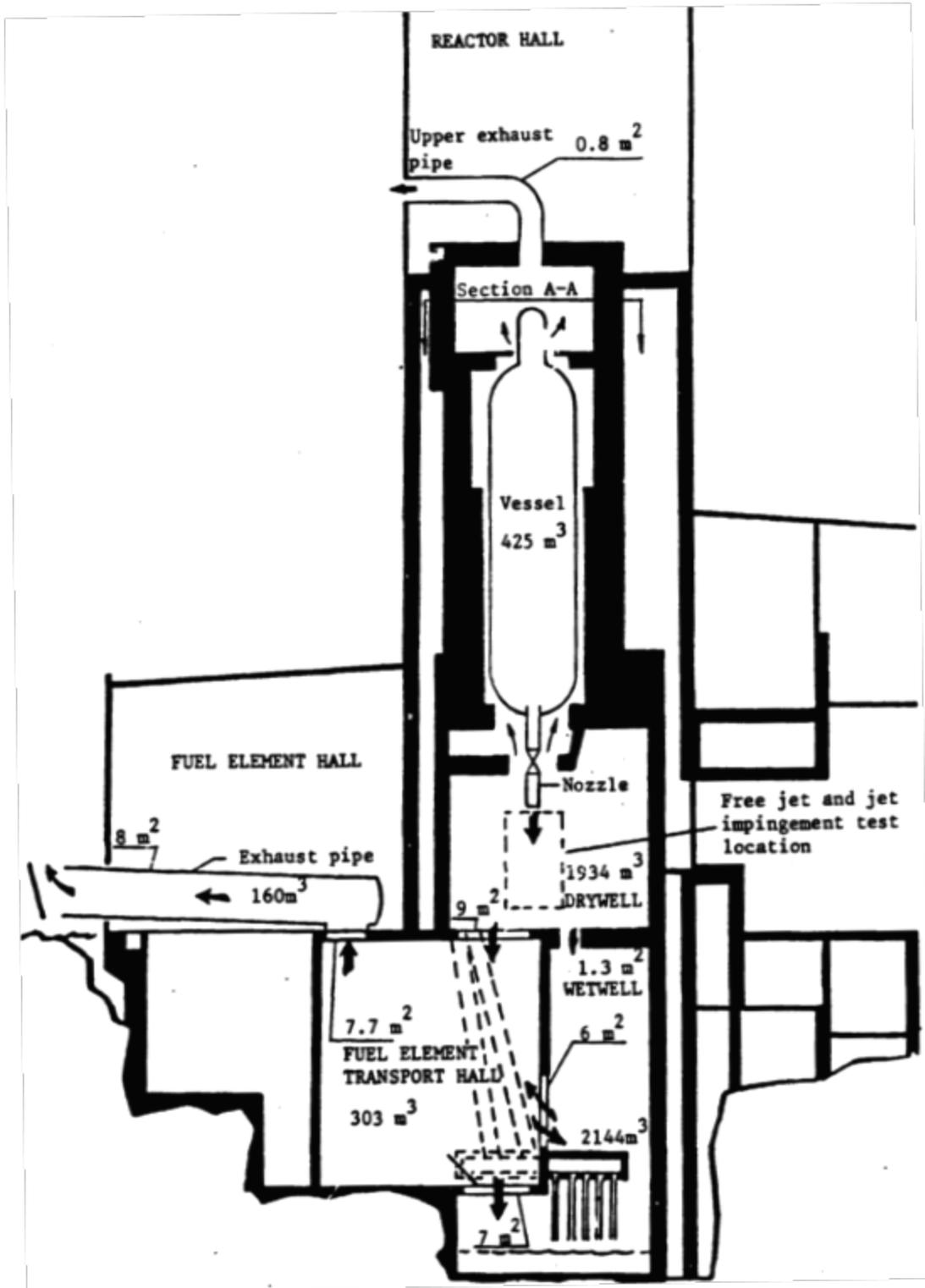
Figure 2-8 Experimental Setup for Jet Impingement in Large-scale Test (Marklund, 1985b)

2.2.2.1.2 Non-flashing Water Jets

The non-flashing water jets occur when the fluid initial temperature is below the fluid boiling point under ambient conditions, which is 100°C. For incompressible water jets, the velocity is significantly below the fluid's speed of sound and shock waves are not present. The thrust coefficient for non-flashing water was investigated in the experimental study by Kawanishi et al. (1986). It was found that the thrust coefficient for high subcooling water (0.8 MPa < P_0 < 2.5 MPa; 0 °C < ΔT < 110 °C) is about 1.95.

2.2.2.1.3 Steam-water Mixture Jets

For saturated water and subcooled water (temperature above 100°C), steam-water jet can occur after the break. The thrust coefficients for steam-water jet have been investigated in Mitsubishi test (Kawanishi et al., 1986) and JAERI test (Yano et al., 1984). In the study by Kawanishi et al. (1986), the C_T was investigated and the results are compared with Henry and Fauske model (1971) as shown in Figure 2-9. As shown in the figure, the C_T for the round edge nozzle is about 1.1 - 1.2 in the two-phase region. For the sharp nozzle, C_T reduces about 20% compared to round nozzle. In Yano et al. (1984), the thrust coefficients for BWRs LOCA conditions are investigated and C_T is found to be around 1.15. These experimental studies are used to for model evaluation in Section 3.2.3.
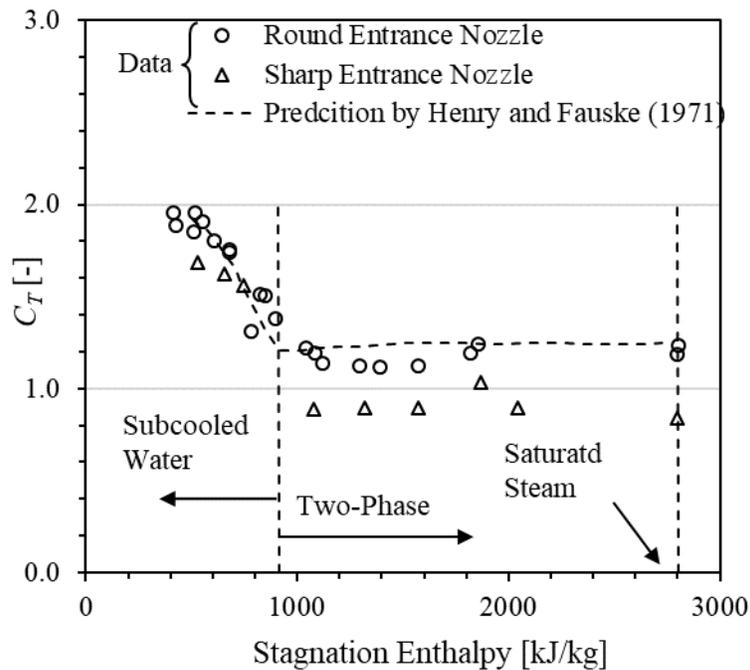
Figure 2-9 Thrust Coefficient for Subcooled Water and Two-phase Mixture Jets (Kawanishi et al., 1986)

2.2.2.2 Jet Geometry

The jet geometry determines the zone of influence and the development of the jet in the spatial domain. The discussion of the jet geometry is usually separated into jet core region and jet expansion region. The jet core is a region after the break where the thermodynamic properties of the choked flow are preserved for subcooled water jets. The geometry of the jet core is characterized by the jet core length, and that of the jet expansion region is characterized by the jet spreading angle. The jet core was investigated by Celata et al. (1986) using X-rays, and the jet expansion for steam jet was investigated by a recent CRIEPI-Hitachi test (2016) using PIV system.

2.2.2.2.1 Jet Core Length

To simulate the LOCA accidents in LWRs, Celata et al. (1986) investigated the length of jet core for high subcooling conditions ($0.8 \text{MPa} < P_0 < 2.5$ MPa; $0 < \Delta T < 110$ °C). The lengths of the jet core are obtained by X-rays images. In this work, the effect of friction on jet core length is also investigated. A sample X-rays image is shown in Figure 2-10. From the X-rays image, the length of the jet core can be obtained, and the results are shown in Figure 2-11. In the figure, the jet core length is normalized by the break diameter. It is found that increasing the degree of subcooling increases the jet core length and increasing the nozzle length L_p generally decreases the jet core length. This indicates that the effect of increasing friction is similar to that of decreasing subcooling of the fluid. In the work by Celata et al. (1986), the experimental data were also compared to the existing model by Tomasko et al. (1981). It can be seen the model generally captures the trend but significantly underestimates the experimental values.
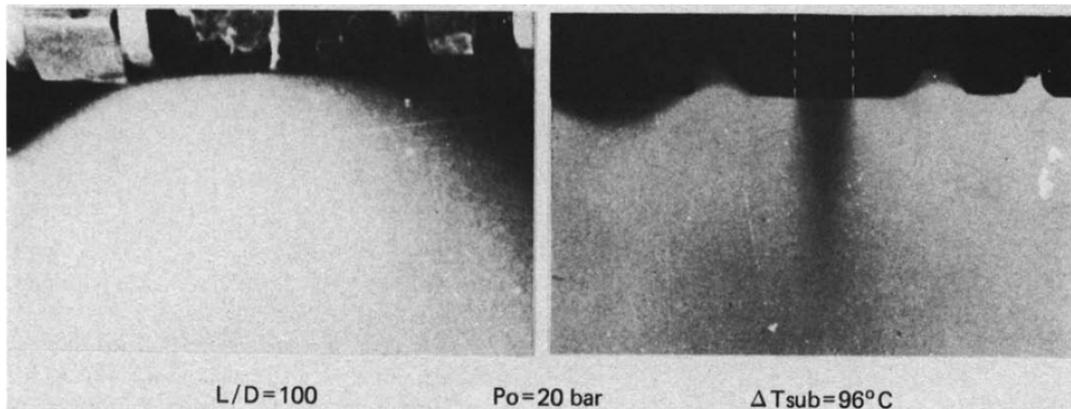
Figure 2-10 Typical Photographic Image (Left) and X-rays Image (Right) Taken in the Same Thermodynamic Conditions (Celata et al., 1986)
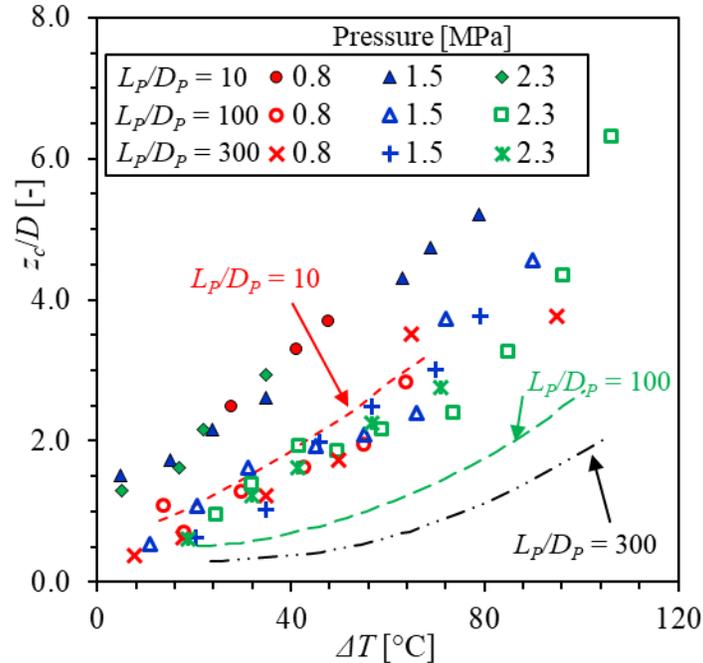
Figure 2-11 Dimensionless Jet Core Length (z_c) with Respect to the Inlet Subcooling for Three Employed Test Sections and for Different Stagnation Pressures (Celata et al., 1986)

2.2.2.2.2 Steam Jet Expansion

The jet expansion for steam jets was investigated by a recent CRIEPI-Hitachi test. In this test, saturated steam of up to 1.6 MPa was supplied continuously from a high-pressure steam boiler. The controlled steam was supplied to the reservoir tank (ID 100 mm) in the test section and the supersonic steam jet flow was blown out from the jet nozzle (ID 8 mm with 200 mm length). The steam jet was investigated using particle image velocimetry (PIV) visualization and computational fluid dynamics analysis (CFD) simulation. An in-house 3-dimensional unsteady compressible steam flow CFD code was employed, which is based on finite difference method. This code is applicable to superheated and wet steam including condensation with assumption of homogeneous flow and equilibrium condensation. 3D Navier-Stokes equations are discretized with the 5th-order Monotone Upstream-centered Schemes for Conservation Law (MUSCL) scheme for a convective term and the 6th-order central difference scheme for a viscous term. SLAU 2 scheme (Simple Low-dissipation Advection Upstream Splitting Method) (Kitamura and Shima, 2013) and Lower-Upper Symmetric-Gauss-Seidel (LU-SGS) algorithm for matrix inversion are applied. The discharged superheated steam jet became wet steam due to the supersonic flow. Therefore, water droplet in the wet steam was used as a seeding material for the visualization and additional seeding material was not used. Table 2-2 summarizes the test conditions investigated in experiments and CFD simulations in the CRIEPI-Hitachi test.

Table 2-2 A Summary of Experimental Conditions and CFD Conditions in CRIEPI-Hitachi Test (Morita et al., 2016; Takahashi et al., 2016; Xu et al., 2016)

Case	Nozzle Diameter [mm]	Inlet Pressure [MPa]	Inlet Temperature [°C]	Experimental Test	CFD Simulation
1	8	0.40	152	√	√
2	8	0.58	165	√	√
3	8	0.82	177	√	√
4	12	0.23	137	√	×
Ref_1	8	1.5	137	×	√
Ref_2	8	3.0	Saturation	×	√
Ref_3	8	5.0	Saturation	×	√
Ref_4	8	7.0	Saturation	×	√
Ref_5	8	7.5	Saturation	×	√
Ref_6	8	13.0	Saturation	×	√

A comparison between experimental measurements and CFD simulation in this test was found to be reasonable as shown in Figure 2-12. From the images, vertical shock wave and rapid velocity deceleration after the shock wave were observed clearly in both experimental study and CFD simulation. The comparison on jet axial and radial velocities is also presented and shown in Figure 2-13. The axial velocity profile in Figure 2-13 also shows the existence of shock wave, and maximum velocity reaches 1000 m/s before the shock wave. From the velocity profiles, the similarity between the flow pattern, velocity magnitude, jet width and shock position generally validate the CFD simulation in this test.

Based on the experimental study and CFD simulation, the jet expansion was investigated for regions before and after the asymptotic plane (Morita et al., 2016). In this study, the maximum expanded jet position was defined as the asymptotic plane. The definitions of the asymptotic length (La), asymptotic area (Aa), and spread angle (θ) are shown in Figure 2-14. Based on the CFD simulation, the relation between the spread angle and pressure ratio (the ratio of vessel pressure with respect to ambient pressure) is obtained and is shown in Figure 2-15. Since high pressure and high-density steam expands more than lower pressure and density steam, the spread angle becomes larger as pressure increases. Considering the zone of influence, a larger spread angle will give a conservative affected region. However, larger spread angle will also make the average impact pressure smaller, which may underestimate the impingement force if the pressure distribution within the jet is not considered.

The spread angle after the asymptotic plane was also investigated in this test (Takahashi et al., 2016). Figure 2-16 shows comparison on jet spread angle after the asymptotic plane between experimental study and CFD simulation. The spread angle is found to be around 7°, when the jet boundary is defined at the position where local jet velocity (allowable velocity) is less than 30 m/s. It is found that this spread angle slightly changes as the allowable velocity changes. However, this angle is between 4° and 8°, when allowable velocity changes from 70 m/s to 10 m/s. Meanwhile, this spread angle is found to be independent of the initial vessel pressure.
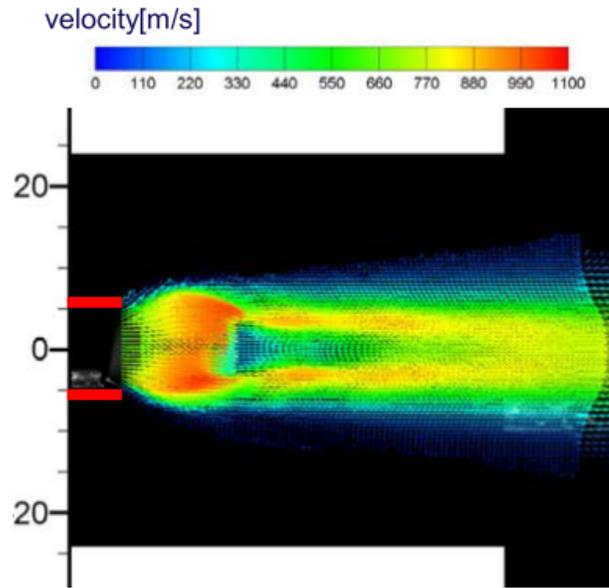
(a) PIV visualization
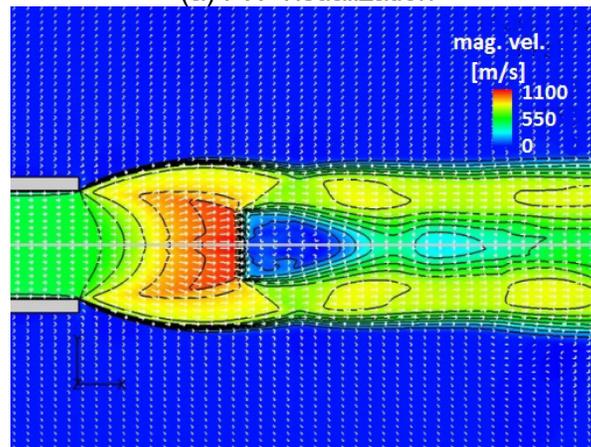
(b) CFD calculation

Figure 2-12 Comparison between Experimental Measurements and CFD Simulation on Jet Structure, Case 1: Pressure 0.40 MPa and Temperature 152°C (Morita et al., 2016)
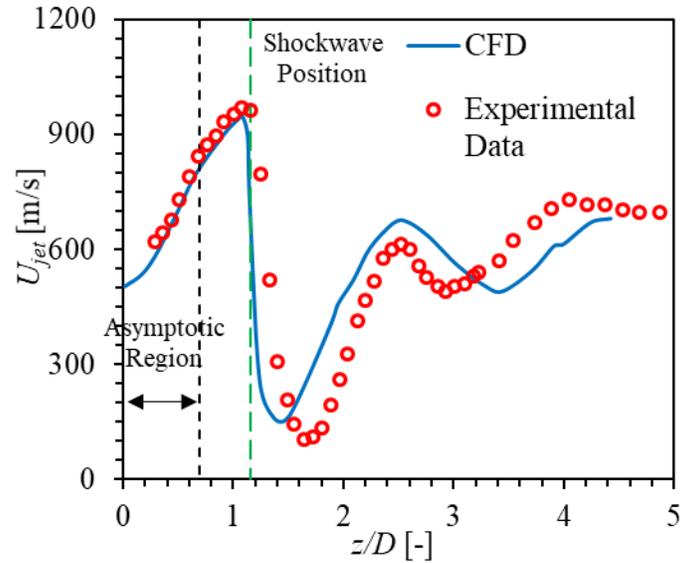
(a) Flow direction (nozzle center)
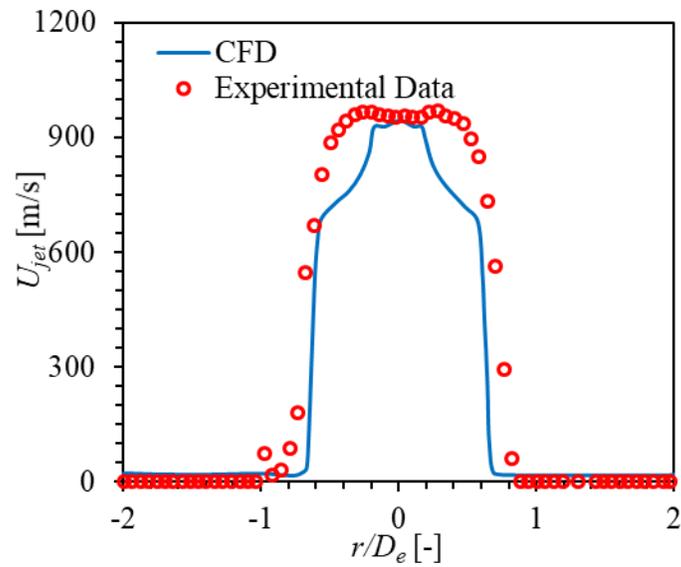
(b) Radial direction at z/D = 1

Figure 2-13 Comparison between Experimental Measurements and CFD Simulation on (a) Axial and (b) Radial Velocity, Case 1: Pressure 0.40 MPa and Temperature 152°C (Morita et al., 2016)
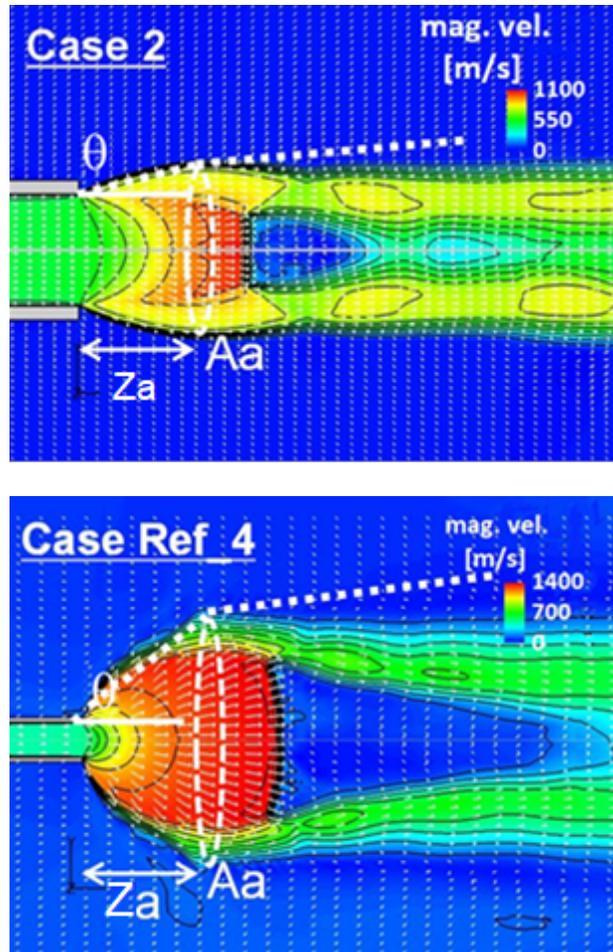
Figure 2-14 Definition of Asymptotic Length (z_a), Asymptotic Area (A_a), and Spread Angle (θ) (Morita et al., 2016)
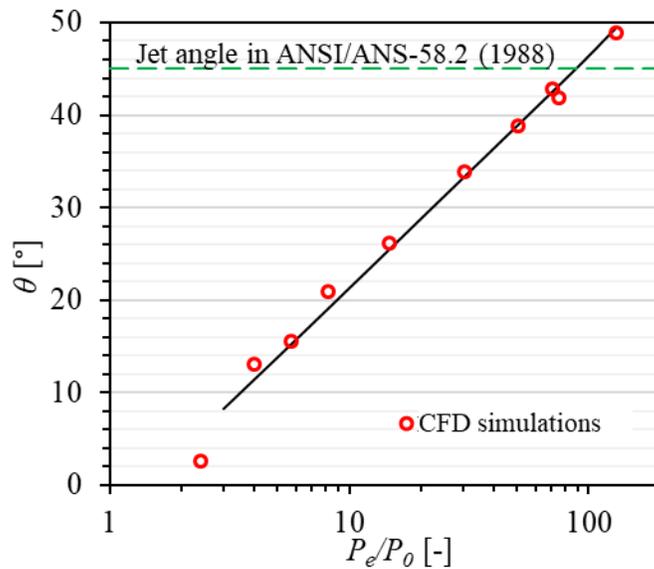
Figure 2-15 Relation between Spreading Angle and Pressure Ratio (Morita et al., 2016)
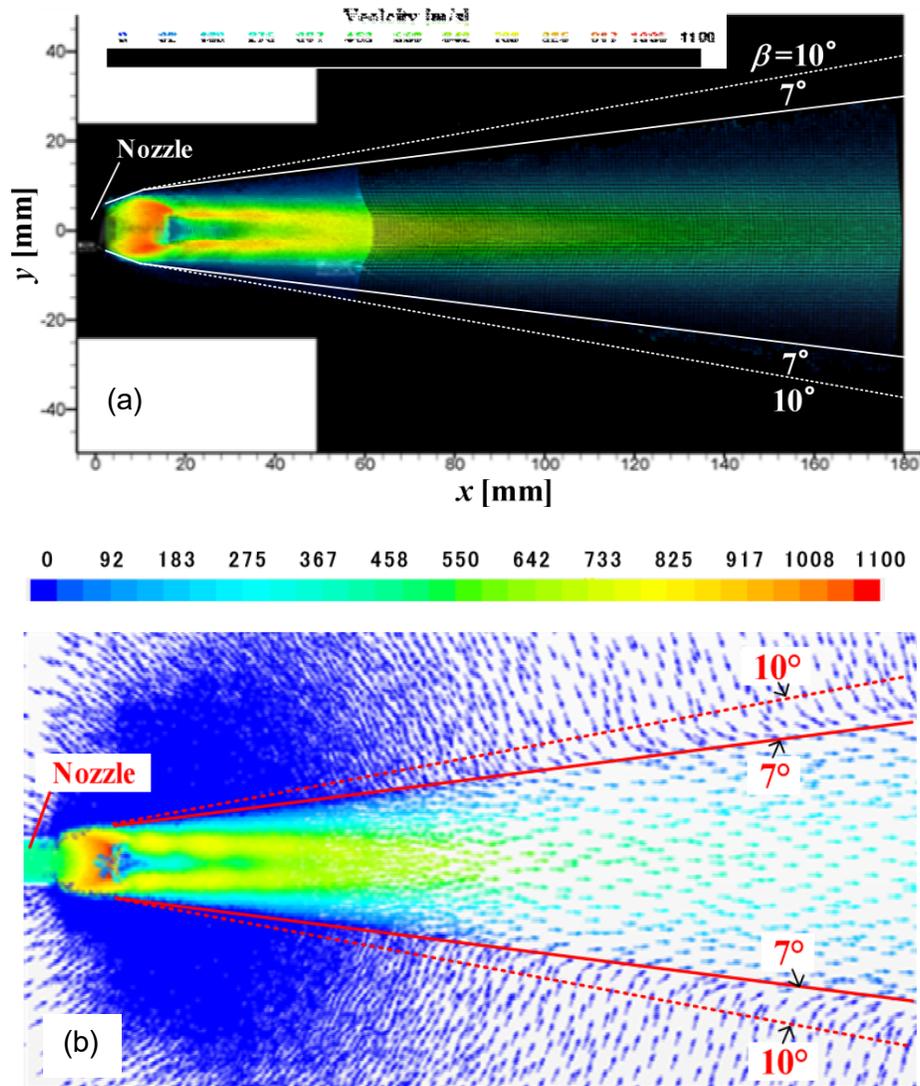
Figure 2-16 Comparison on Jet Spread Angle after the Asymptotic Plane between (a)
Experimental Study and (b) CFD Simulation (Morita et al., 2016)

2.2.2.3   Pressure Distribution

The pressure distribution in radial and axial direction within the jet characterizes the strength of
the jet, and directly determines the impingement force on the target. Therefore, the pressure
distribution within the target needs to be investigated. In the literature, the pressure distribution
for steam jets has been investigated in Kitade et al. (1979), Masuda et al. (1981) and Marklund
(1985a), while that for steam-water jets has been investigated by Kastner and Rippel (1988) and
Yano et al. (1984).

2.2.2.3.1   Saturated and Superheated Steam Jets

The pressure distributions within both free steam jets and impinging steam jets have been
investigated in previous studies. The pressure profiles measured by Masuda et al. (1981) for
free and impinging steam jets are shown in Figure 2-17 and Figure 2-18, respectively. It is found
that for both free jet and impinging jets, the pressure distribution changes from center-peak to

edge-peak and to center-peak profile again, as the measurement location moves away from the break. The edge-peak profile is formed approximately at the position where the Mach disk is located. This trend was also observed for the impinging jet by Kitade et al. (1979). Meanwhile, as shown in these figures, the normalized pressure decreases rapidly as the measurement location moves away from the break. The normalized pressure decreases to about 5% at 4.3 D for free jet and at 3.3 D for impinging jet.

For the stagnation pressure at the center of the plate (P_c), Kitade et al. (1979) developed a correlation based on the experimental results for steam jets:

$$P_c^* = \frac{P_c - p_{amb}}{P_0 - p_{amb}} = 0.65 \left(\frac{z}{D} \right)^{-2} \tag{2-39}$$

where P_c^* is the dimensionless pressure, P_c is the center stagnation pressure at the plate, P_0 is the vessel stagnation pressure, p_{amb} is the ambient pressure, z is the distance between measurement point and break, and D is the break diameter. The comparison between this correlation and the experimental data is shown in Figure 2-19. The correlation is found to agree well with the experimental data. In fact, the Marviken data (Marklund, 1985b) is also found to agree well with this correlation as shown in Figure 2-20.

2.2.2.3.2 Saturated-water Mixture Jets

The pressure distribution on a target for steam-water mixture jets has been investigated by Yano et al. (1984) and Kastner and Rippel (1988). Yano et al. (1984) investigated the pressure distribution for BWRs under LOCA conditions. The measured pressure at the target for two different pressure conditions is shown in Figure 2-21. It is found that the pressure at the target center decreases to about 10% of vessel pressure at $2D_e$ for both experiments. Kastner and Rippel (1988) investigated saturated pressurized water discharging on a flat plate with a circular nozzle with 65 mm inner diameter. The pressure distribution measured for quasi-steady-state flow against flat plates is found to follow a Gaussian distribution curve as shown in Figure 2-22. From the measurement, it is also found that the pressure decreases to about 10% vessel pressure at $2D_e$, which agrees well with the data from Yano et al. (1984).

For the stagnation pressure at the center of the plate, Yano et al. (1984) developed a correlation based on the experimental results for steam-water mixture jets:

$$P_c^* = \frac{P_c - p_{amb}}{P_0 - p_{amb}} = 0.40 \left(\frac{z}{D} \right)^{-2} \qquad \text{for } z/D > 1 \tag{2-40}$$

where P_c is the center stagnation pressure at the plate, P_0 is the vessel pressure, p_{amb} is the ambient pressure, z is the distance between measurement point and break, and D is the break diameter. The comparison between this correlation and the experimental data is shown in Figure 2-23. The correlation is found to agree well with the experimental data. In fact, the Marviken data (Marklund, 1985b) is also found to agree well with this correlation as shown in Figure 2-24.
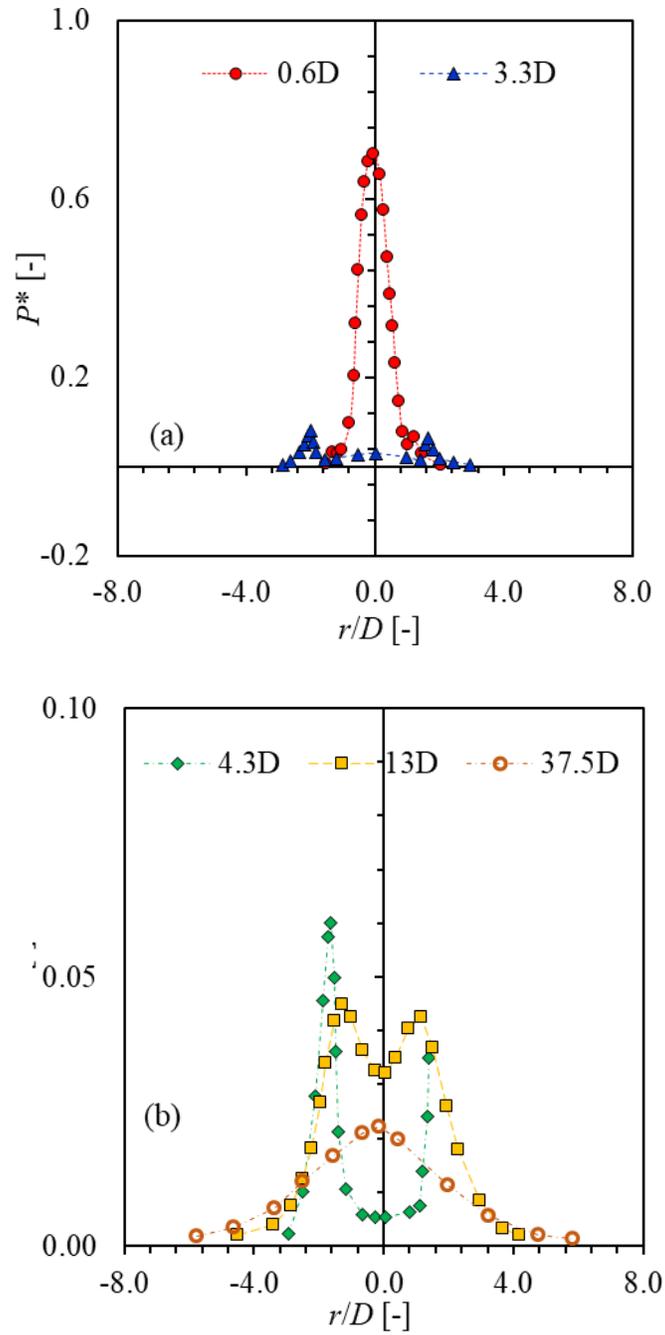
Figure 2-17 Pressure Distribution within Free Steam Jet (Masuda et al., 1981)
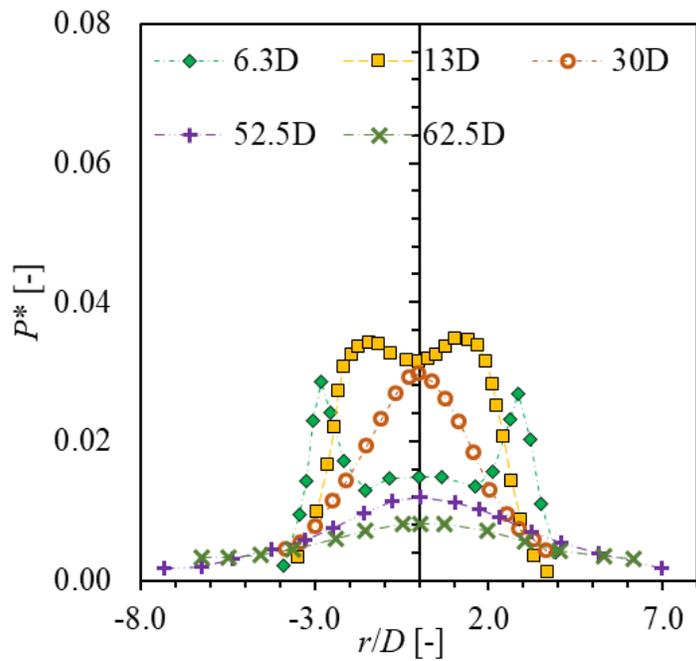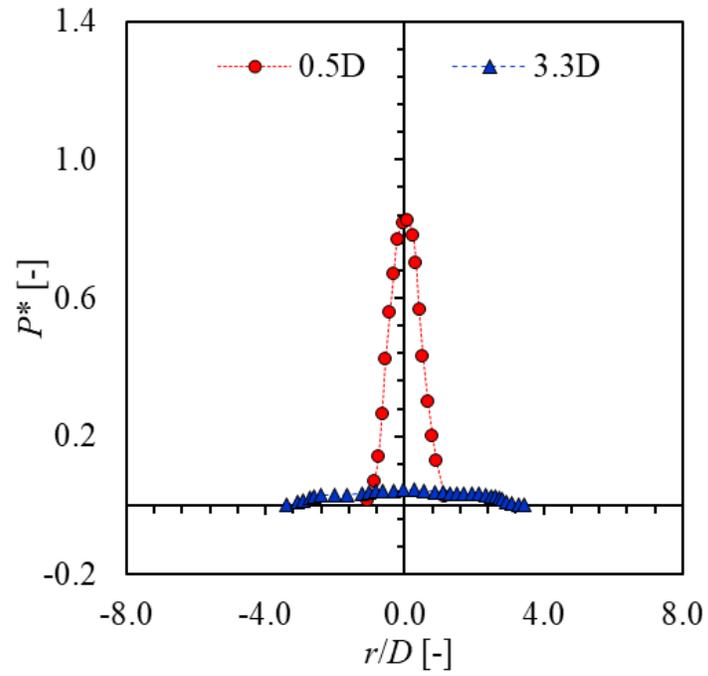
Figure 2-18 Pressure Distribution within Impinging Steam Jet (Masuda et al., 1981)
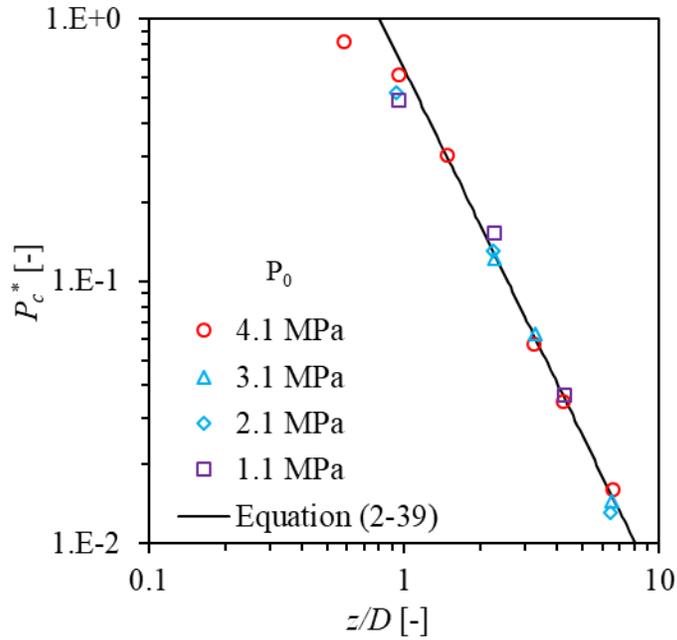
Figure 2-19 Comparison on Pressure at the Center Plate between Experimental Data and Correlation in Equation (2-39) (Kitade et al., 1979)
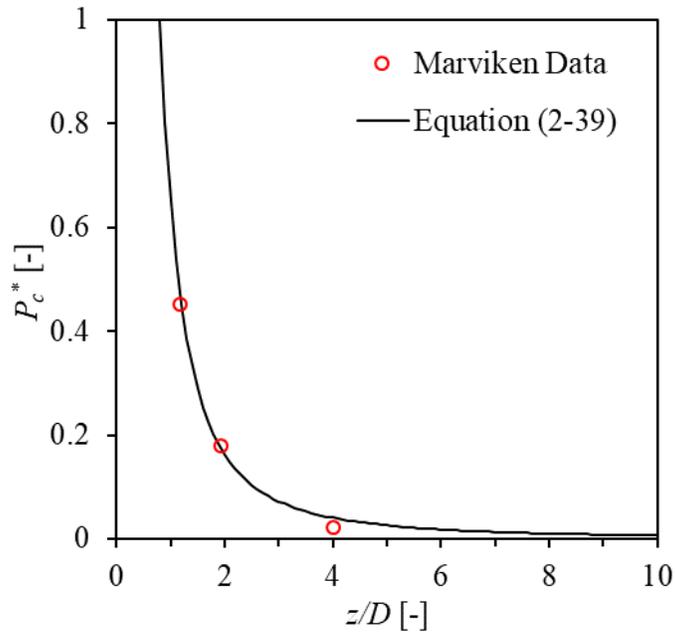
Figure 2-20 Comparison on Pressure at the Center Plate between Experimental Data from Marviken Test (P_0 = 2 MPa, D = 500 mm) and Correlation in Equation (2-39) (Marklund, 1985b)
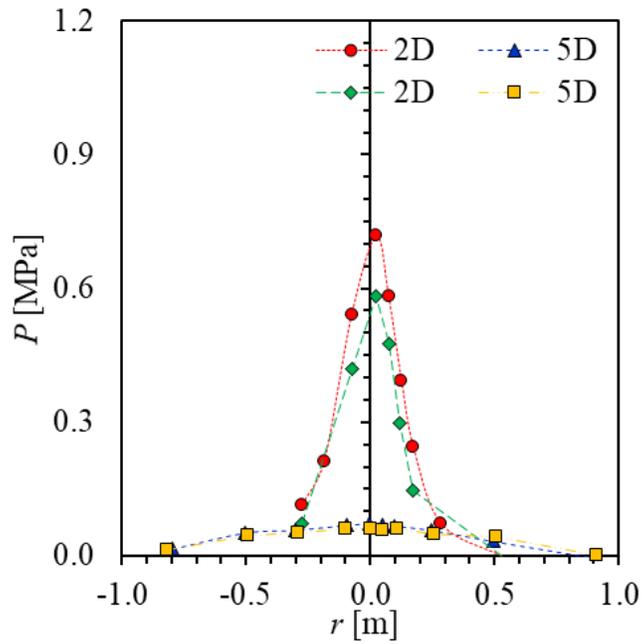
Figure 2-21 Pressure Distribution on Target for Impinging Steam-water Mixture Jets (Yano et al., 1984)
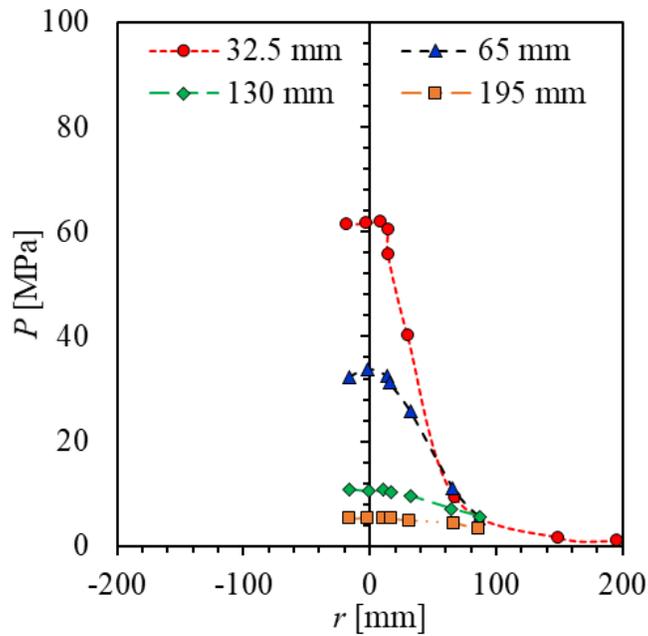
Figure 2-22 Pressure Distribution on Target for Impinging Steam-water Mixture Jets (Kastner and Rippel, 1988)
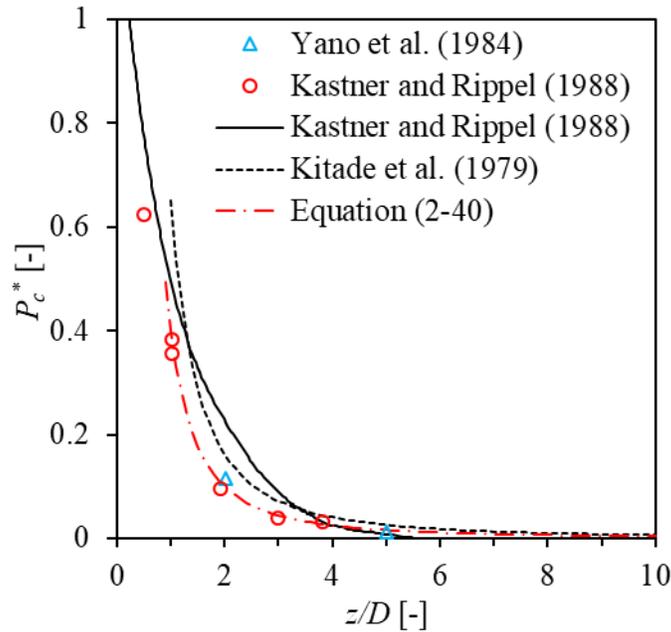
Figure 2-23 Comparison on Pressure at the Center Plate between Experimental Data and
Correlation (Yano et al., 1984)
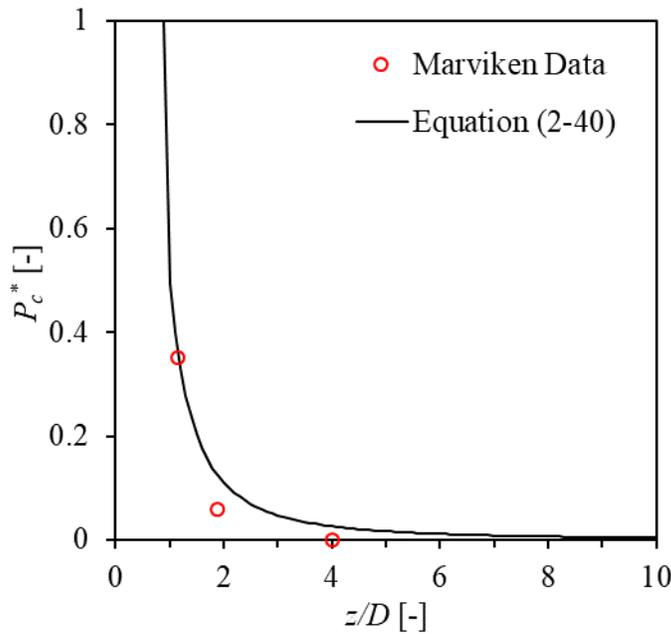
Figure 2-24 Comparison on Pressure at the Center Plate between Experimental Data and
Correlation in Equation (2-40) (Marklund, 1985b)

2.2.2.4 Jet Impingement Force

Due to the momentum conservation, the impingement force cannot be greater than the thrust force. Accounting for jet expansion, friction, momentum and energy exchange, heat transfer, and effect of target area, using thrust force to estimate impingement force can be considered as a conservative approach. Yano et al. (1984) measured thrust force and impingement force simultaneously just after the break for BWRs LOCA conditions. It was found that the ratio of the impingement force to the thrust force is ~ 0.9. The comparison between thrust force (T) and impinging force (F_j) is shown in Figure 2-25.

After the review on experimental studies, it can be seen that since the workshop on jet impingement and pipe whip in 1981, additional experiments have been performed focusing on small to medium scale break sizes (5 ~ 152 mm). Experiments for different inlet fluid conditions were investigated, including subcooled water (ENEA test, Ontario-Hydro test, and KWU test), saturated water (JAERI test) and saturated steam (CRIEPI-Hitachi test). The pressure distribution within the jet and jet geometry have been studied, which are greatly useful in model development.
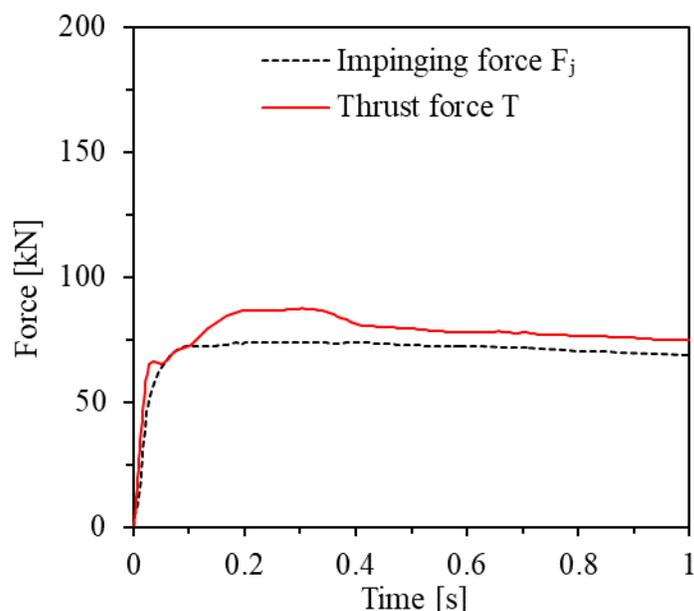
Figure 2-25 Comparison between Thrust Force and Impinging Force for BWR LOCA (D = 150 mm) Conditions (Yano et al., 1984)

2.3 Review of Jet Impingement Models and CFD Simulations

This section performs literature review on existing jet impingement models and CFD simulations.

2.3.1 Jet Impingement Models

2.3.1.1 ANSI/ANS-58.2 (1988)

There are four appendices in ANSI/ANS standard (ANSI/ANS-58.2, 1988) which include: (1) Appendix A. Derivation of fluid force equations; (2) Appendix B. An acceptable simplified method for calculation of fluid thrust forces; (3) Appendix C. Acceptable models for jet geometry; and (4) Appendix D. Acceptable simplified methods for evaluation of jet impingement effects. Appendix A has been discussed in Section 2.1.1, and the models in other appendices are summarized as follows.

2.3.1.1.1 Appendix B. An Acceptable Simplified Method for Calculation of Fluid Thrust Forces

Considering that the thrust force can be time dependent, due to the time rate of change in fluid momentum, the ANSI/ANS-58.2 (1988) uses a conservative approximation for thrust force by knowing initial and steady state forces, as shown in Figure 2-26. As shown in the figure, the Standard assumes the steady state thrust coefficient for the initial stage of the blowdown. In fact, Lahey and Moody (1977) has shown that the initial thrust coefficient is less than 1 for frictionless flow, when pressure is between 1.4 MPa and 14 MPa. On the other hand, the steady state thrust coefficient is greater than 1.2 for frictionless flow. Therefore, the approximation in the Standard is conservative.

The modeling of thrust coefficient was performed separately for steam, steam-water mixture and non-flashing water. The Standard model employs 1.26 for steam and 2.0 for non-flashing water. These values are derived theoretically (Moody, 1969; Webb, 1976; Areva NP Inc., 2013). For incompressible flow, the exit pressure is equal to the environment pressure. From the Bernoulli equation, the exit velocity is as follows with P_0 equal to the stagnation pressure in psia:

$$u_e = \sqrt{\frac{2g_c}{\rho_f}(P_0 - p_{amb})} \tag{2-41}$$

Therefore,

$$T = 2(P_0 - p_{amb})A_e \tag{2-42}$$

The thrust coefficient for incompressible flow is equal to 2.0.

For steam, the ideal gas law is employed to calculate the exit critical velocity, critical mass flow rate, and exit pressure:

$$U_{cr} = \sqrt{\frac{2k}{k+1}RT_0} \tag{2-43}$$

$$\dot{m} = A\frac{P_0}{T_0^{\frac{1}{2}}}\sqrt{\frac{k}{R}\left(\frac{2}{k+1}\right)^{\frac{(k+1)}{(k-1)}}} \tag{2-44}$$

$$P_e = P_0\left(\frac{2}{k+1}\right)^{k/(k-1)} \tag{2-45}$$

where k is the ratio of specific heats, R is the universal gas constant, T_0 is the stagnation temperature and P_0 is the stagnation pressure. Combining Equations (2-43) through (2-45) and (2-5), the thrust force simplifies to

$$T = \left[(1+k) \left(\frac{2}{k+1} \right)^{k/(k-1)} \right] P_0 A_e - p_{amb} A_e \qquad (2\text{-}46)$$

Since the value of k depends on exit plane pressure, the thrust coefficient also depends on exit plane pressure. As presented in ANP-10318NP (Areva NP Inc., 2013), the thrust coefficient is

$$C_T = 1.26 - p_{amb}/P_0 \qquad (2\text{-}47)$$

when the exit plane pressure is 0.1 MPa and is

$$C_T = 1.3 - p_{amb}/P_0 \qquad (2\text{-}48)$$

when the exit plane pressure is 5.2 MPa.

The thrust coefficient for two-phase mixture employed in the Standard was developed by Lahey and Moody (1977). The work calculated thrust coefficients for both separated flow and homogeneous flow. With the separated flow model being more conservative, it is currently being employed in the Standard. Additionally, it was found that the vessel stagnation pressure has a slight effect on the thrust coefficient for the two-phase mixture, and the value varies between 1.2 and 1.3 for separated two-phase flow.

While the above discussion focuses on frictionless flow, increasing friction is found to decrease the thrust coefficient. The upstream restriction will also decrease the thrust coefficient. The friction effect on thrust coefficient is investigated in Lahey and Moody (1977) for steam, steam-water mixture and non-flashing flow. The results are employed by the Standard.

Once the steady state thrust force is determined, the time to reach steady state is the only parameter left for the model. It should be noted that the gravitational constant is actually specified in the Standard in British unit:

$$g_c = 32.174 \left[\frac{lbm - ft}{lbf - s^2} \right] \qquad (2\text{-}49)$$

2.3.1.1.2 Appendix C. Acceptable Models for Jet Geometry

Acceptable and simplified models for defining the geometry are presented in the Standard. The jet fluid can be subcooled or saturated liquid, two-phase mixture or vapor. The models define three regions in the jet as shown in Figure 2-27.

In the Standard, it is assumed that the circumferential break would result in full separation of the two severed pipes ends, but if the pipe is physically restrained the extent of separation would be limited. The model for longitudinal break is assumed to be the same as the circumferential break

with full separation, while a slightly different model is employed for circumferential break with limited separation.
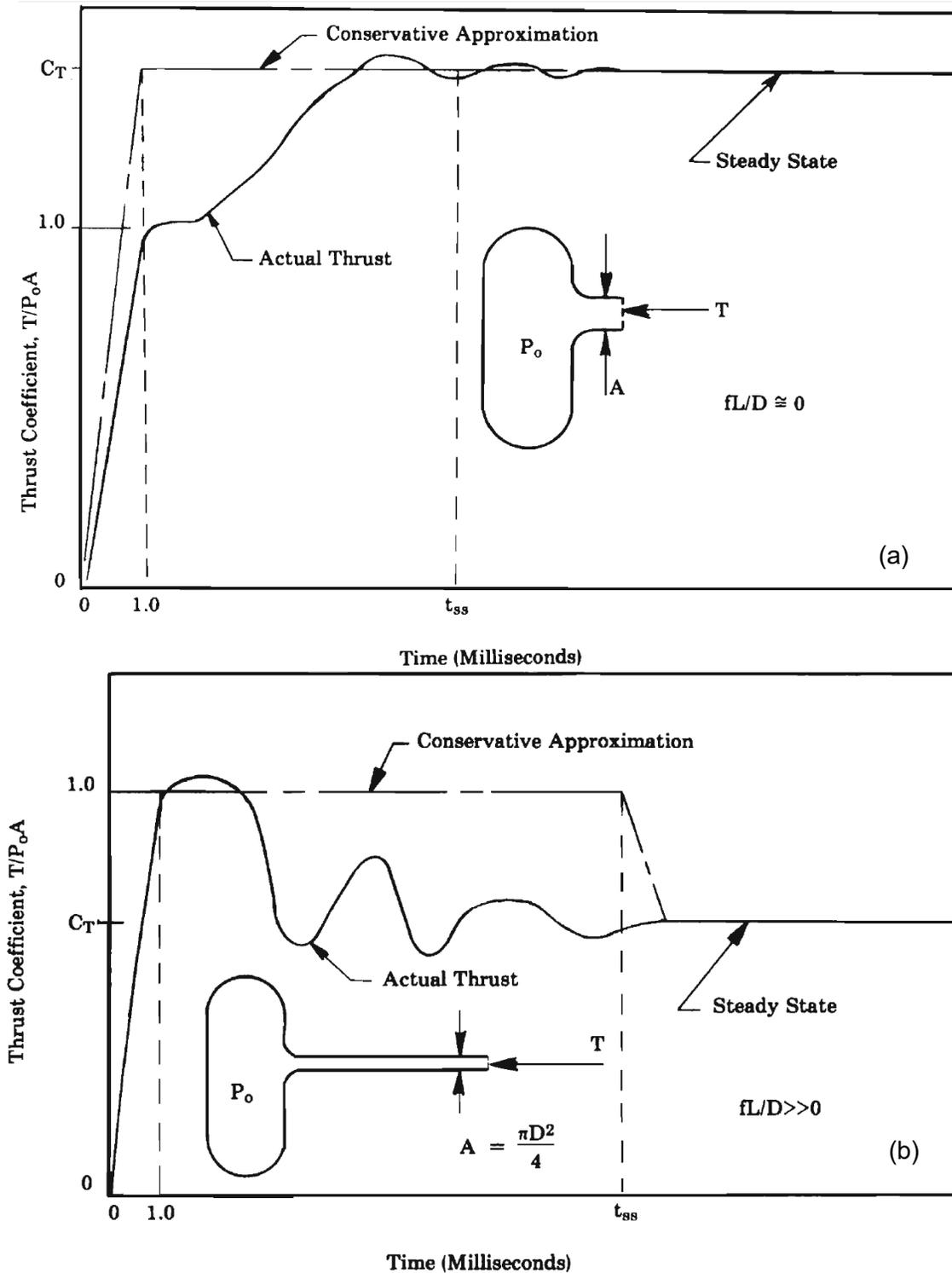
Figure 2-26 Conservative Approximation of Transient Thrust Force: (a) Very Low Friction Flow and (b) Friction Flow (ANSI/ANS-58.2, 1988)
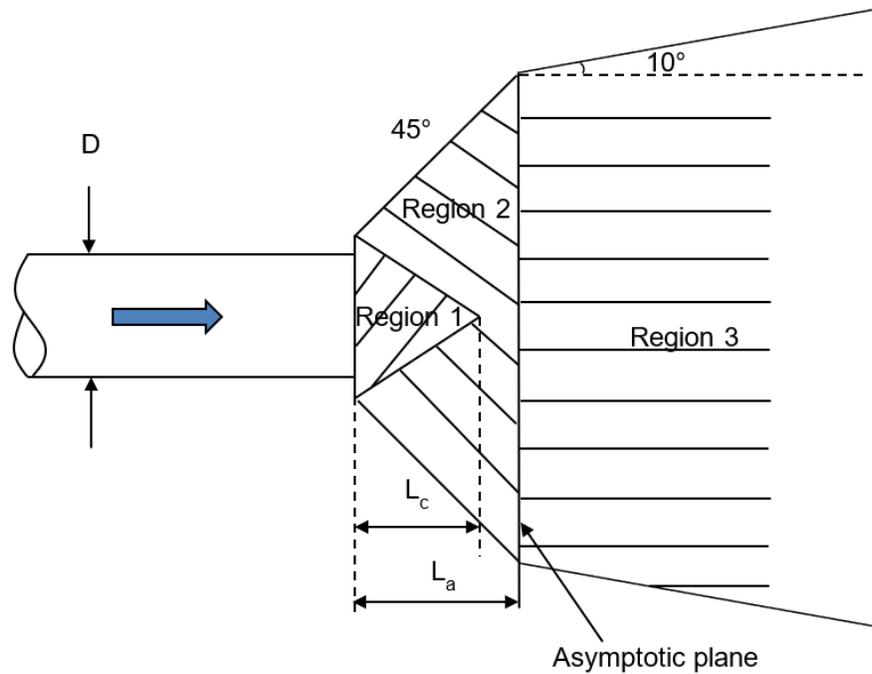
Figure 2-27 Fluid Jet Geometry for Circumferential Break with Full Separation (ANSI/ANS-58.2, 1988)

For the model of circumferential break with full separation, the following observations are made. For region 1, which is the cone-shaped region containing the jet core and the remainder of the jet, the jet core length is related to the jet subcooling (Equation (C-1) in the Standard):

$$\frac{z_c}{D} = 0.26\sqrt{\Delta T} + 0.5 \tag{2-50}$$

where z_c is jet core length, D is break diameter and ΔT is jet subcooling at break plane under stagnation condition and has a unit of °F. However, in order for this equation to have consistent units, the constant value of 0.26 must have a unit of $[1/T^{1/2}]$.

Region 2 is defined from the break plane to the asymptotic plane. For the asymptotic plane area (Equation (C-3) of the Standard), it should be noted that the gravitational constant is specified in British unit as was the case in Equation (B-9) of the Standard. The distance from the break plane to the asymptotic plane is given by the Standard (Equation (C-5)):

$$\frac{z_a}{D} = \frac{1}{2}\left(\sqrt{\frac{A_a}{A_e}} - 1\right) \tag{2-51}$$

Equation (2-51) assumes a jet angle of 45° to calculate the distance z_a. However, this angle is from the inner pipe edge instead of the jet edge at the break plane, because D is employed instead of $D\sqrt{C_{Te}^*}$. The value of $\sqrt{C_{Te}^*}$ is 2.0 for $\Delta T > 0$, and $\sqrt{C_{Te}^*}$ is 1.26 for $\Delta T = 0$.

Region 3 is defined as the fluid jet after the asymptotic plane. The jet area in Regions 1 and 2 at any location from the break plane to the asymptotic plane may be calculated by (Equation (C-6) of the Standard):

$$\frac{A_j}{A_{je}} = \left[1 + \frac{z}{z_a} \left(\frac{A_a}{A_{je}} - 1 \right) \right] \tag{2-52}$$

Rearranging Equation (2-52), it becomes:

$$\frac{A_j - A_{je}}{A_a - A_{je}} = \frac{z}{z_a} \tag{2-53}$$

However, this equation is not correct because:

$$\frac{D_j - D_{je}}{D_a - D_{je}} = \frac{z}{z_a} \tag{2-54}$$

Therefore, the correct formulation to calculate area A_j should be:

$$\frac{A_j}{A_{je}} = \left[1 + \frac{z}{z_a} \left(\frac{D_a}{D_{je}} - 1 \right) \right]^2 \tag{2-55}$$

where $A_{je} = C_{Te}^* A_e$ is the jet area at the break plane. For the model of circumferential break with limited separation, following observations are made. As found similarly in Equation (C-1) of the Standard, the constant value of 0.26 must also have a unit of $[1/T^{1/2}]$ in order for Equation (C-8) of the Standard to be consistent in unit:

$$\frac{z_c}{W_f} = 0.26\sqrt{\Delta T} + 0.5 \tag{2-56}$$

Here, ΔT has a unit of °F. The distance from the break plane to the asymptotic plane is given by (Equation (C-10) of the Standard):

$$\frac{z_c}{W_f} = \frac{1}{4} \left[\sqrt{\left(\frac{D}{W_f} - 1 \right)^2 + 4\frac{D}{W_f}\left(\frac{A_a}{A_f} \right)} - \left(1 + \frac{D}{W_f} \right) \right] \tag{2-57}$$

This distance assumes 45° between the line connecting pipe inner edge point to asymptotic plan edge point and the line parallel to flow direction. As found similarly in Equation (2-51), this angle is from the inner pipe edge instead of the jet edge at the break plane since W_f is employed instead of $W_f = C_{Te}^*$.

The jet area at any radial location from the break to the asymptotic plane is given by (Equation (C-11) of the Standard):

$$\frac{A_j}{A_{jf}} = \left[1 + \frac{z}{z_a} \left(\frac{A_a}{A_{jf}} - 1 \right) \right]$$

(2-58)

where $A_{jf} = C_{Te}^* A_f$, A_f is break flow area. Rearranging this equation, we get:

$$\frac{A_j - A_{jf}}{A_a - A_{jf}} = \frac{z}{z_a}$$

(2-59)

However, this equation is not correct because:

$$\frac{W_j - W_{jf}}{W_a - W_{jf}} = \frac{z}{z_a}$$

(2-60)

Therefore, the correct equation for jet area should be:

$$\frac{A_j}{A_{jf}} = \left[1 + \frac{z}{z_a} \left(\frac{W_a}{W_{jf}} - 1 \right) \right] \left(\frac{D + 2z}{D} \right)$$

(2-61)

It needs to be noted that the model for jet geometry might be over simplified for supersonic jets as discussed in Ransom (2004) and Wallis (2004). The internal structure of the supersonic jets consists of normal and oblique shocks and the jets go through a series of expansion and compression. Depending on the jet static pressure at the break plane (P_e), the jets can be over-expanded ($P_e < p_{amb}$) or under-expanded ($P_e > p_{amb}$). For jet impingement in nuclear power plants, the jets are under-expanded and as such expansion occurs at the break plane. The angle between jet boundary tangent and axis is usually defined as Prandtl-Meyer angle and can be calculated as follows:

$$v = \frac{360}{2\pi} \left[\sqrt{\frac{\gamma + 1}{\gamma - 1}} \cdot \arctan\left[\sqrt{\left(\frac{\gamma - 1}{\gamma + 1}\right)\left(M^2 - 1\right)} \right] - \arctan\left(\sqrt{M^2 - 1} \right) \right]$$

(2-62)

where Mach number (M) is calculated by:

$$M = \sqrt{ \left(\frac{2}{k-1} \right) \left(\left(\frac{p_{amb}}{P_0} \right)^{\frac{1-k}{k}} - 1 \right) }$$

(2-63)

where P_0 is the vessel stagnation pressure, p_{amb} is the ambient static pressure.

2.3.1.1.3 Appendix D. Acceptable Simplified Methods for Evaluation of Jet Impingement Effects

The Appendix D of ANSI/ANS-58.2 (1988) provides simplified models for evaluation of jet impingement force. When the target is large enough, the entire force is applied to the target. However, when a fraction of the jet is intercepted by the target, the impingement load may be estimated by accounting for a correction factor which is the shape factor. This factor is a measure of target's potential for changing the momentum of the jet, which depends on the target shape and orientation with respect to the jet. In the Appendix D, this shape factor is related to the drag coefficient.

2.3.1.2 NUREG/CR-2913 (Weigand et al., 1983)

The two-phase jet loads model was first discussed in Tomasko et al. (1981) in the workshop on jet impingement and pipe whip, which was extended into NUREG/CR-2913 (Weigand et al., 1983). This model only investigates the initial conditions that result in two-phase flows (steam-water) at pressure above ambient conditions as shown in Table 2-3. The two-phase jet load geometry employed in the study is shown in Figure 2-28. Here, several assumptions are made to simplify the problem: (a) the vessel is assumed to be sufficiently large such that there will be a relatively long period of time until the rate of change in the flow becomes important; (b) the exit pipe has fluid with the same thermodynamic state as that inside the vessel; (c) the other end of the guillotine break is ignored such that there is no interaction between the two jets and (d) the target has no curvature and has a large enough radius, such that the entire jet is intercepted by the target.

In NUREG/CR-2913, three characteristic regions are identified in the two-phase jet flow field:
  (a) The break region where an exit core which has the same thermodynamic properties as the choked flow, projects a distance downstream of the break. The length of the exit core depends on the degree of subcooling.
  (b) Free jet region where the jet expands almost as free, isentropic expansion. The flow in this region is supersonic. The free jet region terminates at a stationary shock wave near the target.
  (c) Target region where the local flow field imposes the pressure loading on the target.

2.3.1.2.1 Calculated Results Presented in NUREG/CR-2913

In NUREG/CR-2913, the two-phase jet calculation was performed by modified CSQ (**C**HARTD **Sq**uared, where CHARTD stands for **C**oupled **H**ydrodynamics **A**nd **R**adiation **T**ransport **D**iffusion), which is a finite difference code solving a homogeneous equilibrium set of equations for a specified flow field. The flow chart showing the calculation procedure by two-phase jet loads model is presented in Figure 2-29 (This flow chart is created based on the information found in NUREG/CR-2913 for clarity). It needs to be noted that the critical mass flux in Appendix D of NUREG/CR-2913 was calculated using homogeneous equilibrium flow model (HEM). The results of computer code calculation are presented in the appendices A and C for "target pressure and load distribution" and "length of jet exit core", respectively.

Apart from the calculation results presented in the appendices, detailed results for two particular test conditions (P_0 = 17 MPa, ΔT_0 = 70 °C; and P_0 = 15 MPa, ΔT_0 = 0 °C) are presented in Section 4 of NUREG/CR-2913, including:
  (a) Pressure and density contours in the jet flow;
  (b) Velocity, sound speed, temperature, and pressure distributions along the radius of the target; and
  (c) Density, temperature and pressure distributions along the centerline of the jet flow.

These results can be used for model evaluation if experimental data are available or interpolation of the experimental data is possible.

Table 2-3 Two-Phase Jet Model Calculation Matrix Base (Weigand et al., 1983)

Temperature/Quality	subcooling, ΔT (°C)	70, 50, 35, 15, 0
	Qualities	0, 0.01, 0.05, 0.1, 0.2, 0.33, 0.75, 0.99
Pressures	Pressure, P_0 (MPa)	6, 8, 10, 13, 15, 17
Position	Target positions (z/D)	0.5, 0.75, 1.0, 1.25, 1.50, 1.75, 2.0, 2.5, 3.0, 4.0, 8.0
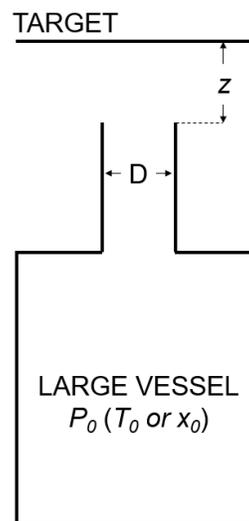
Figure 2-28 Idealized Two-phase Jet Loads Geometry Used in Two-phase Jet Loads Model NUREG/CR-2913 (Weigand et al., 1983)

2.3.1.2.2 The Length of Exit Core in NUREG/CR-2913

As discussed in Section 2.2.2.2, there will be an exit core in the break region, which will remain critical flow beyond the break. The length of the exit core calculated by the two-phase jet loads model is given in the Appendix C of NUREG/CR-2913 and also shown here in Figure 2-30. The figure indicates that this length is greater than 0.5 of the exit diameters and increases with increasing subcooling. Meanwhile, it needs to be noted that the friction effect is not considered in NUREG/CR-2913 model. As such, considering that it acts similar to decrease the subcooling, and therefore the exit core length, the NUREG/CR-2913 model can be considered conservative.

Also shown in Figure 2-30, the red lines are the predictions made by the exit core length model employed in ANSI/ANS 58.2 (1988), which is given by Equation (2-50). It is found that the exit core length in NUREG/CR-2913 decreases with increasing pressure, while that in ANSI/ANS 58.2 (1988) is independent on pressure. This inconsistency is reflected in Figure 2-30, such that the core length calculated by the model in ANSI/ANS 58.2 (1988) is smaller than that in NUREG/CR-2913 in relatively low-pressure region, but greater in relatively high-pressure region. The effect of pressure on exit core length needs to be investigated by experimental data in the future.
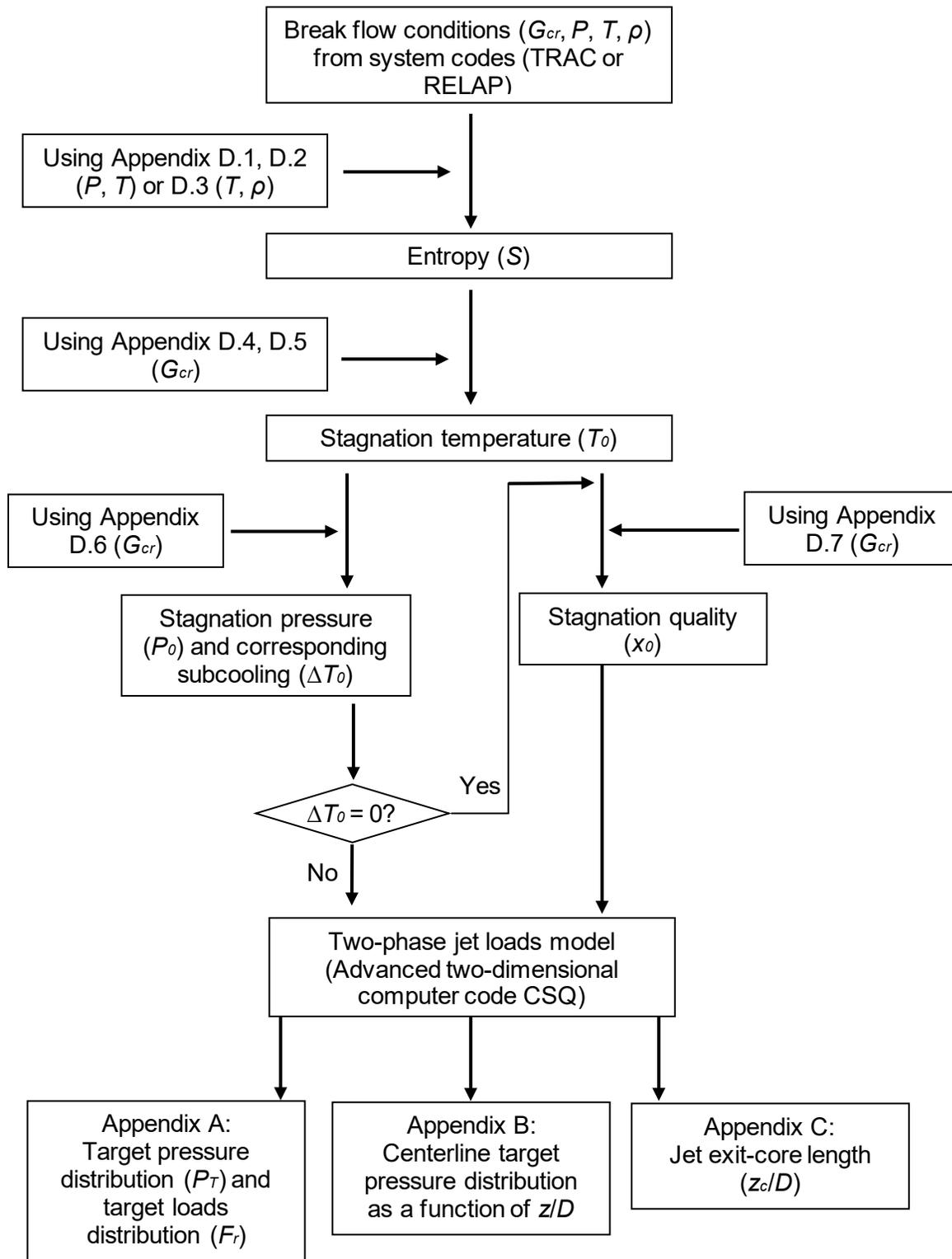
Figure 2-29 Flow Chart Showing the Calculation Procedure by Two-phase Jet Loads Model in NUREG/CR-2913. G_{cr}: Mass Flux, P: Pressure, T: Temperature, and x: Quality
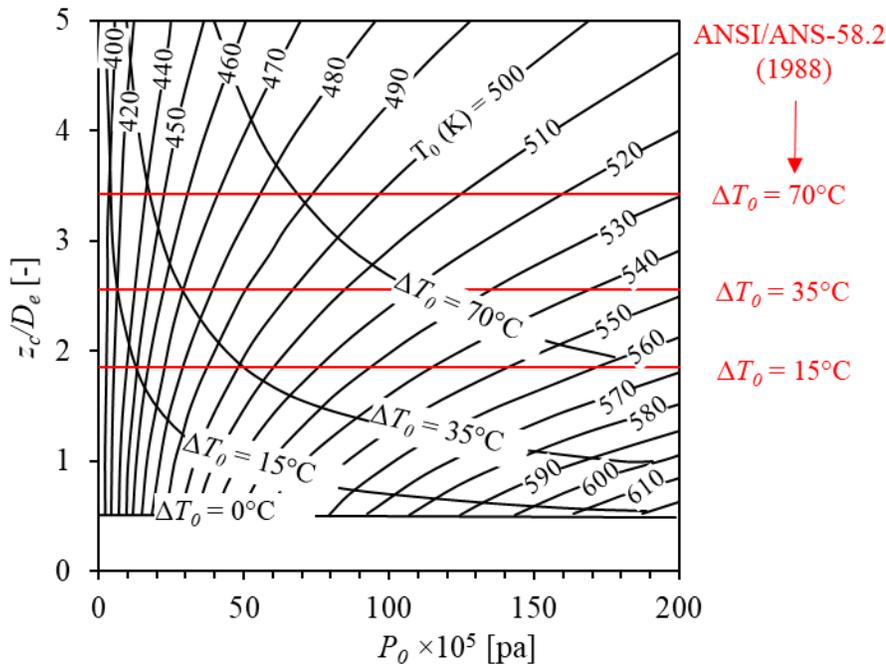
Figure 2-30 Comparison on Exit Core Length between Two-phase Jet Loads Model (NUREG/CR-2913) and ANSI/ANS 58.2 (1988). Black: NUREG/CR-2913 and Red: ANSI/ANS 58.2 (1988)

2.3.1.2.3 Approximate Models

Apart from the above two-phase jet loads calculated by CSQ, approximate models for axial and target pressure calculation are also introduced in Chapter 6 of NUREG/CR-2913. The approximate models include free jet expansion model and shock model. In the free jet expansion model, the jet is assumed to be isentropic and expands at a 45° angle. The axial pressure calculated by the free jet expansion model was found to agree well with those by the CSQ calculation and experimental data (Ontario-Hydro test and Marviken test). In the shock model, the shock at the target center is assumed to be normal and coincident with the target surface. Using the free jet expansion calculation as boundary condition, the pressure after shock can be calculated by the shock model and it agrees well with the CSQ calculation. The results calculated by the approximate models are presented in the Appendix B of NUREG/CR-2913.

2.3.1.3 One-dimensional Jet Loading Model (Moody, 1969)

The one-dimensional jet loading model developed by Moody studies (Lahey and Moody, 1977; Moody, 1973; 1969) was employed in the design basis for structural supports including jet deflectors, snubbers, and pipe restraints in nuclear power plants. This model provides a simple way to estimate the zone of influence, thrust force and loading force, although it is inappropriate for multidimensional flow jets especially for two-phase flow jets.

2.3.1.3.1 Thrust Coefficient

In Moody (1969), the theoretical expressions for thrust coefficients of compressible fluid and compressible gas are derived and employed in the ANSI/ANS-58.2 (1988). The thrust

coefficient for two-phase mixture jets with critical flow model of slip flow (slip ratio of $(v_g/v_f)^{1/3}$) has been developed for frictionless flow in Moody (1969) and further extended by accounting for friction effects in Moody (1973) and Lahey and Moody (1977). The resulting thrust coefficient for two-phase mixture jets is used in ANSI/ANS-58.2 (1988).

2.3.1.3.2 Jet Expansion (Asymptotic jet area)

In Moody (1969), the fully expanded one-dimensional asymptotic jet properties are estimated. In this estimation, the effects of friction, diffusion, turbulent momentum and energy exchange, and heat transfer with environment are neglected. The asymptotic plane is determined at the place where pressure within the jet approaches the environment pressure. The asymptotic jet total area can be obtained by combining:

$$\frac{F_j}{A_e} = \frac{A_e}{A_a} \frac{G_e^2 v_{M,a}}{g_c} = \frac{A_a}{A_e} \frac{G_a^2 v_{M,a}}{g_c} \tag{2-64}$$

and the forward momentum conservation for jet at the asymptotic plane leads to equality of thrust force and impinging force:

$$\frac{T}{A_e} = \frac{F_j}{A_e} \tag{2-65}$$

where T, F_j, A_e, A_a, G_e, G_a, $v_{M,a}$, are thrust force, impinging force, break area, asymptotic plane area, mass flux at break plane, mass flux at asymptotic plane, momentum specific volume at asymptotic plane, respectively. Therefore, the asymptotic jet total is:

$$\frac{A_a}{A_e} = \frac{G_e^2}{g_c} \frac{v_{M,a}}{T/A_e} \tag{2-66}$$

For two-phase mixture jets, the areas occupied by liquid and gas can be obtained:

$$\frac{A_{j,a}}{A_e} = \frac{G_{cr}^2}{g_c} \frac{\left[(1-x)v_f\left(xS+(1-x)\right)\right]_a}{T/A_e} \tag{2-67}$$

$$\frac{A_{g,a}}{A_e} = \frac{A_{f,a}}{A_e}\left(\frac{1}{S}\frac{x}{1-x}\frac{v_g}{v_f}\right)_a \tag{2-68}$$

In these expressions, the quality x at the asymptotic plane needs to be determined. If the interaction with environment is negligible, the stagnation enthalpy will be constant for ideal jet expansion. Meanwhile, the kinetic energy of the jet can also be neglected due to low density of gas phase. As such, x can be estimated from the following equation:

$$h_0 = h_a + kinetic \quad energy \approx \left(h_f + xh_{fg}\right) \tag{2-69}$$

where h_0 and h_a is the specific enthalpy at the stagnation condition and the asymptotic plane, respectively. For saturated or superheated steam jets, the asymptotic plane area is:

$$\left. \frac{A_{g,a}}{A_e} \right|_{x=1} = \frac{G_{cr}^2}{g_c} \frac{v_{g,a}}{T/A_e} \tag{2-70}$$

The results calculated using this approach by employing different slip ratio are shown in Figure 2-31. It should be noted that f_P is the Darcy friction factor of the pipe.

For the asymptotic plane distance, Moody (1969) assumes that axial and radial velocities are approximately the same magnitude. Therefore, the model assumes a 45-degree angle for the asymptotic plane and the distance is given by:

$$\frac{z_a}{D} \approx \frac{1}{2}\left(\sqrt{\frac{A_a}{A_e}} - 1 \right) \tag{2-71}$$

This relation is employed in ANSI/ANS-58.2 (1988).

2.3.1.4   A generalized analytical jet model (Luxat, 2017)

Luxat (2017) developed a generalized analytical jet model to predict the jet geometry or jet expansion, local distribution of pressure and temperature within the jet for a wide range of initial fluid conditions. The model captures the characteristics of high-energy fluid jets in nuclear power plants.

2.3.1.4.1   Pressure at and after the Exit Plane

The pressure at the exit plane P_e might be different from the vessel pressure P_0. In Luxat (2017), the pressure losses upstream the break plane due to frictional loss and minor loss are considered:

$$P_e = P_0 - \left(\frac{fL}{D} + k \right) \frac{G_{cr}^2}{2\rho} \tag{2-72}$$

Depending on whether the jet is subcooled jet or two-phase jet, the critical mass flux G_{cr} can be evaluated based on different models. If the jet is subcooled at the exit plane, the orifice discharge model is used for G_{cr}:

$$G_{cr} = C_D \sqrt{2\rho\left(P_e - p_{amb} \right)} \tag{2-73}$$

where C_D is the discharge coefficient.

For two-phase jet at the exit plane, the Henry-Fauske discharge model is used for G_{cr}:

$$G_{cr} = \xi\left(P_e, h_e \right) \sqrt{P_e} \tag{2-74}$$
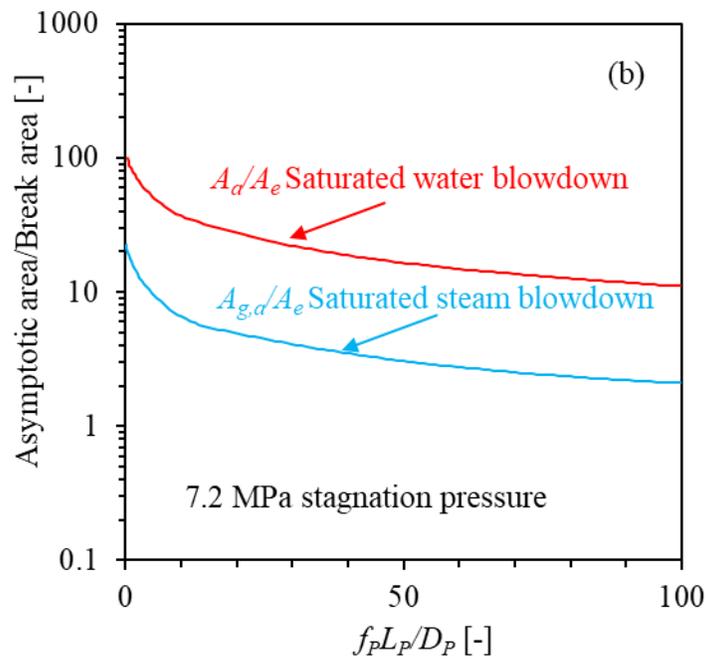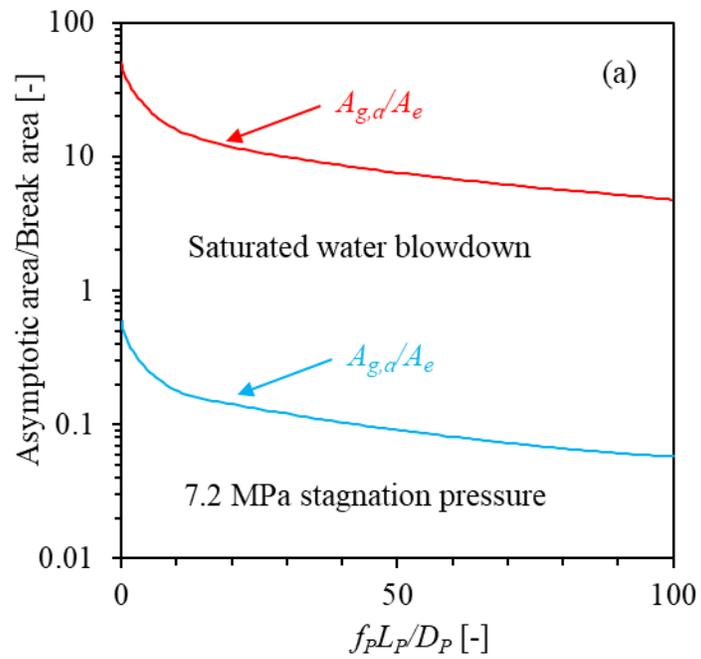
Figure 2-31 Jet Asymptotic Area: (a) Saturated Water Jet with Slip Ratio of $(v_g/v_f)^{1/3}$ and (b) Saturated Water and Steam Jet with Slip Ratio of 1 (Moody, 1969)

2.3.1.4.2 Pressure within the Jet

The pressure (P) as functions of axial (z) and radial (r) locations for flashing two-phase jet is given by Equation (2-75). The radial pressure distribution follows a general Gaussian distribution, while the axial distribution decays rapidly with respect to the axial distance from the exit plane.

$$P^* = \exp\left[K(z/D)\right]\exp\left[-C\left(r/D\right)^2\right]$$ (2-75)

where P^* is defined in Equation (2-40), and

$$K\left(z/D\right) = -\left(z/D - 0.5\right)$$ (2-76)

$$C = 1.4 - 0.4\varphi$$ (2-77)

$$\varphi = P\left(h_e\right)/P_e$$ (2-78)

Here, D is the break diameter and φ describes the subcooling of the initial fluid at the break plane. When φ approaches 0, the fluid is cold water, while when φ approaches 1, the fluid is in the saturated state. The comparison on pressure at the jet centerline between the current model and experimental data is shown in Figure 2-32.

2.3.1.4.3 Jet Core Length

The length of the jet core (z_c) for steam-water mixture jets is estimated by the following equation:

$$\frac{z_c}{D} = 0.5 + \left[-\ln\left(\frac{\varphi P_e - p_{amb}}{P_e - p_{amb}}\right)\right]$$ (2-79)

where φ is the subcooling parameter as defined in Equation (2-78). The comparison between this model and experimental data is shown in Figure 2-33.

2.3.1.4.4 Jet Geometry

The radial expansion of the jet is governed by the volumetric expansion of the fluid. At any distance downstream the jet break, the fraction of fluid energy used for radial expansion is defined by the local quality:

$$x = \frac{h_e - h_f\left(z\right)}{h_{fg}\left(z\right)}$$ (2-80)

At the exit plane:

$$h_e = h_f\left(P_e\right) + x_e h_{fg}\left(P_e\right)$$ (2-81)

where x is the local thermodynamic quality of the region occupied by the projected area of the exit plane, and x_e is that at the exit plane. This assumes that the fluid that has expanded out of the core region is no longer available for further expansion. By applying the mass conservation, the normalized jet area (A) and jet diameter (D_j) can be obtained:

$$\frac{A_j(z)}{A_e} = \frac{\overline{\rho_e}}{\rho(z)} \tag{2-82}$$

$$\frac{D_j(z)}{D} = \sqrt{\frac{A_j(z)}{A_e}} \tag{2-83}$$

with flow density

$$\overline{\rho_e} = \frac{1}{\left[x/\rho_g + (1-x)/\rho_f \right]} \tag{2-84}$$

The thermodynamic fluid properties in Equations (2-82) to (2-84) are evaluated by the local dynamic pressure averaged over the projected exit plane area:

$$\overline{P_j(z)} = \frac{4}{C} \left[1 - \exp(-C/4) \right] \eta(z) + p_{amb} \tag{2-85}$$

With

$$\eta(z) = (P_e - p_{amb}) \exp(-K(z/D)) \tag{2-86}$$

This approach was found to agree well with the experimental data as shown in Figure 2-34. The experimental data was for 225 °C water discharging from 6mm nozzle at 2.76 MPa.
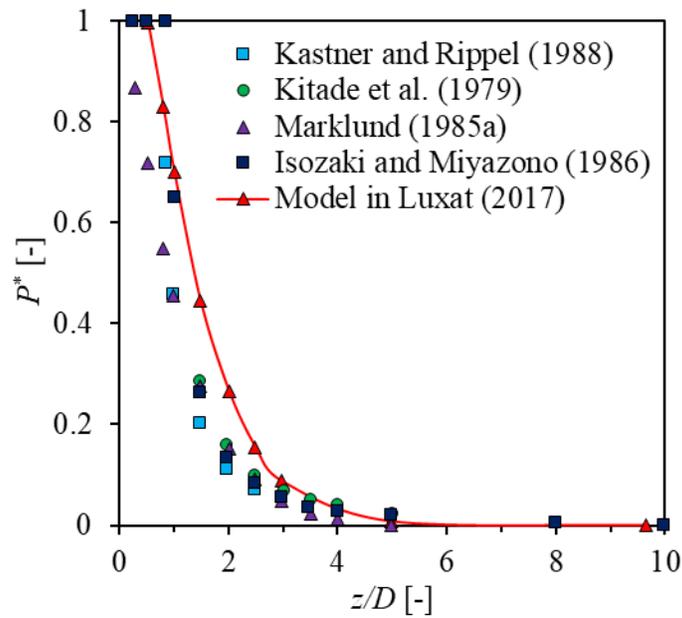
Figure 2-32 Comparison on Pressure at the Jet Centerline between Model and Experimental Data. Plot from Luxat (2017)
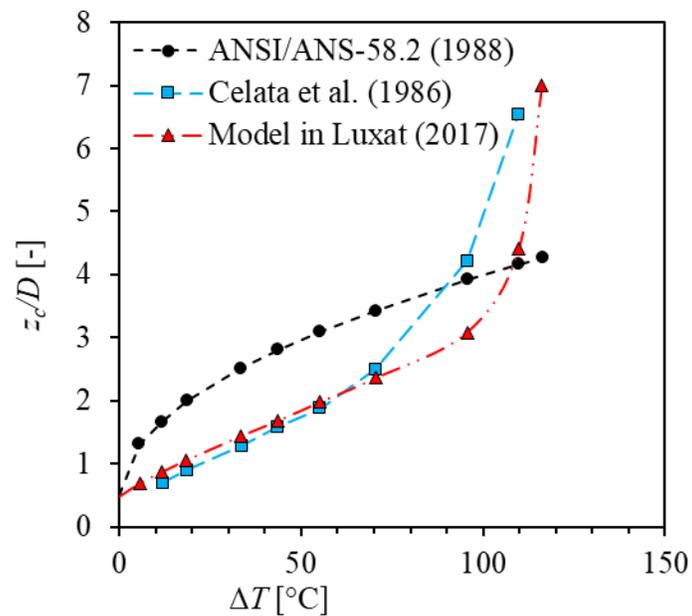
Figure 2-33 Comparison on Jet Core Length between Model and Experimental Data (Celata et al., 1986), and Model in ANSI/ANS-58.2 (1988). Plot from Luxat (2017)
.
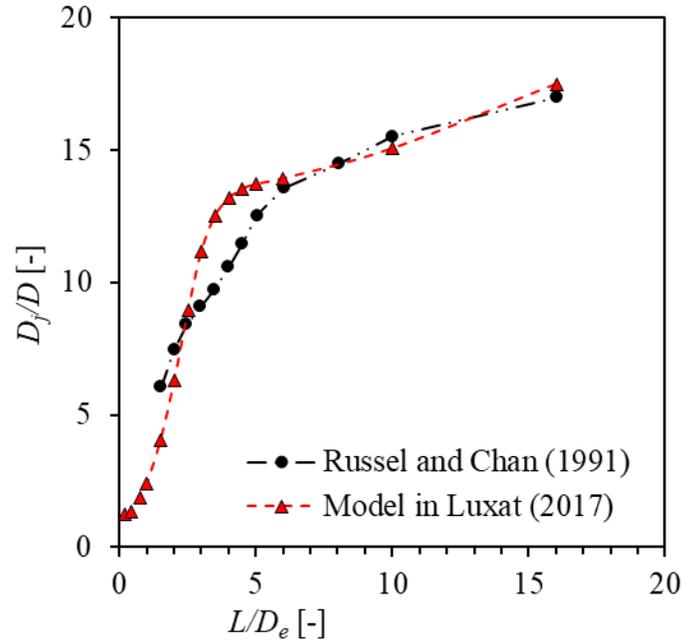
Figure 2-34 Comparison on Jet Geometry between Model and Experimental Data from Russel and Chan (1991). Plot from Luxat (2017)

2.3.2 CFD Simulations

2.3.2.1 Numerical evaluation of affected region by flashing jet flow

The flashing jets were investigated by Morita et al. (2018) to evaluate the affected region using the same CFD code as in CRIEPI-Hitachi test (Section 2.2.2.2.2). To extend the CFD code to the water region, the pre-conditioning method and pseudo sonic speed to the governing equations were applied. The ambient pressure saturated steam was assumed outside of the nozzle instead of air, such that the jet is adiabatically-expanded and the interaction with air is neglected. The test conditions investigated in the current work are summarized in Table 2-4. The effects of vessel pressure and fluid subcooling on maximum velocity, shockwave position, and asymptotic length (z_a) and width (H_a) are investigated. Here, the asymptotic plane is defined as the maximum expanded position as shown in Figure 2-35, which is the same as in steam jet simulation (Figure 2-14). However, the spread angle for the steam-water jet is found to be much larger than that of the steam jet.

It is found that the shock wave position, asymptotic length (z_a) and width (H_a) become larger as the inlet pressure increases, or when the subcooling temperature increases at the same inlet pressure. The maximum velocity is more sensitive to inlet pressure than the subcooling temperature. The increasing inlet pressure increases the fluid pressure and density at the nozzle exit plane, leading to a larger expansion of the flow. Those parameters are found to correlate with the density ratio (ρ_e/ρ_{amb}) and pressure ratio (P_e/p_{amb}) very well:

$$z_a = 0.3 \times \sqrt{\frac{\rho_e}{\rho_{amb}}}$$
(2-87)

$$H_a = 0.008 \times \frac{\rho_e}{\rho_{amb}} + 1 \tag{2-88}$$

$$u_{max} = 110 \times \sqrt{\frac{P_e}{p_{amb}}} \tag{2-89}$$

where subscripts e and amb indicate condition at the exit plane and ambient condition, respectively. With these results, the affected area (H_a and z_a) and dynamic pressure (ρu_{max}^2) at the asymptotic plane can be evaluated. Considering that the spread angle for steam-water mixture jet is much larger that the steam jet, it is better to consider the affected region to be a round cylinder with diameter H_a and length z_a.

2.3.2.2   Single- and Two-phase Jet CFD Models

The study by Schneider et al. (2012) established CFD models for both single- and two-phase jets. The commercial software ANSYS Fluent 14.0 was employed in this study and a structured mesh was imposed using ANSYS meshing program which is built into the workbench. The CFD simulations were to provide the pressure, temperature and velocity field for a given initial fluid and geometric condition. Inlet conditions for each simulation were taken from benchmarking conditions and the outlet zones are set at atmospheric pressure and room temperature. The simulation of single phase supersonic free jets was benchmarked with experimental results of both steam (Masuda et al., 1981) and air (Teske et al., 1996; Zerkle, 1996) jets. Comparisons between simulation and experimental data for static pressure and total pressure are made. For two-phase jet simulations, Fluent's evaporation-condensation model predicts the mass transfer from liquid to vapor. The two-phase jets were benchmarked with the experimental results from Kastner and Rippel (1988) and Forrest et al. (1987). The centerline stagnation pressure was found to agree well with experimental data (Kastner and Rippel, 1988). Meanwhile, the ANSI/ANS-58.2 (1988) model was found to be conservative in stagnation pressure calculation by assuming a large jet core region. The static pressure along the centerline from CFD simulation was also compared with the experimental results from Forrest et al. (1987). Good agreement was observed.

After review on jet models and CFD simulations, it can be seen that since the workshop on jet impingement and pipe whip in 1981, CFD simulations have been performed to investigate important jet impingement phenomena. The spreading angles for under-expanded supersonic jets obtained by CRIEPI-Hitachi test are comparable to those presented by Ransom (2004). The CFD simulations by Morita et al. (2018) correlates the jet geometry using jet properties at the exit plane such as jet density and jet static pressure, which is a dynamic approach compared to the model employed in the ANSI/ANS-58.2 (1988). The new model developed by Luxat (2017) also provide a new approach to calculate jet core length and jet geometry.

Table 2-4 Test Conditions in Flashing Jet CFD Simulation (Morita et al., 2018)

Case	Fluid	Inlet Pressure (MPa)	Inlet ΔT (°C)
1	Saturated water	0.5	0
2	Saturated water	2.0	0
3	Saturated water	5.0	0
4	Saturated water	7.0	0
5	Subcooled water	2.0	10
6	Subcooled water	2.0	20
7	Subcooled water	7.0	10
8	Subcooled water	7.0	20
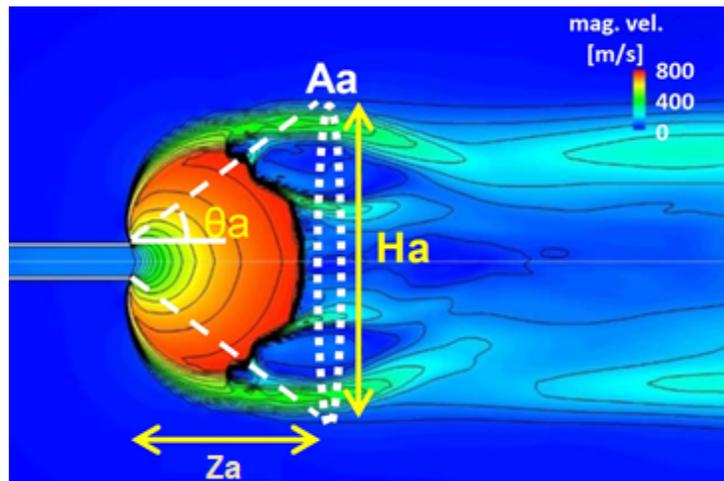
Figure 2-35 Definitions of Asymptotic Length (z_a), Asymptotic Width (H_a), and Spread Angle (θ_a) (Morita et al., 2018)

3   DATA ANALYSIS AND MODEL EVALUATION

3.1   Data Analysis

The experimental databank is first established based on the experiments reviewed in Section 2.2. Those include large-scale Marviken tests (Marklund, 1985a, 1985b), medium-scale JAERI tests (Isozaki et al., 1984; Yano, 1984; Yano et al., 1984, 1983) and Ontario-Hydro tests (Forrest et al., 1987), and small-scale Mitsubishi tests (Kawanishi et al., 1986; Kitade et al., 1979; Masuda et al., 1981), KWU tests (Kastner and Rippel, 1988), and CRIEPI-Hitachi tests (Morita et al., 2016; Takahashi et al., 2016; Xu et al., 2016).

Considering that the above experiments were performed under different thermal-hydraulic conditions, break geometries, target geometries, etc., the experimental data are first non-dimensionalized to compile an organized databank. This will make the data easier to interpret and process. Meanwhile, the effects of initial fluid condition (i.e., stagnation pressure, temperature or void fraction/ quality) and break size on pressure profiles downstream of the break plane can be easily investigated. The generated dimensionless parameters include:

$$p^*(z,t) = \frac{p(z,t) - p_{amb}(t)}{P_0(t) - p_{amb}(t)} \qquad (3\text{-}1)$$

$$P^*(z,t) = \frac{P(z,t) - p_{amb}(t)}{P_0(t) - p_{amb}(t)} \qquad (3\text{-}2)$$

$$z^* = \frac{z}{D_{eff}} \qquad (3\text{-}3)$$

$$D_{eff}^2 = D^2 - D_{probe}^2 \qquad (3\text{-}4)$$

where p^* and P^* are the dimensionless static and stagnation pressure, z^* is the dimensionless axial distance, D_{eff} is the effective break diameter, p, P, P_0, p_{amb}, z, D, and D_{probe} are the static pressure, stagnation pressure, vessel stagnation pressure, ambient atmospheric pressure, axial distance, break diameter, and central probe diameter, respectively. The central probe was employed in one of the tests (Marviken tests) to measure static pressure at the center of the free jets. Additional information on the central probe will be provided in Section 3.1.1.1.

3.1.1   Experimental Data

The established experimental databank based on the data available in literature is discussed. The collected data included those from Marviken tests, Mitsubishi tests, JAERI tests, and KWU tests.

3.1.1.1   Marviken Tests

Large scale free and impinging jet tests were performed at the Marviken test facility in Sweden. The Marviken pressure vessel was initially filled with water, which was heated to a specified temperature and pressure level. In these tests, rupture discs were employed to simulate the

break and the vessel contents were discharged through a nozzle to form the jets. Three nozzle sizes of 200, 299, and 509 mm diameter were used. In total, six free jet tests and six impinging jet tests were performed. Important parameters including pressure, temperature, and fluid density were measured during the blowdown, using the pressure transducer, thermocouples, and a three-beam gamma densitometer system. The static and stagnation pressures were obtained in the free jet tests and the stagnation pressure at the targets was obtained in the impinging jet tests. In the current report, the stagnation pressure measured at horizontal beams or targets are used to evaluate models. The maximum error for these measurements is calculated to be 40 kPa in Marviken report. Considering that the measured minimum pressure is around 200 kPa, a ±20% error bar is used for Marviken data in this work.

3.1.1.1.1 Free jets (Tests 1 through 6)

In total six tests were performed to investigate the free jets. The initial stagnation pressures for free jets were set to 5.0 MPa, and the initial subcooling is 0°C, 30°C, and 50°C. The nozzle used in the tests has a diameter of 0.2 m, 0.3 m, and 0.5 m. A brief summary of the free jets in Marviken tests is shown in Table 3-1. A schematic drawing of the measurement system for free jets in Marviken tests is shown in Figure 3-1. The system consists of a central probe, horizontal structural support beams (A and B) and horizontal measurement beams (0-6). The central probe has a diameter of 100 mm and was used to measure the static pressure in the jet center. The horizontal measurement beams are used to measure both static and stagnation pressures at different axial and radial locations. As shown in the figure, the horizontal measurement beams are arranged at different angles to minimize their effects on measurements. The stagnation pressure measured at a radial location of 70 mm was assumed to be that at the center of the jet and is used for model evaluation. The arrangement of the instrumentation and support beams for the free jets in Marviken tests are listed in Table 3-2. The experimental data for static and stagnation pressures were collected in the free jet tests and are presented here.

Among the six free jet tests, Tests 1 and 2 are shakedown tests. The central probe and instrumented beams were found to move during Tests 3 and 4, at about 6.6 s and 1.2 s, respectively. As such additional support beams (A and B) are added for Tests 5 and 6 as shown in Figure 3-1. Therefore, Tests 5 and 6 provide the best experimental results for free jets. In the current report, the measured static and stagnation pressures for Tests 5 and 6 are presented as an example.

Table 3-1 Summary of Free Jets in Marviken Tests

Test number	Initial Pressure (MPa)	Initial ΔT (°C)	Nozzle Diameter (mm)
1	5.0	30	509
2	5.0	30	299
3	5.0	50	509
4	5.0	30	200
5	5.0	0	299
6	5.0	30	509

Table 3-2 Arrangement of the Instrumentation and Support Beams for Free Jets in Marviken Tests (Marviken report MXD-101, OECD Nuclear Energy Agency, 1882)

Beam	Distance below nozzle (mm)	Used in tests	Beam length (mm)	Beam width (mm)	Beam height (mm)
0	150	3 ~ 6	1,740	34	250
1	500	1 ~ 6	1,740	34	250
2	1,000	1 ~ 6	1,740	34	250
3	1,000	1 ~ 6	1,740	34	250
4	1,500	1 ~ 6	1,740	34	250
5	2,000	1 ~ 6	1,740	34	250
6	2,000	1 ~ 6*	1,740	34	250
A	225	5 ~ 6	1,570	20	150
B	350	5 ~ 6	1,570	20	150

* not instrumented in Tests 3 ~ 6.
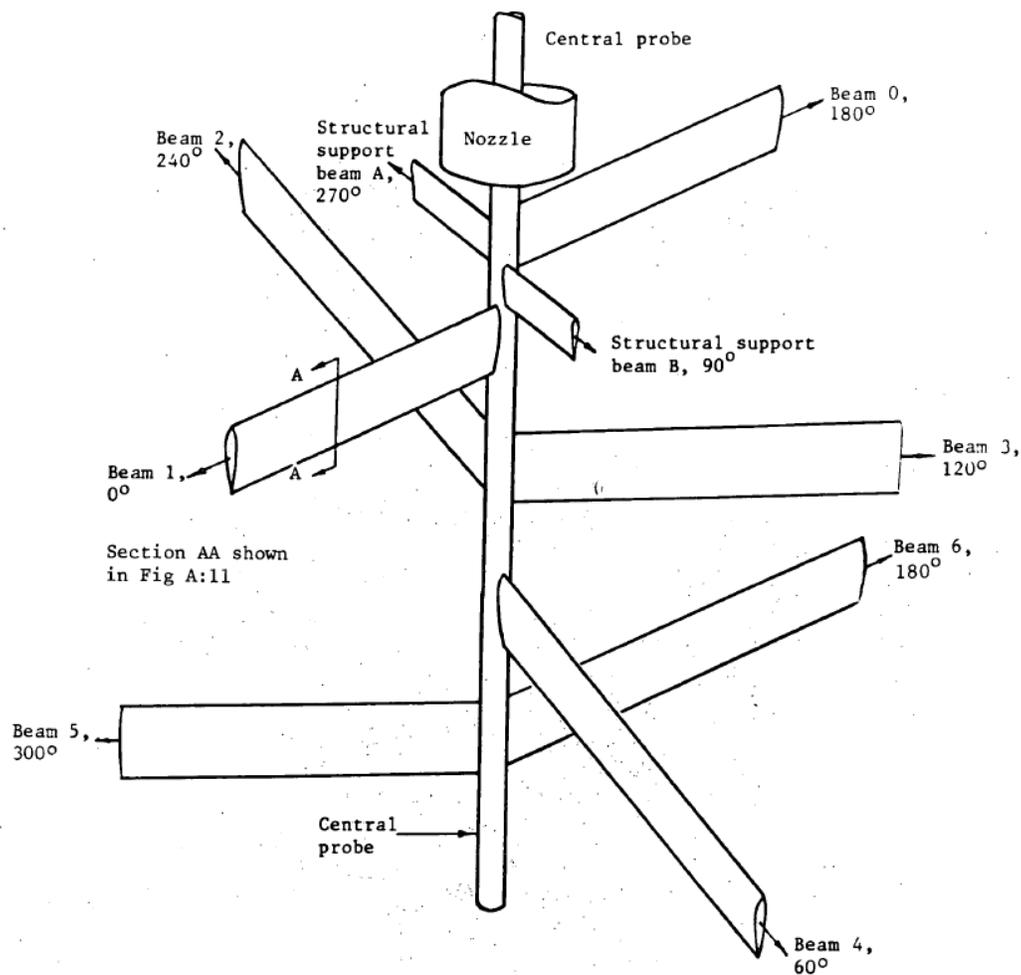
Figure 3-1 Schematic Diagram of the Measurement System for Free Jets in Marviken Tests (Marklund, 1985b)

In Test 5, the saturated steam jet was investigated at an initial stagnation pressure of 5.0 MPa. A particular standpipe was used inside the vessel such that the discharge pipe entrance can be raised into the vapor space. In this test, a nozzle with 299 mm ID was used. Figure 3-2 shows the time histories of both static and stagnation pressures in Test 5. Only the measured data at the center of the jets are shown here. As shown in Figure 3-2 (a) and (c), the pressure decreases with the process of blowdown. This is due to the decreasing stagnation pressure in the vessel. After non-dimensionalizing the pressure, however, it is found that the pressure profiles are nearly flat, which indicates that the dimensionless static and stagnation pressures downstream of the break plane weakly depend on instantaneous vessel stagnation pressure in the vessel. The stagnation pressure in the vessel and ambient pressure are compared in Figure 3-3. As shown in the figure, the ambient pressure almost keeps constant compared to the stagnation pressure in the vessel. Here, the ambient pressure is the static pressure of the room where free jets were released into.

The static and stagnation pressures at the center of the jets at different axial locations downstream of the break plane are shown in Figure 3-4. As shown in the plots, both static and stagnation pressure decrease rapidly downstream of the break plane. The static and stagnation pressures drop below zero at around 1.2 D_{eff} and 3.6 D_{eff}, respectively. Meanwhile, the dimensionless static and stagnation pressures generally resemble at different times as shown in Figure 3-4 (b) and (d), which indicates that the vessel stagnation pressure has negligible effects on these pressures.

The radial profiles of p^* and P^* at certain axial locations are shown in Figure 3-5 and Figure 3-6. Negative values of dimensionless static pressure are observed at the center region of the jets as shown in Figure 3-5 (b) and Figure 3-6 (b), which indicates that the jets are over expanded. Generally, the static pressures at these locations are similar to the ambient pressure. The stagnation pressure at these locations are generally below 20%. Interestingly, a constant peak is observed for stagnation pressure at r/D_{eff} around 1.5. This might be due to the edge peaking pressure profile for steam jets as observed in previous work (Kitade et al., 1979; Masuda et al., 1981). However, it could also be possible that the measurements at this particular radius is not reliable.

Unlike test 5, the initial condition of the vessel fluid in Test 6 is subcooled water with a degree of subcooling of 30 °C at an initial stagnation pressure of 5 MPa. In both Tests 5 and 6, the instrumentation in the vicinity of the nozzle exit was improved because horizontal beam 0 was added for measurements. A standpipe was installed inside the vessel to increase the duration of the steam discharge period. The standpipe was found to collapse during the test and this increases the duration of saturated liquid jets. Based on the discussion in Marviken report, the subcooled flow period was not affected. Saturated flow data with an extended quality range were obtained, and low-pressure steam data were obtained at the end of the test. Although the collapsed standpipe will afftect the upstream condition, the fluid condiotion (e.g., stagnation pressure, temperature) and critical mass flux were measured at the end of nozzle. Therefore, these data in Test 6 are stil included for data analysis and model evaluation in the current work.
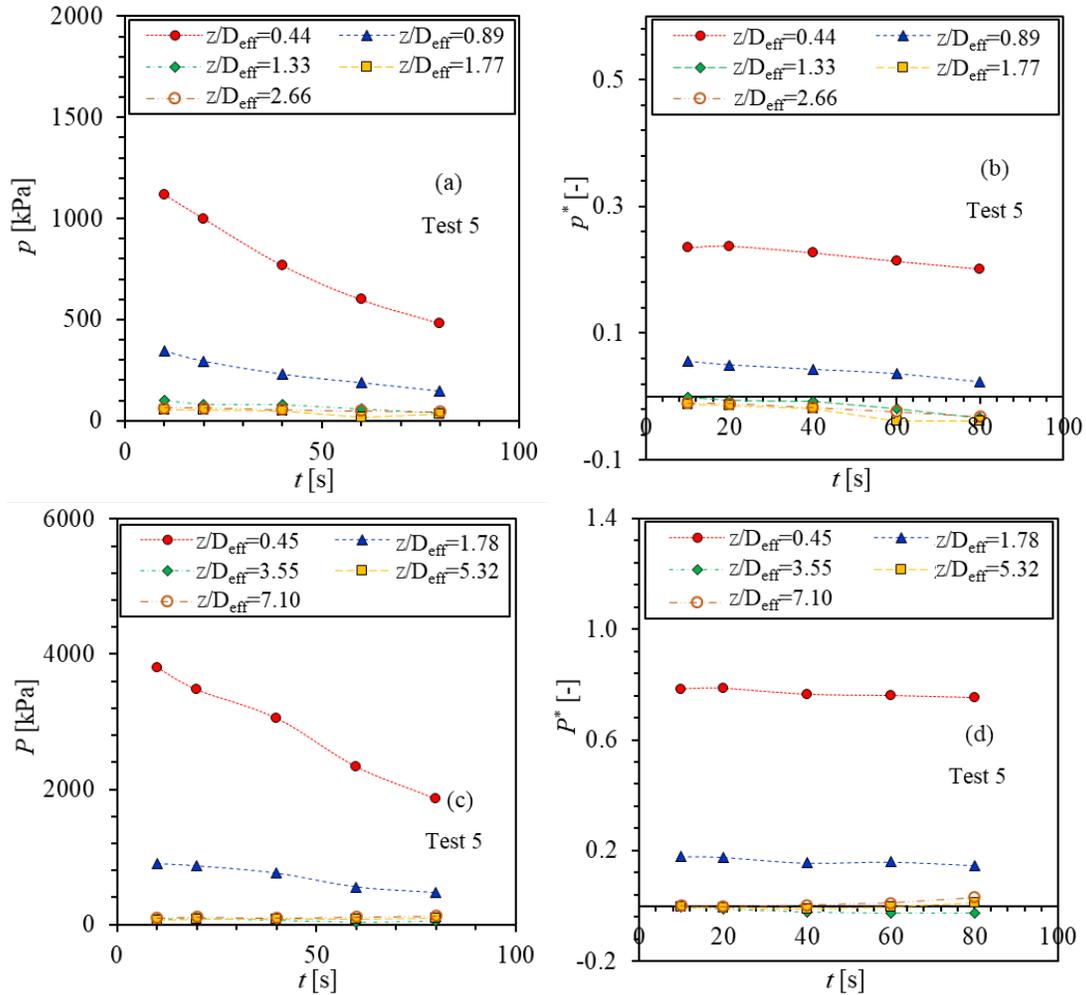
Figure 3-2 Time Histories of Pressure at the Center of the Jet for Free Jet Test 5: (a) and (b) Static Pressure, (c) and (d) Stagnation Pressure
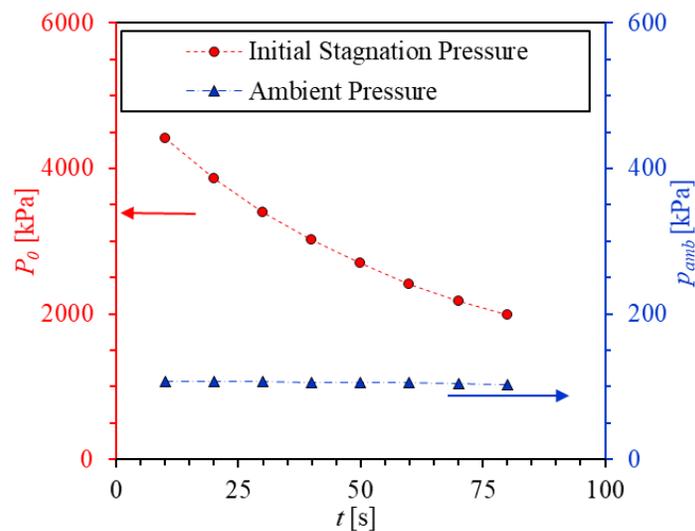
Figure 3-3 Time Histories of Vessel Stagnation Pressure and Ambient Pressure for Free Jet Test 5
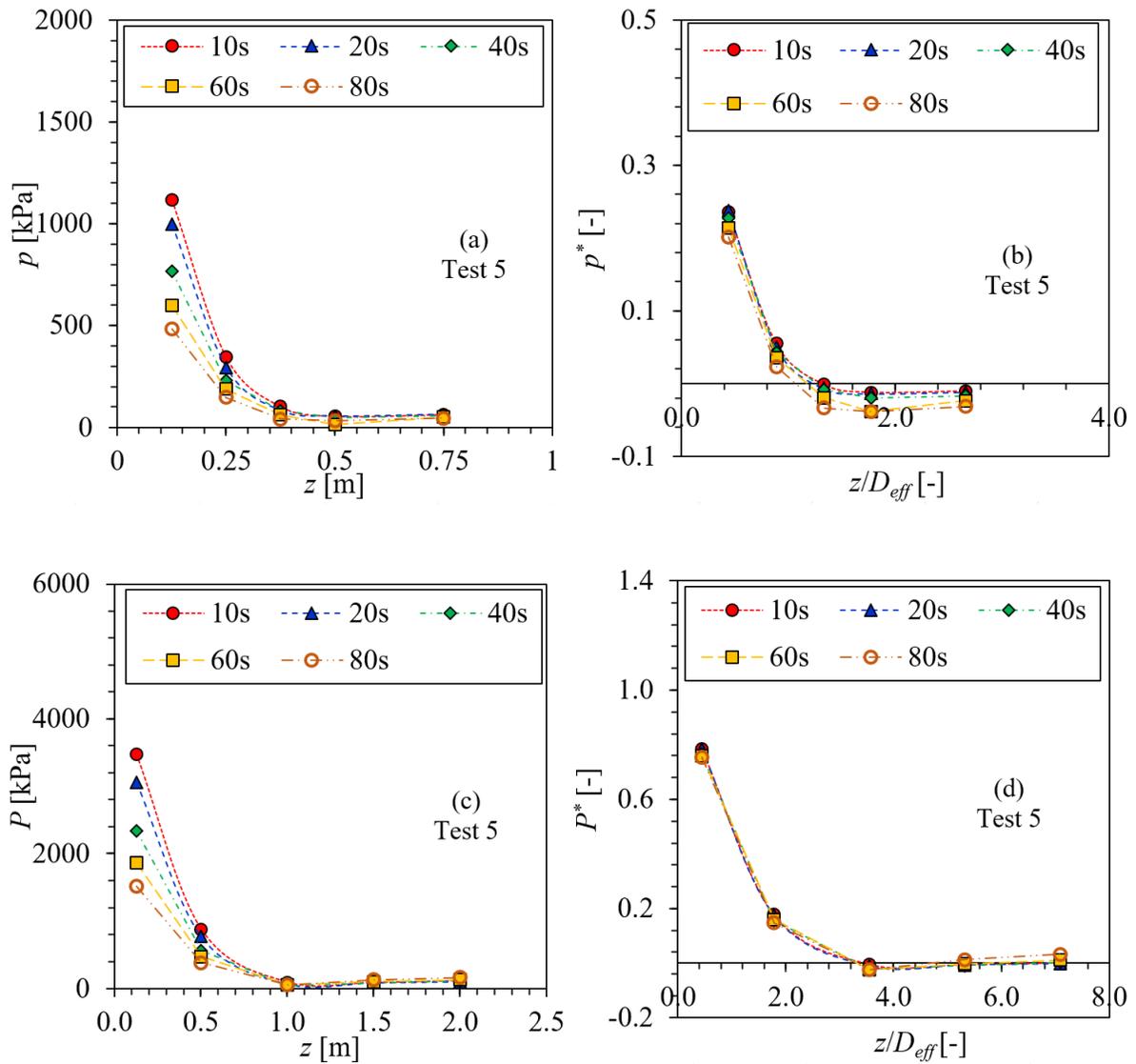
Figure 3-4 Pressure Profiles at the Center of the Jet as a Function of Axial Distance for Free Jet Test 5: (a) and (b) Static Pressure, (c) and (d) Stagnation Pressure
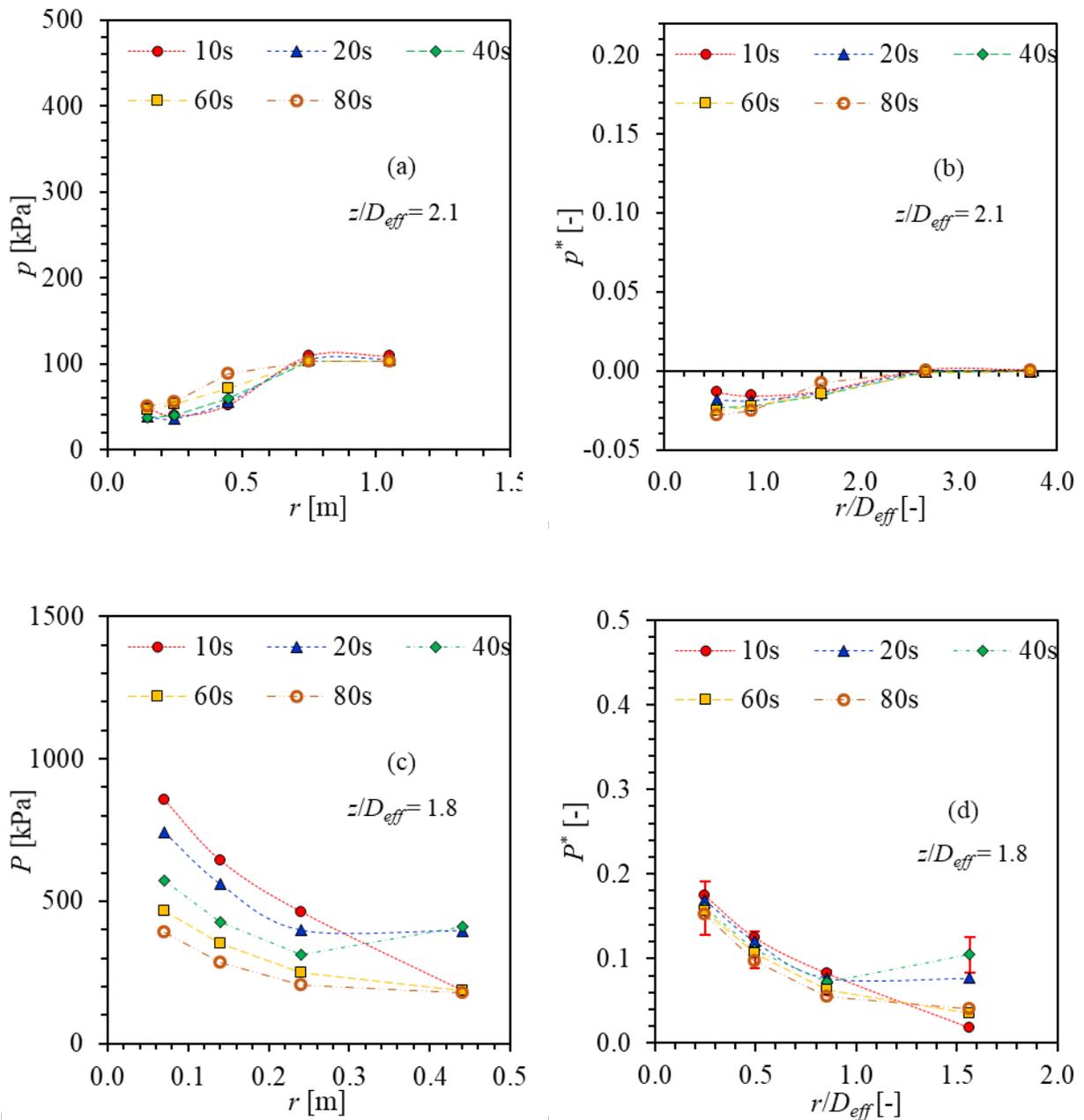
Figure 3-5 Pressure Profiles at Axial Location $z/D_{eff} \sim 1.8$ as a Function of Radial Distance for Free Steam Jet Test 5: (a) and (b) Static Pressure, (c) and (d) Stagnation Pressure
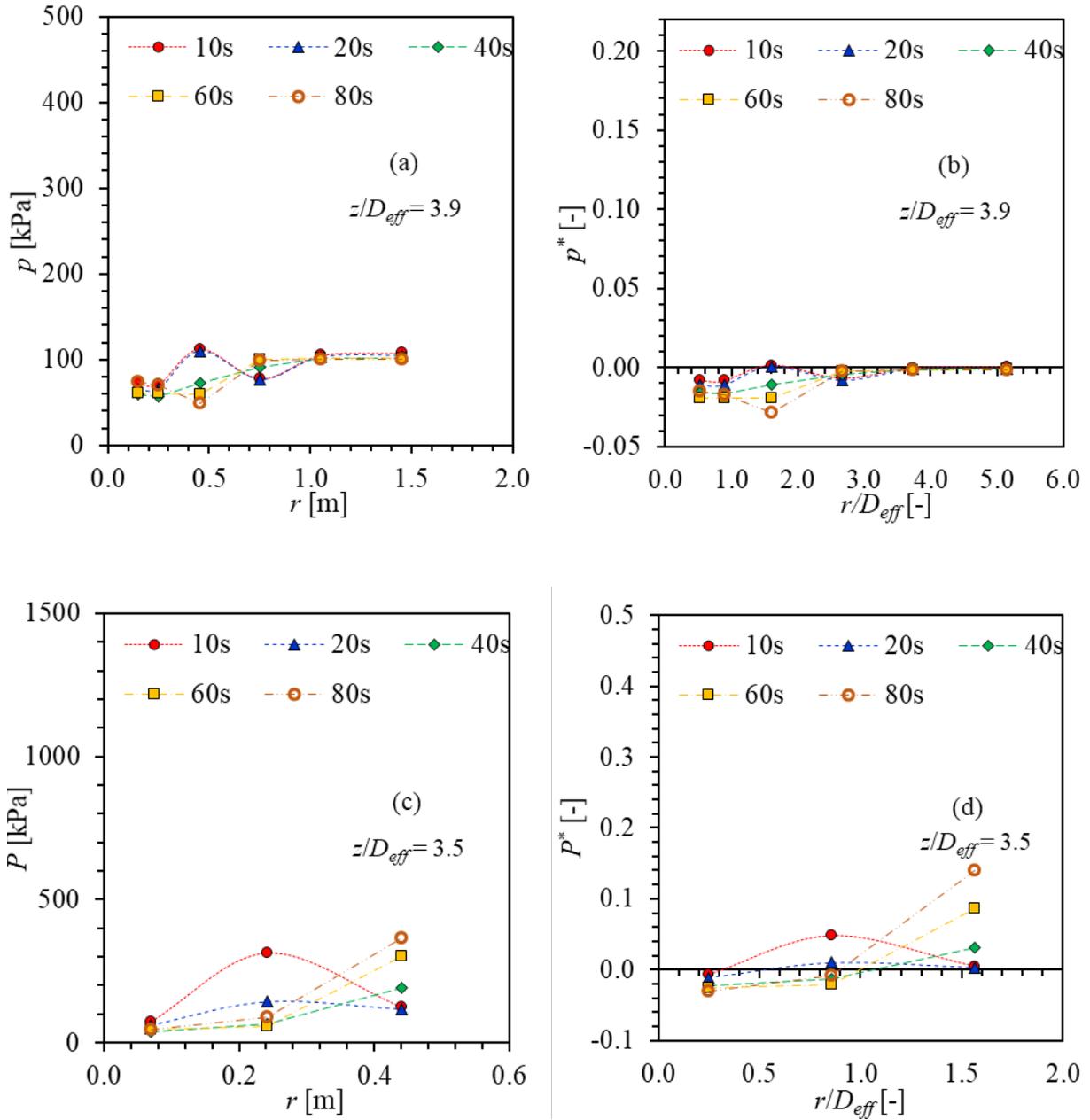
Figure 3-6 Pressure Profiles at Axial Location $z/D_{eff} \sim 3.5$ as a Function of Radial Distance for Free Steam Jet Test 5: (a) and (b) Static Pressure, (c) and (d) Stagnation Pressure

Figure 3-7 shows the time histories of the static and stagnation pressures for Test 6 as an example. As shown in the plots, the blowdown is divided into three phases based on the initial fluid condition at the nozzle inlet: subcooled water, saturated water/two-phase and saturated steam. This is due to the gradual decrease of pressure in the vessel. The subcooled regime existed from about 0 s to 36 s, during which the subcooling at the nozzle inlet gradually decreases from about 20°C at a pressure of 4.1 MPa to saturated liquid at about 3.1 MPa. The saturated regime existed from about 36 s to 73 s with the pressure from 3.1 MPa to 1.6 MPa. This regime can also be divided into the liquid-dominated saturated flow at the first 12 s and saturated flow with intermediate steam qualities between 48 s and 73 s. The steam-dominated saturated flow existed after 73 s, with void fraction at the nozzle exit in excess of 0.99 and steam quality of 0.65.

Both static and stagnation pressures decrease with respect to time as shown in Figure 3-7 (a) and (c). This is because the pressure in the vessel keeps decreasing during the blowdown. After non-dimensionalizing the pressure, however, they show different trends. As shown in Figure 3-7 (b), the value of p^* at the vicinity of the break first increases then decreases. However, instead of decreasing, the value of P^* remains nearly constant at $z/D_{eff} = 0.25$, and that at $z/D_{eff} = 0.50$ first decreases then increases. According to Equations (3-1) and (3-2), the profiles of p^* (or P^*) will be similar to those of p (or P) when P_0 and p_{amb} are constant. However, this is not the case for transient blowdown test as in Marviken test, where both P_0 and p_{amb} are not constants as shown in Figure 3-8. Therefore, the profiles of p^* (or P^*) does not resemble those of p (or P).

In addition, it is found that both the static and stagnation pressures decrease very rapidly in the first two diameters of the break as shown in Figure 3-7 (b) and (d). At axial location around 0.75 $D_{eff} \sim 1.5$ D_{eff}, the saturated steam jet over-expanded to pressures less than the ambient containment pressure (t ~ 75 s) as shown in Figure 3-7 (b). Although not shown in the plots, the static pressure recovered to the containment pressure at further distances downstream. Figure 3-9 shows the pressure profiles at the center of the jet as a function of axial location. It is observed that the dimensionless static pressure (p^*) drops below zero for the saturated steam jet at around 0.7 D_{eff} as shown in Figure 3-9 (b), which indicates that the jet is over expanded at this axial location. Meanwhile, both static and stagnation pressures are found to decrease rapidly downstream of the break plane. The values of p^* and P^* decrease to zero at around 1.5 D_{eff} and 3 D_{eff}, respectively.

Figure 3-10 and Figure 3-11 show the pressure profiles as a function of radial location at different axial locations. Negative values of static pressure are observed at the center region of steam jets as shown in Figure 3-10 (b) and Figure 3-11 (b), which is consistent with Test 5 and this indicates that the jets are over expanded. For the jets with other initial fluid conditions, the p^* is greater than ambient pressure for subcooled water jets at the vicinity of the break ($z/D_{eff} = 1.2$). The stagnation pressure basically drops below 10% within 1 D_{eff} at both axial locations.
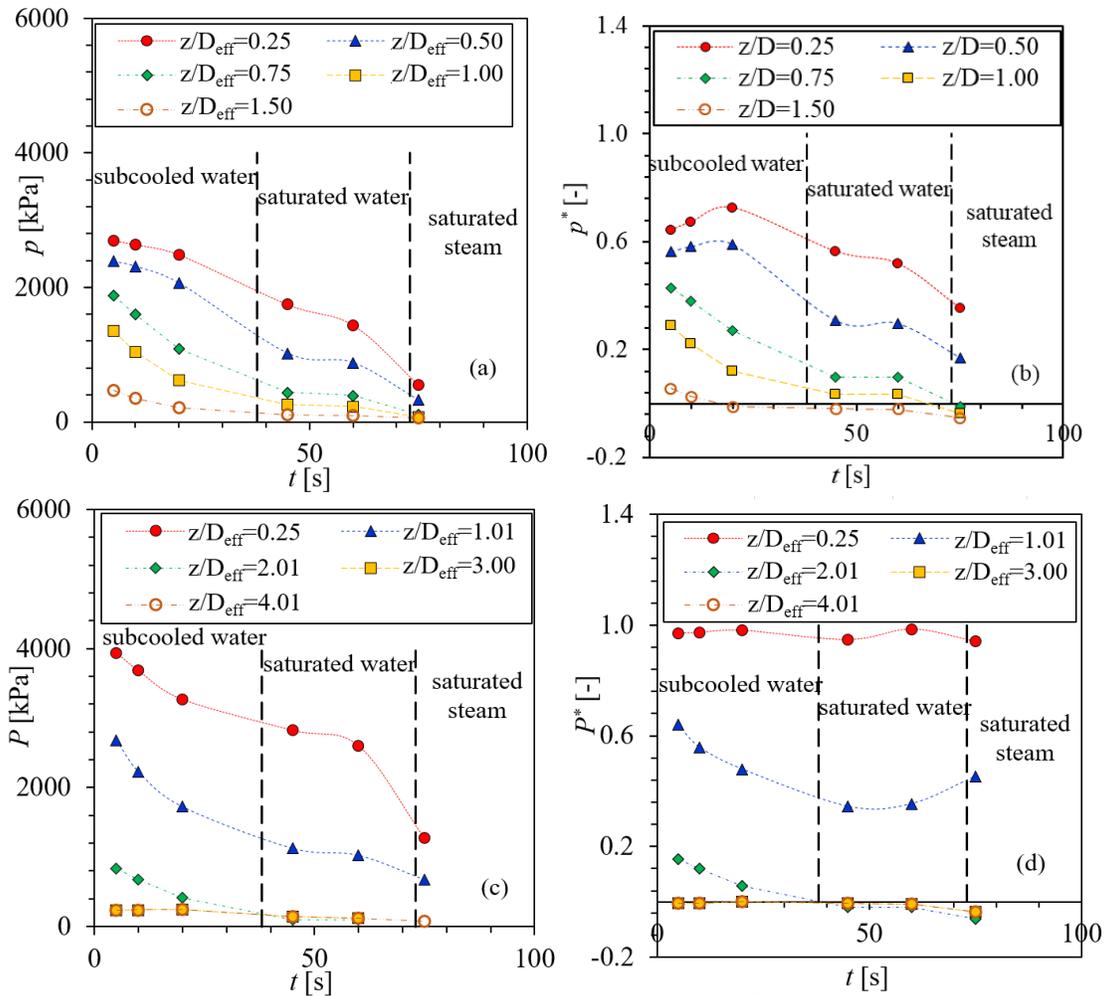
Figure 3-7 Time Histories of Pressure at the Center of the Jet for Free Jet Test 6: (a) and (b) Static Pressure, (c) and (d) Stagnation Pressure
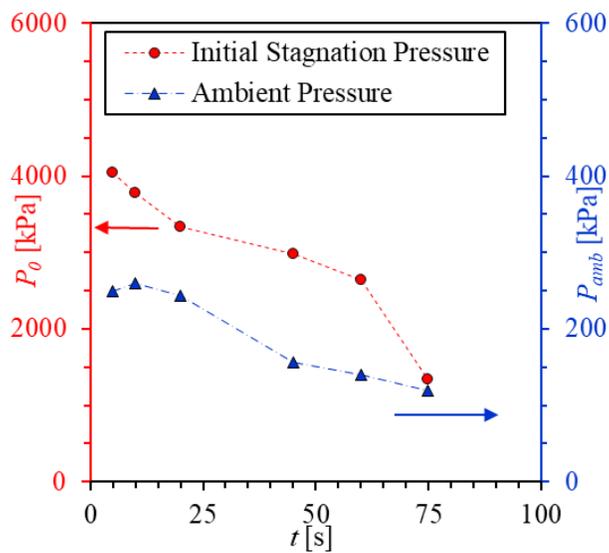
Figure 3-8 Time Histories of Vessel Stagnation Pressure and Ambient Pressure for Free Jet Test 6
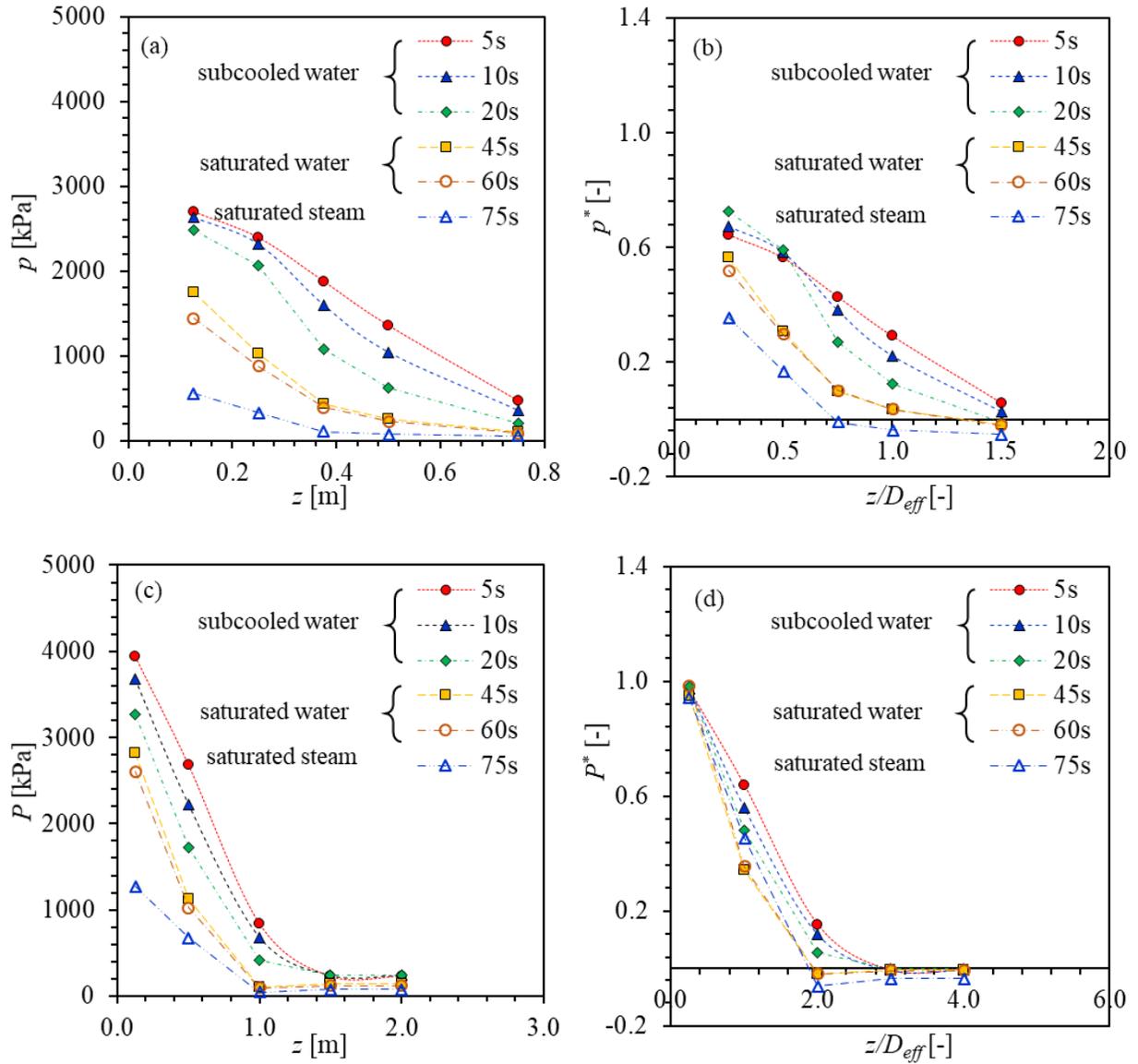
Figure 3-9 Pressure Profiles at the Center of the Jet as a Function of Axial Distance for Free Jet Test 6: (a) and (b) Static Pressure, (c) and (d) Stagnation Pressure
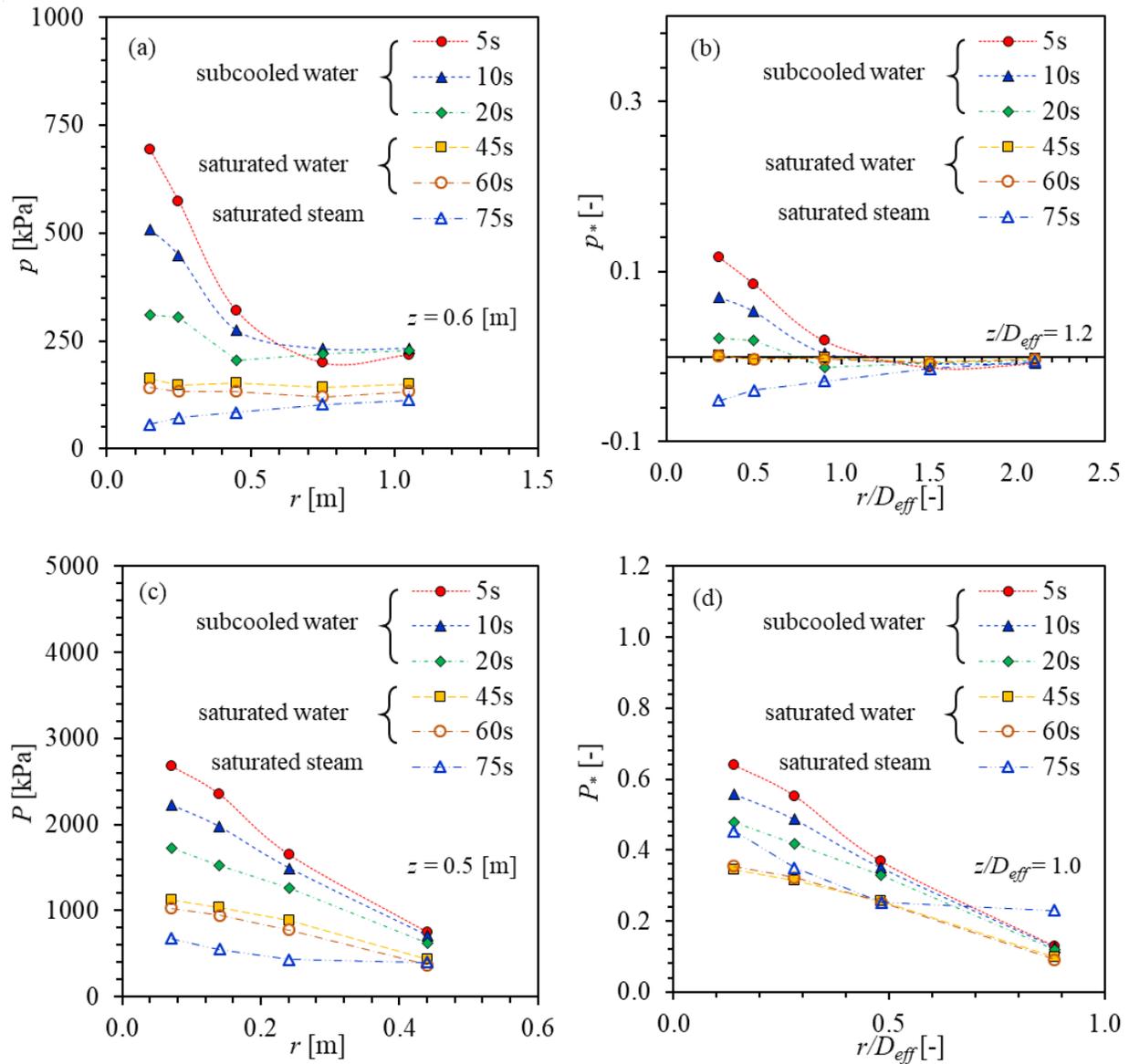
Figure 3-10 Pressure Profiles at Axial Location z/D_{eff} ~ 1.0 as a Function of Radial Distance for Free Jet Test 6: (a) and (b) Static Pressure, (c) and (d) Stagnation Pressure
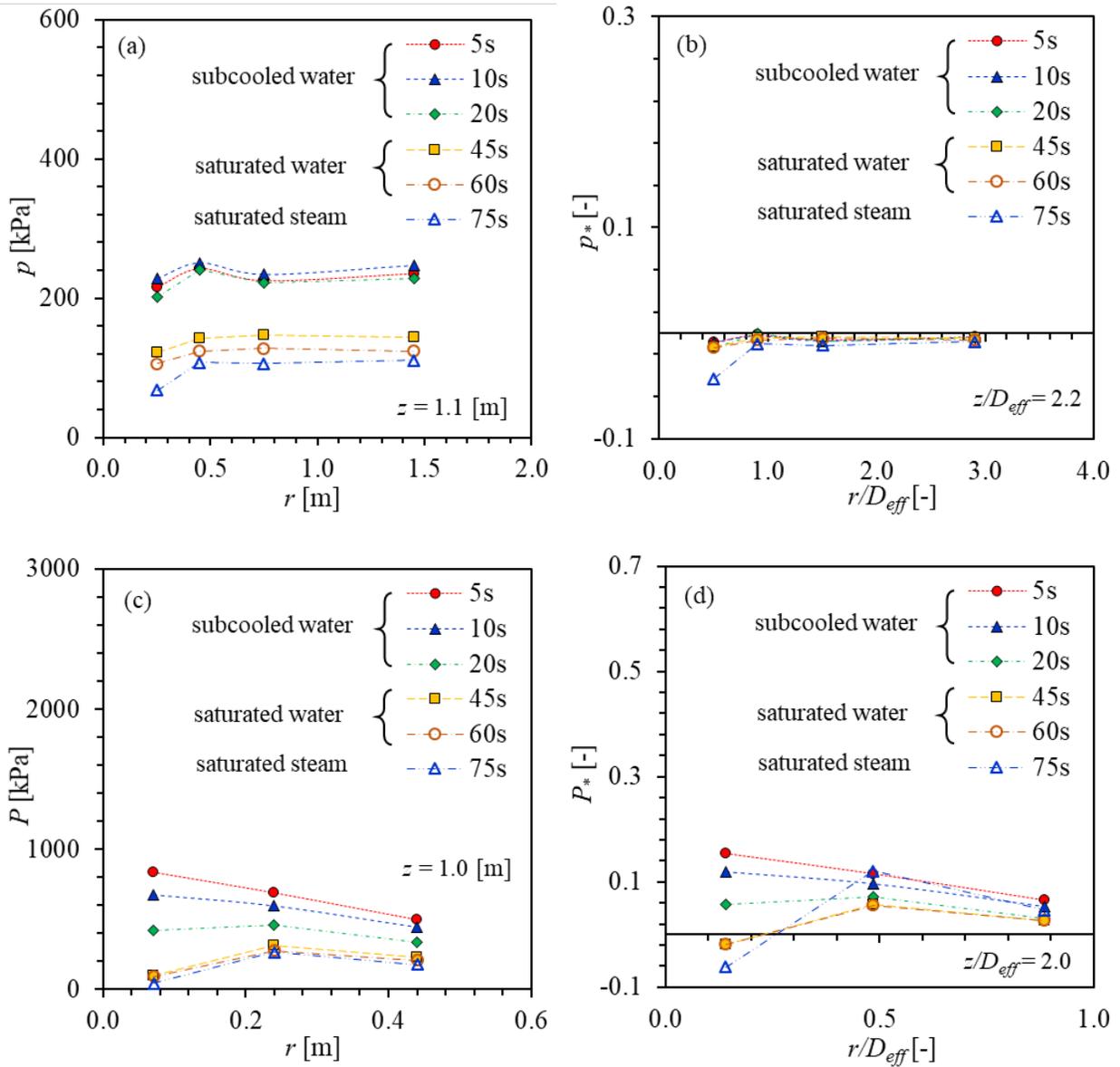
Figure 3-11 Pressure Profiles at Axial Location z/D_{eff} ~ 2.0 as a Function of Radial Distance for Free Jet Test 6: (a) and (b) Static Pressure, (c) and (d) Stagnation Pressure

3.1.1.1.2 Impinging jets (Tests 7 through 12)

In total six tests were performed to investigate the impinging jets. The initial stagnation pressure for free jets were set to 5.0 MPa, with the initial subcooling of 0°C, 30°C, and 50°C. The nozzle used in the tests has a diameter of 0.2 m, 0.3 m, and 0.5 m. Different target geometries including flat plate, cavity, and pipe were used. A brief summary of the impinging jets in Marviken tests is shown in Table 3-3. The target distance (z^*) in the table is defined by Equation (3-3). For the impinging jets tests, the central probe employed in the free jets tests was removed. In this case, $D_{probe} = 0$ and $D_{eff} = D$.

Table 3-3 Summary of Impinging Jets in Marviken Tests

Test number	Initial Pressure (MPa)	Initial ΔT (°C)	Break Diameter D (mm)	Target	Target distance (z^*)
7	5.0	30	509	Flat plate	4.05
8	5.0	30	509	Flat plate	2.06
9	5.0	30	200	Cavity	5.24
10	5.0	30	509	Flat plate	1.27
11	5.0	0	299	Flat plate	2.15
12	5.0	30	509	Pipe	2.95

In Tests 7, 8, and 10, the only difference is the target location. As such, they can be used to investigate the pressure distribution on target at different locations downstream of the break plane. Figure 3-12 shows the time histories of the stagnation pressure at the center of the target plates for these three impinging tests. As shown in the plots, the blowdown is divided into three phases based on the initial fluid condition at the nozzle inlet: subcooled water, saturated water/two-phase and saturated steam. Since the initial fluid conditions are the same for all these three tests, the blowdown process show similar transient behavior. The subcooled regime existed from about 0 s to 25 s, during which the subcooling at the nozzle inlet gradually decreases from about 19°C at a pressure of 4.3 MPa to saturated liquid at about 3.1 MPa. The saturated regime existed from about 25 s to 45 s with the pressure from 3.1 MPa to 2.5 MPa. The steam-dominated saturated flow existed after 50 s, with void fraction in excess of 0.99 and steam quality of 0.7.

As shown in Figure 3-12 (b), generally the stagnation pressure is the highest for subcooled water jets at the vicinity of the break plane (Tests 10 and 8). That of saturated water/two-phase and saturated steam jets are comparable. Meanwhile, the P^* decreases very quickly downstream of the break plane. At 4.05 D, the P^* at the target plate is generally zero. Figure 3-13 shows the vessel stagnation pressure and ambient pressure for these three tests. As shown in the figure, both pressures change with time. Good repeatability was observed for these three tests, which indicates that the obtained data are reliable.

Figure 3-14 shows the radial pressure profiles for these three impinging jets. Generally, the stagnation pressure drops to zero at a radius of 2 D at different axial locations. The stagnation pressure drops more quickly for subcooled water jets than saturated water/two-phase and steam jets.
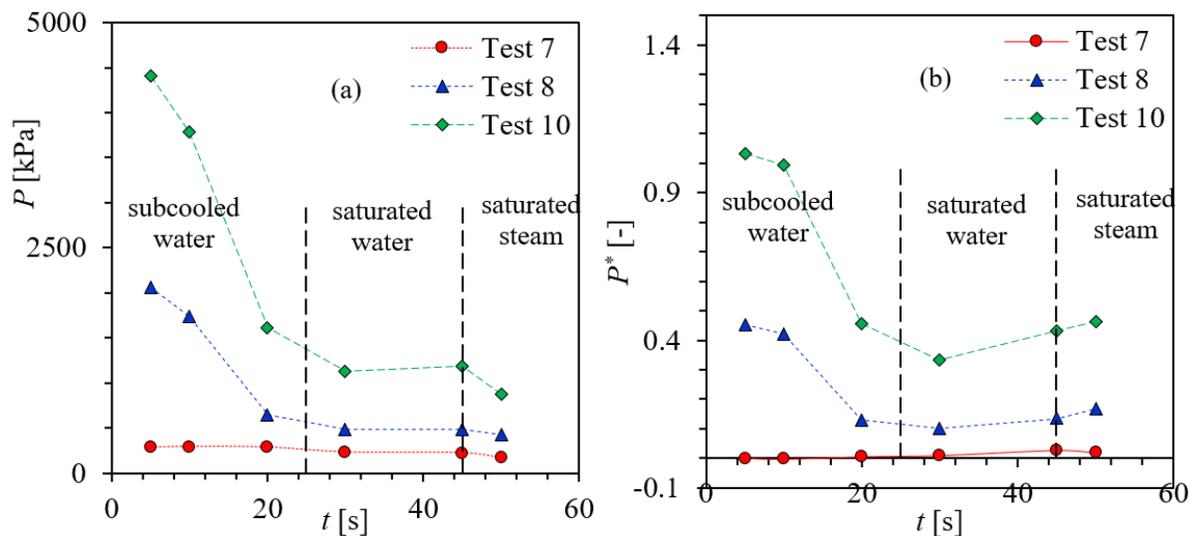
Figure 3-12 Time Histories of Stagnation Pressure at the Center of the Target Plates for Impinging Jets Tests 7 (4.05 D), 8 (2.06 D), and 10 (1.27 D)
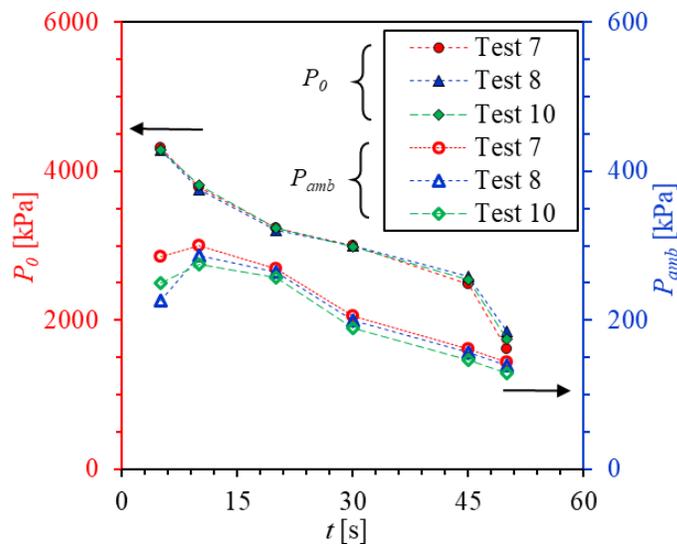
Figure 3-13 Time Histories of Initial Stagnation Pressure and Ambient Pressure for Impinging Jets Tests 7 (4.05 D), 8 (2.06 D), and 10 (1.27 D)
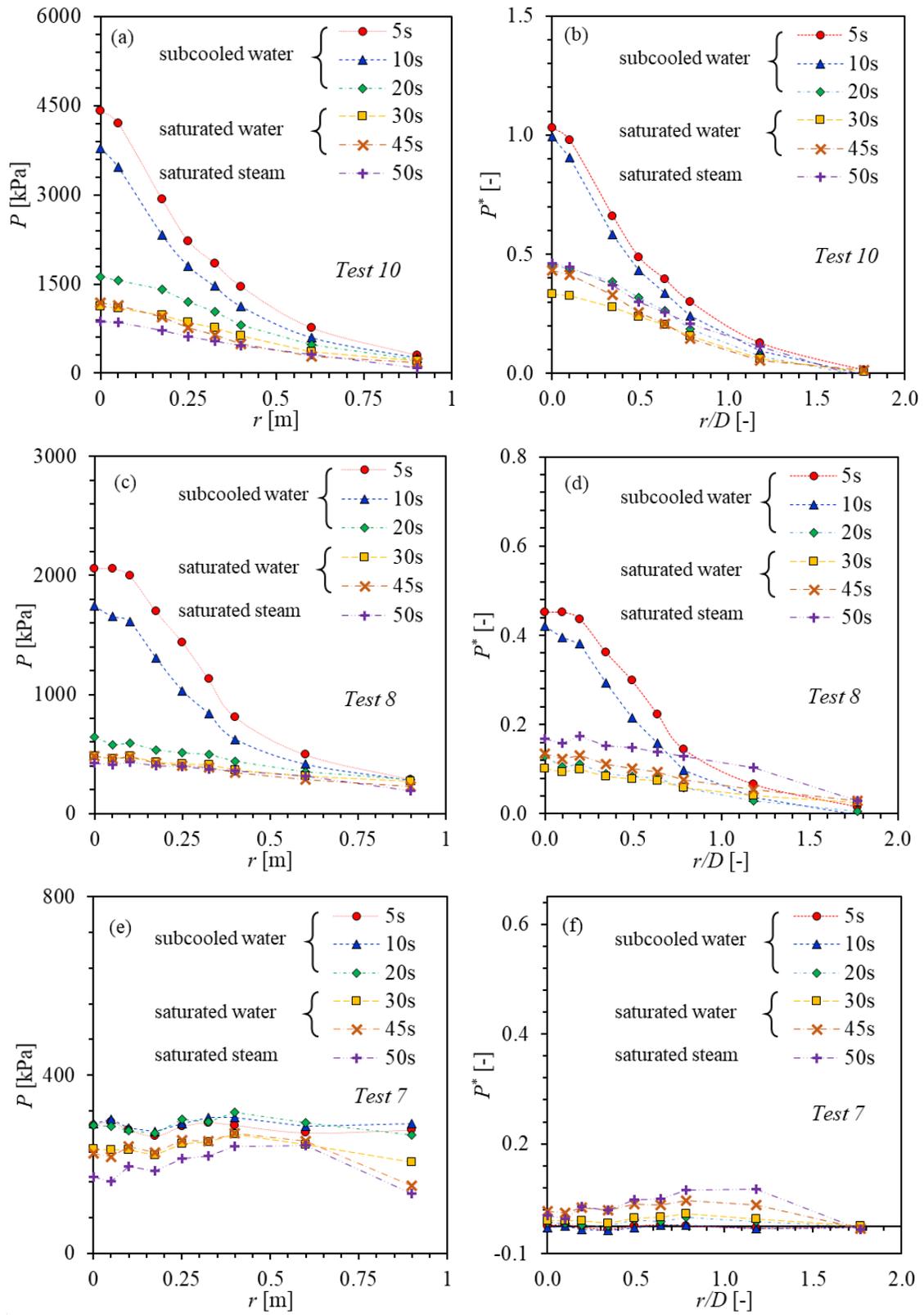
Figure 3-14 Stagnation Pressure Profiles at Different Axial Location as a Function of Radial Distance: (a) and (b) Test 10 (1.27 *D*), (c) and (d) Test 8 (2.06 *D*), (e) and (f) Test 7 (4.05 *D*)

In Test 12, a pipe is used as the target as shown in Figure 3-15. As shown in the side view, measurements were made along the length of the pipe (*l*) for 4 different angles around the pipe (i.e., 0°, 90°, 180°, 270°). Therefore, the measurement for 0° is for stagnation pressure and the data along other angles are for static pressure.
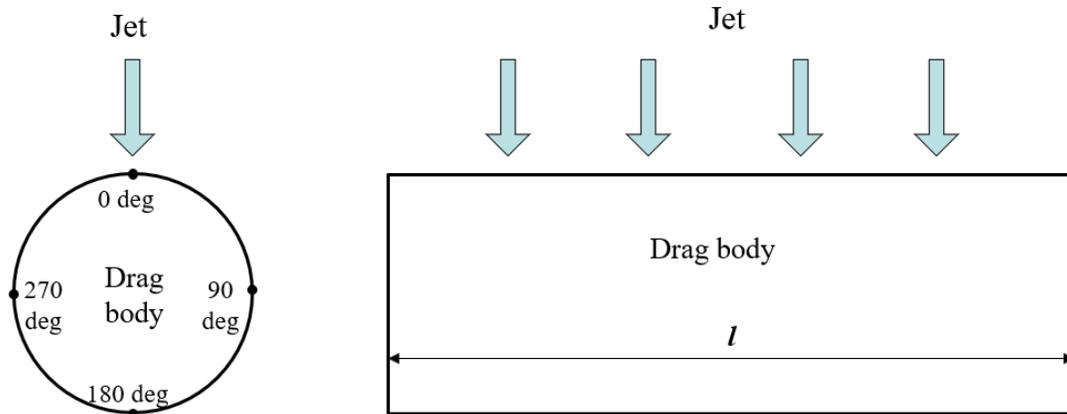
Figure 3-15 Target (Pipe) Employed in Test 12 of the Marviken Tests (Marviken Report MXD-212, OECD Nuclear Energy Agency, 1982). Left: Side Vew and Right: Front View

3.1.1.2 Mitsubishi Tests

The experimental data in Mitsubishi tests are collected to extend the experimental databank. These include the impinging steam jets in Kitade et al. (1979) as shown in Figure 3-16, free and impinging steam jets in Masuda et al. (1981) as shown in Figure 3-17, and free and impinging jets in all three flow regimes (steam, saturated water, and subcooled water) in Kawanishi et al. (1986) as shown in Figure 3-18. In Kawanishi et al. (1986), only the stagnation pressure at the center of the target plate was presented. From the data in steam jets, it is found that the stagnation pressure drops below 10% at around 3 *D* for both free and impinging jets. Meanwhile, the edge-peaking pressure profiles are observed between 4.5 *D* and 13 *D* (axial locations) for steam jets. In Mitsubishi tests, the measurement uncertainties were not discussed and a ±20% error bar is used for model evaluation in Section 3.2.
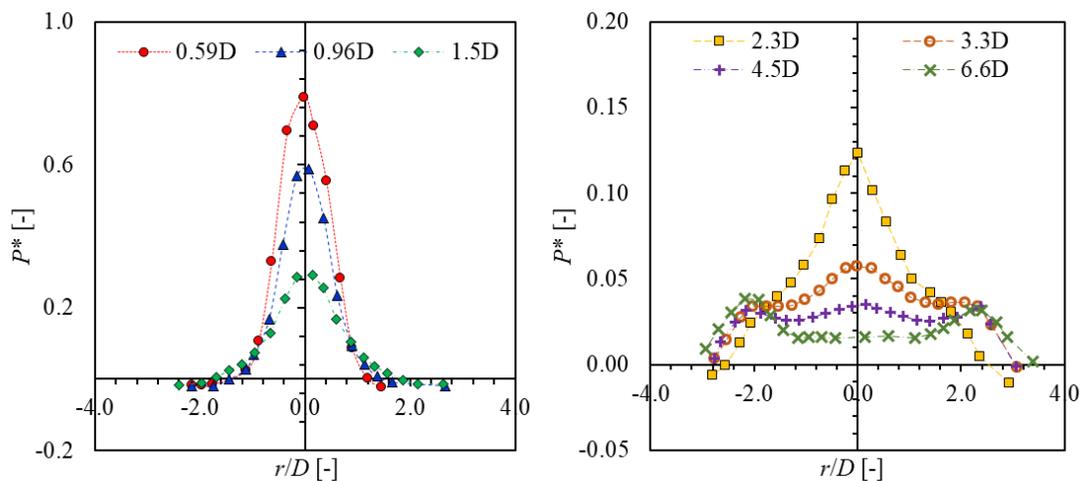
Figure 3-16 Impinging Steam Jets in Kitade et al. (1979): Stagnation Pressure at the Target Plate Downstream of the Break Plane at Different Axial Locations (P_0 = 4.02 MPa, *D* = 9.4mm)
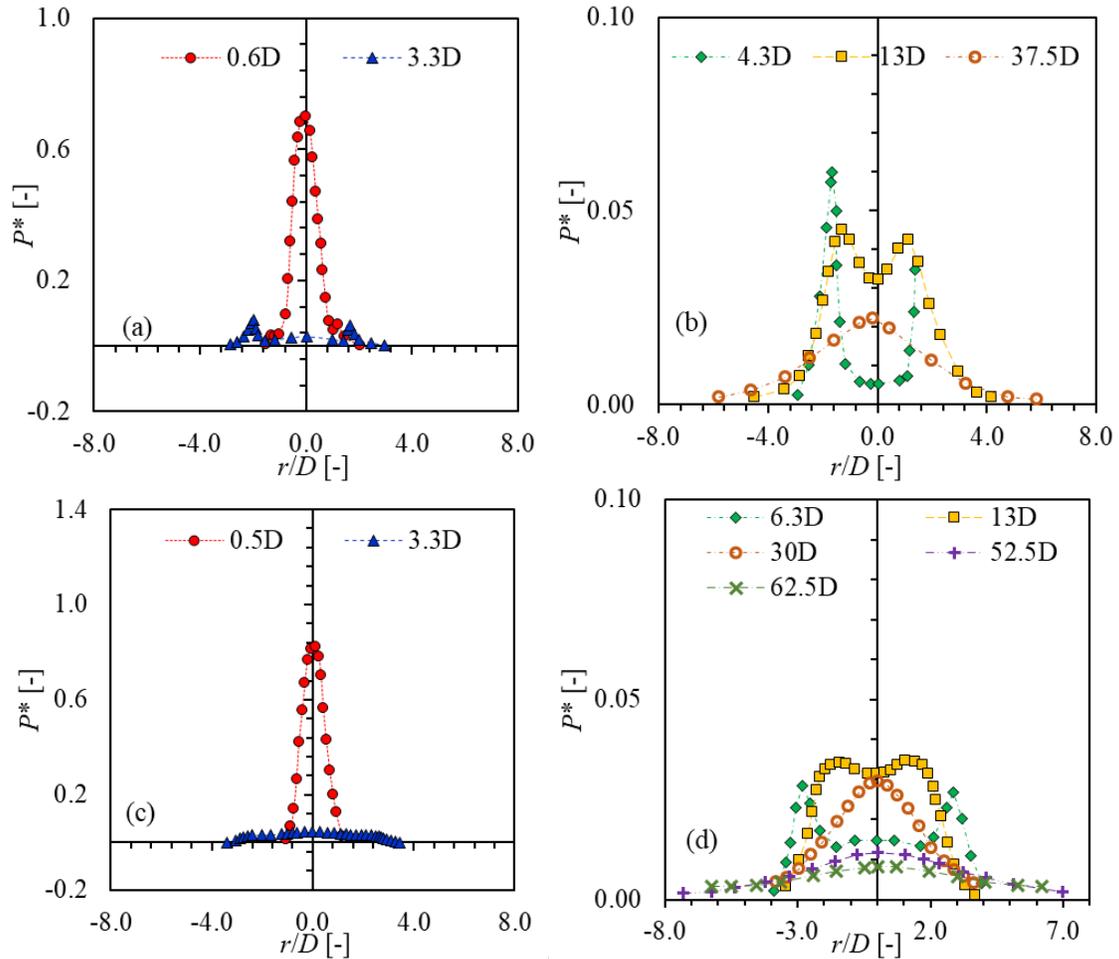
Figure 3-17 Stagnation Pressure Downstream of the Break Plane at Different Axial Locations in Masuda et al. (1981): (a) and (b) Free Steam Jets, (c) and (d) Impinging Steam Jets (P_0 = 4.02 MPa, D = 10 mm)
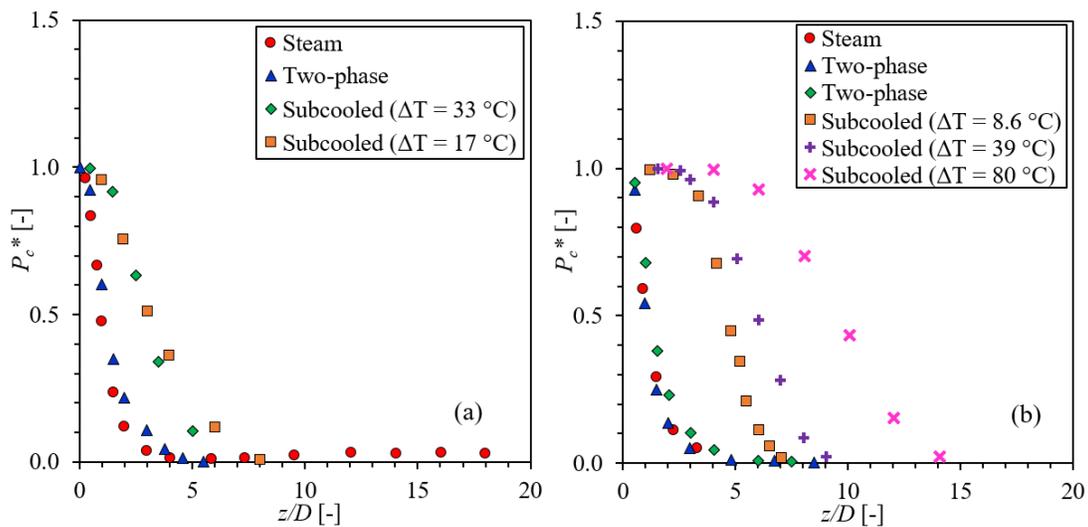
Figure 3-18 The Stagnation Pressure at the Center of Target Plate Downstream of the Break Plane at Different Axial Locations: (a) Free Jets and (b) Impinging Jets in Kawanishi et al. (1986). (P_0 = 4.02 MPa, D = 5 mm)

3.1.1.3 JAERI Tests

The experimental data in JAERI tests include these presented in Yano et al. (1984). The stagnation pressure measured at the target plate for saturated water jets are shown in Figure 3-19. Experiments for two initial stagnation pressure conditions were performed. Similar pressure profiles are obtained after non-dimensionalizing the stagnation pressure at the targets, which indicates that the initial stagnation pressure has negligible effect on dimensionless profiles. In addition, negative values for P^* are observed at 5 D downstream of the break plane. This indicates an overexpansion in the jets at this axial location. In the work by Yano et al. (1984), the measurement uncertainties were not discussed and a ±20% error bar is used for model evaluation in Section 3.2.
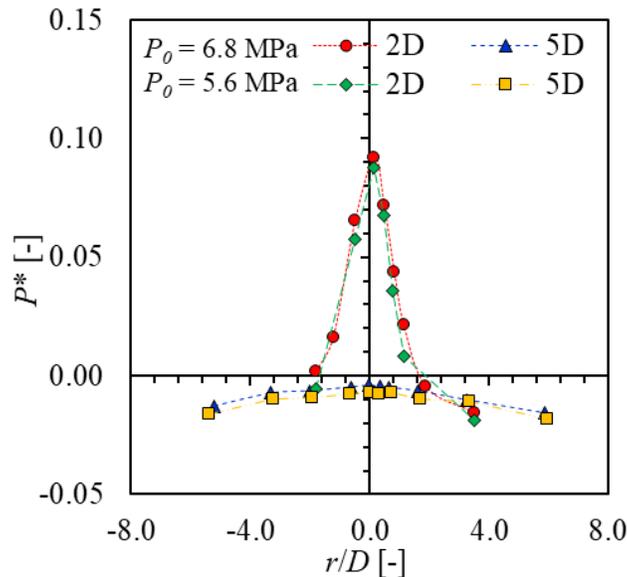
Figure 3-19 Impinging Saturated Water Jets in Yano et al. (1984): Stagnation Pressure at the Target Plate Downstream of the Break Plane for Two Initial Stagnation Pressure Conditions (D = 150 mm)

3.1.1.4 KWU Tests

The experimental data in KWU tests (Kastner and Rippel, 1987) are shown in Figure 3-20. Experiments were performed using saturated water to investigate the impinging jet with an initial stagnation pressure of 10 MPa. It is found that the value of P^* at the center of the target at the axial location of 2 D is approximately 10%, which agrees with that in Yano et al. (1984) as shown in Figure 3-19. This may indicate that the distribution of P^* is independent of initial stagnation pressure and break size for saturated water jets. However, additional data are needed to confirm this conclusion. In the work by Kastner and Rippel (1987), the measurement uncertainties were not discussed and a ±20% error bar is used for model evaluation in Section 3.2.
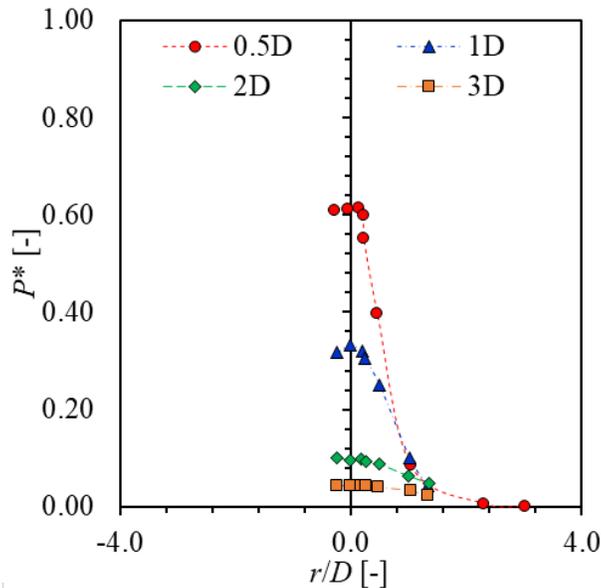
Figure 3-20 Impinging Saturated Water Jets in Kastner and Rippel (1987): Stagnation Pressure at the Target Plate Downstream of the Break Plane (P_0 = 10 MPa, D = 65 mm)

3.1.2   Data Analysis

Detailed data analysis is performed using the experimental database. The effects of different parameters including initial fluid conditions (i.e., stagnation pressure, subcooling or void fraction/quality), pipe size, and axial location downstream of break plane on both static and stagnation pressures are analyzed.

3.1.2.1   Free Jets

The effects of different parameters on both static and stagnation pressures in free jets are analyzed. The discussion is divided based on the initial fluid condition prior to the break: saturated steam, saturated water/two-phase, and subcooled water.

3.1.2.1.1   Saturated Steam Jets

All the free saturated steam jets in the Marviken tests and other tests are collected and analyzed. The saturated steam jets are defined when inlet flow has a quality greater than 0.7 ($x \geq 0.7$). The static (p_c^*) and stagnation (P_c^*) pressures at the center of the steam jets are shown in Figure 3-21 and Figure 3-22, respectively. The initial fluid pressure of the conditions investigated in the plots covers a wide range from 4.4 MPa to 1.3 MPa. The figures also include data from different break sizes of 0.28 m and 0.50 m. As shown in Figure 3-21 (a) and Figure 3-22 (a), the measured pressures show different trends for different conditions. However, after non-dimensionalizing the pressure and axial distance, all the data generally follow the same trend. This may indicate that both nondimensional static and stagnation pressures at the center of the free steam jets are independent on the initial stagnation pressure and break size.

It is found that the following equations can predict the data very well for static pressure as shown in Figure 3-21 (b) and for stagnation pressure as shown in Figure 3-22 (b). It needs to be noted that the best fitting line in Figure 3-22 (b) is developed by including all the experimental data in Marviken tests, Masuda et al. (1981), and Kawanishi et al. (1986):

$$p_c^* = 0.12 \left(\frac{z}{D_{eff}} \right)^{-0.89} - 0.1 \quad 0.25 \le \frac{z}{D_{eff}} \le 2.7$$

for static pressure at the center of steam jets $\qquad$ (3-5)

$$P_c^* = 0.41 \left(\frac{z}{D_{eff}} \right)^{-0.87} - 0.1 \quad 0.25 \le \frac{z}{D_{eff}} \le 7.1$$

for stagnation pressure at the center of steam jets $\quad$ (3-6)
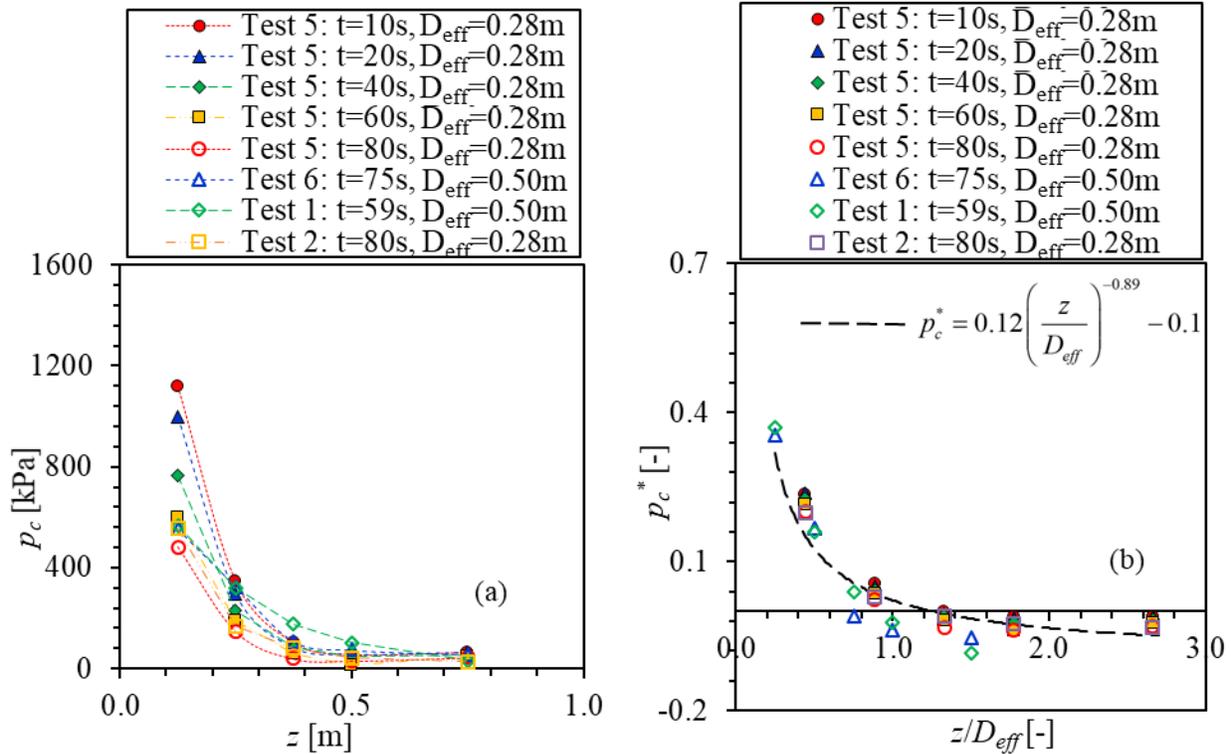
Figure 3-21 Static Pressure Profiles at the Center of the Free Steam Jets as a Function of Axial Distance. The Best Fitting Line in Figure (b) is Given by Equation (3-5)

3.1.2.1.2 Saturated Water/Two-phase Jets

All the free saturated water/two-phase jets in the Marviken tests and other tests are collected and analyzed. The saturated water/two-phase jets are defined when inlet flow has zero subcooling with a quality between 0 and 0.7 ($\Delta T = 0$, $0 \le x < 0.7$). The static (p_c^*) and stagnation (P_c^*) pressures at the center of the saturated water/two-phase jets are shown in Figure 2-23 and Figure 2-24, respectively. The initial fluid pressure of the conditions investigated in the plots covers a wide range from 3.9 MPa to 2.6 MPa with relatively low quality ($x < 0.7$). The figures also include data from different break sizes of 0.28 m and 0.50 m. As shown in Figure 2-23 (a) and Figure 2-24 (a), the measured pressures show different trends for different conditions. However, after non-dimensionalizing the pressure, all the data generally follow the same trend. This may indicate that both nondimensional static and stagnation pressures at the center of the free saturated water/two-phase jets are independent on the initial stagnation pressure and break size, except for the small break jets (D ~ 0.005 m).
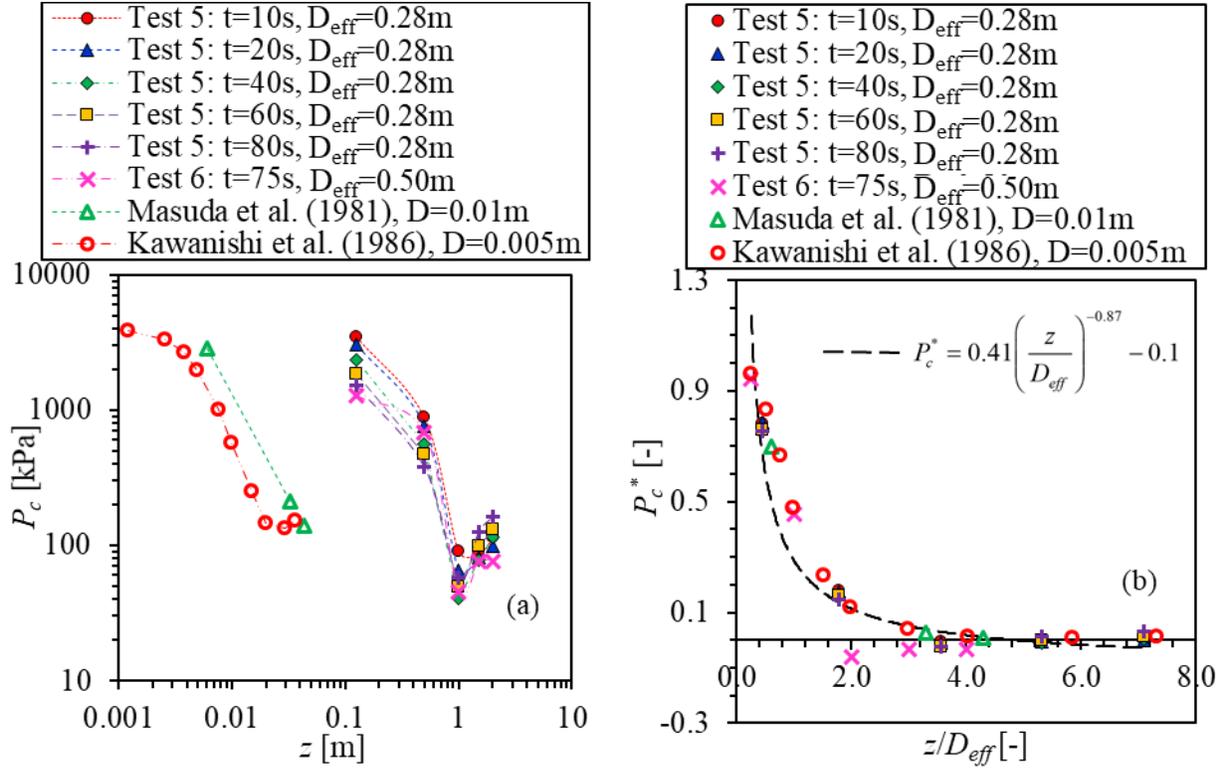
Figure 3-22 Stagnation Pressure Profiles at the Center of the Free Steam Jets as a Function of Axial Distance. The Best Fitting Line in Figure (b) is Given by Equation (3-6)

It is found that the following equations can predict the data very well for static pressure as shown in Figure 3-23 (b). For stagnation pressure, the data in Marviken tests generally cannot match that in Kawanishi et al. (1986). Additional data are need to confirm the best fitting line for P^* in saturated water/two-phase jets. The best fitting lines in Figure 3-23 and Figure 3-24 are given as follows. It needs to be noted that the best fitting line in Figure 3-24 (b) is developed based on the experimental data in Marviken tests:

$$p_c^* = 0.16 \left(\frac{z}{D_{eff}} \right)^{-1.03} - 0.1 \quad 0.25 \leq \frac{z}{D_{eff}} \leq 2.66$$

for static pressure at the center of saturated water/two-phase jets

(3-7)

$$P_c^* = 0.29 \left(\frac{z}{D_{eff}} \right)^{-0.99} - 0.1 \quad 0.25 \leq \frac{z}{D_{eff}} \leq 5.51$$

for stagnation pressure at the center of saturated water/two-phase jets

(3-8)
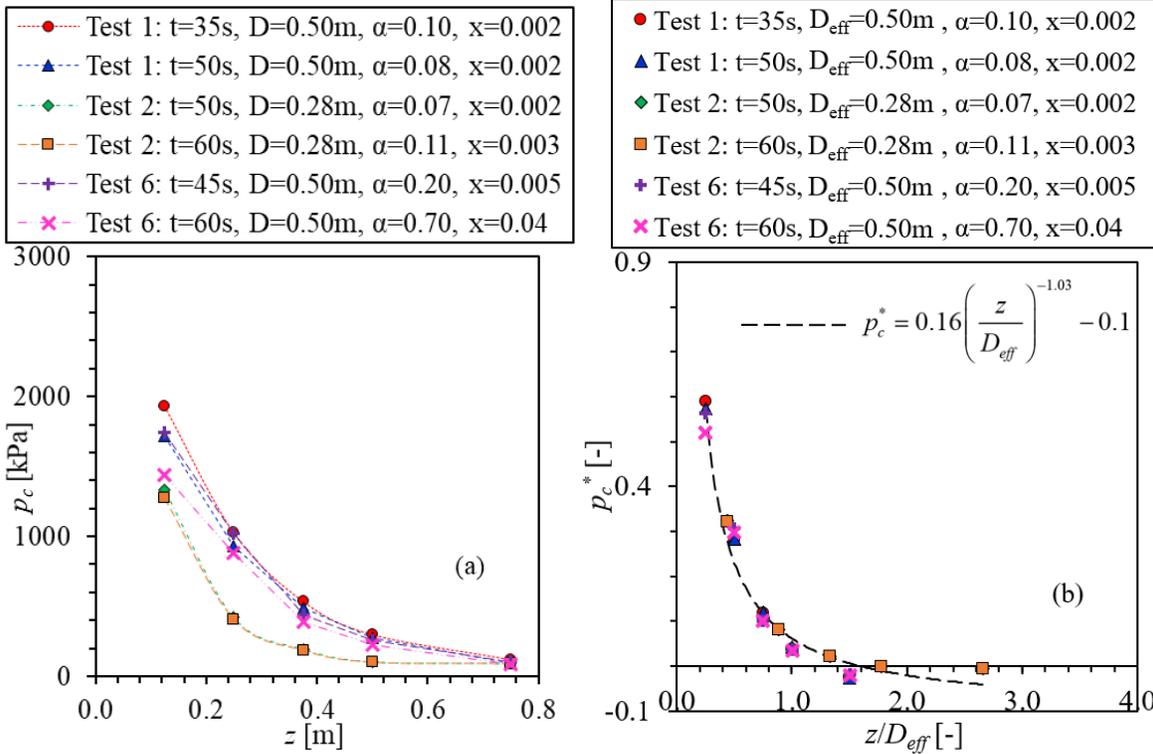
Figure 3-23 Static Pressure Profiles at the Center of Free Saturated Water Jets as a Function of Axial Distance. The Best Fitting Line in Figure (b) is Given by Equation (3-7)
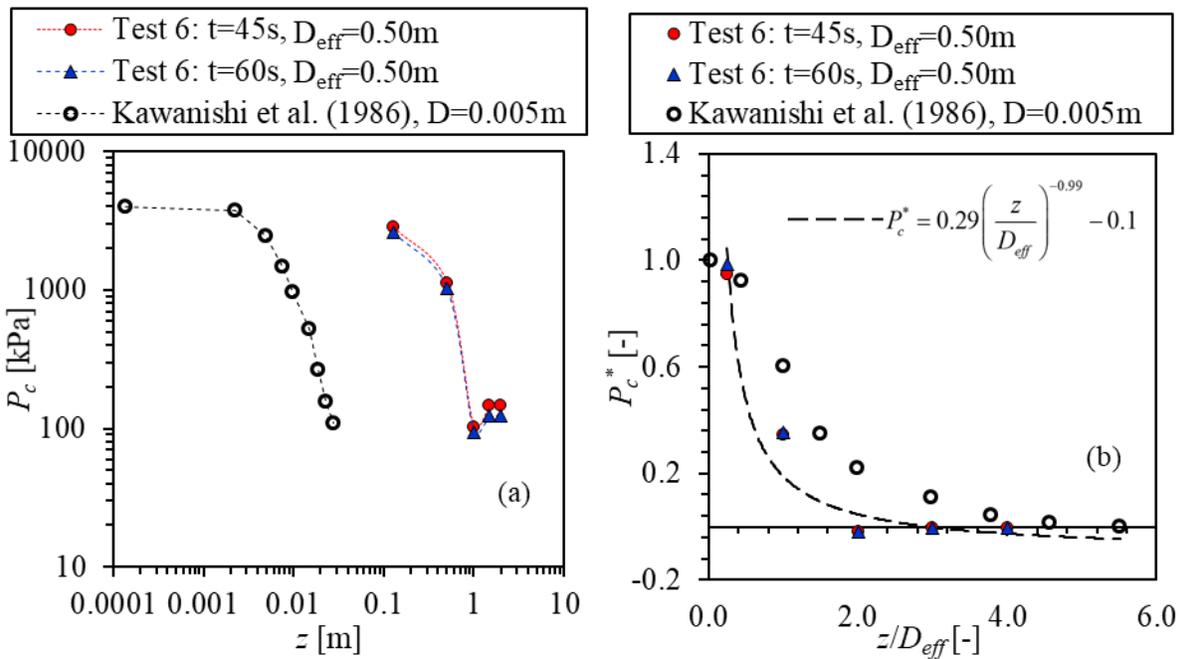
Figure 3-24 Stagnation Pressure Profiles at the Center of Free Saturated Water Jets as a Function of Axial Distance. The Best Fitting Line in Figure (b) is Given by Equation (3-8)

3-23

3.1.2.1.3 Subcooled Water Jets

All the free subcooled water jets in the Marviken tests and other tests are collected and analyzed. The subcooled water jets are defined when inlet flow has a subcooling greater than 0 ($\Delta T > 0$). The static pressure (p_c^*) at the center of the subcooled water jets are shown in Figure 3-25 with relatively high subcooling conditions and in Figure 3-26 with relatively low subcooling conditions. The initial fluid stagnation pressure of the conditions investigated in the plots covers a wide range from 4.3 MPa to 3.3 MPa. The figures also include data from different break sizes of 0.28 m and 0.50 m. As shown in Figure 3-25 (a) and Figure 3-26 (a), the measured pressures show different trends for different conditions. However, after non-dimensionalizing the pressure and axial distance, all the data generally follow the same trend. This may indicate that the nondimensional static pressure at the center of the free subcooled water jets is independent on the initial stagnation pressure and break size for large break jets ($D > 280$ mm).

It is found that the following equations can predict the data very well for static pressure as shown in Figure 3-25 (b) and Figure 3-26 (b):

$$p_c^* = 0.15\left(\frac{z}{D_{eff}}\right)^2 - 0.74\left(\frac{z}{D_{eff}}\right) + 0.86 \quad 0.25 \leq \frac{z}{D_{eff}} \leq 2.50 \quad 14°C \leq \Delta T \leq 20°C$$

for static pressure at the center of subcooled water jets   (3-9)

$$p_c^* = 0.45\left(\frac{z}{D_{eff}}\right)^2 - 1.38\left(\frac{z}{D_{eff}}\right) + 1.05 \quad 0.25 \leq \frac{z}{D_{eff}} \leq 1.77 \quad 5.0°C \leq \Delta T \leq 6.5°C$$

for static pressure at the center of subcooled water jets   (3-10)

For the stagnation pressure in subcooled water free jets, only one condition at 5s of Test 6 is analyzed due to limited experimental data. It is found that the following equation can predict the data well for stagnation pressure as shown in Figure 3-27 (b):

$$P_c^* = 1.25\exp\left(\frac{z}{D_{eff}}\right)^{-0.72} - 0.1 \quad 0.25 \leq \frac{z}{D_{eff}} \leq 4.01 \quad \Delta T \sim 16°C$$

for stagnation pressure at the center of subcooled water jets   (3-11)

However, the data collected in Kawanishi et al. (1986) do not agree with those in Marviken test. Additional experimental data might be needed for free subcooled water jets.

3.1.2.2 Impinging Jets

The effects of different parameters on stagnation pressure in impinging jets are analyzed. The discussion is divided based on the initial fluid condition prior to the break: saturated steam, saturated water, and subcooled water.
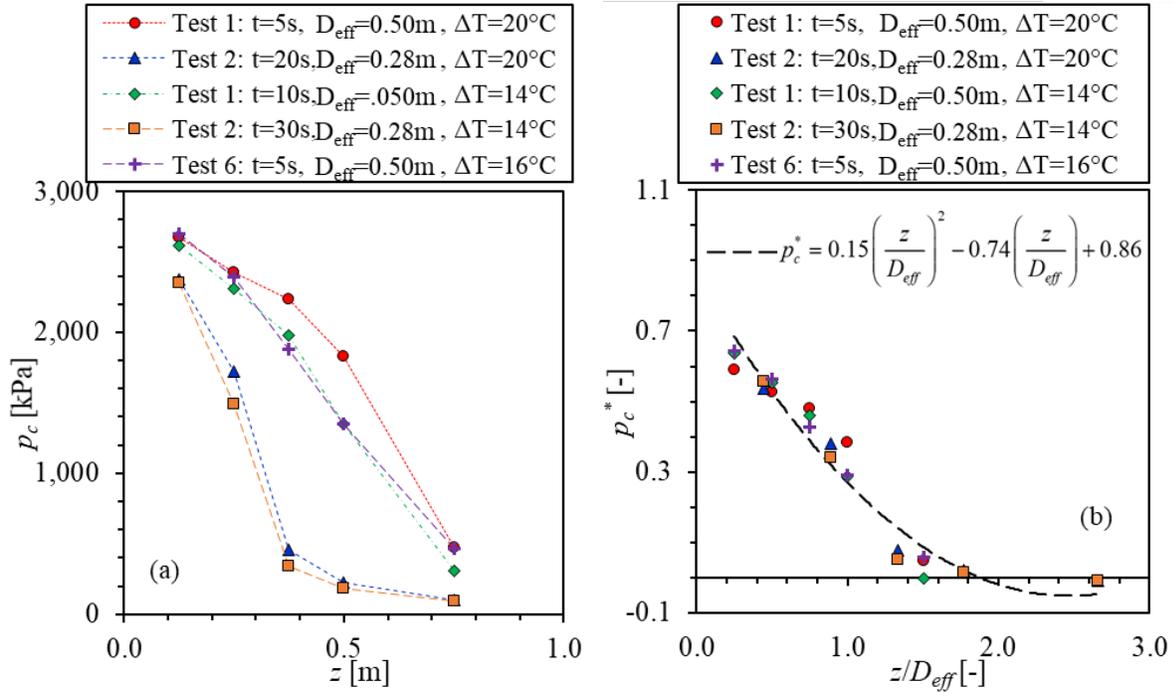
Figure 3-25 Static Pressure Profiles at the Center of Free Subcooled Water Jets (ΔT = 14°C ~ 20°C) as a Function of Axial Distance. The Best Fitting Line in Figure (b) is Given by Equation (3-9)
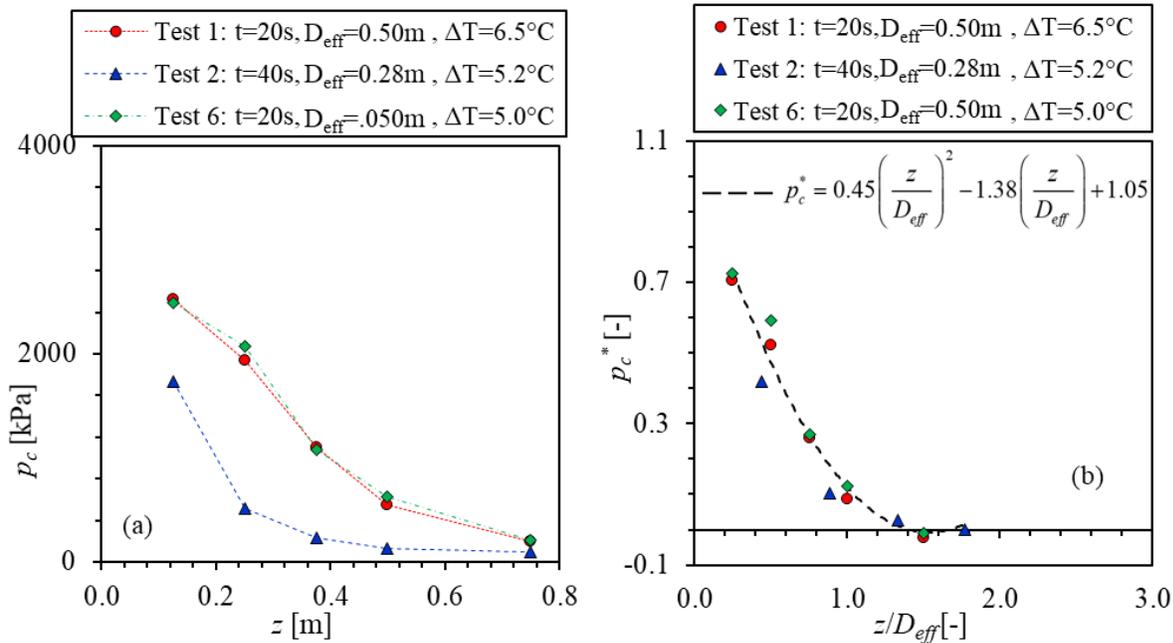
Figure 3-26 Static Pressure Profiles at the Center of Free Subcooled Water Jets ($\Delta T \sim 5$°C) as a Function of Axial Distance. The Best Fitting Line in Figure (b) is Given by Equation (3-10)
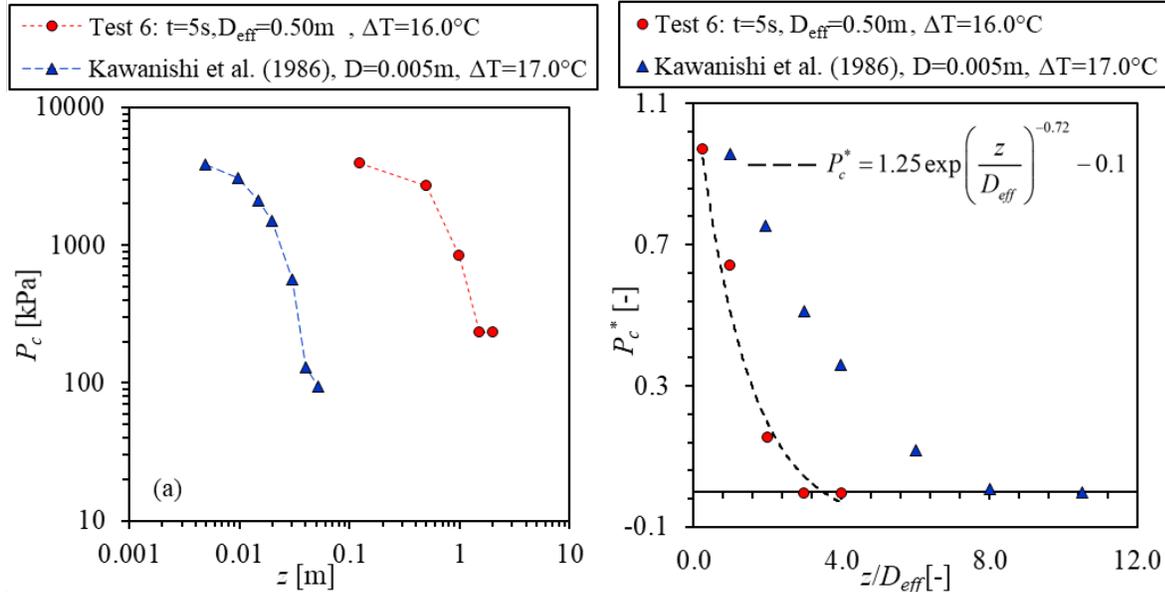
Figure 3-27 Stagnation Pressure Profiles at the Center of Free Subcooled Water Jets (ΔT ~ 16°C) as a Function of Axial Distance. The Best Fitting Line in Figure (b) is Given by Equation (3-11)

3.1.2.2.1 Saturated Steam Jets

All the impinging saturated steam jets in the Marviken tests and other tests are collected and analyzed. The stagnation pressures (P_c^*) at the center of the steam jets are shown in Figure 3-28. The initial fluid pressure of the conditions investigated in the plots covers a wide range from 1.6 MPa to 4.5 MPa. The figures also include data from different break sizes of 0.30 m and 0.50 m. As shown in Figure 3-28 (a), the measured pressures show different trends for different conditions. However, after non-dimensionalizing the pressure and axial distance, all the data generally follow the same trend. This may indicate that the nondimensional stagnation pressures at the center of the impinging steam jets are independent on the initial stagnation pressure and break size.

It is found that either a power law or an exponential function can predict the data very well for stagnation pressure as shown in Figure 3-28 (a). While the following correlation developed by Kitade et al. (1979):

$$P_c^* = 0.65 \left(\frac{z}{D} \right)^{-2}$$

(3-12)

is shown in Figure 3-28 (b), the best fitting lines can be achieved by:

$$P_c^* = 0.49 \left(\frac{z}{D} \right)^{-1.8} \qquad 0.5 \le \frac{z}{D} \le 6.53$$

for stagnation pressure at the center of saturated steam jets (3-13)

$$P_c^* = 1.75 \exp\left(-1.14 \frac{z}{D}\right) \quad 0.5 \leq \frac{z}{D} \leq 6.53$$

for stagnation pressure at the center of saturated steam jets (3-14)

It needs to be noted that the best fitting lines in Figure 3-28 (b) are developed based on all the experimental data in the plot.
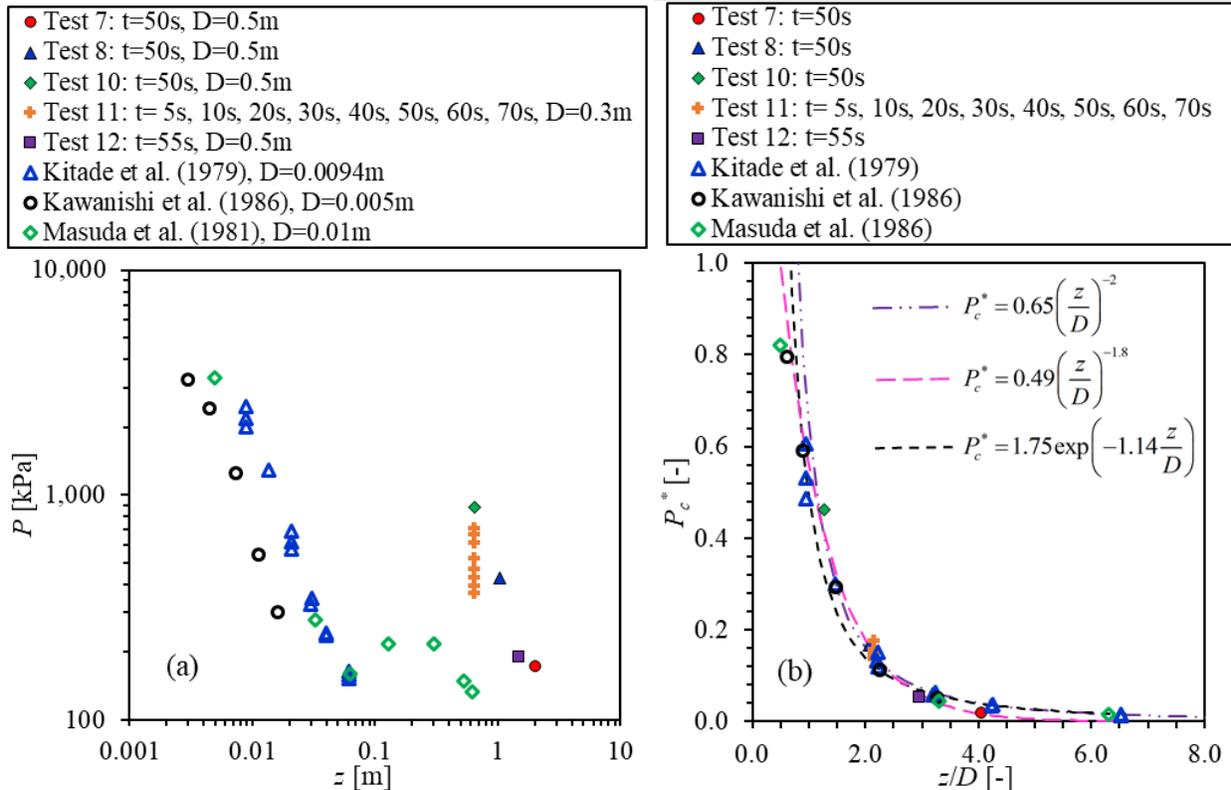
Figure 3-28 Stagnation Pressure Profiles at the Center of Impinging Saturated Steam Jets as a Function of Axial Distance. The Best Fitting Lines in Figure (b) are Given by Equations (3-13) and (3-14), respectively

3.1.2.2.2 Saturated Water/Two-phase Jets

All the impinging saturated water/two-phase jets in the Marviken tests and other tests are collected and analyzed. The stagnation pressures at the center of the saturated water/two-phase jets for relatively low- and high-quality conditions are shown in Figure 3-29 and Figure 3-30, respectively. The initial fluid pressure of the conditions investigated in the plots covers a wide range from 2.5 MPa to 3.0 MPa. The analysis includes data from a break size of 0.50 m. As shown in Figure 3-29 (a) and Figure 3-30 (a), the measured pressures show different trends for different conditions. However, after non-dimensionalizing the pressure and axial distance, all the data generally follow the same trend. This may indicate that the nondimensional stagnation pressures at the center of the impinging saturated water/two-phase jets are independent on the initial fluid conditions (i.e., stagnation pressure and quality).

It is found that either a power law or an exponential function can predict the data very well for stagnation pressure as shown in both Figure 3-29 (a) and Figure 3-30 (b). While the following correlation developed by Yano et al. (1984):

$$P_c^* = 0.40 \left(\frac{z}{D} \right)^{-2} \tag{3-15}$$

is shown in both plots, the best fitting lines can be achieved for relatively low-quality conditions ($x < 0.02$):

$$P_c^* = 0.36 \left(\frac{z}{D} \right)^{-1.91} \quad 0.5 \leq \frac{z}{D} \leq 4.8$$

for stagnation pressure at the center of saturated water/two-phase jets (3-16)

$$P_c^* = 1.20 \exp \left(-1.10 \frac{z}{D} \right) \quad 0.5 \leq \frac{z}{D} \leq 4.8$$

for stagnation pressure at the center of saturated water/two-phase jets (3-17)

For relatively high-quality conditions ($x > 0.15$), the following best fitting lines are achieved:

$$P_c^* = 0.55 \left(\frac{z}{D} \right)^{-1.93} \quad 0.5 \leq \frac{z}{D} \leq 4.0$$

for stagnation pressure at the center of saturated water/two-phase jets (3-18)

$$P_c^* = 1.70 \exp \left(-1.06 \frac{z}{D} \right) \quad 0.5 \leq \frac{z}{D} \leq 4.0$$

for stagnation pressure at the center of saturated water/two-phase jets (3-19)

3.1.2.2.3 Subcooled Water Jets

All the impinging subcooled water jets in the Marviken tests are collected and analyzed. The stagnation pressures at the center of the subcooled jets are shown in Figure 3-31. The initial fluid pressure of the conditions investigated in the plots covers a range from 3.9 MPa to 4.8 MPa, and with a subcooling in a range of 12.5 °C to 24.2 °C. The analysis includes data from a break size of 0.50 m. As shown in Figure 3-31 (a), the measured pressures show different trends for different conditions. After non-dimensionalizing the pressure and axial distance as shown in Figure 3-31 (b), the experimental data in Test 8 do not follow the trend as others in Marviken test. The best fitting lines based on the experimental data in Figure 3-31 (a) are as follows:

$$P_c^* = 9.78 \left(\frac{z}{D} \right)^{-6.4} \quad 1.27 \leq \frac{z}{D} \leq 4.05 \quad 12.5^\circ C \leq \Delta T \leq 24.2^\circ C$$

for stagnation pressure at the center of subcooled water jets (3-20)

$$P_c^* = 43.59 \exp \left(-2.73 \frac{z}{D} \right) \quad 1.27 \leq \frac{z}{D} \leq 4.05 \quad 12.5^\circ C \leq \Delta T \leq 24.2^\circ C$$

for stagnation pressure at the center of subcooled water jets (3-21)

3-28

In addition, the data collected in Kawanishi et al. (1986) do not agree with those in Marviken test as shown in Figure 3-31 (b). This difference might be caused by different nozzle size. The nozzle employed in Kawanishi et al. (1986) has a diameter of 5 mm while that in the Marvikent test has a diameter of 500 mm. As such, the surface area to volume ratio is different between small diameter and large diameter nozzles. Additional experimental data might be needed for impinging subcooled water jets as well as saturated water jets.
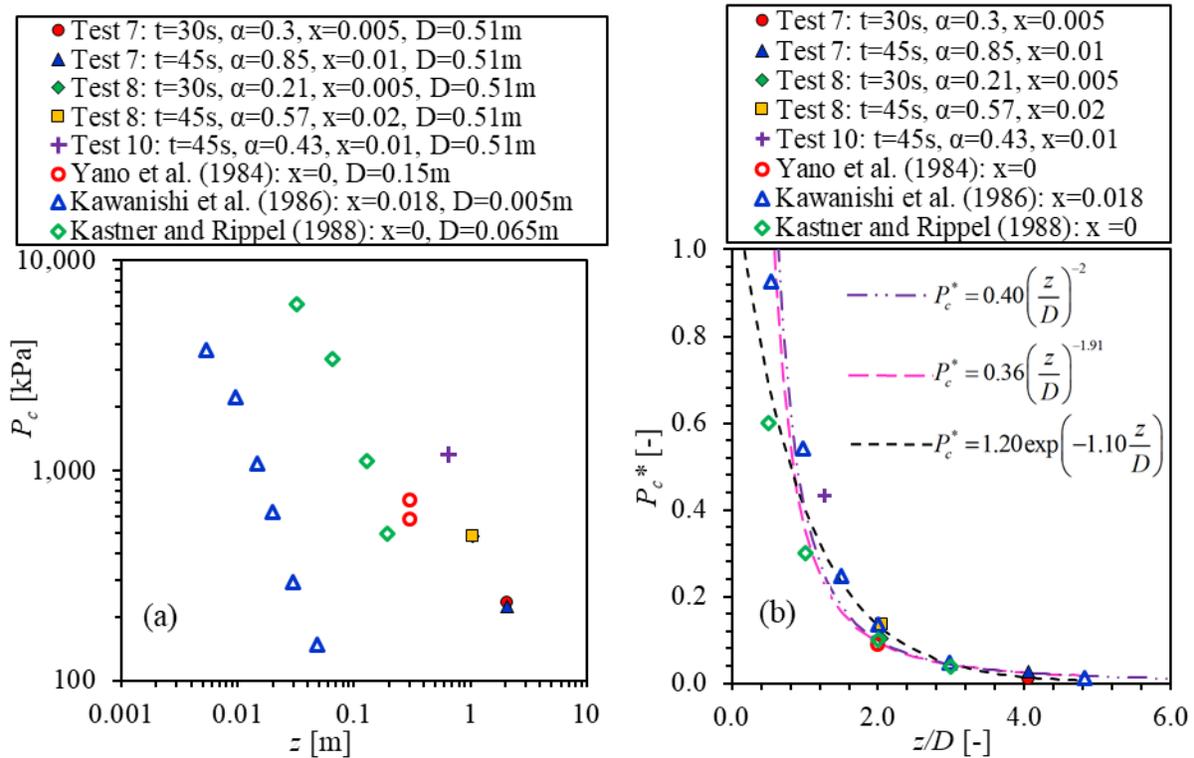
Figure 3-29 Stagnation Pressure Profiles at the Center of Impinging Saturated Water/Two-phase Jets as a Function of Axial Distance: Relatively Low-quality Conditions. The Best Fitting Lines in Figure (b) are Given by Equations (3-16) and (3-17), respectively
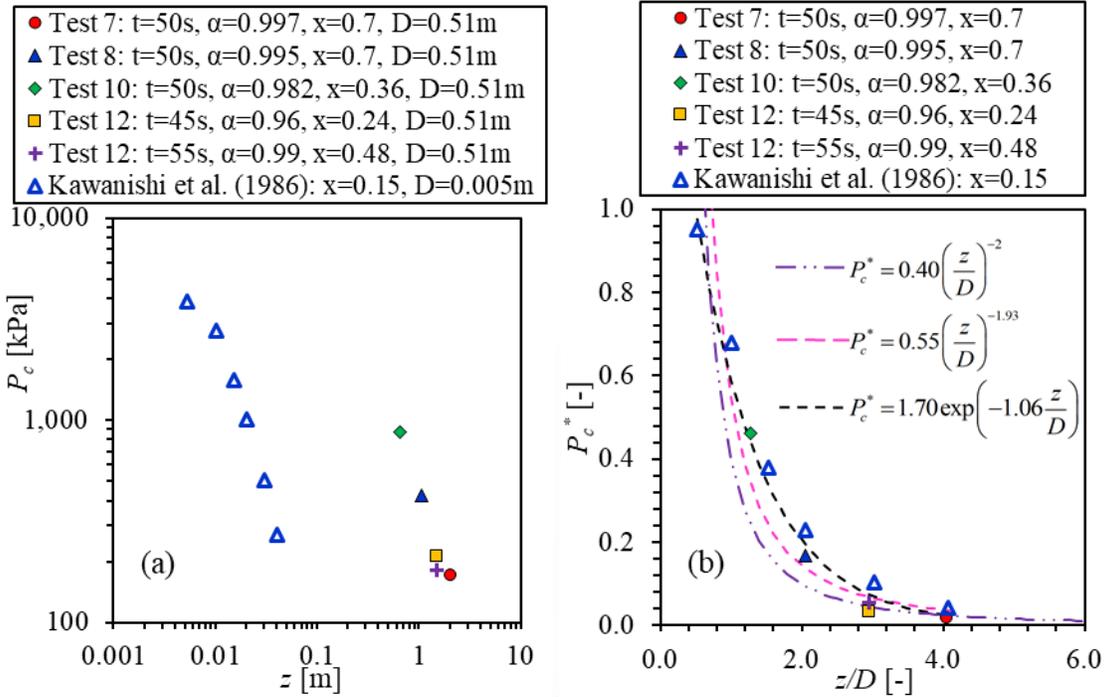
Figure 3-30 Stagnation Pressure Profiles at the Center of Impinging Saturated Water/Two-phase Jets as a Function of Axial Distance: Relatively High-quality Conditions. The Best Fitting Lines in Figure (b) are Given by Equations (3-18) and (3-19), respectively
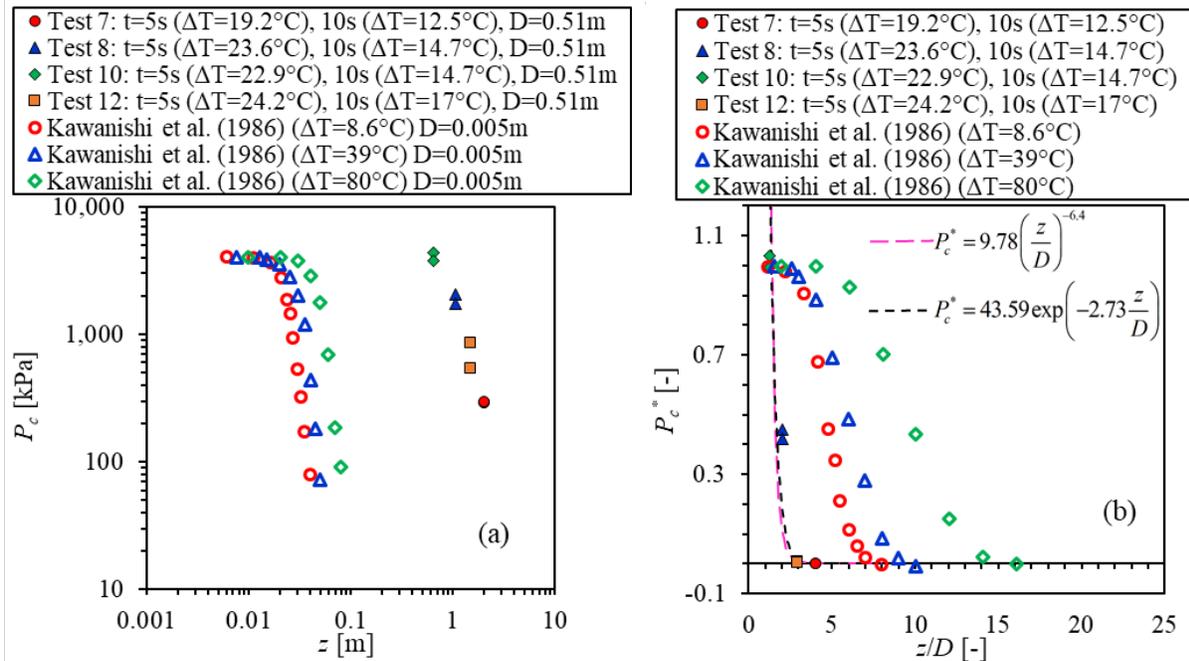

Figure 3-31 Stagnation Pressure Profiles at the Center of Impinging Subcooled Water Jets as a Function of Axial Distance. The Best Fitting Lines in Figure (b) are Given by Equations (3-20) and (3-21), respectively

3-30

3.1.2.3 Comparison between Free and Impinging Jets

Using the comprehensive experimental data in both free and impinging jets, the comparison between free and impinging jets is performed in the current section. All the experimental data analyzed in Sections 3.1.2.1 and 3.1.2.2 are included for comparison as shown in Figure 3-32. The discussion is divided based on different inlet conditions. For saturated steam jets and saturated water/two-phase jets, the measured stagnation pressures generally agree well with each other and the difference can be assumed negligible. For subcooled water jets, experimental data including Marviken test ($D \sim 0.5$ m) and Kawanishi et al. (1986) ($D = 0.005$ m) are plotted separately due to different break sizes as in Figure 3-32 (c) and (d). For both large- and small-break jets, a significant difference is observed between free and impinging jets, which may require additional systematic investigation. Higher values of stagnation pressure are observed for impinging jets.

3.2 Model Evaluation

This section discusses model evaluation based on the established experimental databank. The Standard model in ANSI/ANS-58.2 (1988) and the two-phase jet loads model (NUREG/CR-2913) are evaluated. Important parameters including pressure distribution, thrust coefficient, and critical mass flux are assessed.

3.2.1 Pressure Distribution

The pressure distribution in radial and axial directions within the jet characterizes the strength of jet. The impingement force can be calculated by integrating the local stagnation pressure over the target. As such, the pressure distribution within the jet is one of the key parameters to evaluate in jet impingement.

3.2.1.1 Standard model (ANSI/ANS-58.2, 1988)

The Standard model presented in ANSI/ANS-58.2 (1988) appendices is among the most widely used models for jet impingement, which has been employed in the design and safety analysis in nuclear power plants. The ANSI/ANS-58.2 (1988) model is a series of formulas presented in the four appendices. In the current work, a FORTRAN code developed by the NRC (Jet11p4) is employed to perform the Standard model calculation. The following boundary conditions are required for the code:
    (a) vessel stagnation pressure,
    (b) mixture vapor mass quality at the break,
    (c) subcooling (if x at the break is 0) or superheat (if x at the break is 1),
    (d) break diameter,
    (e) ambient pressure.
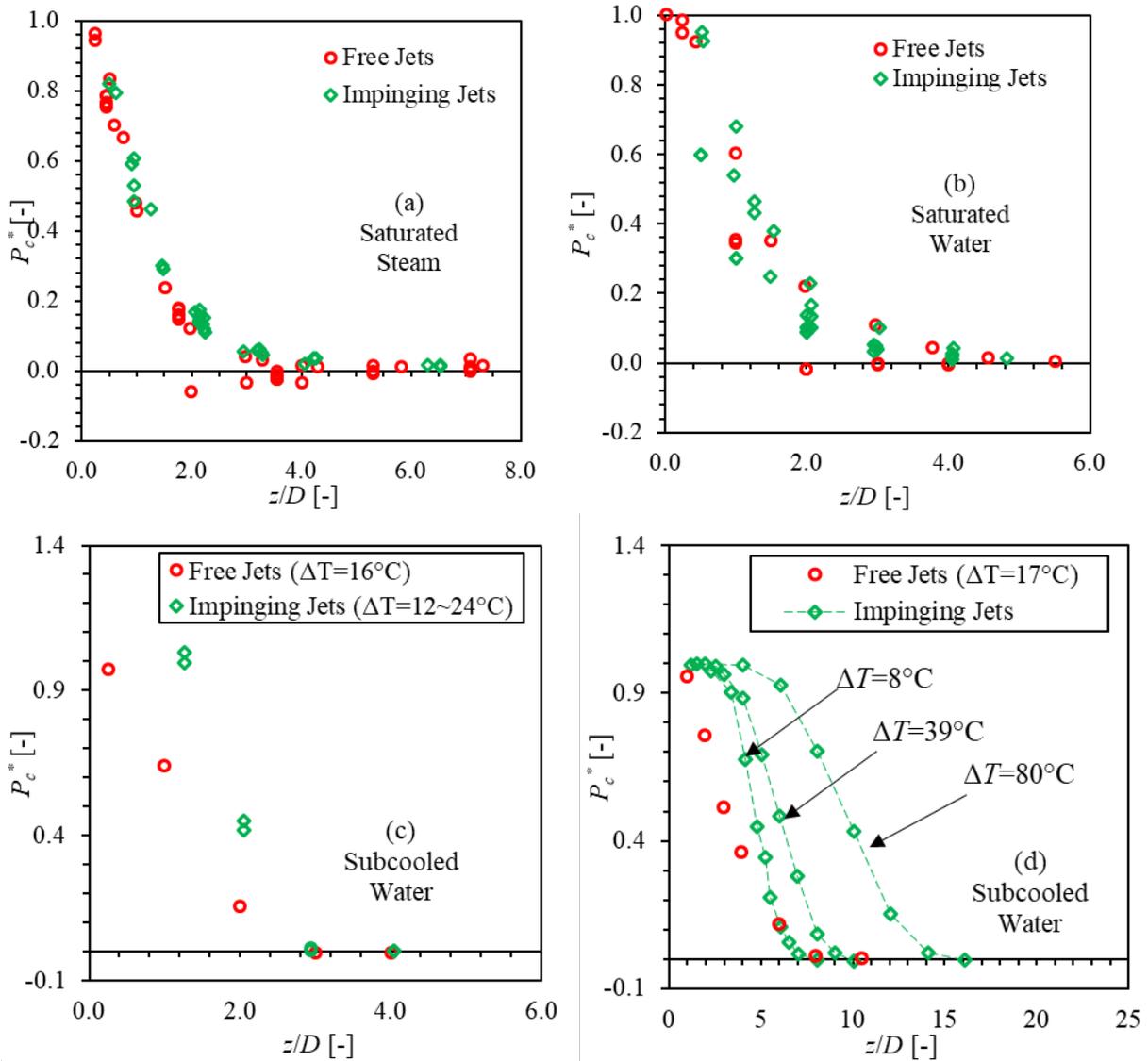
Figure 3-32 Comparison on Stagnation Pressure at the Center of the Jets between Free and Impinging Jets: (a) Saturated Steam Jets ($x \geq 0.7$), (b) Saturated Water/Two-phase Jets ($0 \leq x < 0.7$), (c) Subcooled Water Jets in Marviken Test ($D \sim 0.5$ m), and (d) Subcooled Water Jet in Kawanishi et al. (1986) ($D \sim 0.005$ m)

The calculated output parameters include:
  (a) steady-state thrust coefficient,
  (b) jet core length,
  (c) distance from break to the asymptotic plane,
  (d) static pressure at the asymptotic plane,
  (e) mass quality at the asymptotic plane,
  (f) jet area (or jet diameter) at the asymptotic plane,
  (g) jet boundary downstream of the break plane,
  (h) distribution of impingement pressure within the jet.

In the current work, the impingement pressure calculated by the Standard model is compared with the stagnation pressure measured on target for impinging jets, or at certain axial locations for free jets. The discussion of the results is divided into three sections based on the initial fluid state: subcooled water jets, saturated water/two-phase jets and steam jets. Before discussing the model evaluation, code verification was first performed and comparisons were made with hand calculations. The code calculations were also compared with a previous NRC report (ML121010475) and discussion can be found in Appendix A.

3.2.1.1.1 Saturated Steam Jets

This section discusses the model evaluation results for saturated steam jets. The experimental data employed in the assessment include those in Marviken tests (both free and impinging jet) and Mitsubishi tests (Kitade et al., 1979; Masuda et al. 1981; Kawanishi et al., 1986).

Among the six free jets in Marviken tests, selected times in Tests 1, 2, 5, and 6 for saturated steam jets are used for model evaluation. The time after 6.6s in Test 3 and all the time in Test 4 are not used due to unreliable data caused by the movement of the central probe and instrumented beams. In total, 8 conditions for free steam jets in the Marviken tests are evaluated. A summary of the boundary conditions of the chosen test times is shown in Table 3-4. It can be seen that the selected conditions cover a wide range of initial stagnation pressure from 1.3 MPa to 4.4 MPa with quality above 0.7 in different pipe sizes. A complete boundary conditions for each test can be found in Table B-1 through Table B-5 of Appendix B. The calculated fluid temperature and critical mass flux from the Standard model by the NRC FORTRAN code Jet11p4 are also included in these tables of Appendix B. The differences between measured and calculated critical mass flux are summarized in the last row.

Table 3-4 Summary of Selected Conditions in Marviken Free Jet Tests for ANSI/ANS-58.2 (1988) Evaluation: Saturated Steam Jets

Test Number	Times (s)	Quality (-)	Initial Stagnation Pressure (kPa)	Break size (m)
Test 1	59	0.91	1,315	0.5
Test 2	80	0.79	2,387	0.28
Test 5	10	0.97	4,407	0.28
	20	0.97	3,860	0.28
	40	0.99	3,022	0.28
	60	0.99	2,414	0.28
	80	0.97	1,984	0.28
Test 6	75	0.7	1,345	0.5

In the evaluation, the dimensionless pressures at different axial and radial locations are plotted. The pressures at the center of the jets (70 mm) were not measured in Tests 1 and 2 but measured in Tests 5 and 6. Figure 3-33 shows the axial distribution of dimensionless pressures at the center of the jets for one time condition each in Tests 5 and 6 as an example. The profiles at other times are similar for the same test and a complete comparison can be found in Appendix B. As shown in the plots, the Standard model can predict the nondimensional stagnation pressure at the center of the jets very well, especially in the vicinity of the break plane. Further downstream from the break plane, the Standard model can overestimate the pressure significanlty.

While the pressures at center of the jets can be predicted conservatively, it may not bound all the pressure at different radial locations due to the edge peaking pressure profile as shown in Figure 3-34. For the selected conditions in Tests 5 and 2, the pressures at the edge of the jets are underestimated. However, except for these two conditions, the pressure in other conditions investigated in Tests 5, 2 and all the conditions in Tests 1 and 6 can be predicted conservatively. In general, the Standard model can predict the stagnation pressure in free steam jets well.

Among the six impinging jets in Marviken tests, selected times in Tests 7, 8, 10, 11, and 12 for saturated steam jets are used for model evaluation. In Test 9, a cavity was used as the target, which was made by placing a cylindrical wall on a plane. Therefore, water was accumulated in the cavity dueing the test. However, no data are available for the height of the accumulated water column in the cavity so it is difficult to calculate the pressure and compare it with experimental data. As such, the experimental data in Test 9 are not used for model evaluation. In total, 12 conditions for saturated steam jets in the Marviken tests are evaluated. A summary of the boundary conditions of the chosen conditions is shown in Table 3-5. It can be seen that the selected conditions cover a wide range of initial stagnation pressure from 1.3 MPa to 4.5 MPa in different pipe sizes and axial locations. A complete boundary conditions for each test can be found in Table B-6 through Table B-10 of Appendix B. The calculated fluid temperature and critical mass flux from the Standard model by the NRC FORTRAN code Jet11p4 are also included in these tables of Appendix B. The differences between measured and calculated critical mass flux are summarized in the last row.

In the evaluation, the dimensionless pressures at different radial location are plotted. The experimental data in different tests provide model evalution at different axial locations. It is found that the Standard model can generally predict the stangation pressure at the targets for all selected saturated steam jet conditions as shown in Figure 3-35 as an example. The complete comparisons for the saturated steam jets for all conditions can be found in the Appendix B.
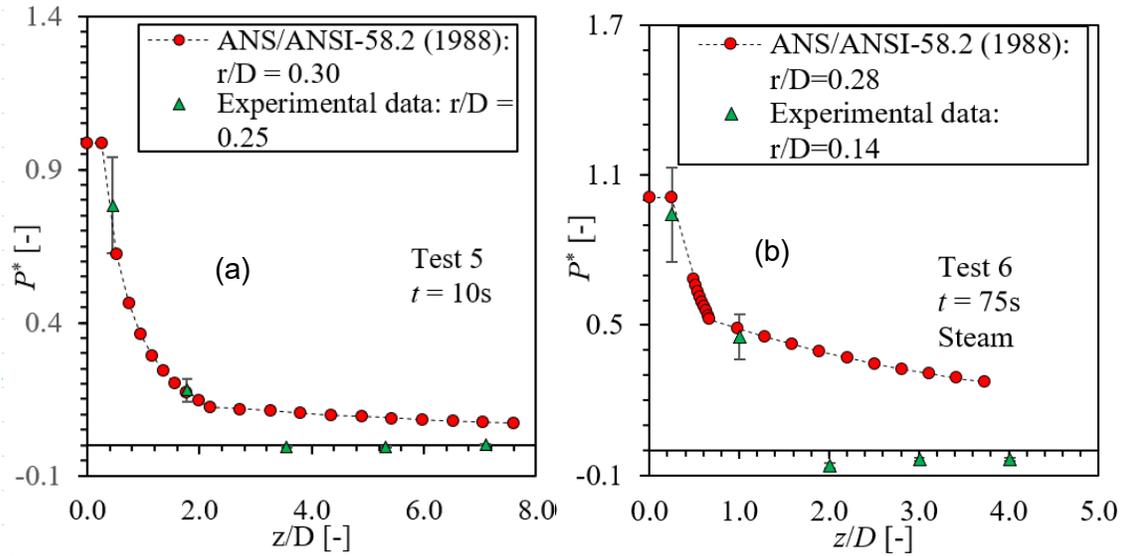
Figure 3-33 Pressure Profiles at Different Axial Locations: (a) 10 s in Test 5 and (b) 75 s in Test 6. Error Bar: ±20%
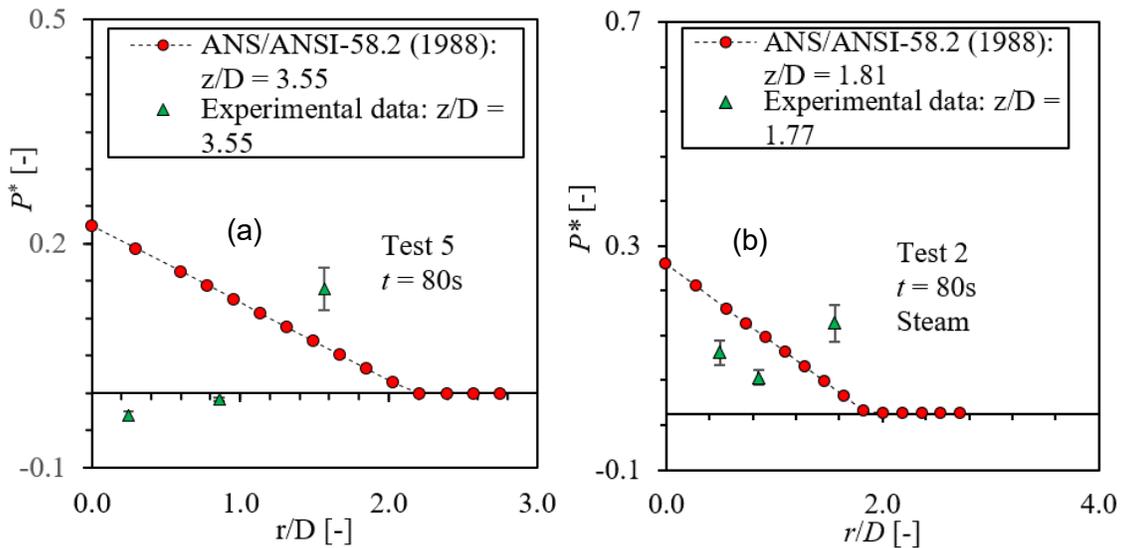
Figure 3-34 Pressure Profiles at Different Axial Locations: (a) 80 s in Test 5 and (b) 80 s in Test 2. Error Bar: ±20%

Table 3-5 Summary of Selected Conditions in Marviken Impinging Jet Tests for ANSI/ANS-58.2 (1988) Evaluation: Saturated Steam Jets

Test Number	Times (s)	Quality (-)	Initial Stagnation Pressure (kPa)	Break size (m)	z/D (-)
Test 7	50	0.7	1,615	0.5	4.05
Test 8	50	0.7	1,845	0.5	2.06
Test 10	50	0.36	1,743	0.5	1.27
Test 11	5	1.0	4,467	0.3	2.15
	10	1.0	4,155	0.3	2.15
	20	0.7	3,627	0.3	2.15
	30	0.99	3,178	0.3	2.15
	40	0.99	2,796	0.3	2.15
	50	0.89	2,468	0.3	2.15
	60	0.99	2,191	0.3	2.15
	70	0.99	1,952	0.3	2.15
Test 12	55	0.48	1,340	0.5	2.95
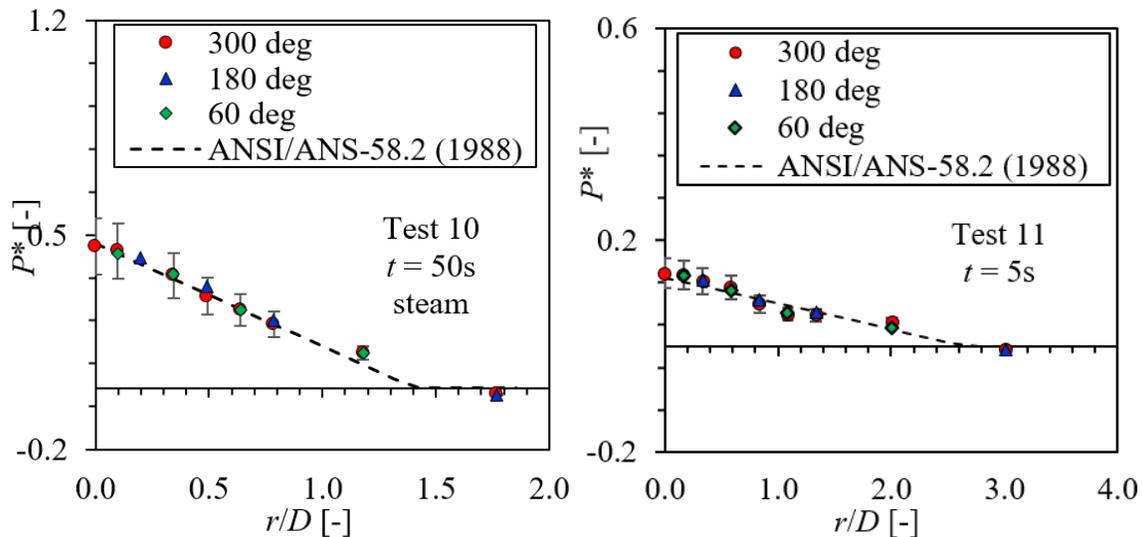
Figure 3-35 Pressure Profiles at Different Axial Locations: (a) 50 s in Test 10 and (b) 5 s in Test 11. Error Bar: ±20%

Experiments for impinging saturated steam jets were investigated in the Kitade et al. (1979) (Mitsubishi tests) with an initial stagnation pressure of 4.02 MPa in a break size of 9.4 mm. The stagnation pressure at targets were measured at multiple axial locations of 0.59 D, 0.96 D, 1.5 D, 2.3 D, 3.3 D, 4.5 D, and 6.6 D. The evaluation results using the experimental data in Kitade et al. (1979) are shown in Figure 3-36. In these plots, the stagnation pressures can generally be predicted well within an axial distance of 3.3 D. For axial distances of 4.5 D and 6.6

D, although the Standard model tries to capture the edge peaking pressure profile, the experimental data are generally underestimated. Meanwhile, the stagnation pressures at the center of the jets are significantly underestimated.
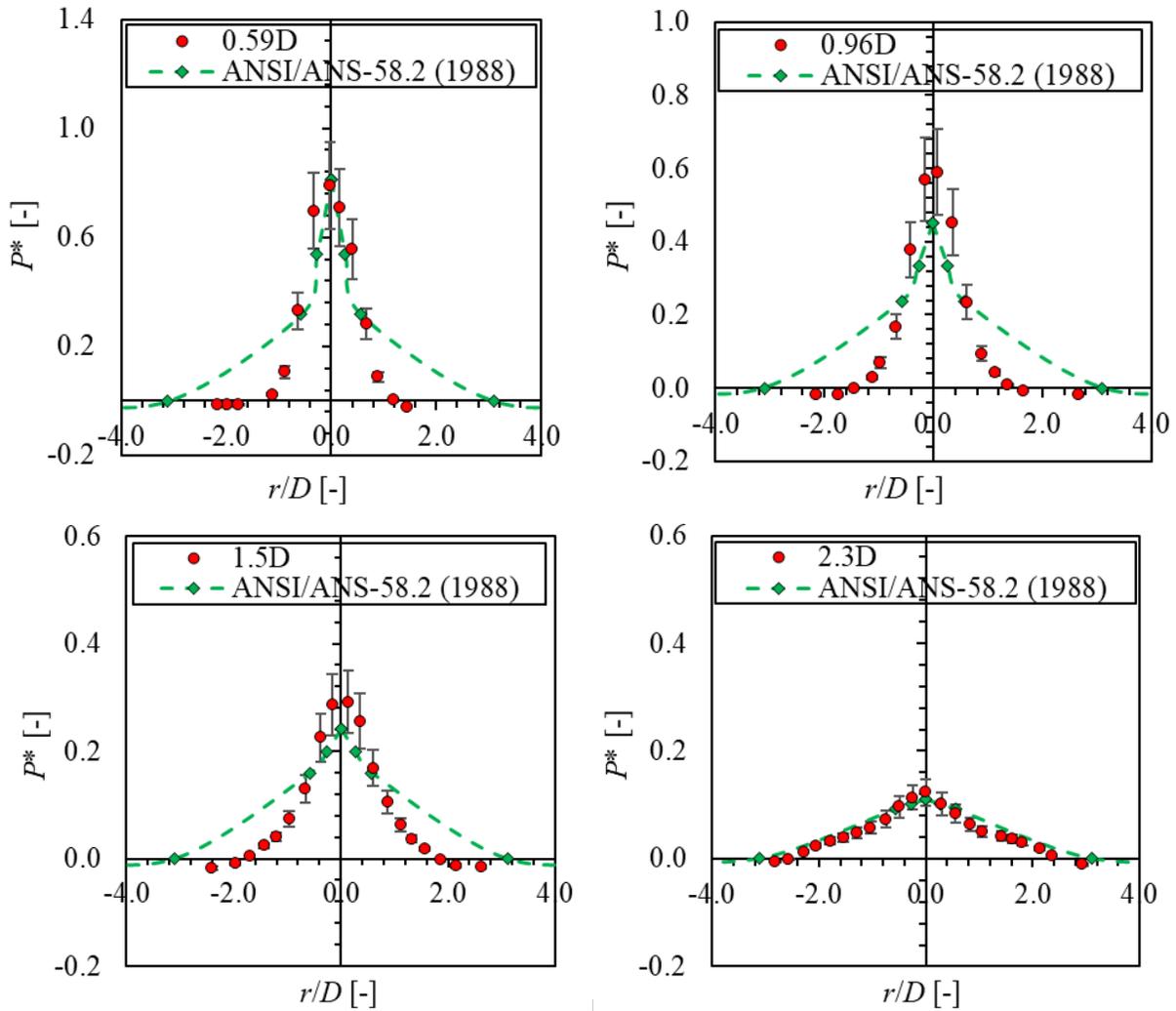
Figure 3-36 Comparison between Standard Model Calculation (ANSI/ANS-58.2, 1988) and Experimental Data of Impinging Steam Jets in Kitade et al. (1979) of Mitsubishi Tests. Error Bar: ±20%
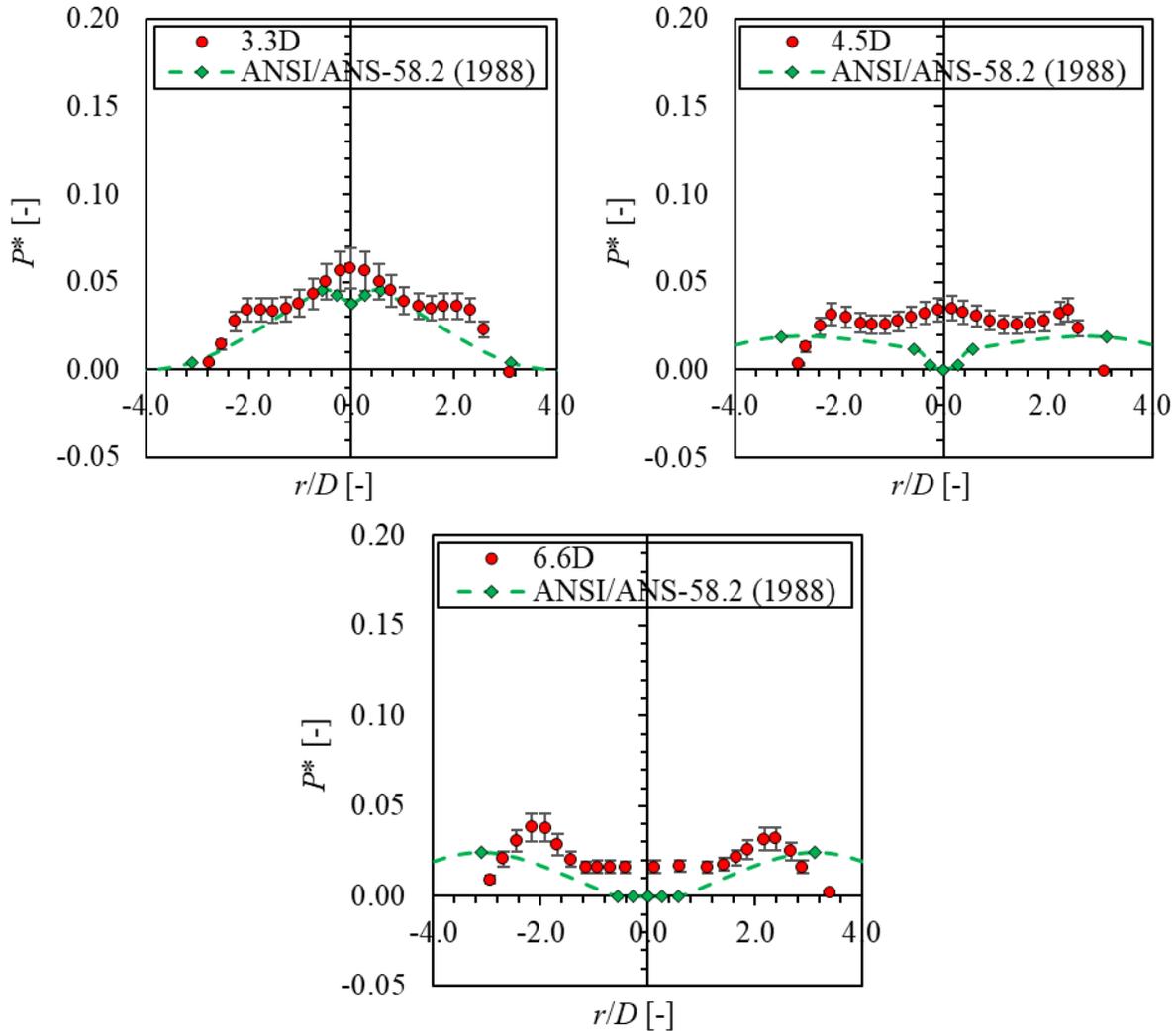
Figure 3 36 Comparison between Standard Model Calculation (ANSI/ANS-58.2, 1988) and Experimental Data of Impinging Steam Jets in Kitade et al. (1979) of Mitsubishi Tests. Error Bar: ±20% (cont.)

Experiments for both free and impinging saturated steam jets were investigated in Masuda et al. (1981) (Mitsubishi tests) with an initial stagnation pressure of 4.02 MPa in a break size of 10 mm. The stagnation pressure at targets were measured at multiple axial locations in these jets. The evaluation results using the experimental data in Masuda et al. (1979) are shown in Figure 3-37 and Figure 3-38. In these plots, the stagnation pressures can generally be predicted well in the vicinity of the break plane (0.6 D for free jets and 3.3 D for impinging jet).

For the free saturated steam jets, while the Standard model can predict the stagnation pressure at the center of the jets well, the radial profiles especially the edge-peaking values are underestimated significantly. However, the values of P^* are generally below 10% downstream an axial distance of 3.3 and below 5% downstream 13 D. For impinging jets, the comparisons are relatively better. The edge-peaking pressures can generally be predicted well at 6.3 D. Although the stagnation pressures are generally underpredicted at the center of the jets downstream of 6.3 D, the values of P^* are generally below 0.07.

Experiments for both free and impinging saturated steam jets are investigated in the work by Kwanishi et al. (1986) with an initial stagnation pressure of 4.02 MPa in a break size of 5 mm. The evaluation results using the experimental data in Kawanishi et al. (1986) are shown in Figure 3-39. In these plots, the Standard model generally can predict stagnation pressures at the center of the jets very well along the axial direction. The comparisons are within ±20% for both free and impinging jets.
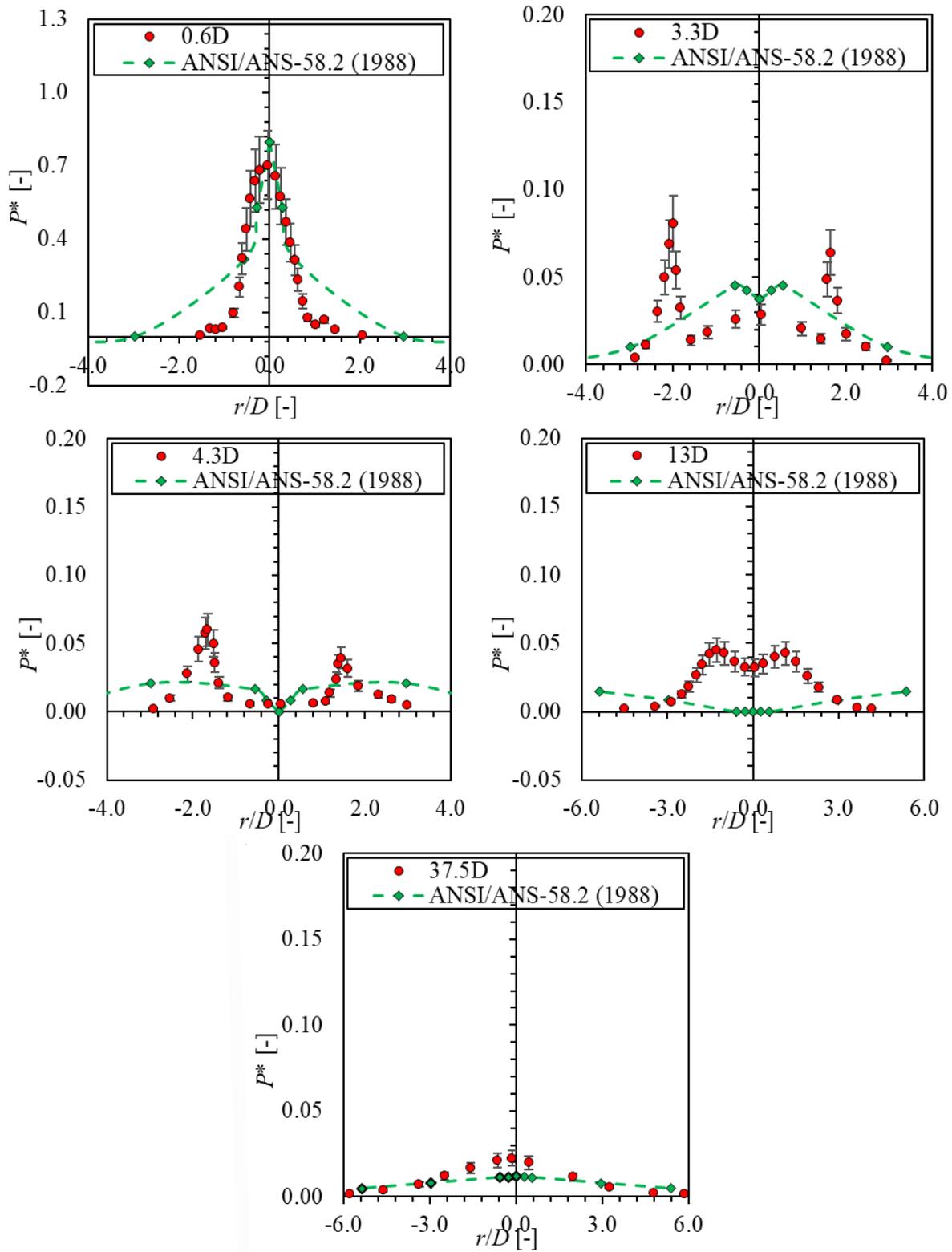
Figure 3-37 Comparison between Standard Model Calculation (ANSI/ANS-58.2, 1988) and Experimental Data of Free Steam Jets in Masuda et al. (1981) of Mitsubishi Tests. Error Bar: ±20%
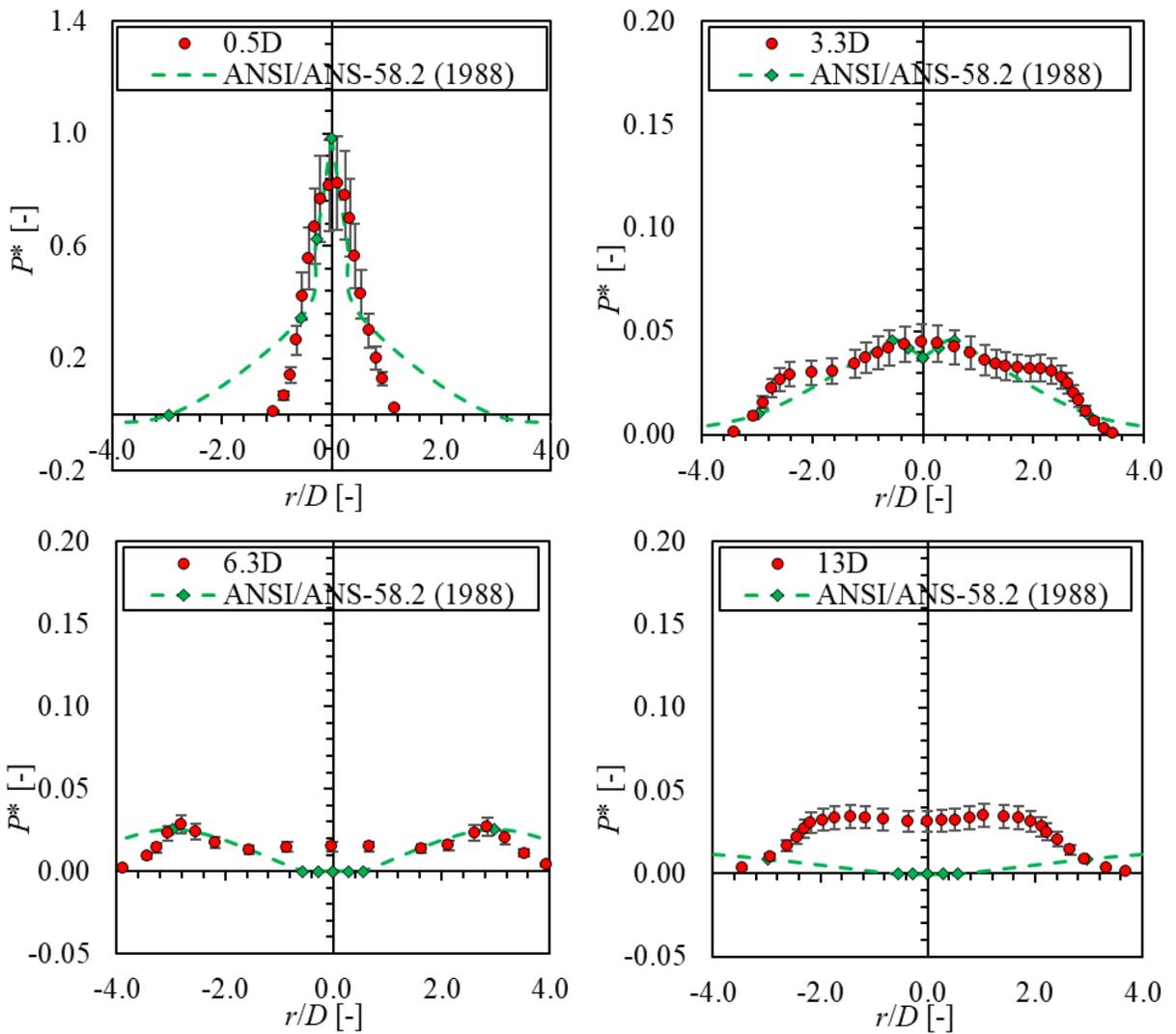
Figure 3-38 Comparison between Standard Model Calculation (ANSI/ANS-58.2, 1988) and Experimental Data of Impinging Steam Jets in Masuda et al. (1981) of Mitsubishi Tests. Error Bar: ±20%
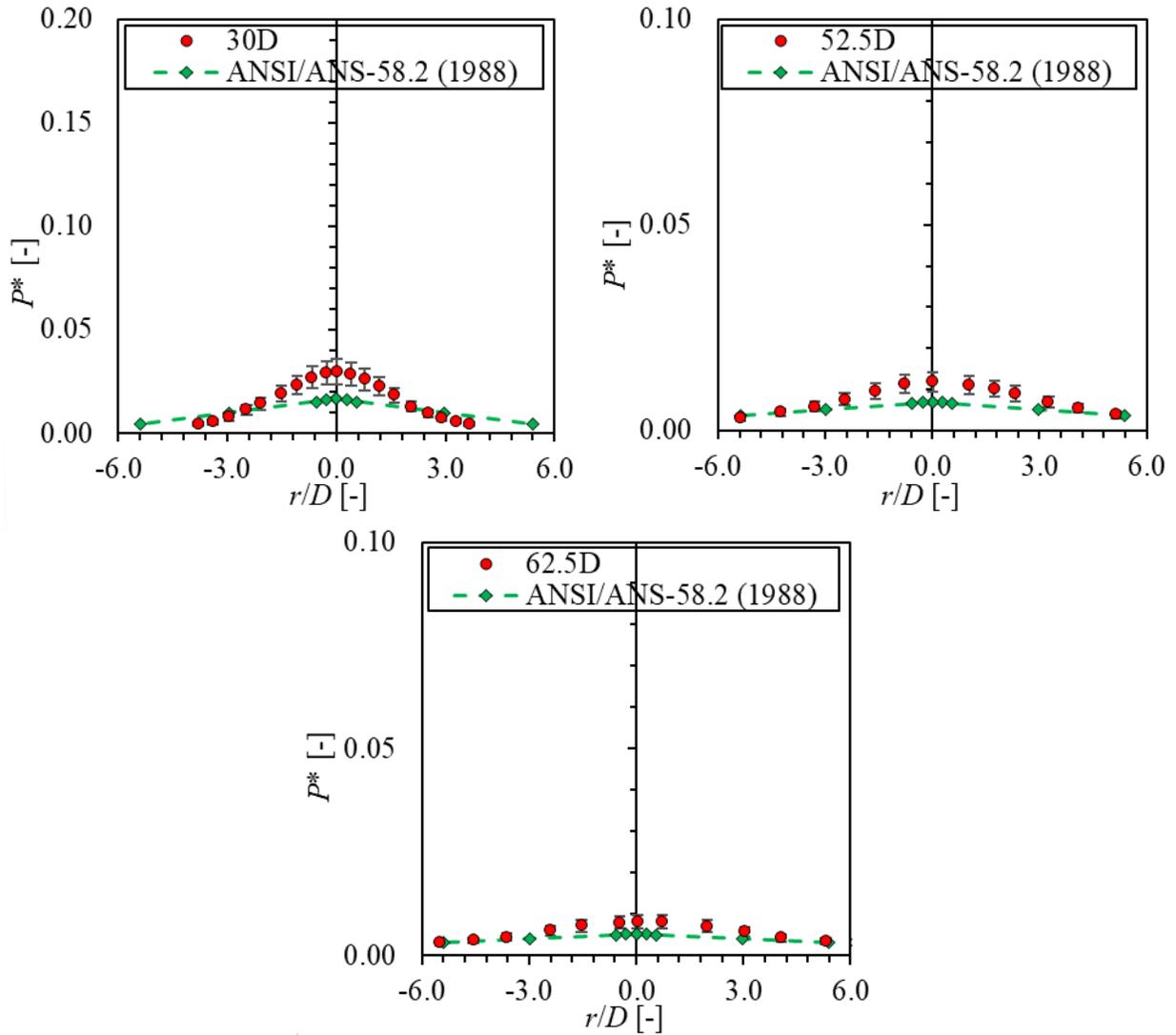
Figure 3 38 Comparison between Standard Model Calculation (ANSI/ANS-58.2, 1988) and Experimental Data of Impinging Steam Jets in Masuda et al. (1981) of Mitsubishi Tests. Error Bar: ±20% (cont.)
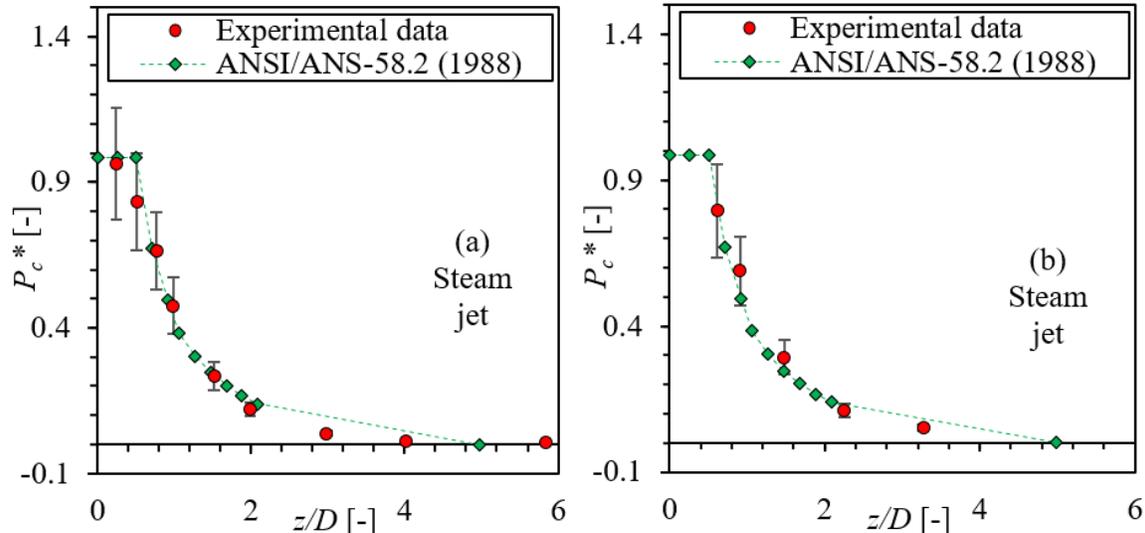
Figure 3-39 Comparison between Standard Model Calculation (ANSI/ANS-58.2, 1988) and Experimental Data of Saturated Steam Jets (a) Free Jet and (b) Impinging Jets in Kawanishi et al. (1986) of Mitsubishi Tests. Error Bar: ±20%

3.2.1.1.2 Saturated Water/two-phase Jets

This section discusses the model evaluation results for saturated water/two-phase jets. The experimental data employed in the assessment include those in Marviken tests (both free and impinging jet), Mitsubishi tests (Kawanishi et al., 1986), JAERI tests, and KWU tests.

Among the six free jets in Marviken tests, selected times in Tests 1, 2, and 6 for saturated water/two-phase jets are used for model evaluation. The experimental data in Test 5 are not used because saturated water/two-phase jets are not investigated. The time after 6.6 s in Test 3 and all the time in Test 4 are not used due to unreliable data caused by the movement of the central probe and instrumented beams. In total, 6 conditions for free saturated water/two-phase jets in the Marviken tests are evaluated. A summary of the boundary conditions of the chosen test times is shown in Table 3-6. The selected conditions from different pipe sizes have a quality below 4% as shown in the table. A complete boundary conditions for each test can be found in Table B-1 through Table B-5 of Appendix B. The calculated fluid temperature and critical mass flux from the Standard model, and the differences between measured and calculated critical mass flux are included in these tables of Appendix B.

Table 3-6 Summary of Selected Conditions in Marviken tests for ANSI/ANS-58.2 (1988) Evaluation: Free Saturated Water/Two-phase Jets

Test Number	Times (s)	Quality (-)	Initial Stagnation Pressure (kPa)	Break size (m)
Test 1	35	0.0022	3,146	0.5
	50	0.0015	2,874	0.5
Test 2	50	0.0017	3,881	0.28
	60	0.0027	3,752	0.28
Test 6	45	0.0045	2,974	0.5
	60	0.04	2,640	0.5

In the evaluation, the dimensionless pressures at different axial and radial locations are plotted. In Tests 1 and 2, the pressures at the center of the jets (70 mm) were not measured but the measurement was performed in Test 6. Figure 3-40 shows the axial distribution of dimensionless pressures for one time condition in Test 6 as an example. The profiles at other times are similar for the same test and a complete comparison can be found in Appendix B. In the current work, the radial location closest to $r = 70$ mm from the Standard calculation is used for comparison as shown in Figure 3-40. From the plots, the pressure predicted by the Standard model can be slightly underestimated within about 1 D of the jet. As the distance from the break plane increases, the Standard model can predict conservative values for the stagnation pressure. The underestimation was also observed for Tests 2 and 6 by plotting the radial pressure profiles as shown in Figure 3-41. For larger axial locations in Tests 2 and 6 and all the locations in Test 1, the pressure can be predicted with conservative values.

Among the six impinging jets in Marviken tests, selected times in Tests 7, 8, 10, and 12 for saturated water/two-phase jets are used for model evaluation. In Test 11, the only saturated steam jets and no saturated water/two-phase jets were investigated. In total, 6 conditions for impinging saturated water/two-phase jets in the Marviken tests are evaluated. A summary of the boundary conditions of the chosen test times is shown in Table 3-7. The selected conditions from different pipe sizes have a quality below 24% as shown in the table. A complete boundary conditions for each test can be found in Table B-6 through Table B-10 of Appendix B. The calculated fluid temperature and critical mass flux from the Standard model, and the differences between measured and calculated critical mass flux are included in these tables of Appendix B.
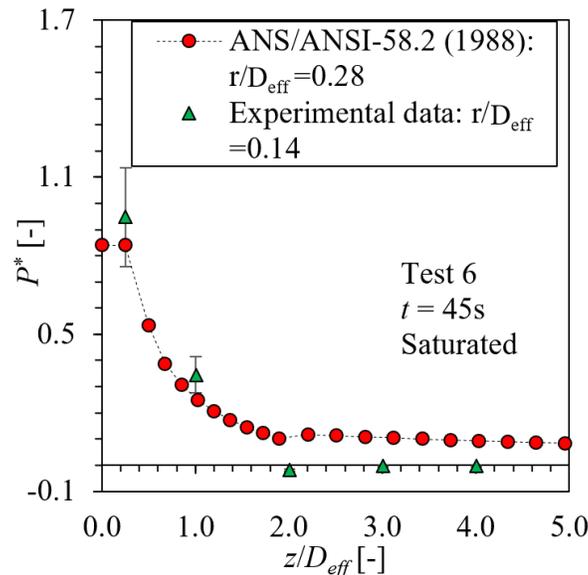
Figure 3-40 Pressure Profiles at Different Axial Locations at 45 s in Test 6. Error Bar: ±20%
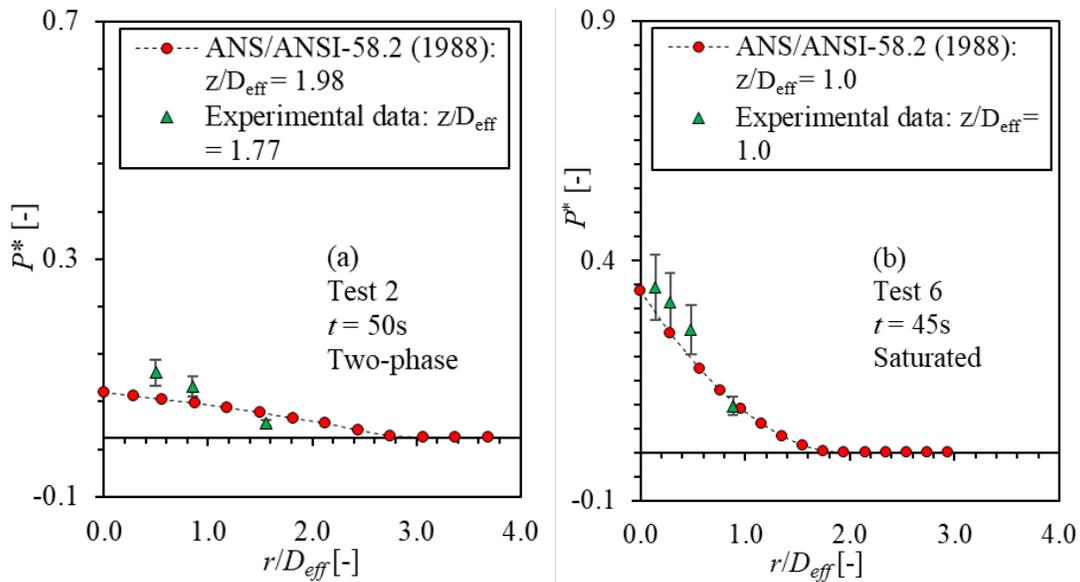
Figure 3-41 Pressure Profiles at Different Radial Locations: (a) 50 s in Test 2 and (b) 45 s in Test 6. Error Bar: ±20%

In the evaluation, the dimensionless pressures at different radial locations are plotted. The experimental data in different tests provide model evaluation at different axial locations. It is found that the Standard model can generally predict conservative values for nondimensional stagnation pressure at larger axial distances as in Test 7 (z/D = 4.05), Test 12 (z/D = 2.95), and Test 8 (z/D = 2.06) as shown in Figure 3-42 for example. A complete comparison for the saturated water jets in Tests 7, 8, and 12 can be found in the Appendix B.

For the conditions in the vicinity of the break plane such as Test 10 (z/D = 1.27), the dimensionless pressures are underestimated at certain radial locations as shown in Figure 3-43. A complete comparison for saturated water jets in Test 10 can be found in the Appendix B.

Table 3-7 Summary of Selected Conditions in Marviken Tests for ANSI/ANS-58.2 (1988) Evaluation: Impinging Saturated Water/Two-phase Jets

Test Number	Times (s)	Quality (-)	Initial Stagnation Pressure (kPa)	Break size (m)	z/D (-)
Test 7	30	0.005	3,003	0.5	4.05
	45	0.1	2,489	0.5	4.05
Test 8	30	0.0049	2,995	0.5	2.06
	45	0.0199	2,580	0.5	2.06
Test 10	45	0.0112	2,549	0.5	1.27
	50	0.364	1,743	0.5	1.27
Test 12	45	0.2439	2,212	0.5	2.95
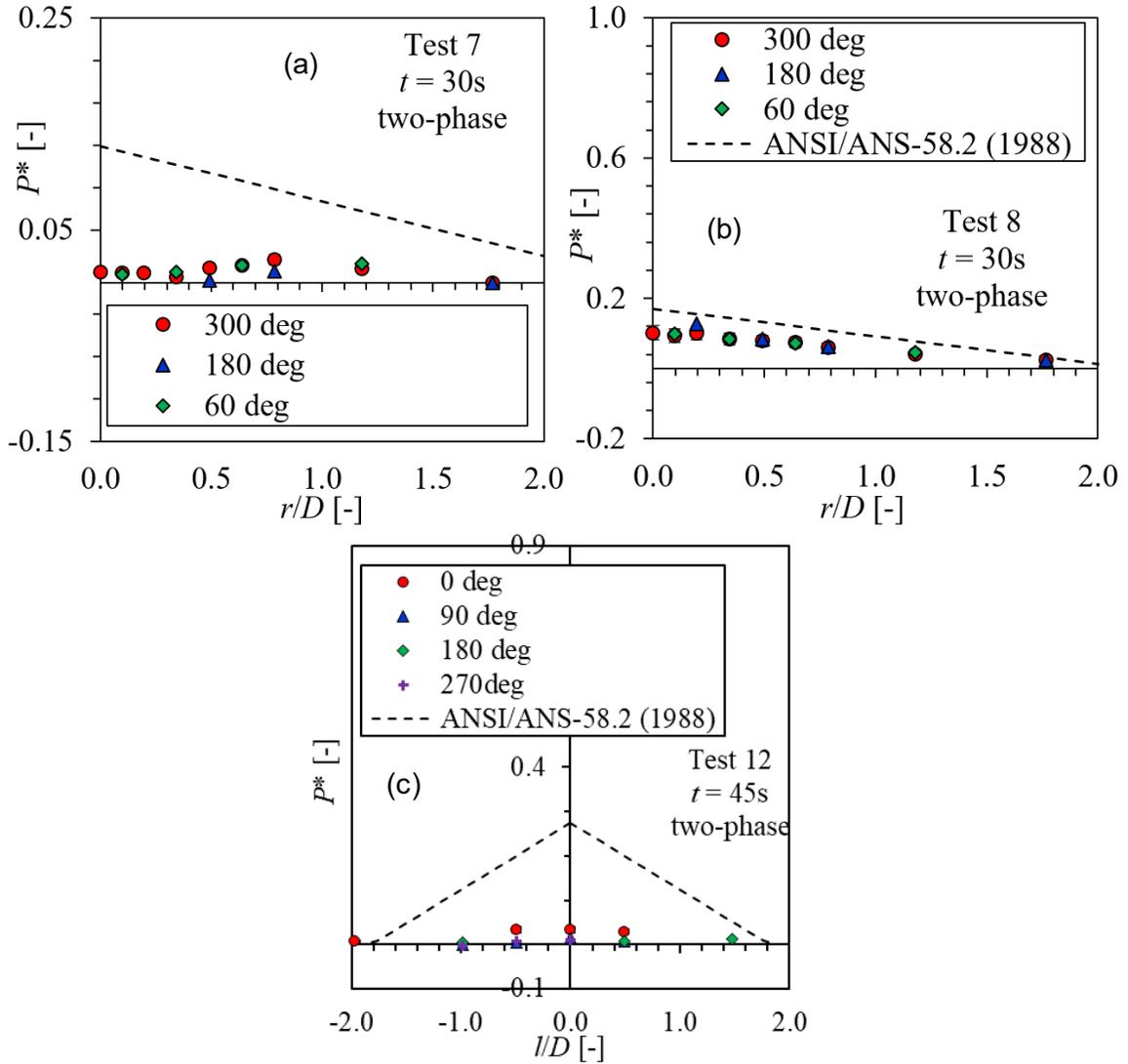
Figure 3-42 Pressure Profiles at Different Axial Locations: (a) 30 s in Test 7, (b) 30 s in Test 8, and (c) 45 s in Test 12. Error Bar: ±20%
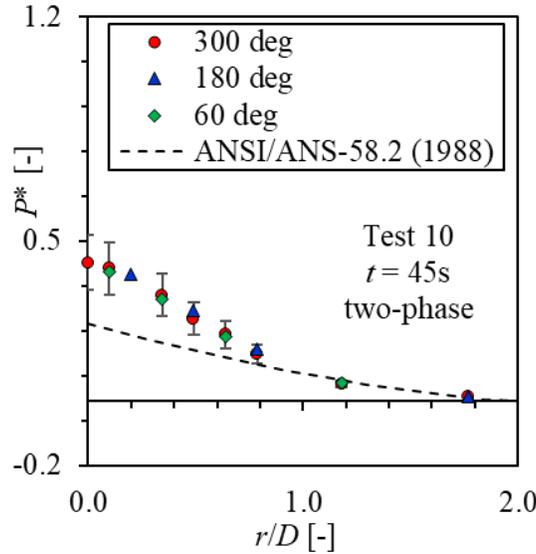
Figure 3-43 Pressure Profiles at Different Axial Locations: 45 s in Test 10. Error Bar: ±20%

In Kawanishi et al. (1986), only the stagnation pressure at the center of the jets are measured. Both free and impinging jets are investigated. The quality of the conditions studied in this work is below 2% in a break size of 5 mm. The evaluation results using the experimental data in Kawanishi et al. (1986) are shown in Figure 3-44. In these plots, the Standard model generally underestimates the nondimensional stagnation pressure along the axial direction of the jets. The degree of underestimation is within 20% in the vicinity of the break plane, but increasesin Regions 2 and 3 of the jets. The predicted values by the Standard model generally become comparable with the experimental data again at around 3 D in the axial location.
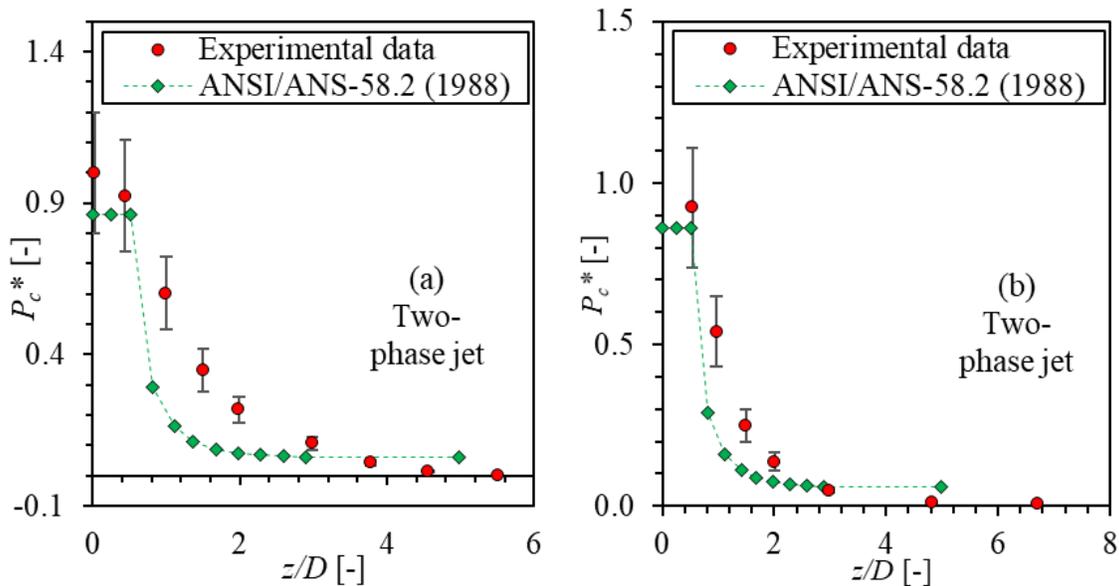
Figure 3-44 Comparison between Standard Model Calculation (ANSI/ANS-58.2, 1988) and Experimental Data of Two-phase Jets (a) Free Jet and (b) Impinging Jet in Kawanishi et al. (1986) of Mitsubishi Tests. Error Bar: ±20%

Experiments for two saturated water jets were investigated in the JAERI tests (Yano et al., 1984) with an initial stagnation pressure of 6.8 MPa and 5.6 MPa in a break size of 150 mm. The stagnation pressure at targets were measured at two different axial locations of 2 *D* and 5 *D*. The evaluation results using the experimental data in Yano et al. (1986) are shown in Figure 3-45. In these plots, the Standard model significantly underestimates the stagnation pressure at the center region of the jets. The nondimensional stagnation pressure at the center of the jets can be underestimated by 70% at an axial distance of 2 *D*. At a radius outside of 1 *D*, the Standard model can predict the experimental data with conservative values. At an axial distance of 5 *D*, the measured pressures are smaller than the ambient pressure due to overexpansion of the jets, while the Standard model predicts positive values.
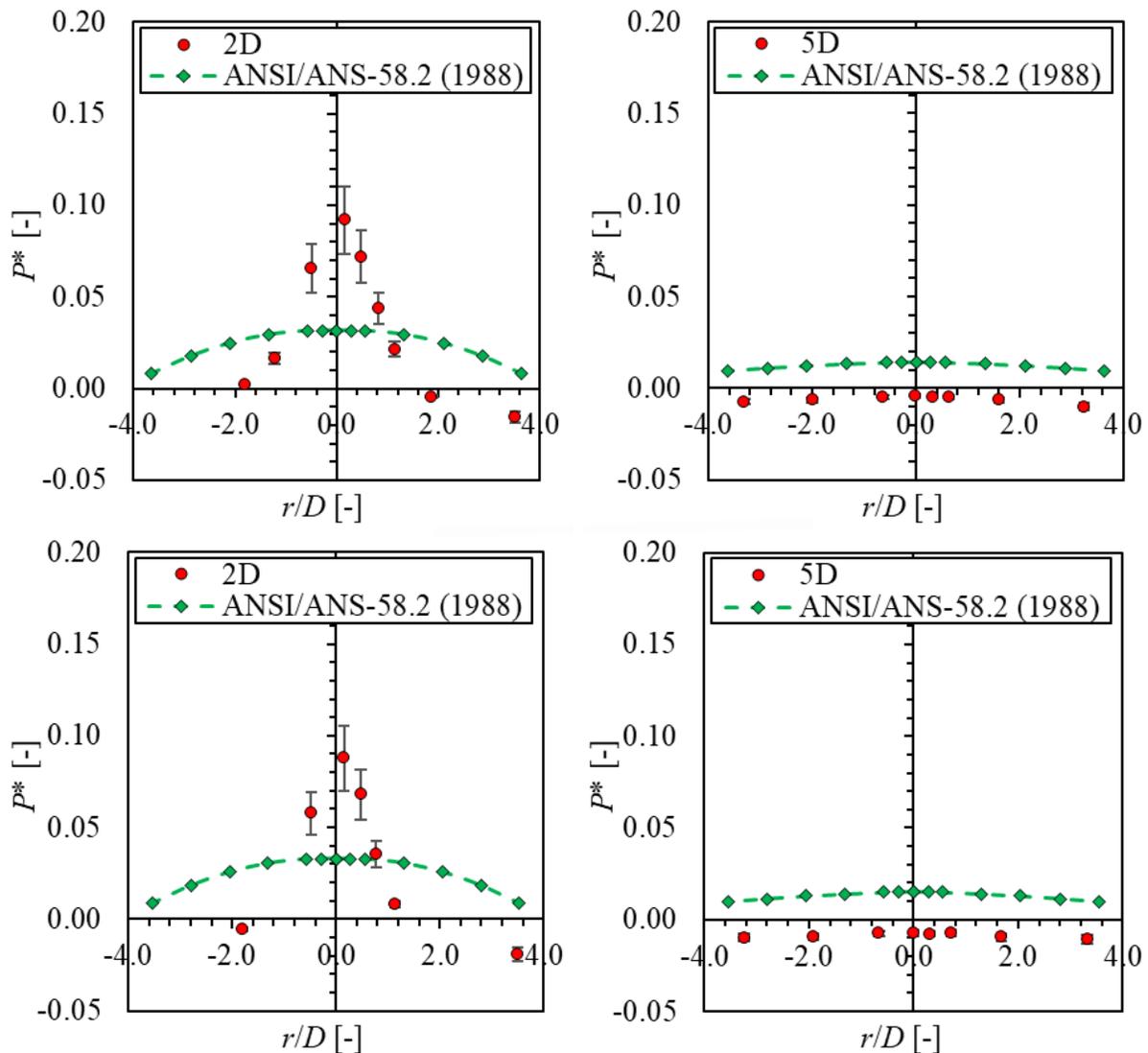
Figure 3-45 Comparison between Standard Model Calculation (ANSI/ANS-58.2, 1988) and Experimental Data of Impinging Saturated Water Jets in Yano et al. (1984) of JAERI Tests. Error Bar: ±20%

Experiments were performed to investigate the saturated water jets in KWU tests (Kastner and Rippel, 1987) with an initial stagnation pressure of 10 MPa in a break size of 65 mm. The stagnation pressure at targets were measured at four different axial locations of 0.5 D, 1 D, 2 D and 3 D. The evaluation results using the experimental data in Kastner and Rippel (1987) are shown in Figure 3-46. In these plots, the Standard model can predict the stagnation pressure at the center of the jet conservatively at an axial location of 0.5 D. However, for stagnation pressure at other radial and axial locations, the stagnation pressures are significantly underestimated.
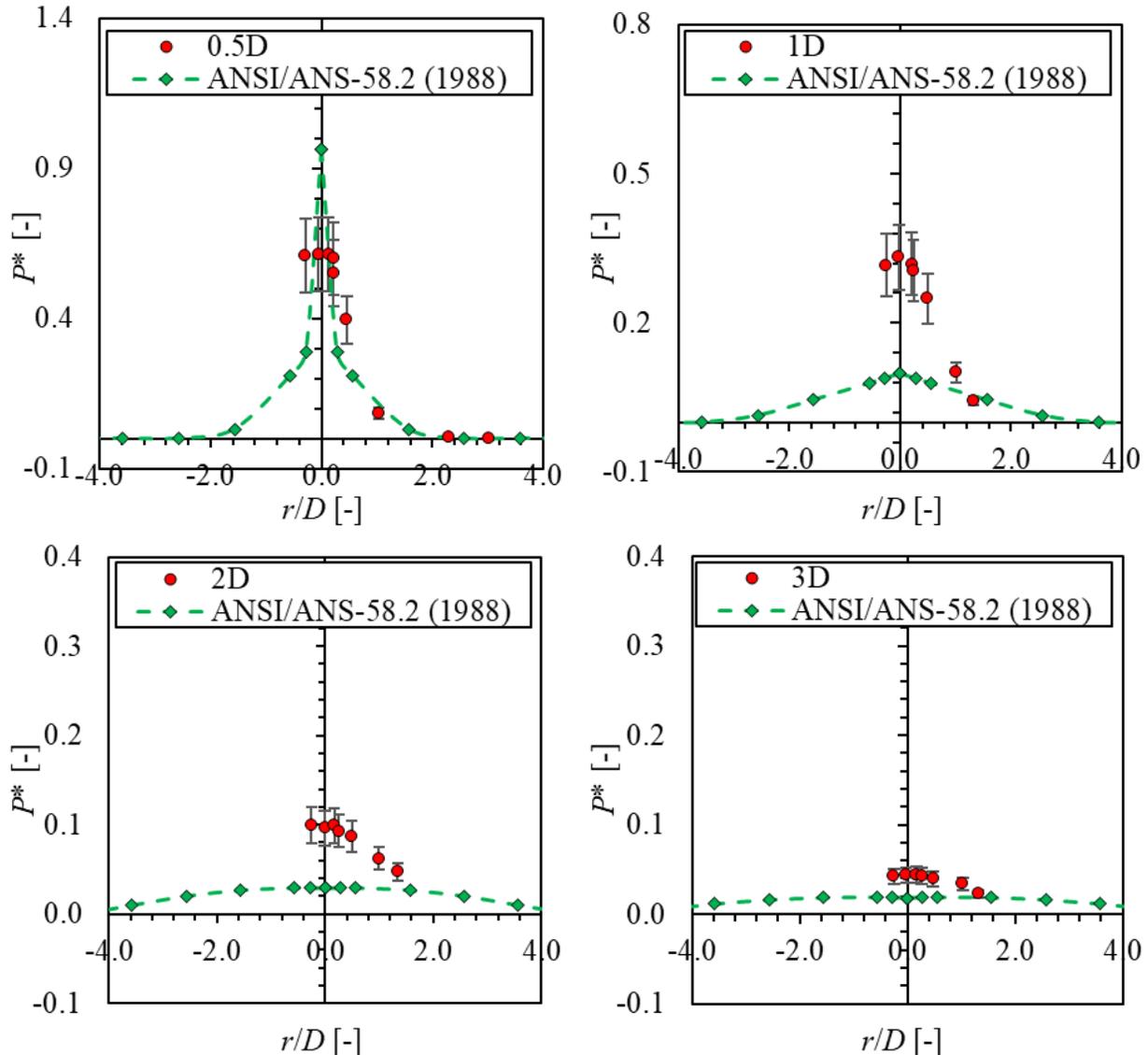
Figure 3-46 Comparison between Standard Model Calculation (ANSI/ANS-58.2, 1988) and Experimental Data of Impinging Saturated Water Jets in Kastner and Rippel (1987) of KWU Tests. Error Bar: ±20%

3.2.1.1.3 Subcooled Water Jets

This section discusses the model evaluation results for subcooled water jets. The experimental data employed in the assessment include those in Marviken tests (both free and impinging jet) and Mitsubishi tests (Kawanishi et al., 1986).

Among the six free jets in Marviken tests, selected times in Tests 1, 2, and 6 for subcooled water jets are used for model evaluation, which are representative for different flow regimes. In Test 5, no subcooled water jets were available for investigation. The time after 6.6 s in Test 3 and all the time in Test 4 are not used due to unreliable data caused by the movement of the central probe and instrumented beams. In total, 12 conditions for free subcooled water jets in the Marviken tests are evaluated. A summary of the boundary conditions of the chosen test times is shown in Table 3-8. It can be seen that the selected conditions cover a wide range of subcooling from 5.2°C to 45.4°C in different pipe sizes. Complete boundary conditions for each test can be found in Table B-1 through Table B-5 of Appendix B. The calculated fluid temperature and critical mass flux from the Standard model by the NRC FORTRAN code Jet11p4 are also included in these tables of Appendix B. The differences between measured and calculated critical mass flux are summarized in the last row.

Table 3-8 Summary of Selected Conditions in Marviken Tests for ANSI/ANS-58.2 (1988) Evaluation: Free Subcooled Water Jets

Test Number	Times (s)	Subcooling (°C)	Initial Stagnation Pressure (kPa)	D_{eff} (m)
Test 1	5	20.5	4,330	0.5
	10	14.5	3,926	0.5
	20	6.5	3,461	0.5
Test 2	10	24.8	4,622	0.28
	20	19.5	4,313	0.28
	40	5.2	3,984	0.28
Test 3	2	45.4	4,604	0.5
	4	42.1	4,390	0.5
	5.5	39.0	4,161	0.5
Test 6	5	16.0	4,049	0.5
	10	11.0	3,778	0.5
	20	5.0	3,330	0.5

In the evaluation, the dimensionless pressures at different axial and radial location are plotted. In tests 1 and 2, the pressures at the center of the jets (70 mm) were not measured but the measurement was performed in Tests 3 and 6. Figure 3-47 shows the axial distribution of dimensionless pressures for one time condition each in Tests 3 and 6 as an example. The profiles at other times are similar for the same test and a complete comparison can be found in Appendix B. As shown in the plots, the pressure predicted by the Standard model can be very high in the vicinity of the break plane. This corresponds to the Region 1 in the jet geometry modeled by the Standard (ANSI/ANS-58.2, 1988). As the jet moves further away from the break plane, the pressures drop very rapidly. The axial position where the pressure drops significantly is different for the two conditions presented. Based on the Standard model, the length of Region 1 in the axial direction (z_c) depends on the subcooling of the initial fluid prior to the break as

shown in Equation (2-50). Since the condition shown in Test 3 has a much higher subcooling than that in Test 6, the pressure starts to decrease at a further distance.

In addition, it is observed that the Standard model can predict conservative values for the stagnation pressure in all the axial locations. However, the pressure is significantly overstimated in Region 1. In the axial distance downstream, the Standard model prediction agrees better with the experimental data. Meanwhile, the degree of over estimation is stronger in Test 3 in the vicinity of the break plane than that in Test 6. It is found that this is related to the crtical mass flux prediction. In the Standard model, the stagnation pressure is predicted by Equation (A-2), in which the jet impingement force is calculated by the greater values of the two forces:

$$F_b = \frac{G_e^2 A_e}{\rho_e g_c} + A_e \left(P_e - p_{amb} \right) \tag{3-22}$$

$$F_j = A_e \left(C_T P_0 - p_{amb} \right) \cong C_T P_0 A_e \tag{3-23}$$

where F_b is the jet blowdown force from the generalized momentum equation, and F_j is a conservative quasi-steady-state jet impinging force. G_e, A_e, P_e, P_0 are the critical mass flux, break area, fluid pressure at the break plane, and the initial stagnation pressure, respectively. For the subcooled water jets, the Standard model predicts the critical mass flux using the Henry-Fauske model (1971). While this model slightly overestimates the critical mass flux for conditions with relatively low subcooling, it can significantly overestimates that with high subcooling.
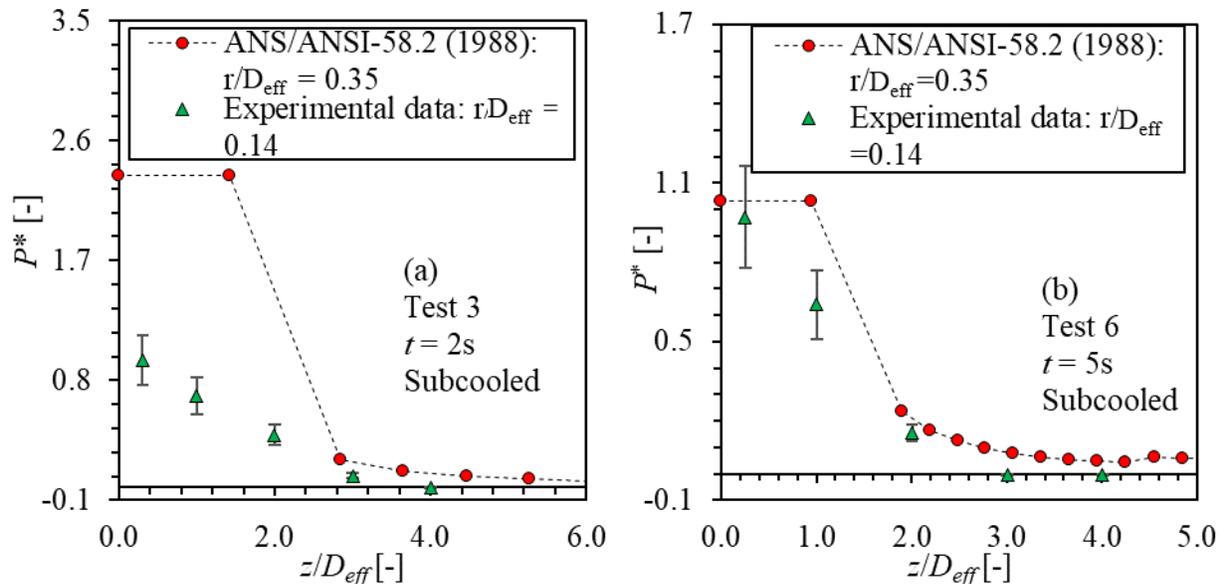
Figure 3-47 Pressure Profiles at Different Axial Locations: (a) 2 s (ΔT = 45.4°C) in Test 3 and (b) 5 s (ΔT = 16.0°C) in Test 6. Error Bar: ±20%

Among the six impinging jets in Marviken tests, selected times in Tests 7, 8, 10, and 12 for subcooled water jets are used for model evaluation. In Test 11, only saturated steam jets and no subcooled water jets were investigated. In total, 14 conditions for impinging subcooled water jets in the Marviken tests are evaluated. A summary of the boundary conditions of the chosen

test times is shown in Table 3-9. It can be seen that the selected conditions cover a wide range of subcooling from 0.7°C to 24.2°C in different pipe sizes and axial locations. Complete boundary conditions for each test can be found in Table B-6 through Table B-10 of Appendix B. The calculated fluid temperature and critical mass flux from the Standard model by the NRC FORTRAN code Jet11p4 are also included in these tables of Appendix B. The differences between measured and calculated critical mass flux are summarized in the last row.

Table 3-9 Summary of Selected Conditions in Marviken Tests for ANSI/ANS-58.2 (1988) Evaluation: Impinging Subcooled Water Jets

Test Number	Times (s)	Subcooling (°C)	Initial Stagnation Pressure (kPa)	Break size (m)	z/D (-)
Test 7	5	19.2	4,318	0.5	4.05
	10	12.5	3,784	0.5	4.05
	20	3.3	3,234	0.5	4.05
Test 8	5	23.6	4,285	0.5	2.06
	10	14.7	3,756	0.5	2.06
	20	3.6	3,209	0.5	2.06
Test 10	5	22.9	4,283	0.5	1.27
	10	14.7	3,806	0.5	1.27
	20	3.1	3,238	0.5	1.27
	30	0.7	2,988	0.5	1.27
Test 12	5	24.2	4,321	0.5	2.95
	10	17.0	3,855	0.5	2.95
	20	5.8	3,398	0.5	2.95
	30	1.4	3,163	0.5	2.95

In the evaluation, the dimensionless pressures at different radial location are plotted. The experimental data in different tests provide model evalution at different axial locations. It is found that the Standard model can generally predict conservative values for stagnation pressure at larger axial distances as in Test 7 (z/D = 4.05) and Test 12 (z/D = 2.95) as shown in Figure 3-48 for example. In the plot for Test 12, l indicates the length of the pipe as shown in Figure 3-15. A complete comparison for the subcooled water jets in Tests 7 and 12 can be found in the Appendix B.

For the conditions in the vicinity of the break plane such as Test 8 (z/D = 2.06) and 10 (z/D = 1.27), the dimensionless pressures are underestimated at certain radial locations. The Region 1 of jet geometry as discussed in the free jets is also observed in impinging jets from the Standard model prediction as shown in Figure 3-49. A complete comparison for subcooled water jets in Tests 8 and 10 can be found in the Appendix B.
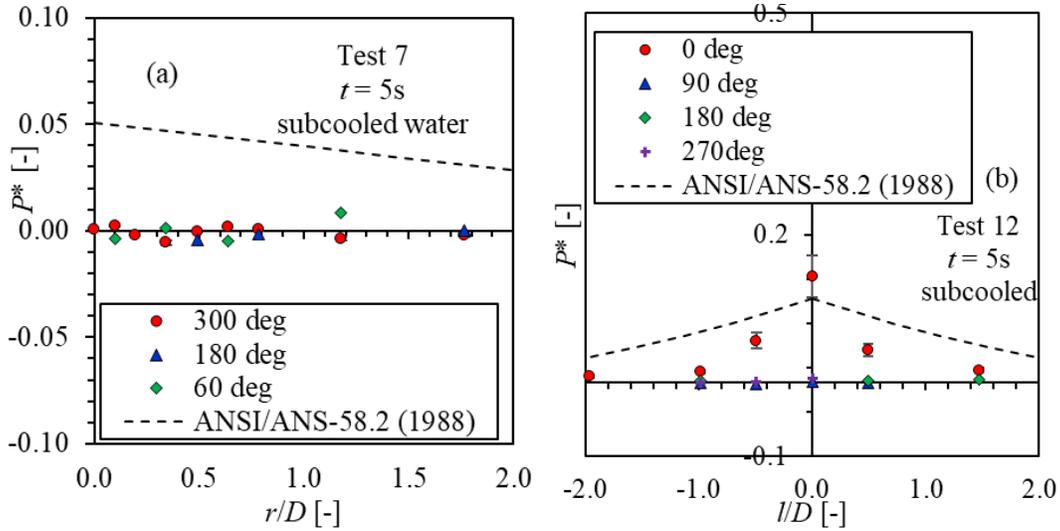
Figure 3-48 Pressure Profiles at Different Radial Locations: (a) 5 s (ΔT = 19.2°C) in Test 7 and (b) 5 s (ΔT = 24.2°C) in Test 12. Error Bar: ±20%
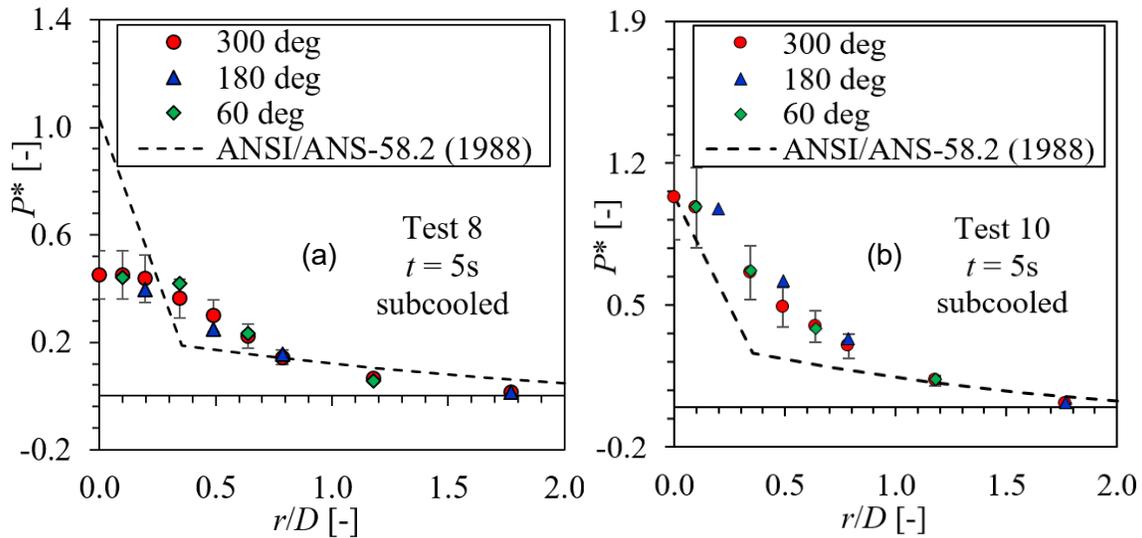
Figure 3-49 Pressure Profiles at Different Radial Locations: (a) 5 s (ΔT = 23.6°C) in Test 8 and (b) 5 s (ΔT = 22.9°C) in Test 10. Error Bar: ±20%

In Kawanishi et al. (1986), only the stagnation pressure at the center of the jets are measured. Both free and impinging jets are investigated. The conditions studied cover a wide range of subcooling from 8.6 °C to 80 °C in a break size of 5 mm. The evaluation results using the experimental data in Kawanishi et al. (1986) are shown in Figure 3-50 and Figure 3-51. In these plots, the Standard model overestimates the stagnation pressure at the center of the jets but underestimates that at further distances. The degree of overestimation is more significant for the relatively high subcooling condition. This is also observed when using the impinging jets data to evaluate the Standard model. As discussed in previous section, this is because the critical flux model is significantly overestimated for conditions with relatively high subcooling.

3-53
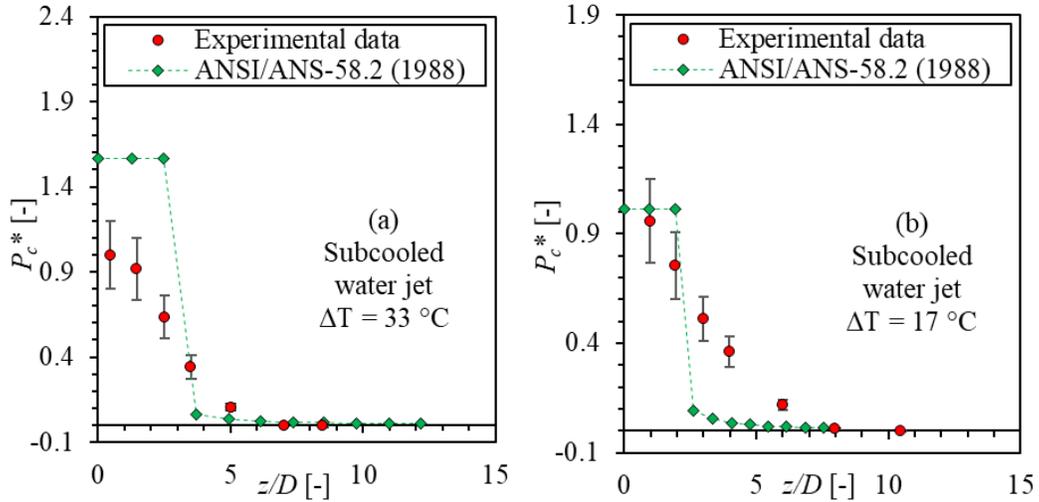
Figure 3-50 Comparison between Standard Model Calculation (ANSI/ANS-58.2, 1988) and Experimental Data of Free Subcooled Water Jets in Kawanishi et al. (1986). Error Bar: ±20%
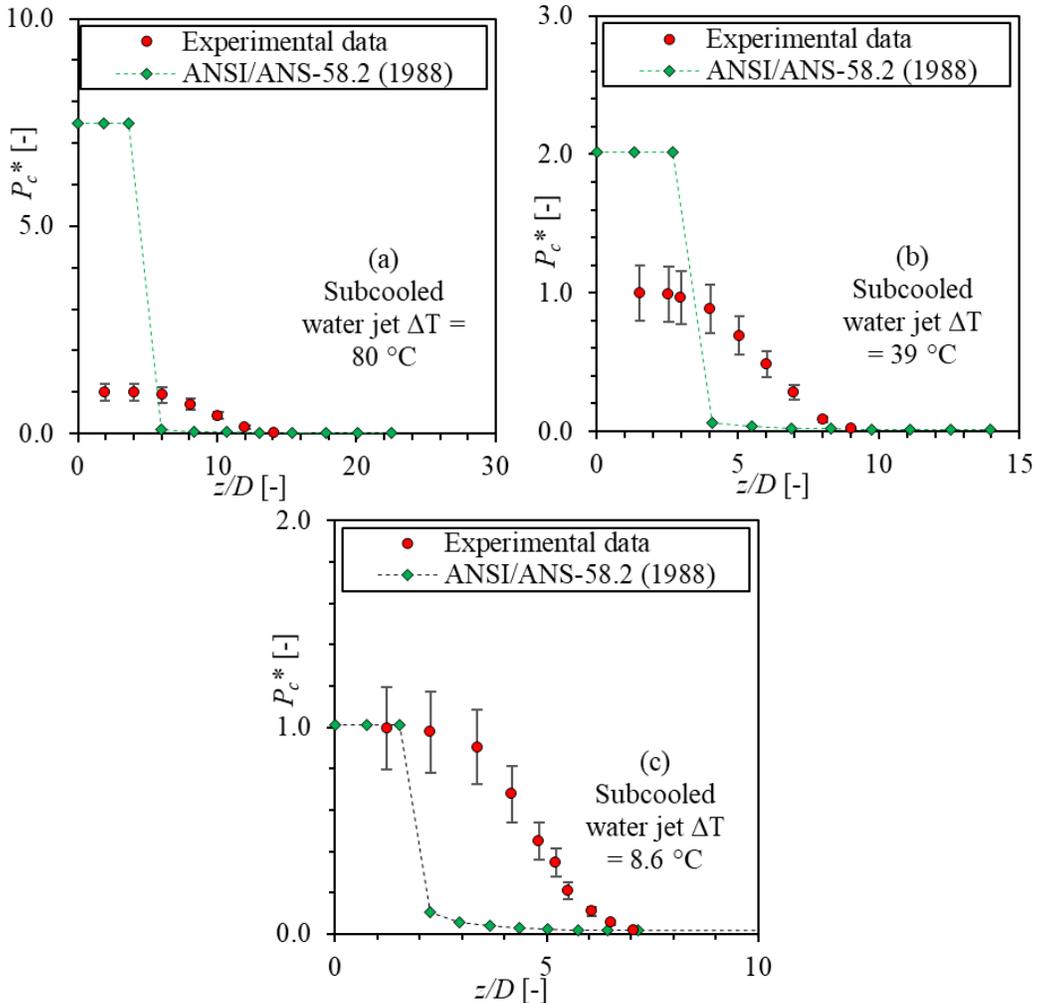
Figure 3-51 Comparison between Standard Model Calculation (ANSI/ANS-58.2, 1988) and Experimental Data of Impinging Subcooled Water Jets in Kawanishi et al. (1986). Error Bar: ±20%

3.2.1.2 Two-phase Jet Loads Model (NUREG/CR-2913)

The NUREG/CR-2913 investigated the initial conditions that result in two-phase jets at pressure above ambient conditions. The model is presented as a series of look-up tables and plots. However, since the initial stagnation pressure of test conditions predicted by NUREG/CR-2013 are above 6 MPa, limited evaluation can be performed using the Marviken tests data, where the stagnation pressure is below 5 MPa. The evaluation shown here are the ones included in NUREG/CR-2913, with axis values added to the figures as shown in Figure 3-52 through Figure 3-54. It is observed that NUREG/CR-2913 can generally predict the data very well.

The prediction for stagnation pressure by ANSI/ANS-58.2 (1988) is also shown in Figure 3-54 for comparison. As explained in Section 3.1.1.2.1, the stagnation pressure is significantly overestimated by the Standard because the critical mass flux is overestimated, by 90% for Test 3.
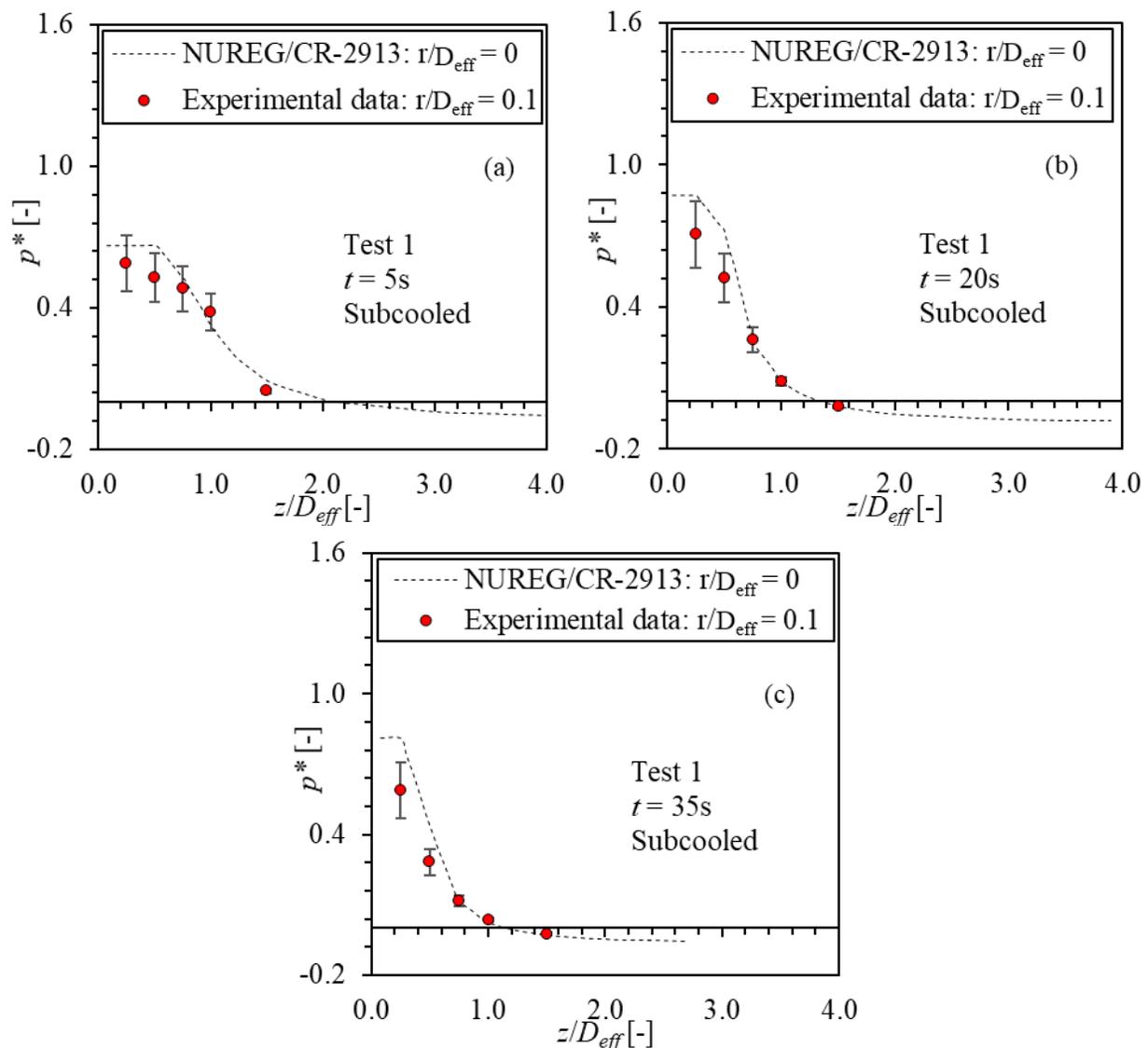
Figure 3-52 Comparison between NUREG/CR-2913 and Experimental Data in Marviken Tests of Test 1 for Static Pressure: (a) 5 s, (b) 20 s, and (c) 35 s. Error Bar: ±20%. Comparisons are Obtained from NUREG/CR-2913
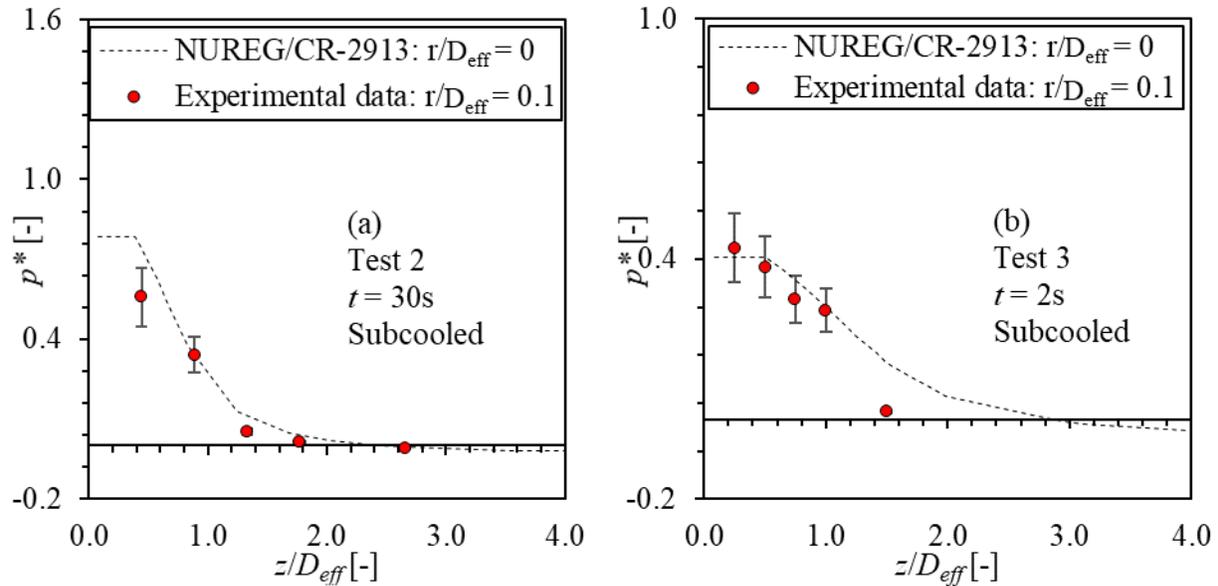
Figure 3-53 Comparison between NUREG/CR-2913 and Experimental Data in Marviken Tests for Static Pressure: (a) Test 2: 30 s, (b) Test 3: 2 s. Error Bar: ±20%. Comparisons are Obtained from NUREG/CR-2913

3.2.2 Jet Core Length

The approach to calculate the jet core length in the Standard model (ANSI/ANS-58.2, 1988) as given in Equation (3-1) is evaluated in the current section. The experimental data obtained by Celata et al. (1986) using X-rays are used. To simulate the LOCA accidents in LWRs, Celata et al. (1986) investigated the length of jet core for subcooled conditions (0.8 MPa < P_0 < 2.5 MPa; 0°C < ΔT < 110°C) in a pipe size of 4.6 mm, where the effect of friction on jet core length is also investigated. Three different frictional lengths are used: L_p/D = 10, 100, and 300. It is found that increasing the degree of subcooling increases the jet core length, while increasing the friction generally decreases the jet core length. This indicates that the effect of increasing friction is similar to that of decreasing the degree of subcooling.

In Figure 3-55, the experimental data for jet core length obtained in Celata et al. (1986) are compared with the model in ANSI/ANS-58.2 (1988) and that in Luxat (2017). All the experimental data for different initial stagnation pressures and frictional lengths are included in the plot. Considering that the approach in the Standard model does not include the effect of friction, it is reasonable to compare the Standard model (Equation (3-1)) to the experimental data with the minimum frictional effect (L_p/D =10). As shown in the plots, the standard model can only predict the experimental data well for a small range of subcooling conditions (< 30°C) under the minimum frictional effect. For conditions with higher subcooling, the Standard model underestimates the jet core length. The underestimation is also observed by the model from Luxat (2017).
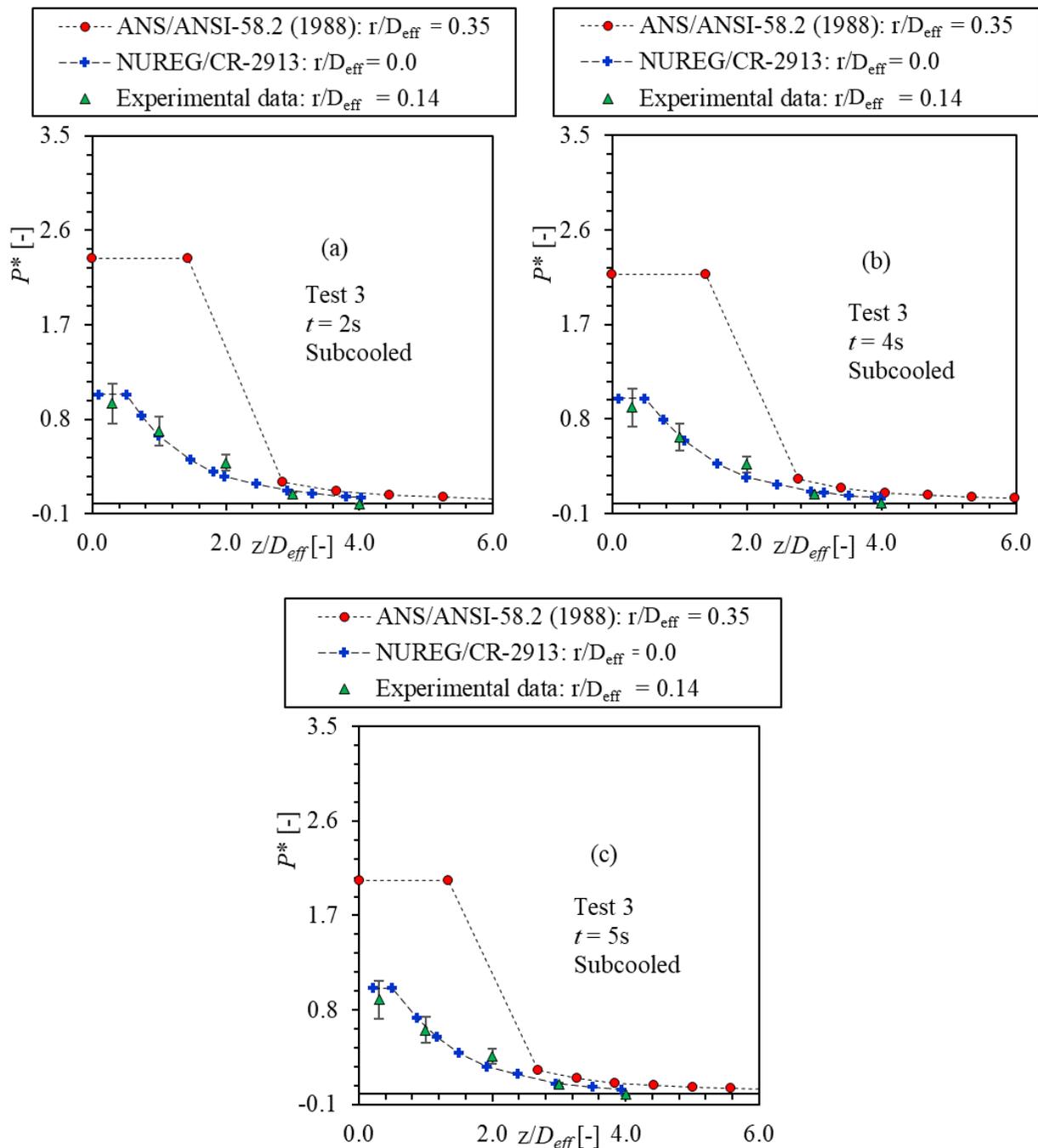
Figure 3-54 Comparison between ANS/ANSI-58.2 (1988), NUREG/CR-2913 and Experimental Data in Marviken Tests of Test 3 for Stagnation Pressure: (a) 2 s, (b) 4 s and (c) 5 s. Error Bar: ±20%. Comparisons between NUREG/CR-2913 and Experimental Data are Obtained from NUREG/CR-2913
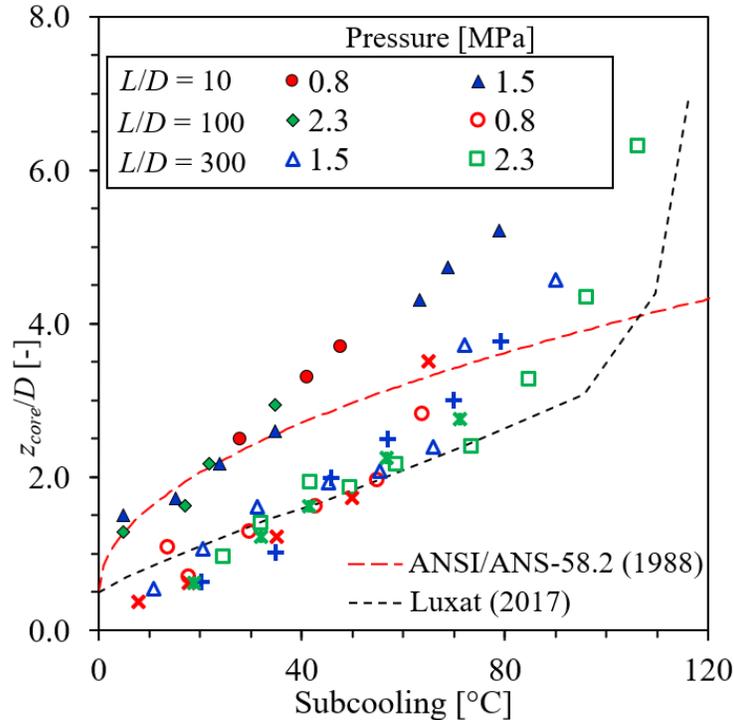
Figure 3-55 Comparison between ANS/ANSI-58.2 (1988), Luxat (2017) and Experimental Data in Celata et al. (1986) on Jet Core Length

3.2.3   Thrust Coefficient

The thrust coefficients for steam-water jet have been investigated in Mitsubishi test (Kawanishi et al., 1986) and JAERI test (Yano et al., 1984). In the study by Kawanishi et al. (1986), the C_T was investigated, and the results for C_T obtained at 2.05 MPa are shown in Figure 3-56. As shown in the figure, the C_T for the round edge nozzle is about 1.1 ~ 1.2 in the two-phase region. For the sharp nozzle, C_T reduces about 20% compared to round nozzle. In the plot, the models for C_T used in the Standard as discussed in Appendix B are also shown for comparison. The equations presented in Section B2 of Appendix B are used to calculated C_T in the subcooled water region and a value of 1.26 is used for saturated steam jets. While the Standard model discusses C_T for saturated water/two-phase jets in Fig. B-5 for different pressure conditions, they are generally around 1.2. As shown in the plot, the Standard model compares well with experimental data.

3.2.4   Critical Mass Flux

3.2.4.1   Evaluation of Critical Mass Flux Model

The evaluation is performed by comparing the critical mass flux calculated by the NRC FORTRAN code (Jet11p4) and the experimental data measured in the Marviken tests (Marklund, 1985a; 1985b). In the Marviken tests, the critical mass flux (G_{cr}) was measured by two independent methods: vessel mass inventory method and pitot-static method. These measurements provide valuable data for critical mass flux model evaluation. This first method calculates the time rate of change of vessel mass using differential pressure measurements. The maximum measurement uncertainty for subcooled and saturated flows using this method is ±12%. The second method calculates the critical mass flux using the pitot-static measurements

in combination with local densities obtained from the gamma densitometer. The maximum measurement uncertainty of this approach is -45% to +30% for subcooled and saturated flows and -45% to +35% for steam flow. The critical mass flux obtained by these two methods generally agree well with each other in the Marviken tests.
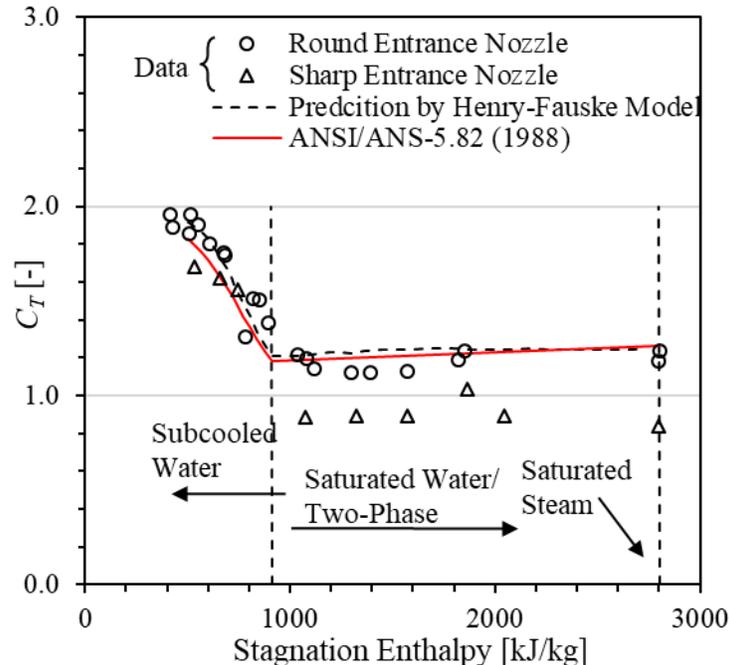
Figure 3-56 Thrust Coefficient for Subcooled Water and Two-phase Mixture Jets at 2.05 MPa (plots from Kawanishi et al., 1986) Compared with the Standard Model (ANSI/ANS-58.2, 1988)

Figure 3-57 shows the comparison between the critical mass flux calculated by the NRC FORTRAN code (Jet11p4) and the experimental data. The comparison is divided into three regions: subcooled water jets ($\Delta T > 0$) with $G_{cr} > $ ~17,500 kg/m^{2}s, saturated water/two-phase jets (water dominant: $0 \leq x < 0.7$) with ~6,000 kg/m^{2}s < G_{cr} < ~17,500 kg/m^{2}s, and saturated steam jets (steam dominant: $x \geq 0.7$) with $G_{cr} < $ ~6,000 kg/m^{2}s.

For subcooled water jets, the maximum value of Homogeneous Equilibrium Model (HEM) calculation ($G_{cr,HEM}$) and Henry-Fauske (HF) model calculation ($G_{cr,HF}$) is chosen for G_{cr}:

$$G_{cr} = \max\left(G_{cr,HEM}, G_{cr,HF}\right)$$
(3-24)

HEM is used to calculated G_{cr} for two-phase jets with an inlet quality of $0 \leq x < 0.9999$ in the code, and the maximum value of HEM calculation ($G_{cr,HEM}$) and isentropic expansion calculation ($G_{cr,IE}$) is chosen for jets with an inlet quality of $x \geq 0.9999$:

$$G_{cr} = \max\left(G_{cr,HEM}, G_{cr,IE}\right)$$
(3-25)

As shown in the comparison, the critical mass flux for saturated water/two-phase and saturated steam jets can be generally predicted within ±30%. However, for subcooled water jets, the

critical mass flux is generally overpredicted using Equation (3-24). Especially for conditions with high subcooling (Test 3: ΔT = 39 ~ 45°C), the critical mass flux can be overestimated by 90%. To investigate the performance of each model, the current work also outputs the G_{cr} calculation from different models in different jet regimes.
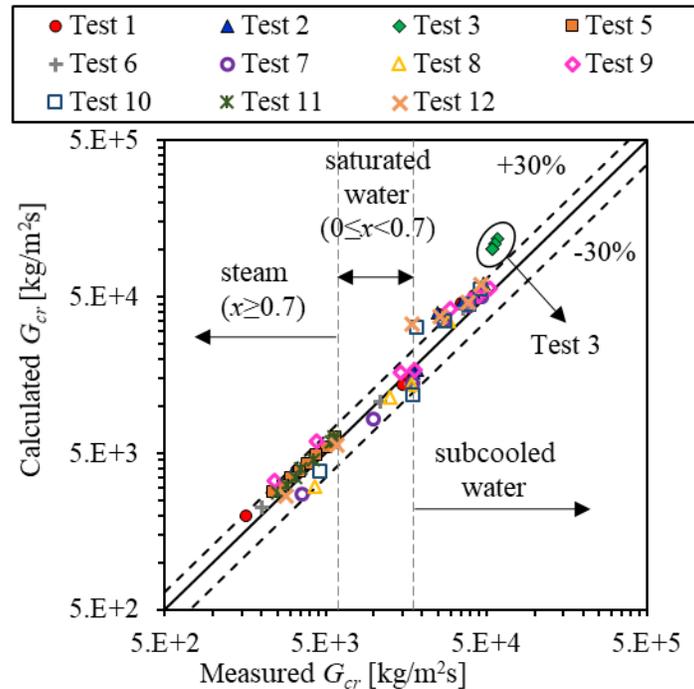
Figure 3-57 Comparison on Critical Mass Flux between Calculated Values by NRC FORTRAN Code (Jet11p4) and Experimental Data in Marviken Tests.

3.2.4.1.1 Subcooled Water Jets

The performance of HEM and the Henry-Fauske model (1971) for subcooled water jets is investigated as shown in Figure 3-58. The comparison between calculated G_{cr} and measured G_{cr} in Marviken tests is shown in Figure 3-58 (a) and the percentage error as a function of the degree of subcooling is shown in Figure 3-58 (b). As shown in the plots, the Henry-Fauske model (1971) predicts the data well in relatively high mass flux region (degree of subcooling > 10 K), but significantly overestimates the data in low mass flux region (degree of subcooling < 10 K). This might be because the Henry-Fauske model does not allow for heat and mass transfer between liquid and gas phases, it can significantly overestimate the critical mass flux. This overestimation becomes more significant as the degree of subcooling decreases. The HEM significantly overestimates the data in high mass flux region (e.g., Test 3) and underestimates the data in low mass flux region. As such, the maximum value given by Equation (3-24) is that calculated by HEM in high mass flux region and that calculated by Henry-Fauske model in low mass flux region.
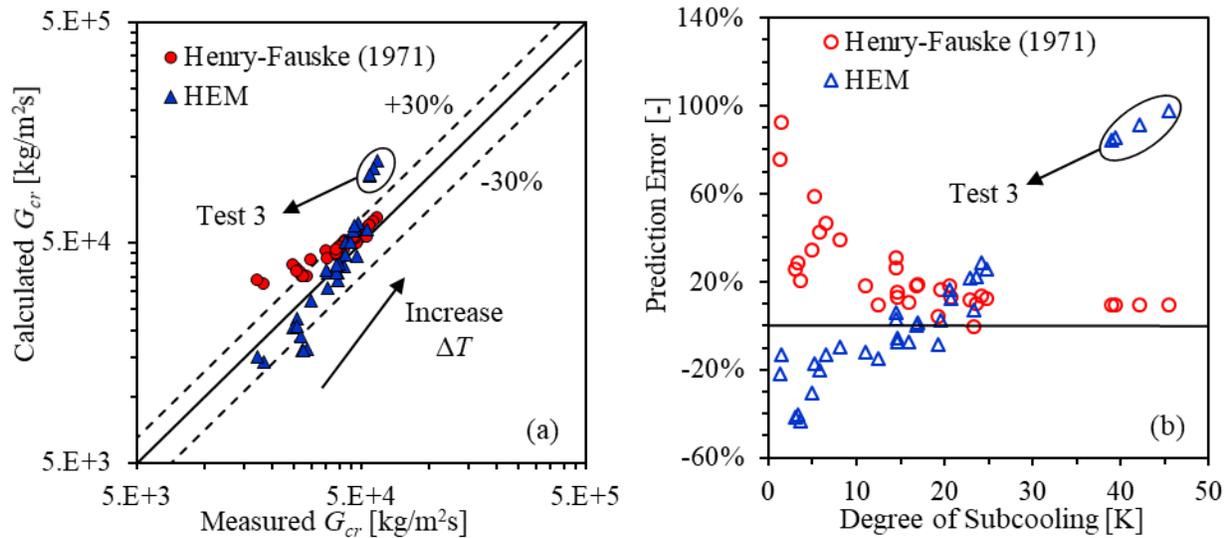
Figure 3-58 (a) Comparison between Calculated G_{cr} and Measured G_{cr} in Marviken Tests for Subcooled Water Jets and (b) Prediction Error as a Function of the Degree of Subcooling

The experimental data for critical mass flux obtained by Celata et al. (1986) are also used for model evaluation. Figure 3-59 (a) shows the experimental data obtained by Celata et al. (1986) in a 4.6 mm pipe. Due to the friction, only the experimental data with minimum frictional effect (L_p/D = 10) are shown in the plots and are compared in the current work. As shown in the figure, the critical mass flux increases with increasing the degree of subcooling and initial pressure in the vessel. These experimental data are compared with HEM prediction and HF model prediction (1971) as shown in Figure 3-59 (b) and (c), respectively. For experimental condition with low subcooling ($\Delta T \sim$ 4°C), HEM underestimates the data, but in general the data for critical mass flux are overestimated. The average percent different using HEM is ±196.6%. Compared to HEM, the HF model also overpredicts the experimental data but with small difference. The average percentage difference using HF model is ±10.2%.

From the above analysis, it can be seen that HF model generally overestimates G_{cr} for subcooled water jets, which is also observed in previous work. Figure 3-60 shows the comparison between HF model and the experimental data collected in Forrest et al. (1987). The critical mass flux for three different subcooling and different nozzle sizes are used. As shown in the figure, the experimental data are generally overestimated, especially in high pressure conditions. However, the nozzle size may have negligible effect on the critical mass flux, based on the experimental data.
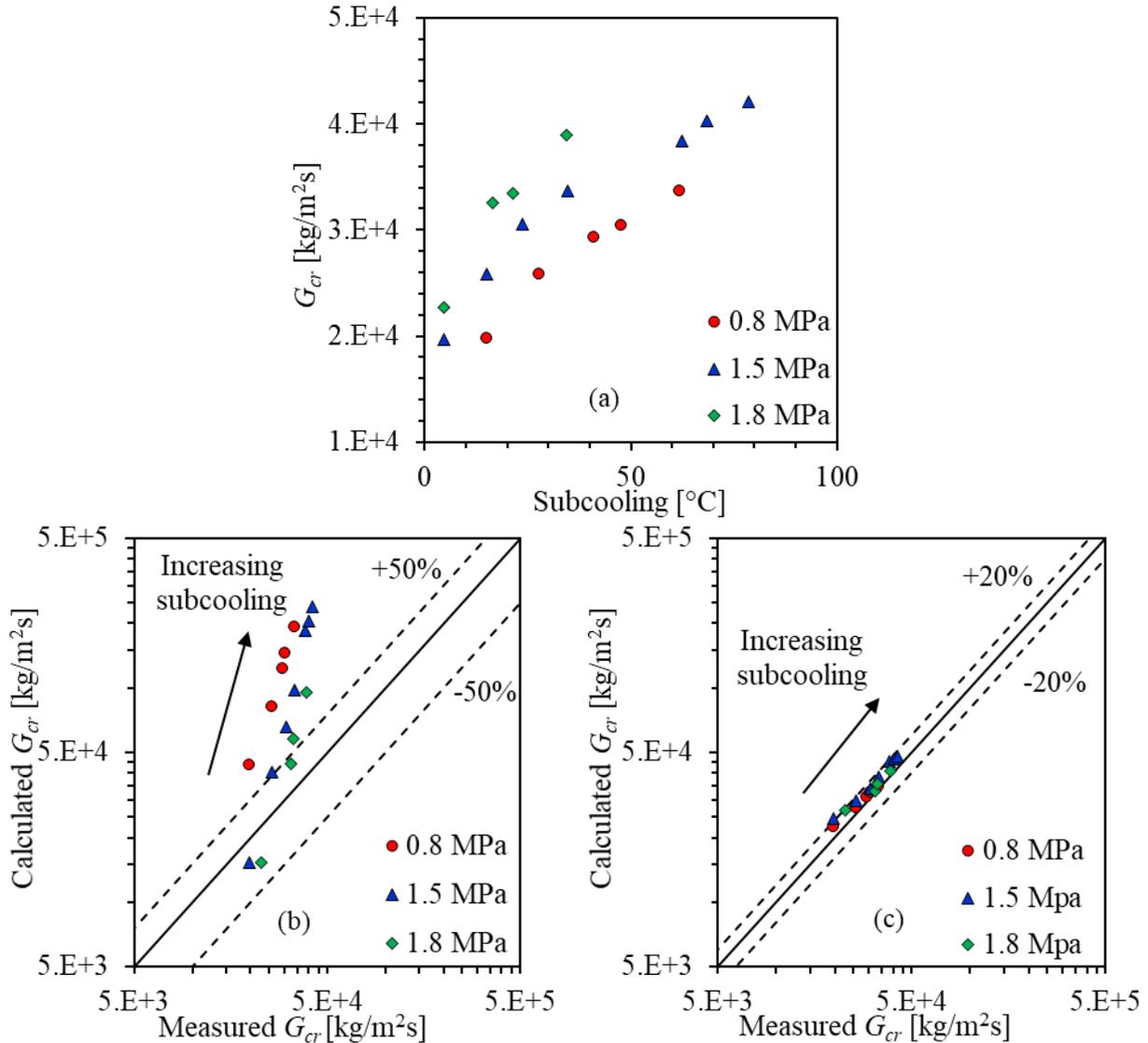
Figure 3-59 Critical Mass Flux for Subcooled Water Jets: (a) Experimental Data in Celata et al. (1986) for L_p/D = 10 in 4.6 mm Pipe, (b) Comparison between Experimental Data and HEM, and (c) Comparison between Experimental Data and Henry and Fauske Model (1971)

3.2.4.1.2 Saturated Water/Two-Phase Jets

The performance of the homogeneous models including HEM and Henry-Fauske model (1971) is compared in Figure 3-61. The comparison between calculated G_{cr} and measured G_{cr} in Marviken tests is shown in Figure 3-61 (a) and the percentage error as a function of the quality is shown in Figure 3-61 (b). As shown in the plots, the Henry-Fauske model (1971) predicts the data well in relatively high-quality region (quality > 0.01), but significantly overestimates the data in low-quality region (quality < 0.01). As explained in the last section, the Henry-Fauske model does not allow for heat and mass transfer between liquid and gas phases. The overestimation of the critical mass flux becomes more significant as the quality of the flow decreases. The HEM can generally predict the data within ±50%.

3-62
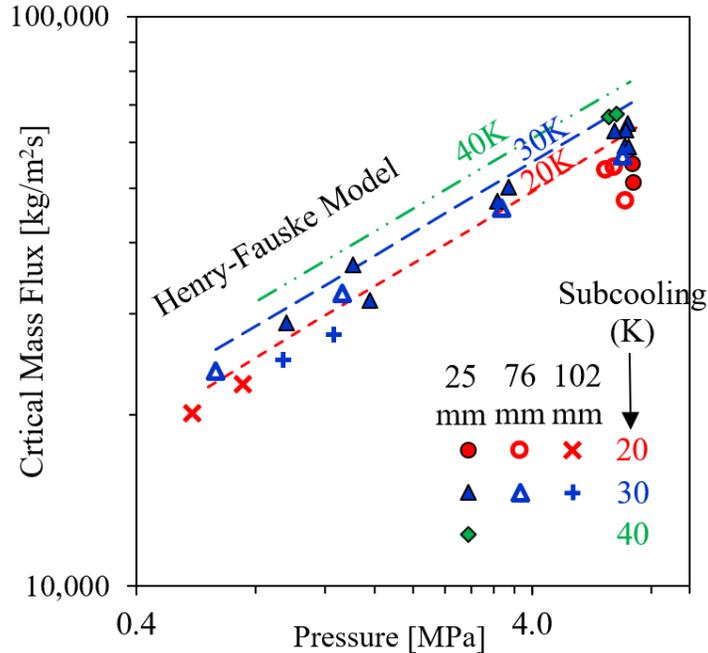
Figure 3-60 Comparison on Critical Mass Flux between Henry-Fauske (1971) and Experimental Data. Plot from Forrest et al. (1987)
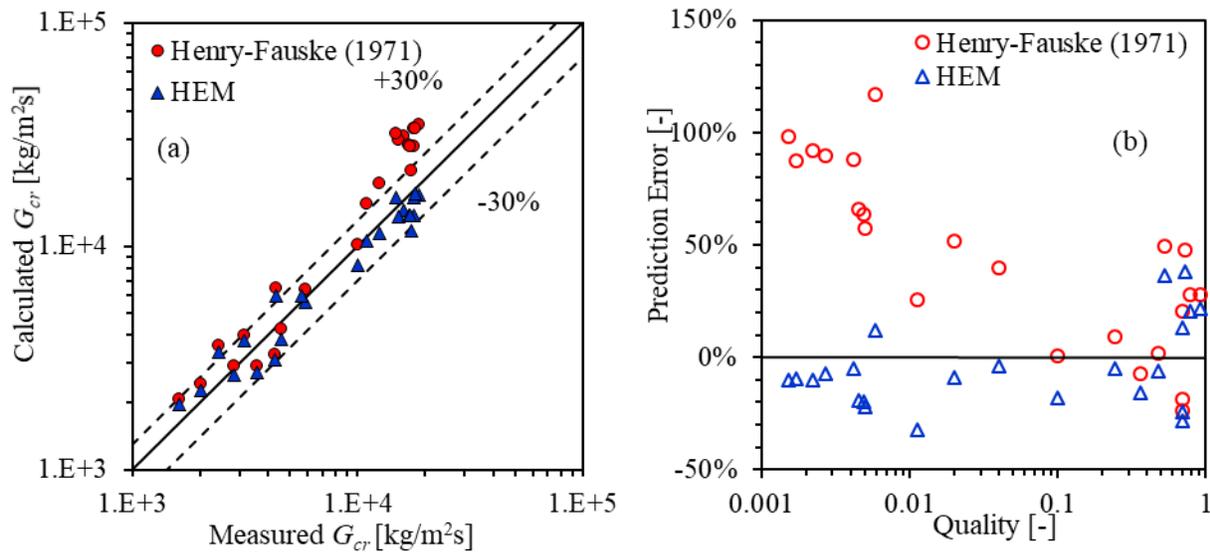
Figure 3-61 Homogeneous Models: (a) Comparison between Calculated G_{cr} and Measured G_{cr} in Marviken Tests for Saturated Water/Two-phase Jets and (b) Prediction Error as a Function of the Quality

3.2.4.1.3 Saturated Steam Jets

The performance of HEM and Isentropic Expansion for high-quality steam jets ($x \geq 0.9999$) is investigated as shown in Figure 3-62. Generally, HEM predicts similar G_{cr} with the isentropic expansion calculation. Both approaches can predict the data very well. The average percentage difference between experimental data and the predicted values are ±5.82% and ±9.52%, respectively, for Isentropic expansion and HEM.
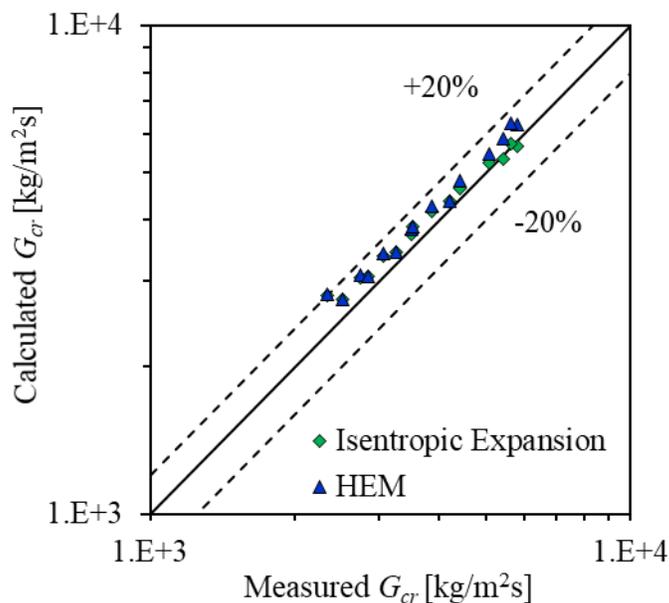
Figure 3-62 Comparison between Calculated G_{cr} and Measured G_{cr} in Marviken Tests for Jets with Inlet $x \geq 0.9999$

3.2.4.2 Summary of Model Performance

The performance of different critical mass flux models for different jet regimes is summarized as shown in Table 3-10. As shown in the table, the Henry-Fauske model (1971) works best for the subcooled-water jets with an average percentage difference of ±22.75%. The HEM works best for the saturated water/two-phase jets with an average percentage difference of ±16.90%. The Isentropic Expansion works best for saturated steam jets with an average percentage difference of ±5.82%, with HEM showing similar performance. These models with best performance are currently used in the ANSI/ANS-58.2 (1988) Standard.

Table 3-10 Summary of Selected Conditions in Marviken Tests for ANSI/ANS-58.2 (1988) Evaluation: Subcooled Water Jets

Models	Subcooled Water Jets	Saturated Water/Two-Phase Jets	Saturated Steam Jets
HEM	±25.73%	±16.90%	±9.52%
Henry-Fauske (1971)	±22.75%	±48.23%	-
Isentropic Expansion	-	-	±5.82%

3-64

3.2.4.3   *Sensitivity of G_{cr} in Jet Prediction*

As shown by the analysis in Section 3.2.4.1, the critical mass flux can be predicted with uncertainty using different models, which will propagate into jet prediction. In order to isolate this uncertainty in jet prediction, the current work uses the experimentally measured G_{cr} as an input. Figure 3-63 shows the comparison on pressure distribution within the jet between experimental data and jet code prediction. In the plots, three different values of G_{cr} are used for jet code prediction, where G_{cr}_HEM, G_{cr}_HF, and G_{cr}_exp are critical mass flux calculated by HEM, HF model and that measured in Marviken tests, respectively. As discussed in Section 3.2.4.1, G_{cr}_HEM is used in the code for further jet prediction and the results are shown in Figure 3-63 (a). Using experimental data and HF model calculated G_{cr}, the pressure can be predicted better as shown in Figure 3-63. Therefore, it can be concluded that the overprediction of G_{cr} using HEM contributes to the major uncertainty of pressure prediction in Test 3.
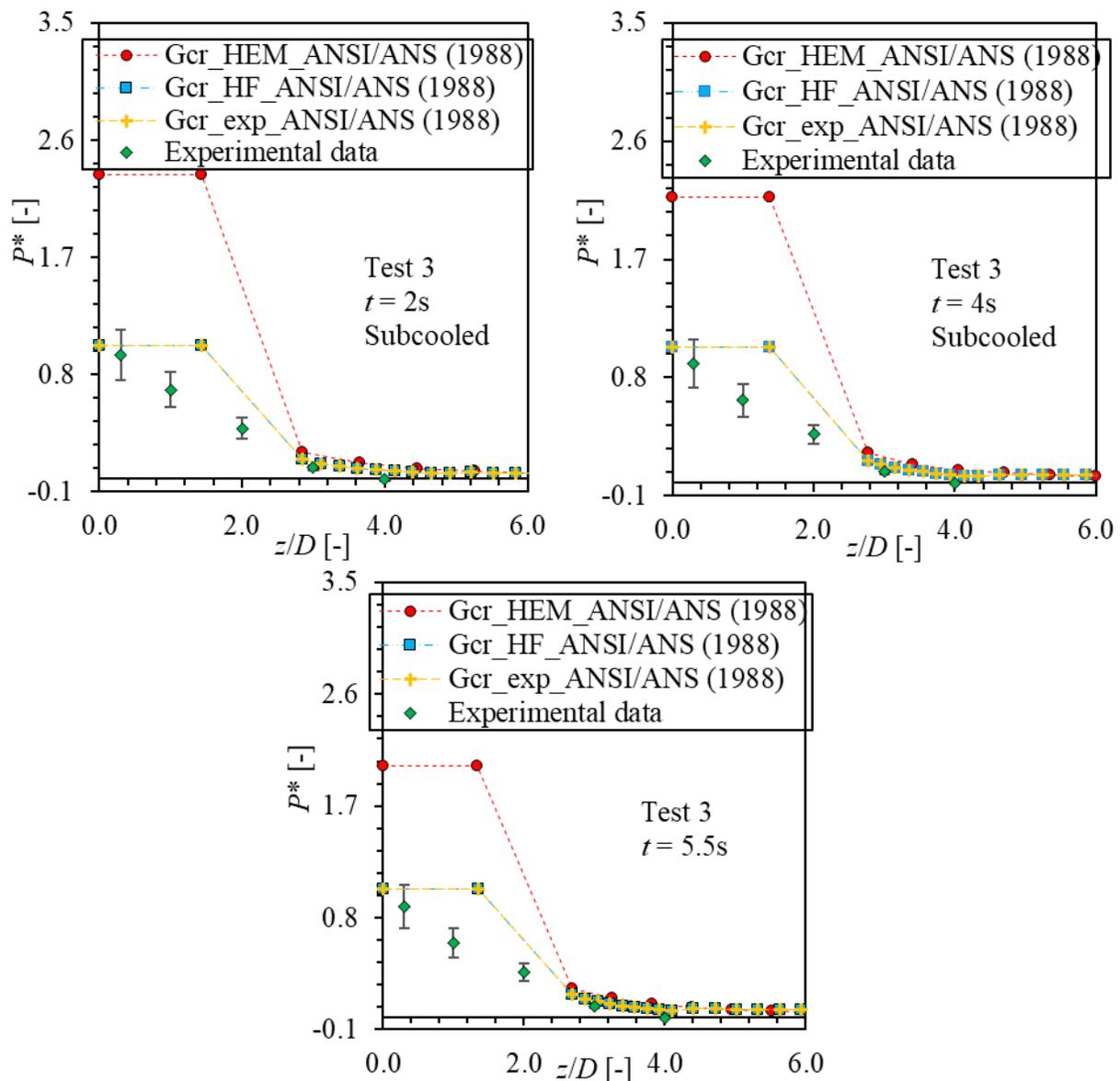
Figure 3-63 Comparison on Experimental and Predicted Pressure within the Free Jet in Marviken Test (Test 3) using Different Critical Mass Flux Values

3-65

3.2.5 Distance between Break Plane and Asymptotic Plane

In ANSI/ANS-58.2 (1988), the asymptotic plane is a plane downstream of the break plane where the static pressure of the jet drops to the ambient condition. It is an important modeling concept used in the Standard model because it separates Region 2 and Region 3, where the jet geometries are defined differently. A constant angle of 45 degree is used for the jet spreading angle in Region 2 while a constant value of 10 degree is used in Region 3. As such, the distance between the break plane and the asymptotic plane will determine the zone of influence and it is important to evaluate the distance predicted by the Standard.

To determine the position of the asymptotic plane, the Standard first calculates the asymptotic jet area:

$$\frac{A_a}{A_e} = \left(\frac{G_{cr}^2}{\rho_a C_T P_0} \right)$$
(3-26)

where A_a, A_e, G_{cr}, ρ_a, C_T, P_0 are jet area at the asymptotic plane, jet area at the break plane, critical mass flux at the break plane, mixture density at the break plane, thrust coefficient, and initial stagnation pressure in the vessel, respectively. With A_a, the distance between the asymptotic plane and the break plane (z_a) is calculated by:

$$\frac{z_a}{D} = \frac{1}{2} \left(\sqrt{\frac{A_a}{A_e}} - 1 \right)$$
(3-27)

where D is the break size. In ANSI/ANS-58.2 (1988), the jet area at any location from the break plane to the asymptotic plane is calculated from:

$$\frac{A_j}{A_e C_{Te}^*} = \left[1 + \frac{z}{z_a} \left(\frac{A_a}{A_e C_{Te}^*} - 1 \right) \right]$$
(3-28)

where A_j and z are jet area at the location of interest and distance between the break plane and location of interest, respectively. As such, Equations (3-27) and (3-28) assume a jet spreading angle of 45° between the break plane and the asymptotic plane.

It needs to be noted that Equation (3-26) to calculate the asymptotic jet area is from an EPRI report (Healzer and Singh, 1986). Since the Standard does not provide enough physical explanation and it is difficult to obtain this EPRI report, it is not clear how Equation (3-26) is derived. Wallis (2004) has the same comment and he suggested that Equation (3-26) might be obtained by manipulating the following two equations:

$$\frac{A_a}{A_e} = \frac{\rho_e u_e}{\rho_a u_a} \qquad \text{continuity equation}$$
(3-29)

$$\frac{A_a}{A_e} = \frac{\rho_e u_e^2 + p_e}{\rho_a u_a^2} \qquad \text{momentum balance}$$
(3-30)

where ρ_e, u_e, u_a, p_e are mixture density at the break plane, jet velocity at the break plane, jet velocity at the asymptotic plane and static pressure at the break plane, respectively. It is found that Equation (3-26) can be obtained by squaring Equation (3-29) and then dividing by Equation (3-30). In this derivation, the definition of the thrust coefficient is used:

$$C_T = \frac{\rho_e u_e^2 + p_e}{P_0}$$
(3-31)

Therefore, depending on which equation to use, the area ratio of A_a with respect to A_e can have different values (i.e., Equation (3-26), Equation (3-29), and Equation (3-30)).

Wallis (2004) presented a rough calculation for a condition of saturated water jet at 2000 psi. It is found that Equation (3-30) predicts the area ratio with the minimum value, while Equation (3-29) predicts that with twice the value of Equation (3-30), and Equation (3-26) predicts that with five times the value of Equation (3-30). When comparing the performance of these equations, Wallis (2004) argues that the expansion of jet from the break is two-dimensional, and the one-dimensional assumption is not valid for this problem. The velocity vector does not only have an axial component but also have a radial component. As such, Equation (3-29) which is from the continuity equation cannot be used to derive the area ratio.

In addition, Wallis (2004) pointed out that the way to calculate the mixture density in the Standard is not correct. In the Standard, the mixture density at the asymptotic plane is calculated based on assumptions that the enthalpy is constant, and the flow is brought to rest at a stagnation condition at the asymptotic plane. However, the jet flow at the asymptotic plane could still be supersonic and a stagnation condition at the asymptotic plane might not be valid. This also contributes to the uncertainty in area ratio calculation. Instead of assuming the constant enthalpy, Wallis (2004) suggested the expansion to be isentropic.

In order to evaluate the comments from Wallis (2004), the experimental data in Marviken tests (Marklund, 1985a) is employed. In this test, the static pressures at different axial locations were measured downstream of the break plane in the free jets, which provide valuable data for the current evaluation. The current report employs the static pressures obtained at the central probe. An example of the static pressure with respect to the dimensionless distance from the break plane (z/D_{eff}) is shown in Figure 3-64, where D_{eff} is the break size accounting for the size of the central probe. The ambient pressure is also shown in the plot to determine the position of the asymptotic plane.

As a result, the dimensionless distances for conditions shown in Figure 3-64 are 2.0 for the subcooled water jet in Figure 3-64 (a), 1.0 for the saturated water/two-phase jet in Figure 3-64 (b), and 1.3 for the saturated steam jet in Figure 3-64 (c), and 0.4 for the saturated steam jet in Figure 3-64 (d). The current work obtained the dimensionless distances for all the valid free jet conditions in the Marviken tests. These conditions have been investigated in Task 2 to evaluate the model prediction on pressure distribution. Complete plots to determine the position of the asymptotic plane for all the conditions investigated can be found in Appendix C.

Using the obtained experimental data, the values predicted by the ANSI/ANS-58.2 (1988) are evaluated. The comparison between the model prediction and the experimental values is shown in Figure 3-65. As shown in the plot, the dimensionless distance is generally overpredicted by the ANSI/ANS-58.2 (1988), except for the conditions of steam jets. The dotted line in the figure indicates an overestimation of 100% for subcooled water and saturated water/two-phase jets.

As such, the zone of influence of these jets is overestimated using the Standard model. This corresponds to an overestimation of area ratio with a factor of 4, which generally agrees with the analysis by Wallis (2004). In addition, this may indicate that Equation (3-30) can predict the distance with a higher accuracy.
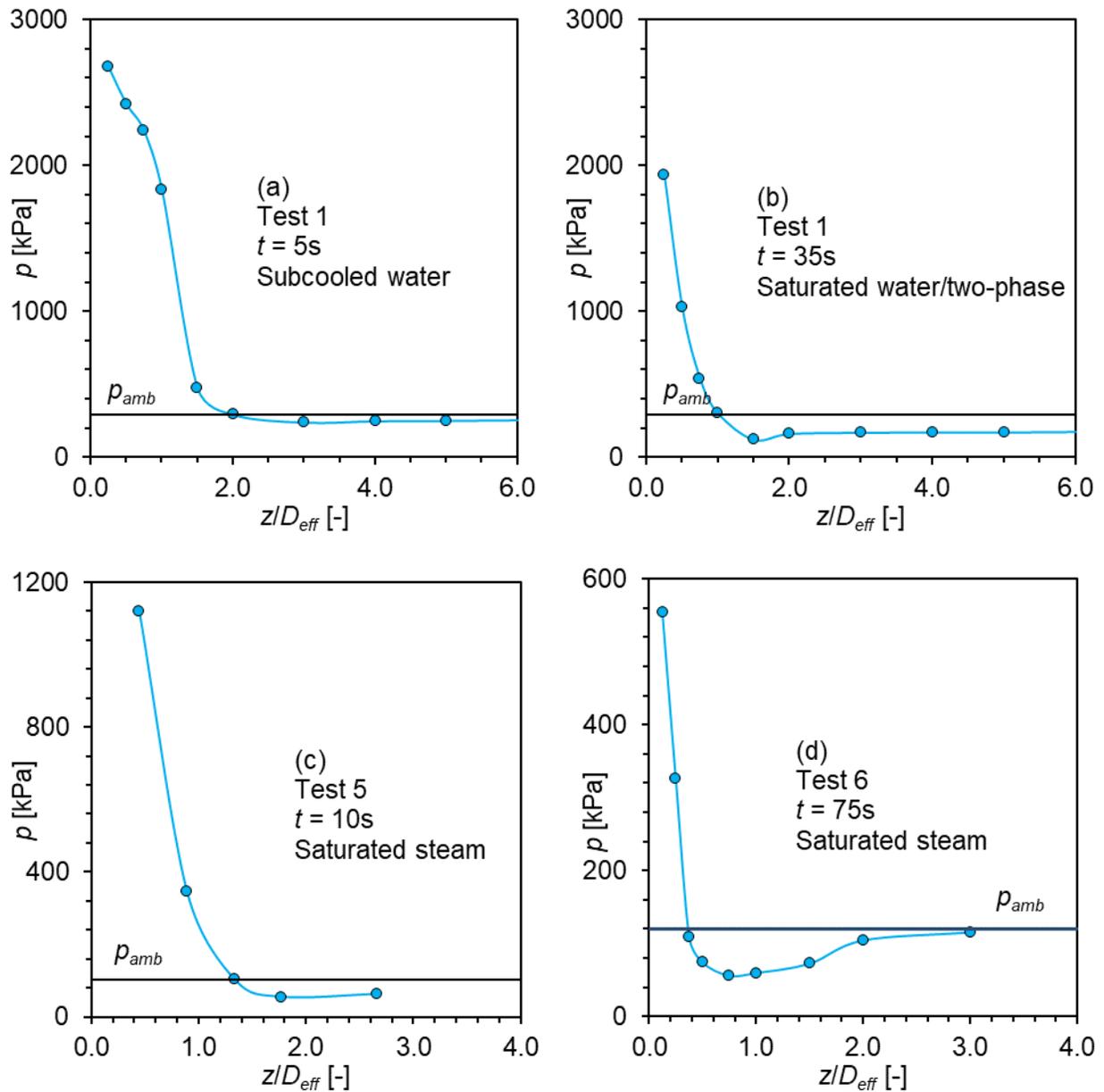
Figure 3-64 Static Pressure along the Axial Direction of Jet Downstream of the Break Plane: (a) Subcooled Water Jet, (b) Saturated Water/Two-phase Jet, (c) and (d) Saturated Steam Jets
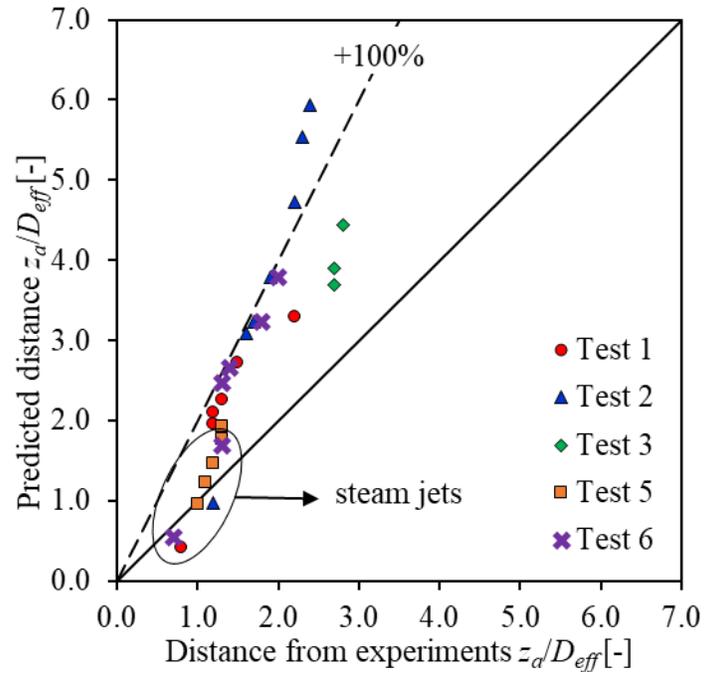
Figure 3-65 Comparison on Dimensionless Distance of the Asymptotic Plane between the Prediction by ANSI/ANS-58.2 (1988) and the Experimental Data from Marviken Tests (Marklund, 1985a)

4 MODEL IMPROVEMENT AND GUIDANCE DEVELOPMENT

Based on the literature review of jet impingement and model evaluation, the Standard model is revised and model guidance is developed in the current chapter to address the potential non-conservatisms as addressed in the Standard Review Plan (2015), which includes (a) blast wave effect, (b) jet plume expansion and zone of influence, (c) distribution of pressure within the jet plume, and (d) jet dynamic loading.

4.1 Model Improvement

4.1.1 Model Revision

Based on the model evaluation results in Chapter 3, the following discussion is provided for potential revision of the Standard model. These recommendations are made based on the existing experimental data in literature. Additional improvements might be needed when more comprehensive and systematic data are available in the future.

4.1.1.1 Jet Core Length

As demonstrated in Section 3.2.2, the jet core length can be under-estimated by the Standard (Equqation (C-1) in Appendix C) for conditions with high degrees of subcooling in small-scale break jets. The current work proposes a new correlation using the experimental data obtained in Celata et al. (1986) ,where jet core length was investigated for subcooled water jets (0.8 MPa < P_0 < 2.5 MPa; 0°C < ΔT < 110 °C) in a pipe size of 4.6 mm. The effect of friction on jet core length was also studied with three different frictional lengths: L_p/D_e = 10, 100, and 300. It was found that increasing the degree of subcooling increases the jet core length, which increasing the friction decreases the jet core length. For model development, the experimental data with minimum friction effect are used, considering that friction decreases the jet core length. As a result, the following correlation is suggested to predict the jet core length:

$$\frac{z_c}{D} = \begin{cases} 0.26\sqrt{1.8\Delta T} + 0.5 & for & 0 \le \Delta T \le 30°C \\ 0.062\Delta T + 0.5 & for & \Delta T > 30°C \end{cases}$$

(4-1)

where ΔT is the degree of subcooling at the break plane with a unit of °C. Therefore, for conditions with low degree of subcooling, the correlation uses the Standard model. While for conditions with high degree of subcooling, a linear relation is used. The comparison between Equation (4-1) and experimental data as well as other models are shown in Figure 4-1.
It needs to be noted that the jet core length predicted by Equation (4-1) cannot be larger than the asymptotic plane distance. In addition, Equation (4-1) is developed based on experimental data with friction effect in a small range of test conditions. A more comprehensive and systematic database is needed in the future.

4.1.1.2 Pressure Distribution

From the evaluation results in Section 3.2.1, the pressure can be predicted well for saturated steam jets except for edge-peaking profiles at far distances ($z > 3.3D$). However, the dimensionless stagnation pressures at these distances are below 0.07. Therefore, revision is not suggested for the pressure prediction of saturated steam jets.
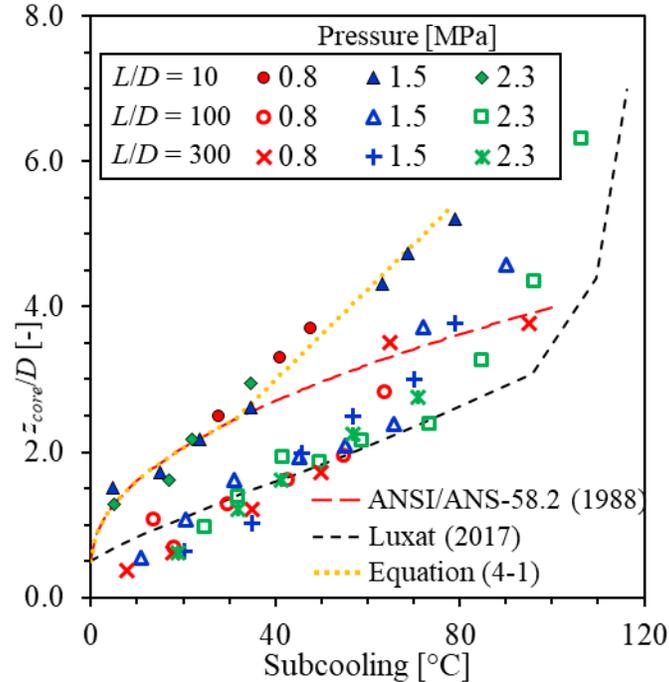
Figure 4-1 Comparison on Jet Core Length Modeling: New Correlation, ANSI/ANS-58.2 (1988), Luxat (2017) and Experimental Data in Celata et al. (1986)

For saturated water/two-phase jets, the pressure can be under-predicted by -20% ~ -60% in small-break jets ($D \le 0.15$ m). As such, the following equation is developed to calculate the pressure at the center of jets:

$$P_c^* = 1.70 \exp\left(-1.06\frac{z}{D}\right) \quad z \ge z_c \text{ for } D \le 0.15 \text{ m}, 0.0001 < x < 0.9999 \tag{4-2}$$

where z_c is the jet core length, and P_c^* is the dimensionless pressure at jets center:

$$P_c^* = \frac{P_c - p_{amb}}{P_0 - p_{amb}} \tag{4-3}$$

where P_c is the pressure at jets center on the target, p_{amb} is the ambient pressure, and P_0 is the initial stagnation pressure prior to break.

As shown in Figure 4-2, Equation (4-2) can predict the pressure the center of jets well for both free and impinging jets. It is recommended to replace Equations (D-11) and (D-13) in the Appendix D of the Standard model for saturated water/two-phase jets.

4-2
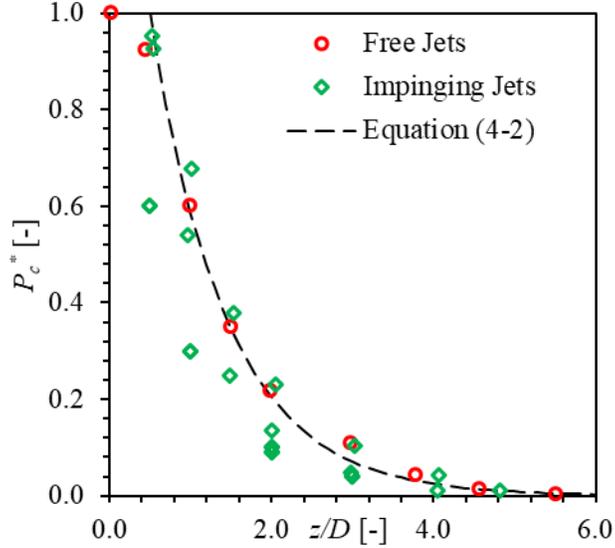
Figure 4-2 Comparison on Pressure Distribution along the Center of Jets between the New Correlation and Experimental Data for Saturated Water/Two-phase Jets

For subcooled water jets, the pressure can be under-predicted by -90% in small-break jets ($D \sim$ 0.005 m). Meanwhile, the pressure is strongly dependent on the degree of subcooling and jet type (i.e., free or impinging) based on the experimental data in Kawanishi et al. (1986) as shown in Figure 4-3. Considering that the break size is relatively small ($D \sim$ 0.005 m), the impinging force and zone of influence will not be significantly large even if the pressure is over-estimated. The current work chooses to use the experimental data with the largest degree of subcooling ($\Delta T \sim 80°C$) to develop correlations. As discussed in Section 4.1.1.1, the jet core length is about 5.5 for a subcooled water jet with $\Delta T \sim 80°C$. By excluding the pressure data within jet core, the fitting curve is obtained as:

$$P_c^* = 0.0069\left(\frac{z}{D}\right)^2 - 0.25\left(\frac{z}{D}\right) + 2.24 \quad z \geq z_c \text{ for } D \leq 0.005 \text{ m} \tag{4-4}$$

After implementing Equation (4-4) to revise the Standard model, discontinuities are observed for some conditions. This is because Equation (4-4) is developed for the condition with the highest degree of subcooling. It can predict higher pressure than the pressure in the jet core for the condition with relatively low degree of subcooling. However, this is not physically correct. Therefore, the following equation is used:

$$P_c^* = \min\left(\frac{F_j}{A_{je}}, 0.0069\left(\frac{z}{D}\right)^2 - 0.25\left(\frac{z}{D}\right) + 2.24\right) \quad z \geq z_c \text{ for } D \leq 0.005 \text{ m} \tag{4-5}$$

with

$$F_j = \max\left(\frac{G_e^2 A_e}{\rho_e g_c} + A_e\left(P_e - P_{amb}\right), A_e\left(C_T P_0 - P_{amb}\right)\right) \tag{4-6}$$

and

4-3

$$A_{je} = C_T A_e \qquad\qquad (4\text{-}7)$$

As shown in Figure 4-3, all the pressure data can be predicted conservatively using Equation (4-4).
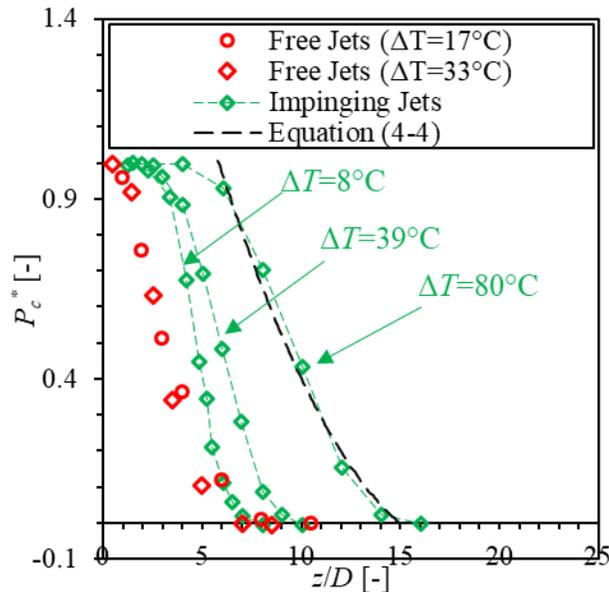
Figure 4-3 Comparison on Pressure Distribution along the Center of Jets between the New Correlation and Experimental Data for Subcooled Water Jets

Based on the above discussion, the proposed recommendations for potential model revision are summarized in Table 4-1. It needs to be noted that the current revision suggestions are made based on the existing experimental data in literature and current model evaluations results. A comprehensive and systematic experimental database is needed to further improve the Standard model in the future.

Table 4-1 Recommendations for Potential Model Revision

Parameters	Jet regimes	Saturated steam ($x \geq 0.7$, $\Delta T = 0$)		Saturated water/two-phase ($0.0001 \leq x < 0.7$, $\Delta T = 0$)		Subcooled water ($\Delta T > 0$)	
	Jet types	Free	Impinging	Free	Impinging	Free	Impinging
Jet core length		ANSI/ANS-58.2 (1988)		ANSI/ANS-58.2 (1988)		**Equation (4-1)**	
Pressure distribution	Region 1	ANSI/ANS-58.2 (1988)		ANSI/ANS-58.2 (1988)		ANSI/ANS-58.2 (1988)	
	Regions 2 and 3 ($z > z_c$)	ANSI/ANS-58.2 (1988)		Large-break ($D > 0.15$ m): ANSI/ANS-58.2 (1988) Small-break ($D \leq 0.15$ m): **Equation (4-2)**		Non small-break ($D > 0.005$ m): ANSI/ANS-58.2 (1988) Small-break ($D \leq 0.005$ m): **Equation (4-5)**	

4.1.2 Evaluation of Revised Model

The U.S. NRC revised the jet code based on the recommendations in Section 4.1.1. In this section, the revised code is evaluated using the experimental data. The conditions for jet impingement with small diameter breaks are investigated since the code revision only affects small diameter jets. In the following comparisons, the predictions of ANSI/ANS-58.2 (1988) are made by the original code jet11p4, and those of Rev ANSY/ANS-58.2 (1988) are made by the revised code jetrev12p0.

4.1.2.1 Saturated Water/Two-Phase Jets

The experimental data in Mitsubishi tests (Kawanishi et al., 1986), JAERI tests (Yano et al., 1984), and KWU tests (Kastner and Rippel, 1987) are used for model evaluation. In Kawanishi et al. (1986), only the stagnation pressure at the center of the jets was measured for three conditions with an initial stagnation pressure of 4.0 MPa and a break size of 5 mm. In Yano et al. (1984), the stagnation pressure for saturated water jets at the targets were measured at two different axial locations of 2 D and 5 D. Two initial stagnation pressure of 6.8 MPa and 5.6 MPa were investigated with a break size of 150 mm. In Kastner and Rippel (1987), the stagnation pressure for saturated water jets at targets was measured at four different axial locations of 0.5 D, 1D, 2 D, and 3 D. An initial stagnation pressure of 10 MPa was investigated with a break size of 65 mm. In evaluating the code using saturated-water data, the quality is set slightly above 0.0001 (i.e., 0.000101) to activate Equation (4-2). The comparisons between revised code and original code as well as experimental data are shown in Figure 4-4 through Figure 4-6. As shown in the comparison in Figure 4-4, the revised code can predict the experimental data well, while the original code underestimates the data downstream of the Region 1. As shown in the comparison in Figure 4-5 and Figure 4-6, the revised code can predict the experimental data conservatively, while the original code significantly underestimates the stagnation pressure at the central region of the jets.

4.1.2.2 Subcooled Water Jets

The evaluation results using the experimental data in Kawanishi et al. (1986) are shown in Figure 4-7 and Figure 4-8 for free jets and impinging jets, respectively. Only the stagnation pressure for subcooled water jets at the center of the jets was measured for five conditions. An initial stagnation pressure of 4.0 MPa was investigated with a break size of 5 mm, two conditions for free jets and three conditions for impinging jets. As shown in the comparison, the revised code predicts conservatively for all the conditions investigated. Meanwhile, the revised code still predicts significantly high pressure in the Region 1 particularly for conditions with high degree of subcooling. As discussed in a previous section, this is because the critical mass flux is significantly overpredicted.
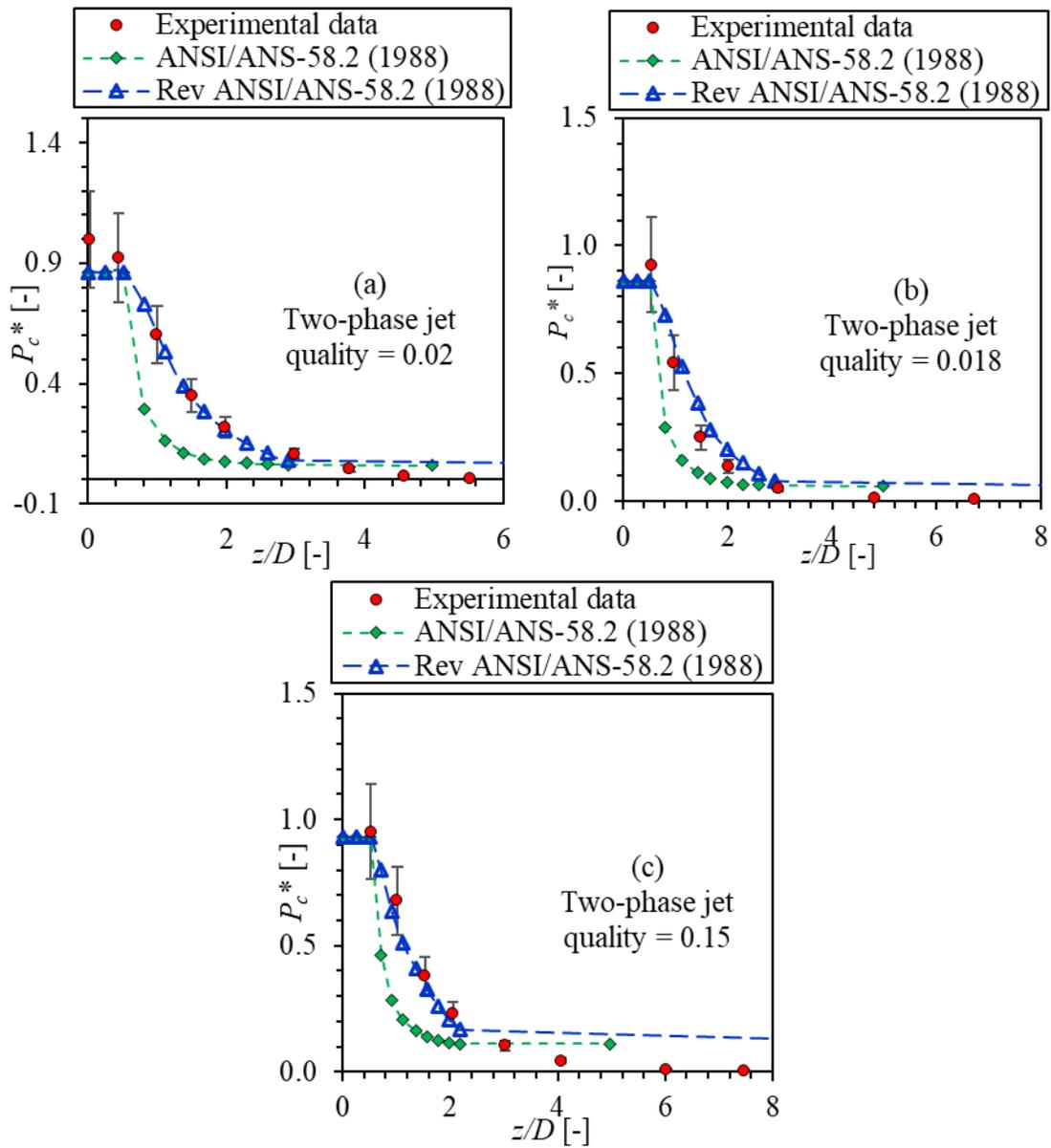
Figure 4-4 Stagnation Pressure at the Center of Two-phase Jets. Comparison between the Original Code (ANSI/ANS-58.2, 1988), Revised Code (Rev ANSI/ANS-58.2, 1988), and Experimental Data: (a) Free Jet, (b) and (c) Impinging Jet in Kawanishi et al. (1986) of Mitsubishi Tests. Error Bar: ±20%
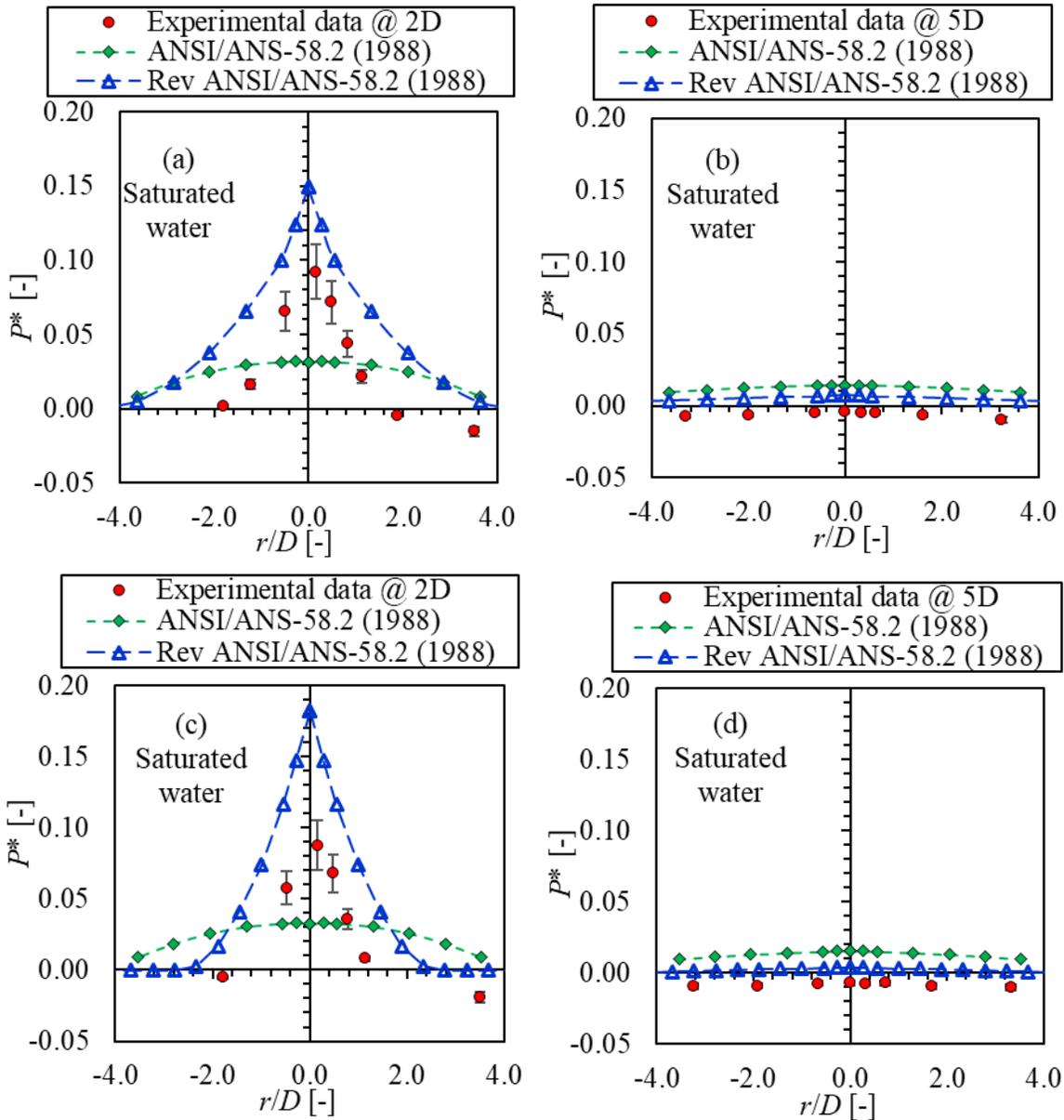
Figure 4-5 Stagnation Pressure at the Center of Targets for Saturated Water Impinging Jets. Comparison between the Original Code (ANSI/ANS-58.2, 1988), Revised Code (Rev ANSI/ANS-58.2, 1988), and Experimental Data in Yano et al. (1984) of JAERI Tests. Error Bar: ±20%
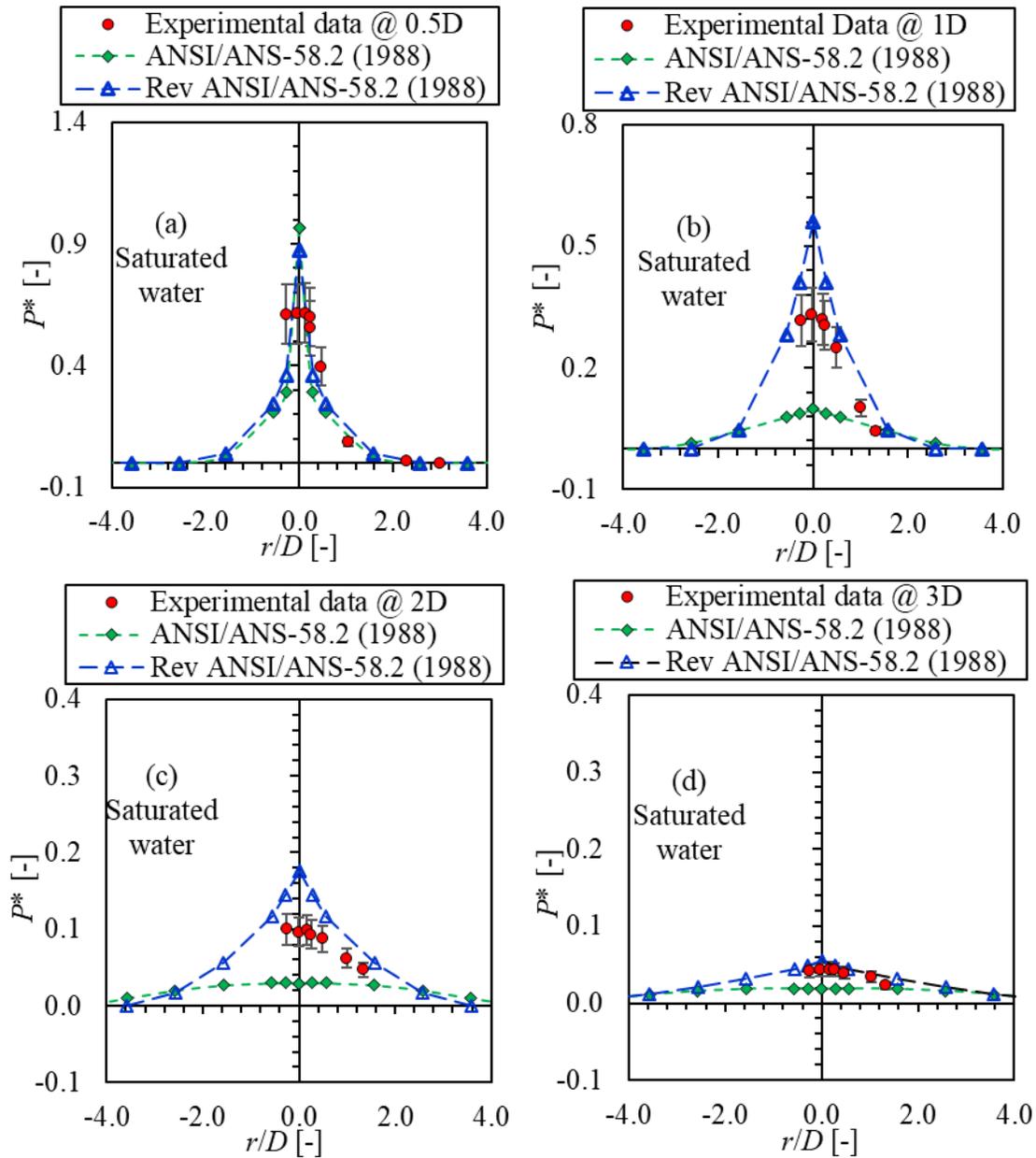
Figure 4-6 Stagnation Pressure at the Center of Targets for Saturated Water Impinging Jets. Comparison between the Original Code (ANSI/ANS-58.2, 1988), Revised Code (Rev ANSI/ANS-58.2, 1988), and Experimental Data in Kastner and Rippel (1987) of KWU Tests. Error Bar: ±20%
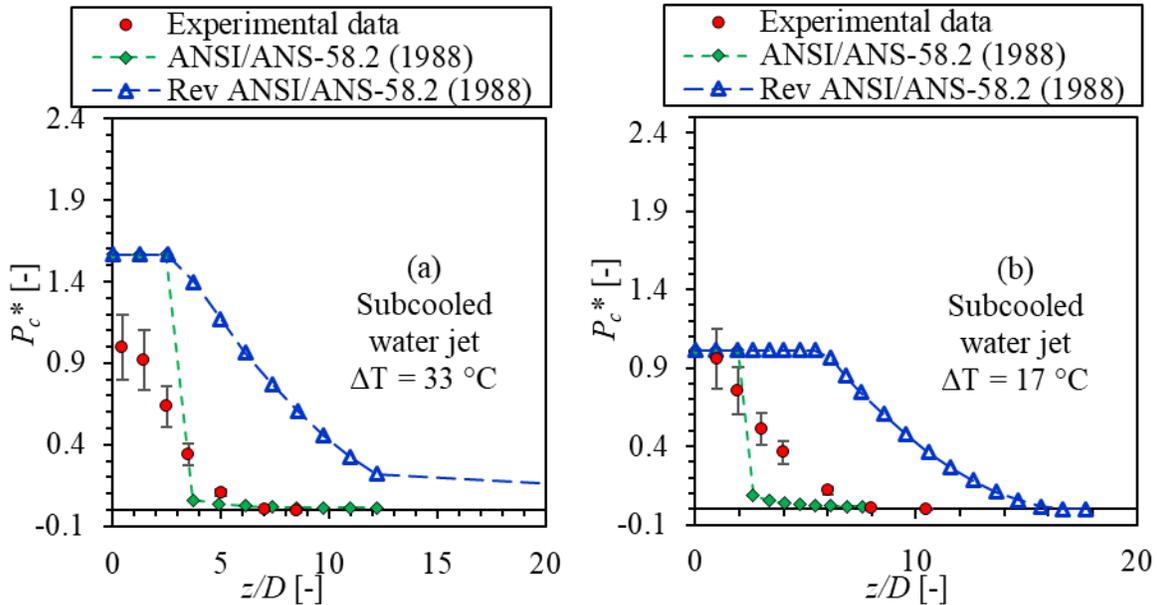
Figure 4-7 Stagnation Pressure at the Center of Subcooled Water Free Jets. Comparison between the Original Code (ANSI/ANS-58.2, 1988), Revised Code (Rev ANSI/ANS-58.2, 1988), and Experimental Data in Kawanishi et al. (1986) of Mitsubishi Tests. Error Bar: ±20%

4.1.3   Summary of Recommended Models

A systematic evaluation of the Standard model (ANSI/ANS-58.2, 1988) in this chapter. Based on the model evaluation results, the performance of various models is summarized for different jet types and regimes. Important jet impingement parameters investigated include jet core length, thrust coefficient, critical mass flux, and pressure distribution within jets. Different jet types including free and impinging jets, and different jet regimes including subcooled water jets, saturated water/two-phase jets, and saturated steam jets are considered. The model performance is summarized here and presented in Table 4-2.

For small break jets (D ~ 0.005 m), the model in ANSI/ANS-58.2 (1988) predicts the jet core length well for conditions with relatively low degree of subcooling ($0 < \Delta T < 30°C$). For conditions with higher degree of subcooling, the Standard underestimates the jet core length. However, the Standard model can predict the jet core length well based on the dimensionless stagnation pressure prediction in large break jets. For saturated wate/two-phas jets and saturated steam jets, the Standard model can predict the jet core length well.

For the thrust coefficient, it can be predicted well using various models for different jet regimes, which are currently recommended and employed in the Standard (ANSI/ANS-58.2, 1988).

For critical mass flux prediction, the Homogeneous Equilibrium Model (HEM) can be used for saturated water/two-phase jets, while Henry and Fauske model (1971) is recommended for subcooled water jets. The Isentropic Expansion model predicts the critical mass flux for saturated steam jets with the best performance, while the HEM can also predict the data well for saturated steam jets. The best performance models for different jet regimes are currently recommended in the Standard.

Table 4-2 Recommended Models and Their Performance for Different Jet Types and Regimes

Parameters		Saturated steam (x ≥ 0.7, ΔT = 0)		Saturated water/Two-phase (0 ≤ x < 0.7, ΔT = 0)		Subcooled water (ΔT > 0)	
Jet types		Free	Impinging	Free	Impinging	Free	Impinging
Jet core length		ANSI/ANS-58.2 (1988)		ANSI/ANS-58.2 (1988)		Large-break (D > 0.28 m)[a]: ANSI/ANS-58.2 (1988); Small-break (D ~ 0.005 m)[b]: Equation (4-1)	
Thrust coefficient		Maximum C_T = 1.26 Webb (1976)[c]; Shapiro (1965)[c]		C_T ~ 1.2 Lahey and Moody (1977)[c]		1.2 ≤ C_T ≤ 2.0 Webb (1976)[c]	
Critical mass flux		For x > 0.9999 Isentropic expansion[c] (±5.82%)[a]; Homogeneous Equilibrium Model (HEM) (±9.52%)[a]		For 0 ≤ x < 0.9999 Homogeneous Equilibrium Model (HEM)[c] (±16.9%)[a]		Henry and Fauske (1971)[c] (±22.75%)[a]	
Pressure at jet center		ANSI/ANS-58.2 (1988)		Large-break (D > 0.28 m): ANSI/ANS-58.2 (1988) Small-break (D < 0.15 m): Equation (4-2)		Large-break (D > 0.28 m): ANSI/ANS-58.2 (1988) Small-break (D ~ 0.005 m): Equation (4-5)	
Pressure (P^*) preduction by ANSI/ANS-58.2 (1988)	Zone 1	-5% ~ +20%		±20%		+20% ~ +200% (ΔT = 40°C) or +700% (ΔT = 80°C)	
	Zone 2	Large-break (D > 0.28 m): P_{model}* = 0 ~ 0.4, while P_{exp}* ~ 0; Small-break (D < 0.01 m): <-20% for 0.5 < z* < 3;		Large-break (D > 0.28 m): P_{model}* = 0 ~ 0.4, while P_{exp}* ~ 0; Small-break (D < 0.15 m): -20% ~ -60 %		Large-break (D > 0.28 m): P_{model}* ~ 0.1, while P_{exp}* ~ 0; Small-break (D ~ 0.005 m): -90%	
	Zone 3	> -20% for z* > 3, however P_{exp}* < 0.07					
Position of the asymptotic plane		ANSI/ANS-58.2 (1988) with an overestimation of 100%					

[a]: Based on the experimental data in Marviken tests (Marklund, 1985a);
[b]: Based on the experimental data in Celata et al. (1986);
[c]: Models recommended and employed in ANSI/ANS-58.2 (1988);
[d]: Correlations developed in Section 3.1.2.

For pressure at the jet center, it is found that the power law can generally provide a good prediction for both free and impinging jets, while the exponential function can also be used for impinging jets in addition to the power law. The Standard model (ANSI/ANS-58.2, 1988) can predict the pressure distribution well for saturated steam jets except for those at far distances ($z > 3.3\,D$). However, the dimensionless stagnation pressures at these distances are below 0.07. For saturated water/two-phase jets, the Standard model can predict the stagnation pressure well for the large-scale tests ($D > 0.28$ m), but underestimates those in the medium-scale and small-scale tests ($D < 0.15$ m).

For the position of the asymptotic plane, the evaluation results have demonstrated that the current model in Standard can predict the distance well for saturated steam jets. For saturated water/two-phase and subcooled water jets, the current model in Standard generally predicts the distance with an overestimation of 100%. As such, the zone of influence of these jets is overestimated using the Standard model. Despite this, the non-dimensional stagnation pressure is predicted conservatively in Region 3 as demonstrated by the current model evaluation. Table 4-3 provides a quick look-up table to summarize the conditions investigated in the current work, which will help readers to find conditions similar to their applications.

4.2   Guidance Development

4.2.1   Potential Blast Wave Effect

A blast wave is generated when a large amount of energy is released rapidly into an environment. The source of the energy release may come from chemical reaction such as TNT explosion, or physical explosions such as steam explosion. The sudden energy release can produce very high temperature and pressure gases, which moves outward supersonically and creates a blast wave (or shock wave) in the surrounding medium. A blast wave in air is termed "airblast" and it attenuates with distance from the source (Cullis, 2001; Weggel, 2010).

In the event of jet impingement in high-energy piping systems, the Advisory Committee on Reactor Safeguards (ACRS) suggested that there is a potential possibility for blast wave to occur (Standard Review Plan, 2015). As such, the surrounding Structures, Systems, and Components (SSCs) could be damaged. In the event of a high-pressure pipe rupture, the first significant fluid load on surrounding SSCs might be induced by a blast wave. In the current report, the manuscript of the ACRS subcommittee on thermal-hydraulics meeting in 2004 is first reviewed. The transient pressure profiles obtained in the Marviken tests (Marklund, 1985a) are studied for potential blast wave effect. Finally, the preliminary modeling guidance for the blast wave effect is developed.

Table 4-3 Summary of Evaluated Conditions

Figure	Regime	Stagnation Pressure	Quality or Subcooling	Break Diameter	Plotted Value	Position
Figure 3-33	Steam	4.4 MPa	$x = 0.97$	0.28 m	Stagnation Pressure	Jet Centerline
Figure 3-33	Steam	1.3 MPa	$x = 0.7$	0.5 m	Stagnation Pressure	Jet Centerline
Figure 3-34	Steam	1.9 MPa	$x = 0.97$	0.28 m	Stagnation Pressure	$z/D = 3.6$
Figure 3-34	Steam	2.4 MPa	$x = 0.79$	0.28 m	Stagnation Pressure	$z/D = 1.8$
Figure 3-35	Steam	1.7 Mpa	$x = 0.7$	0.5 m	Stagnation Pressure	$z/D = 4.1$
Figure 3-35	Steam	4.5 Mpa	$x = 1.0$	0.3 m	Stagnation Pressure	$z/D = 2.2$
Figure 3-36	Steam	4.0 Mpa	$x = 1.0$	0.0094 m	Stagnation Pressure	$z/D = 0.59$, 0.96, 1.5, 2.3, 3.3, 4.5, 6.6
Figure 3-37	Steam	4.0 Mpa	$x = 1.0$	0.005 m	Stagnation Pressure	$z/D = 0.6$, 3.3, 4.3, 13, 37.5
Figure 3-38	Steam	4.0 Mpa	$x = 1.0$	0.005 m	Stagnation Pressure	$z/D = 0.5$, 3.3, 6.3, 13, 30, 52.5, 62.5
Figure 3-39	Steam	4.0 Mpa	$x = 1.0$	0.005 m	Stagnation Pressure	Jet Centerline
Figure 3-40	Saturated	3.0 MPa	$x = 0.0045$	0.5 m	Stagnation Pressure	Jet Centerline
Figure 3-41	Saturated	3.9 MPa	$x = 0.0017$	0.28 m	Stagnation Pressure	$z/D = 1.9$
Figure 3-41	Saturated	3.0 MPa	$x = 0.0045$	0.28 m	Stagnation Pressure	$z/D = 1.0$
Figure 3-42	Saturated	3.0 MPa	$x = 0.005$	0.5 m	Stagnation Pressure	$z/D = 4.1$
Figure 3-42	Saturated	3.0 MPa	$x = 0.005$	0.5 m	Stagnation Pressure	$z/D = 2.1$
Figure 3-42	Two-phase	2.2 MPa	$x = 0.24$	0.5 m	Stagnation Pressure	$z/D = 3.0$
Figure 3-43	Two-phase	2.5 MPa	$x = 0.011$	0.5 m	Stagnation Pressure	$z/D = 1.27$
Figure 4-4	Two-phase	4.0 MPa	$x = 0.02$, 0.018, 0.15	0.005 m	Stagnation Pressure	Jet Centerline
Figure 4-5	Saturated	6.8 MPa 5.6 MPa	$x = 0$	0.15 m	Stagnation Pressure	$z/D = 2, 5$
Figure 4-6	Saturated	10 MPa	$x = 0$	0.065 m	Stagnation Pressure	$z/D = 0.5, 1, 2, 3$
Figure 3-47	Subcooled	4.6 MPa	$\Delta T = 45.4$ °C	0.5 m	Stagnation Pressure	Jet Centerline
Figure 3-47	Subcooled	4.0 MPa	$\Delta T = 16$ °C	0.5 m	Stagnation Pressure	Jet Centerline
Figure 3-48	Subcooled	4.3 MPa	$\Delta T = 19.2$ °C	0.5 m	Stagnation Pressure	$z/D = 4.1$
Figure 3-48	Subcooled	4.3 MPa	$\Delta T = 24.2$ °C	0.5 m	Stagnation Pressure	$z/D = 3.0$
Figure 3-49	Subcooled	4.3 MPa	$\Delta T = 23.6$ °C	0.5 m	Stagnation Pressure	$z/D = 2.1$

Table 4-3 Summary of Evaluated Conditions (cont.)

Figure	Regime	Stagnation Pressure	Quality or Subcooling	Break Diameter	Plotted Value	Position
Figure 3-49	Subcooled	4.3 MPa	$\Delta T = 22.9$ °C	0.5 m	Stagnation Pressure	$z/D = 1.27$
Figure 4-7	Subcooled	4.0 MPa	$\Delta T = 33$ °C	0.005 m	Stagnation Pressure	Jet Centerline
Figure 4-7	Subcooled	4.0 MPa	$\Delta T = 17$ °C	0.005 m	Stagnation Pressure	Jet Centerline
Figure 4-8	Subcooled	4.0 MPa	$\Delta T = 80$ °C	0.005 m	Stagnation Pressure	Jet Centerline
Figure 4-8	Subcooled	4.0 MPa	$\Delta T = 39$ °C	0.005 m	Stagnation Pressure	Jet Centerline
Figure 4-8	Subcooled	4.0 MPa	$\Delta T = 8.6$ °C	0.005 m	Stagnation Pressure	Jet Centerline
Figure 3-56	All	2.05 Mpa	-	0.005 m	Thrust Coefficient	-
Figure 3-58	Subcooled	3.2 ~ 4.6 MPa	$\Delta T = 1.4$ ~ 45.4 °C	0.28 ~ 0.5 m	Critical Mass Flux	Break Plane
Figure 3-59	Subcooled	0.8, 1.5, 1.8	-	0.0046 m	Critical Mass Flux	Break Plane
Figure 3-60	Subcooled	-	$\Delta T = 20, 30, 40$ °C	0.0025, 0.076, 0.102 m	Critical Mass Flux	Break Plane
Figure 3-61	Saturated/ Two-phase	1.3 ~ 3.9 MPa	$x = 0.005$ ~ 0.48	0.28 ~ 0.5 m	Critical Mass Flux	Break Plane
Figure 3-62	Steam	1.3 ~ 4.4 MPa	$x > 0.7$	0.28 ~ 0.5 m	Critical Mass Flux	Break Plane
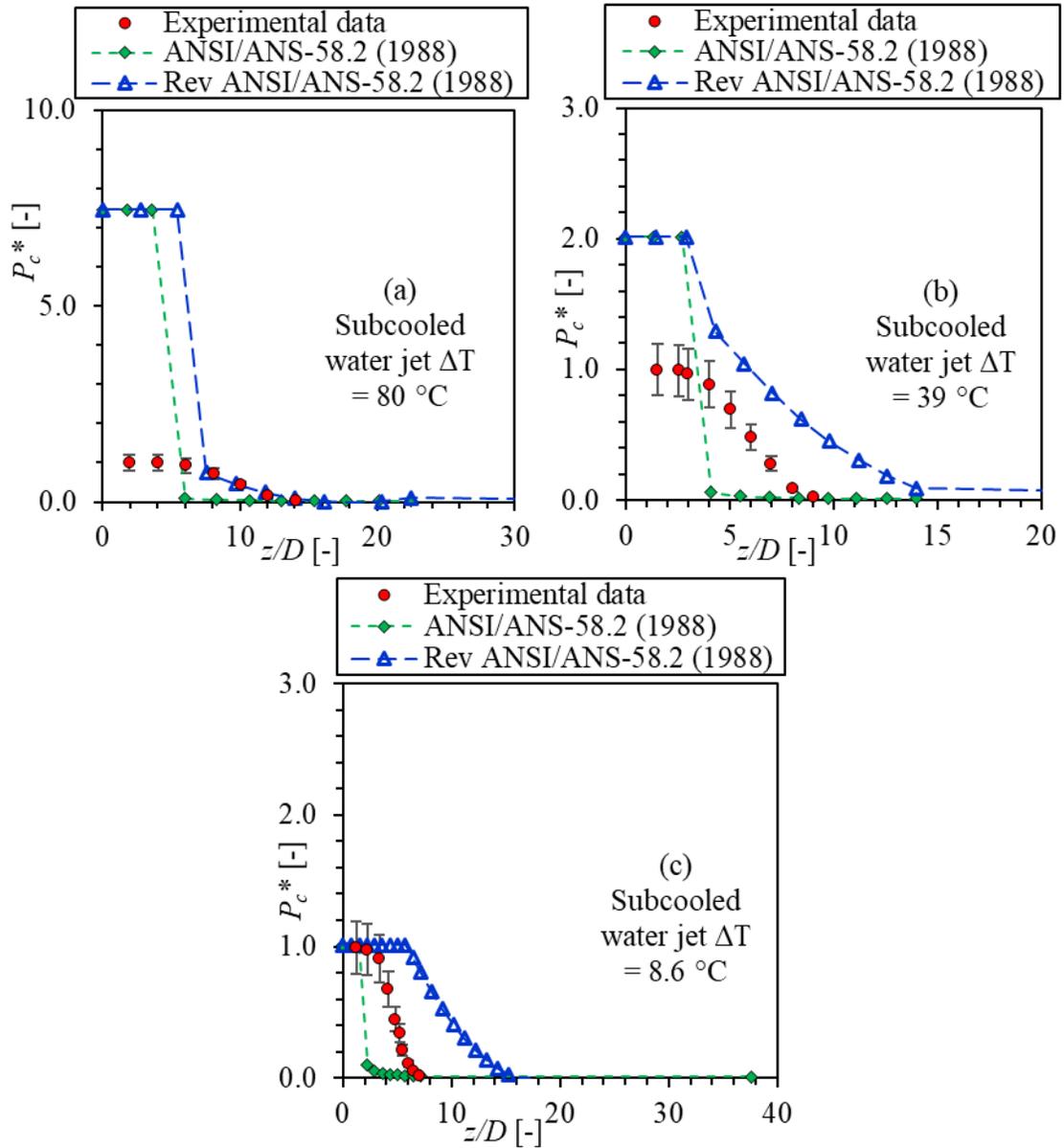
Figure 4-8 Stagnation Pressure at the Center of Subcooled Water Impinging Jets. Comparison between Original Code (ANSI/ANS-58.2, 1988), Revised Code (Rev ANSI/ANS-58.2, 1988), and Experimental Data in Kawanishi et al. (1986) of Mitsubishi Tests. Error Bar: ±20%

4.2.1.1   Review of ACRS Subcommittee on Thermal-hydraulics Meeting

The meeting was convened on September 22, 2004 in Rockville, Maryland to discuss the NRC staff's approach to resolution of several Generic Safety Issues (GSI) related to loss of coolant accidents (U.S. Nuclear Regulatory Commission, 2004). Two reports were mainly discussed in the meeting, including NRC staffs' safety evaluation report related to GSI 191 (NEI 04-07, Volume 2) and the Nuclear Energy Institute Guidance Report (NEI 04-07, Volume 1). The participants include ACRS subcommittee members (Chairman Graham Wallis, F. Peter Ford, Thomas Kress, Graham Leich, Victor Ransom, and John Sieber), NRC staff, researchers from national laboratories, and engineers from industry. The agenda of the meeting was to have NRC staff present results on various topics related to GSI 191, including overview of safety evaluation, pipe break characterization, zone of influence, debris characterization, latent debris accumulation, debris transport, head loss, and physical refinements.

The review of the transcript focuses on the discussion on the blast wave effect in jet impingement of high-energy piping systems. This discussion was initiated by ACRS member Victor Ransom. He argued that "… Another problem with the damage modeling is the test they believe, or I heard the statement that it is the blast wave that actually caused most of the damage. … It was mentioned in the Los Alamos report[1], but then thrown out well at expense, weakens radially so that it was ignored." However, no clear evidence was provided to prove the existence of blast wave effect. He was unclear which damage mechanism was more important, the blast wave or the following impinging jet. The ANSI/ANS-58.2 (1988) has completely ignored the blast wave effect and Victor Ransom believed that "… Nothing was done (on blast wave effect) is kind of appalling…". None of the meeting participants were certain that whether blast wave effect existed or could cause significant damage in the scenario of loss of coolant accidents in nuclear power plants. The discussion on the blast wave effect was concluded by the Chairman Graham Wallis: "… We've said the blast wave might be something that needs to be resolved but we're not quite sure if it's important or not."

In addition, the Chairman Graham Wallis suspected that "…, if the jet was turned on slowly, there wasn't a blast wave at all.". No participant disagreed with this argument. NRC staff Rob Elliott who performed the air jet tests, explained that in the tests conducted in Colorado for the BWRs, rupture disks were used to simulate the instantaneous pipe break. So, blast wave effect should have been considered in the experiments. In these experiments to investigate the debris generation, the maximum or worst case was considered, although it was unknown whether the major damage is caused by the blast wave or the jet impingement. The Chairman Graham Wallis also pointed out that if the blast wave existed, "…, then the blast wave should have damaged stuff that was over here and not in the direction of the jet at all." Although this is a good approach to verify the existence of the blast wave, no replies or comments were provided to Wallis's comment by the researchers who performed the tests.

Victor Ransom agreed that blast wave is a complicated phenomenon. He suggested that transient CFD analysis might be able to understand "what does the blast wave actually look like in this kind of situation" as well as "how it decays and how much the pressure differential across that decays with radius".

---

[1] It is difficult to identify this report since no reference was provided.

4.2.1.2 Investigation of Marviken Tests Data for Potential Blast Wave Effect

In the Marviken tests (Marklund, 1985a), rupture disks were used to simulate the pipe break, and detailed measurements on local static and stagnation pressures were obtained for transient test conditions. These data might provide some information to investigate the potential blast wave effect. In the current report, the stagnation pressure measured at different horizontal beams and targets are investigated here for free and impinging jets, respectively.

As shown in Figure 4-9, the stagnation pressures for both Tests 5 and 6 suddenly increase after the break (t = 0 s). The initial condition for Test 5 is saturated steam at 5.1 MPa and that for Test 6 is subcooled water with a degree of subcooling of 32°C at 5.0 MPa. The plotted pressures in Figure 4-9 are measured at an axial location of z/D_{eff} equals to 0.44, where z is the distance downstream of the break plane and D_{eff} is the equivalent break size. In addition, sudden bursts are observed in both conditions investigated. This might be caused by the blast wave.

The stagnation pressures for impinging jets are shown in Figure 4-10. Tests 7 (z/D = 4.0), 8 (z/D = 2.1), and 10 (z/D = 1.3) used similar initial conditions with subcooled water, which has a degree of subcooling of 32°C at 5.0 MPa. As shown in the plots, sudden bursts are also observed for these impinging jets. However, the strength of the burst is different for targets at different axial locations. Despite this, it is difficult to conclude whether there is a blast wave effect.

4.2.1.3 Modeling Guidance for the Potential Blast Wave Effect

After reviewing the manuscript and the Marviken tests data, it is still not certain whether blast wave effect exists or not. Upon reviewing the available documents (e.g., ML100570364, NUREG CR-6808), technical basis could not be established to assess whether the blast wave should be considered or not in certain conditions. However, some documents identified conditions where the blast wave cannot occur. For a hypothetical loss-of-coolant accident where the fluid upstream of the break location is subcooled (e.g., hot leg, cold leg, and surge line breaks), a blast wave might not be generated. Even if a blast wave does form during the initial moments of a subcooled water pipe break, the effect would be insignificant compared to the forces exhibited by the subsequent jet blowdown (ML100570364).

For saturated water and saturated steam jets, if the break opening time is sufficiently long, a blast wave might not be produced. For example, under a "leak-before-break" assumption, the blast wave effect would be reduced, and it might not need to be considered (NUREG CR-6808).

When the blast wave is generated, it will travel radially until it is reflected from structures such as the containment wall. The spherical shock has a significant initial static overpressure (P_s) that will decrease as the shock expands. The static overpressure is defined as the difference between upstream and downstream static pressures of the shock. Based on the literature review in Section 2.1.3.3, this overpressure can be estimated using the Hopkinson-Cranz scaling law (Equation (2-13)) with additional correlations such as Brode (1955), Henrych (1994), or Weggel (2010) approach as shown in Figure 2-5.
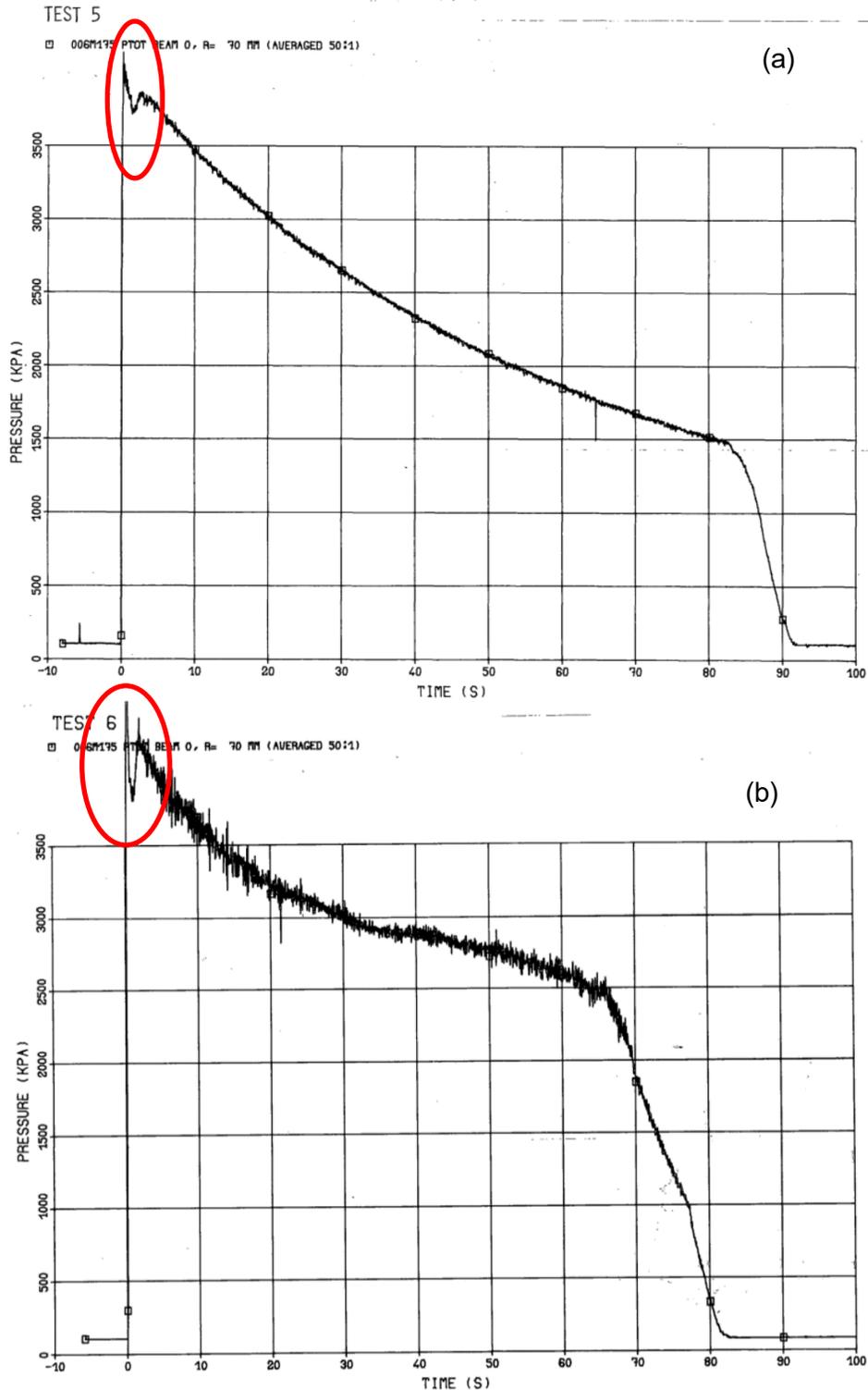
Figure 4-9 Stagnation Pressure near the Center of the Jet Measured at Different Axial
Locations for (a) Test 5 Free Steam Jet (z/D_{eff} = 0.44) and (b) Test 6 (z/D_{eff} = 0.44) of
Marviken Tests (Marklund, 1985a). Initial Vessel Stagnation Pressure: 5.0 MPa

Figure 4-10 Stagnation Pressure at the Center of the Jet Measured at Different Axial Locations for (a) Test 7 (z/D_{eff} = 4.0), (b) Test 8 (z/D_{eff} = 2.1) and (c) Test 10 (z/D_{eff} = 1.3) of Marviken Tests (Marklund, 1985a). Initial Vessel Stagnation Pressure: 5.0 MPa

Figure 4-10 Stagnation Pressure at the Center of the Jet Measured at Different Axial Locations for (a) Test 7 (z/Deff = 4.0), (b) Test 8 (z/Deff = 2.1) and (c) Test 10 (z/Deff = 1.3) of Marviken Tests (Marklund, 1985a). Initial Vessel Stagnation Pressure: 5.0 MPa (cont.)

In general, it is reasonable to assume the blast wave to be spherical, which can simplify the analysis of the wave transport and wave effects. However, in nuclear power plants, the expansion of the potential blast waves may occur in an enclosed space. They can be reflected or deflected from walls and neighboring structures. The reflections of the blast wave depend on the incident angle. Normal reflections occur when the incident angle is zero. The total pressure experienced by the object is the peak reflected pressure P_r, which is a combination of static (P_s) and dynamic (Q_s) pressure. For normal reflections, P_r is given by Equation (2-19) and Equation (2-20) is obtained for air. These relations are derived from the Rankine-Hugoniot relation (Smith and Hetherington, 1994).

However, to use these relations to obtain the total pressure experienced by the object, the equivalent weight of TNT needs to be calculated to get P_s for jet impingement. In the current work, two approaches are developed to obtain the equivalent weight of TNT for jet impingement.

4.2.1.3.1 Vessel Burst Energy (Lees, 2012)

In TNT explosion, the released energy is from chemical reaction, whereas in jet impingement, the energy is from fluid expansion. In Lees (2012), several conditions are discussed for explosion energy. One of the conditions is to calculate the "vessel burst energy" for non-ideal gas, vapor, and flashing liquid. The proposed approach in Lees (2012) is employed as the first method in the current work to determine the equivalent weight of TNT. Based on Lees (2012), the explosion energy in this case is the difference in the internal energy between the initial and

final states of explosion assuming an isentropic expansion, which can be found using thermodynamic diagrams or tables.

Following this approach, the potential blast wave effects for subcooled water, saturated water, and saturated steam jets are investigated. The initial pressure for subcooled water jets is 15.5 MPa (2250 psi) based on PWR operating condition, while that for saturated water and saturated steam jets is 6.9 MPa (1000 psi) based on BWR operating condition. Two values are used for the degree of subcooling for subcooled water jets: 20°C (hot leg) and 65°C (cold leg). To estimate the released energy, the first step is to calculate the mass of fluid (m) released at the initial stage of break to generate the blast wave. In the current work, it is calculated by

$$m = G_{cr} \cdot A_e \cdot t \tag{4-8}$$

where G_{cr} is the critical mass flux, A is the break area, and t is the energy release time when blast wave is generated during the initial stage of break. Based on the previous model evaluation for critical mass flux, the Henry-Fauske (HF) model, Homogeneous Equilibrium Model (HEM), and isentropic expansion model can be used for subcooled water jets, saturated water jets, and saturated steam jets, respectively. By defining the first state to be 1 and the final state to be 2, the released energy E is:

$$E = m\left(e_1 - e_2\right) \tag{4-9}$$

where e is the specific internal energy. In the process of calculating e_2, isentropic expansion is assumed. The steam quality x at the final state is calculated by:

$$s_1 = s_2 = s_{f2} + x \cdot s_{fg2} \tag{4-10}$$

The thermodynamic parameters calculated for saturated steam, saturated water, and subcooled water at initial and final states are shown in Table 4-4. With x, the specific enthalpy and internal energy for the final state are calculated by:

$$h_2 = h_{f2} + x \cdot h_{fg2} \tag{4-11}$$

$$e_2 = e_{f2} + x \cdot e_{fg2} \tag{4-12}$$

In Table 4-4, the pressure of the fluids at final state is assumed to be atmospheric pressure. In reality, the fluids right after the break is still at the high-temperature high-pressure condition, so this assumption is conservative. With Table 4-4, the energy released from saturated steam, saturated water, and subcooled water jets can be estimated, with additional assumptions for break area (A) and energy release time (t). In the work by Cullis (2001), the energy release time for 1kg TNT is in order of approximately 10 μs. The current work investigates the sensitivity of this time scale on the potential blast wave effect. Three different time scales are selected: 0.01 ms, 0.1 ms, and 1 ms. It also needs to be noted that not all of the energy released from fluid expansion is converted to the blast wave. Instead, part of the released energy contributes to kinetic energy of fluids and fragments, residual energy in air, etc. Hence, the current work investigates two cases: 50% conversion and 100% conversion. Considering that the released energy is similar based on specific enthalpy and specific internal energy difference, only internal energy difference is employed as suggested by Lees (2012). The sensitivity study for saturated steam, saturated water, and subcooled water (with two different ΔT) jets are shown in Table 4-5 through Table 4-8, respectively.

Table 4-4 Thermodynamic Parameters of Jets or Fluids at Initial and Final States

Parameters	Saturated steam	Saturated water	Subcooled water	
Initial pressure P_1 [psi] / [MPa]	1000 / 6.9	1000 / 6.9	2250 / 15.5	2250 / 15.5
Degree of subcooling ΔT [°C]	0	0	20	65
Initial specific entropy s_1 [kJ/kg·K]	5.82	3.1	3.47	3.03
Initial specific enthalpy h_1 [kJ/kg]	2774.0	1262.3	1482.0	1229.6
Initial specific internal energy e_1 [kJ/kg]	2582.2	1253.0	1459.0	1209.3
Quality at final state x [-]	0.75	0.30	0.36	0.29
Final pressure P_2 [psi] / [MPa]	14.7 / 0.1	14.7 / 0.1	14.7 / 0.1	14.7 / 0.1
Final specific enthalpy h_2 [kJ/kg]	2101.9	1091.8	1224.9	1060.9
Final specific internal energy e_2 [kJ/kg]	1975.1	1041.1	1164.1	1012.4
Difference of specific enthalpy h_1-h_2 [kJ/kg]	672.2	170.5	257.1	168.7
Difference of specific internal energy e_1-e_2 [kJ/kg]	606.9	211.9	294.9	196.9

Table 4-5 Released Energy for Saturated Steam Jets

Parameters	Case 1	Case 2	Case 3	Case 4	Case 5	Case 6
Critical mass flux [kg/m²s]	8,544					
Break size [m]	1					
Break area [m²]	0.79					
Release time [ms]	0.01	0.1	1	0.01	0.1	1
Fluid mass [kg]	0.07	0.67	6.75	0.07	0.67	6.75
e_1-e_2 [kJ/kg]	607.0					
Percentage of energy to blast wave [-]	50%			100%		
Released energy based on e_1-e_2 [kJ]	20.5	204.9	2,048.6	41.0	409.7	4,097.2
TNT equivalent weight W_e [×10^{-3} kg]	4.94	49.39	493.88	9.88	98.78	987.76
R ($P_r \sim$ 10 bar) [m]	0.3	0.6	1.3	0.4	0.8	1.7

Table 4-6 Released Energy for Saturated Water Jets

Parameters	Case 7	Case 8	Case 9	Case 10	Case 11	Case 12
Critical mass flux [kg/m²s]	25,701					
Break size [m]	1					
Break area [m^2]	0.79					
Release time [ms]	0.01	0.1	1	0.01	0.1	1
Fluid mass [kg]	0.2	2.0	20.3	0.2	2.0	20.3
e_1-e_2 [kJ/kg]	212.0					
Percentage of energy to blast wave [-]	50%			100%		
Released energy based on e_1-e_2 [kJ]	21.5	215.2	2152.2	43.0	430.4	4,304.4
TNT equivalent weight W_e [×10⁻³ kg]	5.2	51.9	518.8	10.4	103.8	1,037.7
R (P_r ~ 10 bar) [m]	0.3	0.6	1.4	0.4	0.8	1.7

Table 4-7 Released Energy for Subcooled Water Jets (ΔT = 20°C)

Parameters	Case 13	Case 14	Case 15	Case 16	Case 17	Case 18
Critical mass flux [kg/m²s]	79,379					
Break size [m]	1					
Break area [m^2]	0.79					
Release time [ms]	0.01	0.1	1	0.01	0.1	1
Fluid mass [kg]	0.63	6.27	62.71	0.63	6.27	62.71
e_1-e_2 [kJ/kg]	294.0					
Percentage of energy to blast wave [-]	50%			100%		
Released energy based on e_1-e_2 [kJ]	92.2	921.8	9,218.2	184.4	1,843.6	18,436.5
TNT equivalent weight W_e [×10⁻³ kg]	22.22	222.23	2,222.3	44.5	444.5	4,444.7
R (P_r ~ 10 bar) [m]	0.5	1.0	2.2	0.6	1.3	2.8

Table 4-8 Released Energy for Subcooled Water Jets (ΔT = 65°C)

Parameters	Case 19	Case 20	Case 21	Case 22	Case 23	Case 24
Critical mass flux [kg/m²s]	155,837					
Break size [m]	1					
Break area [m^2]	0.79					
Release time [ms]	0.01	0.1	1	0.01	0.1	1
Fluid mass [kg]	1.2	12.3	123.1	1.2	12.3	123.1
e_1-e_2 [kJ/kg]	197.0					
Percentage of energy to blast wave [-]	50%			100%		
Released energy based on e_1-e_2 [kJ]	121.3	1,212.6	12,126.5	242.5	2,425.3	24,253.0
TNT equivalent weight W_e [×10⁻³ kg]	29.2	292.4	2,923.5	58.5	584.7	5,846.9
R (P_r ~ 10 bar) [m]	0.5	1.1	2.4	0.7	1.4	3.1

In total, 24 cases are investigated, 6 for saturated steam jets, 6 for saturated water jets, and 12 for subcooled water jets. The calculated static overpressures and reflected pressures for Cases 6, 12, 18, and 24 with respect to the distance from the break are shown in Figure 4-11. The correlation from Weggel (2010) is employed in the P_s calculation. The distance where the pressure drops to 100 bar or 10 bar is shown in the figures. In addition, as shown in Figure 2-5, all the approaches suggest that the over static pressure increases significantly as the distance reduces to 0. However, this might not be applicable for jet impingement. Since the maximum overpressure cannot be higher than the stagnation pressure in the pipe, lines of 15.5 MPa (155 bar) or 6.9 MPa (69 bar) are used for upper limits of P_s and P_r. To compare with the TNT explosion, the pressure in the explosive products is over 45 kbar at 10 μs (right after blast wave is generated) for 1 kg TNT explosion as simulated by Cullis (2001).

It needs to be noted that the pressure profiles in Figure 4-11 are developed based on several assumptions that can be considered quite conservative:
   (1) The jets or fluids immediately after the blast wave generation are at atmospheric pressure condition;
   (2) A break size of 1 m;
   (3) An energy release time of 1 ms;
   (4) 100% of the released energy is converted to blast wave energy.
Additional investigation might be needed to eliminate unrealistically conservative assumptions.

4.2.1.3.2 Peak Pressure in Experimental Measurements

The second approach assumes that the peak pressure measured in the initial stage of blowdown tests is due to the potential blast wave. This measured peak pressure can be used to solve for the equivalent TNT weight in quantifying the blast wave effect. Since energy needs to be released in a very short time to generate the blast wave, the sampling frequency of pressure measurements needs to be very high (> 100 Hz). In the work by Isozaki and Miyazono (1986), pressure on target was measured for subcooled water jets (P_0 = 15.56 MPa, ΔT = 20°C) and saturated-water jets (P_0 = 6.86 MPa) at a relatively high frequency (~ 100 Hz). The peak pressure at the targets (at a distance of approximately one break size) reported for both subcooled water jets and saturated water jets are about 40% of the initial stagnation pressures in vessel. Using this information, the current work quantifies the blast wave effect for subcooled water and saturated water jets with a break size of 1 m.

To calculate the equivalent weight of TNT, it needs to determine whether the maximum pressure measured in experiments is static overpressure or reflected pressure. By assuming it to be the static pressure, the calculated TNT weight will be more conservative. Based on this assumption, the equivalent weight of TNT is calculated to be 15.6 kg and 4.6 kg, respectively, for subcooled water jet and saturated water jet. The profiles for static overpressure and reflected pressure are shown in Figure 4-12.
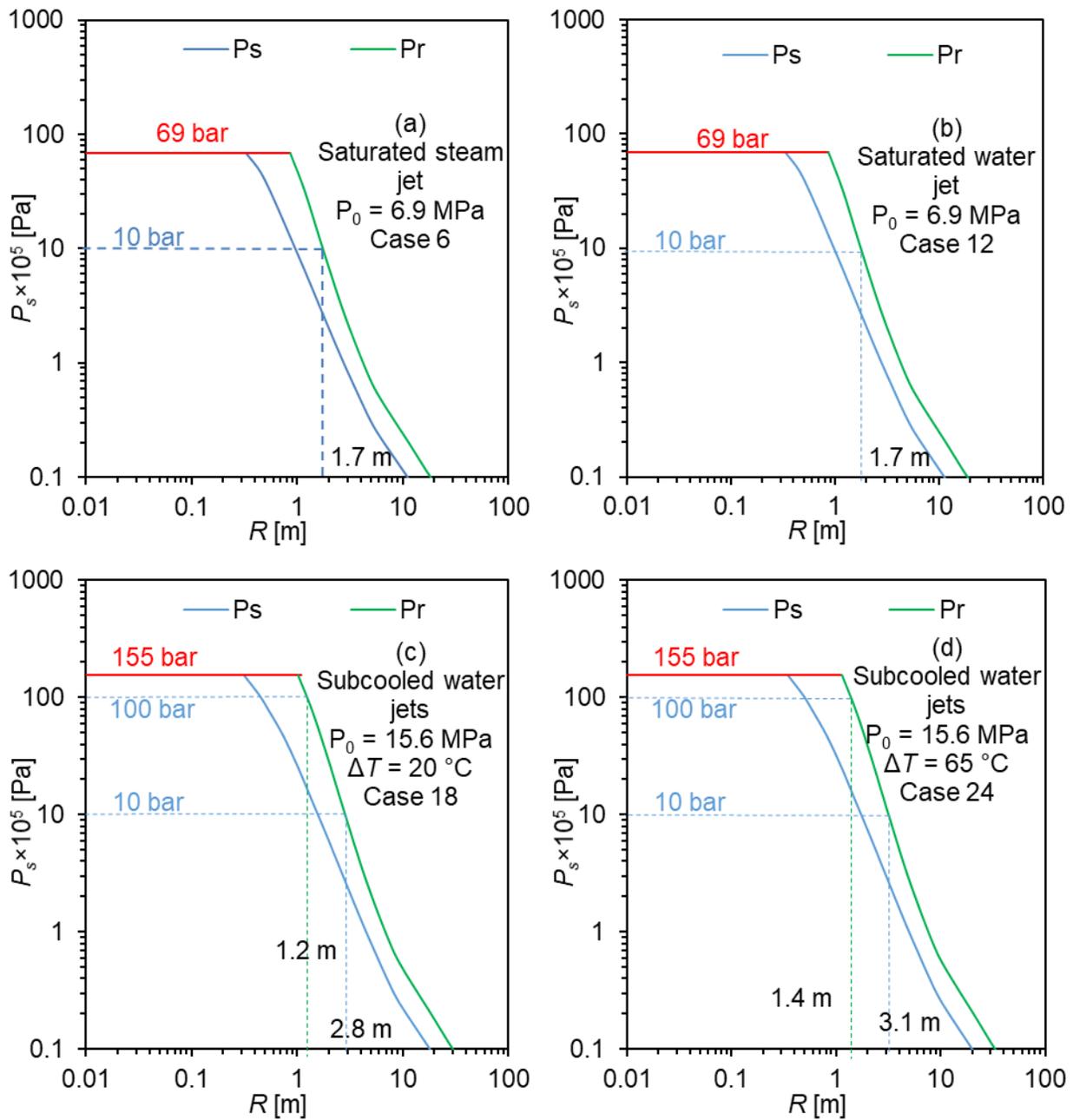
Figure 4-11 Calculated Static Overpressure (P_s) and Reflected Pressure (P_r) for (a) Saturated Steam Jet Case 6, (b) Saturated Water Jet Case 12, (c) Subcooled Water Jet Case 18, and (d) Subcooled Water Jet Case 24
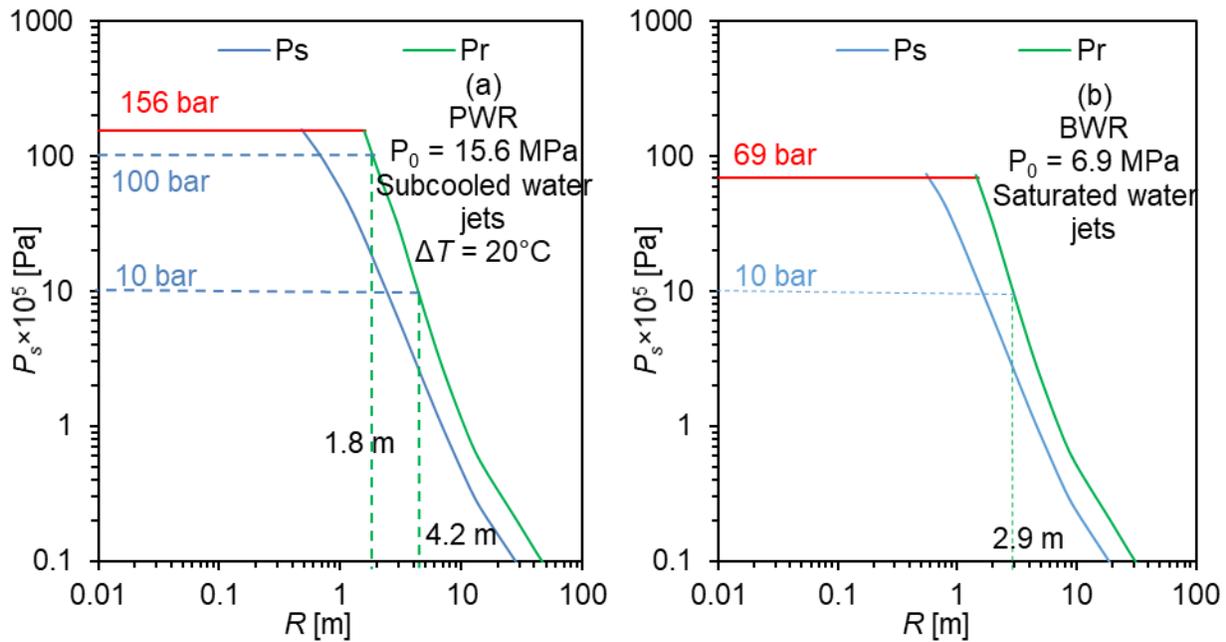
Figure 4-12 Calculated Static Overpressure (P_s) and Reflected Pressure (P_r) for (a) Subcooled Water Jet and (b) Saturated Water Jet
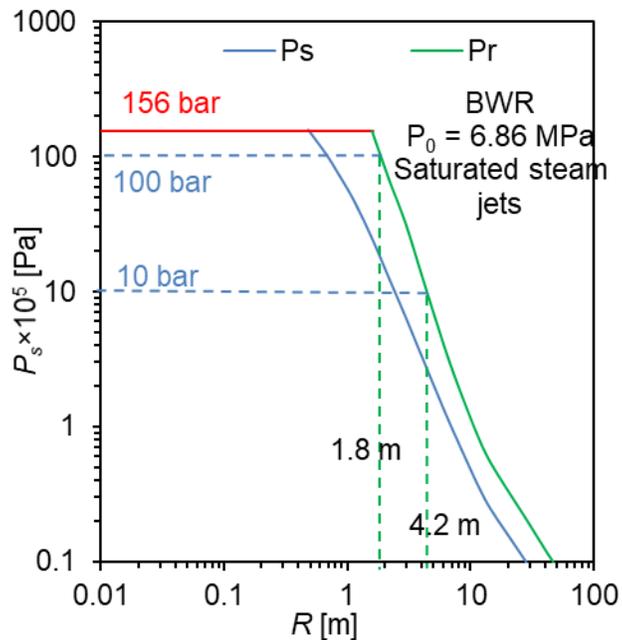
Figure 4-13 Calculated Static Overpressure (P_s) and Reflected Pressure (P_r) for Saturated Steam Jet

For saturated steam jets, there are no experimental data available that can help to determine the potential blast wave effect. Experiments on saturated steam jets were usually performed at a steady-state condition and as such the pressure measurement as a function of time was not presented. For experiments where transient data were presented such as Marviken tests, the measurement frequency might be too low to capture the blast waves (~ 10 Hz). In the current work, an additional assumption is made to quantify the potential blast wave in saturated steam jets. In the Standard model (ANSI/ANS-58.2, 1988), the region 1 of jet is defined as the jet core and the pressure within this region is the same as the initial vessel stagnation pressure prior to break. For saturated steam and saturated water jets, the length of jet core is 0.5 D based on the model in the Standard. As such, in the current work, it assumes that the blast wave has a static overpressure of initial vessel stagnation pressure at an axial location of half break size. For a jet with the break size of 1 m at a BWR operating condition (P_0 = 6.9 MPa), the equivalent weight of TNT is calculated to be 15.6 kg. The profiles of static overpressure and reflected pressure are shown in Figure 4-13.

By comparing the approaches 1 and 2, it can be seen that the both approaches predict the distance, where P_r drop to 10 bars, to be the same order of magnitude. The reflected pressure for normal reflections generally drops to 10 bar within 4 m for all the conditions investigated.

Once the reflected pressure is known, a critical value for reflected pressure ($P_{r,critcal}$) can be defined to calculate a critical radial distance ($R_{critcal}$), within which the blast wave will cause damage. In selecting this critical reflected pressure, the damage pressures of the surrounding SSCs need to be considered. A flowchart showing the logic of the current preliminary modeling guidance on blast wave effect is shown in Figure 4-14.

Jets in high-energy systems

Stagnation pressure (P_0) and corresponding subcooling (ΔT_0)

Subcooled water jets $\Delta T_0 > 0$? — Yes

No

Saturated water and saturated steam jets

Break opening time t

t sufficiently large? or leak-before-break? — Yes

No

Sudden break

Radial distance r

In the vicinity of the break: $r < r_{crit}$? — No

Yes

Equivalent weight of TNT W

Reflected pressure distribution $P_r(r)$

Insignificant blast wave effect*

Figure 4-14 A Flowchart of Preliminary Modeling Guidance on Blast Wave Effect Developed in the Current Work

*: Upon reviewing the available documents (e.g., ML100570364, NUREG CR-6808), technical basis could be established to assess whether the blast wave is significant or not in certain conditions.

4.2.2 Jet Plume Expansion and Zone of Influence

It is pointed out in the Standard Review Plan (2015) that the Standard model assumes that a jet issuing from a high-pressure pipe break will always spread with a fixed 45-degree angle up to an asymptotic plane and subsequently spread at a constant 10-degree angle. The characteristics of the jet, however, are not universal. Initial jet spreading rates are highly dependent on the ratio of the source flow to the ambient conditions. Subsequent spreading rates depend, at a given axial position, on the ratio of the static pressure in the outermost jet flow region to the ambient static pressure.

After a literature review in Section 2.2.2.2.2, it is found that there are several studies to investigate the spreading angle of the jets for different regimes. In these studies, the spreading angle depends on the jet condition and dynamic models are developed for this angle.

For saturated steam jets, jet expansion is investigated by a recent CRIEPI-Hitachi Test (Morita et al., 2016) using experiments and Computational Fluid Dynamics (CFD). The investigated conditions cover a wide range of pressure values from 0.23 MPa to 13 MPa. In the experimental setup, saturated steam of up to 1.6 MPa and 833 kg/h is supplied continuously from high-pressure steam boiler to the reservoir tank with a diameter of 100 mm. The jet nozzle has a diameter of 8 mm and is 200 mm long. The jet velocity was obtained using Particle Image Velocimetry (PIV). In total, four conditions were performed for experiments and nine conditions were performed for CFD simulation. In Morita et al. (2016), the asymptotic plane is defined as the maximum expanded jet position as shown in Figure 2-35. It is found that the spreading angle is dependent on the pressure ratio (inlet pressure/exit pressure), which is given in Figure 2-15. As shown in the plot, the pressure ratio has a good correlation with the spreading angle from near atmospheric pressure condition to main steam pressure in nuclear power plants. Since the high-pressure steam expands more than the low-pressure steam, this tendency is thought to be reasonable. On the other hand, it is found that when the inlet pressure is about 7 MPa, this angle is 45 degree, which is the value used in the Standard.

To evaluate this result, the spreading angle in Figure 2-15 is compared with the Prandtl-Meyer angle for under-expanded supersonic jets given in Ransom (2004). The comparison is shown in Figure 4-15. As discussed, this angle is calculated by finding the location (z_a) of the asymptotic jet area (A_a) in Morita et al. (2016), while for the Prandtl-Meyer angle (Ransom, 2004), this angle is that between the tangential line and the axis. Considering this difference in definition, the comparison on the spreading angle in Figure 4-15 is acceptable. Meanwhile, it is found that the spreading angle defined in Morita et al. (2016), which is close to the definition in ANSI/ANS-58.2 (1988), is between 40° and 50° in a wide range of vessel stagnation pressure conditions.

The spreading angle after the asymptotic plane is investigated by Takahashi et al. (2016) using CFD simulations (saturated steam, pressure range: 1 MPa ~ 7 MPa). Based on the velocity vectors obtained from CFD analysis, the spreading angle can be obtained using different criteria. In this work, the position where jet velocity almost becomes zero is defined as the jet boundary and four different velocities are used as this critical jet velocity (allowable velocity). As a result, the jet angle is determined as shown in Figure 4-16. This angle is found to be between 4° and 8° based on different criteria, which is similar to the 10° that has been used in the Standard model.
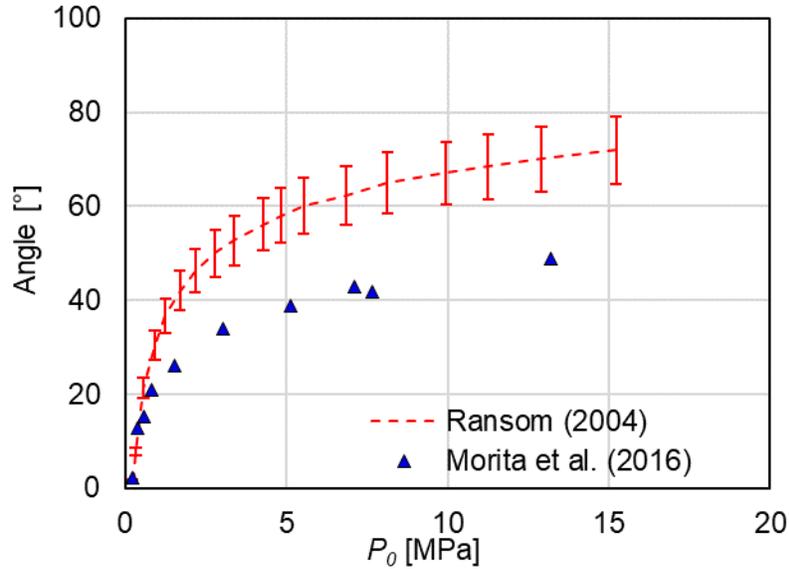
Figure 4-15 Comparison on Prandtl-Meyer Angle between Ransom (2004) and Morita et al. (2016)
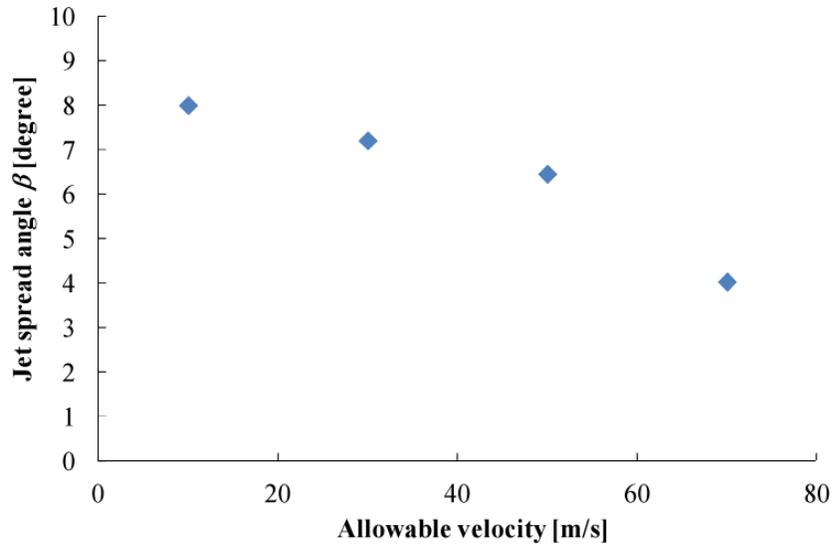
Figure 4-16 Jet Spreading Angle as a Function of Allowable Velocity (Takahashi et al., 2016)

The jet expansion for flashing jets is investigated in Morita et al. (2018) using CFD. The test conditions investigated cover a wide range of pressure conditions from 0.5 MPa to 7.0 MPa for both saturated water and subcooled water. The definition of the spreading angle is same to the steam jets as shown in Figure 2-35. It is found that the spreading angle depends on the density ratio of nozzle exit density (ρ_e) to the ambient steam density (ρ_{amb}):

$$z_a = 0.3 \times \sqrt{\frac{\rho_e}{\rho_{amb}}}$$

(4-13)

$$H_a = 0.008 \times \frac{\rho_e}{\rho_{amb}} + 1 \tag{4-14}$$

where z_a and H_a is the length and width of the asymptotic region as shown in Figure 2-35. As such, the spreading angle can be calculated as:

$$\theta_a = \arctan\left(\frac{H_a - D}{z_a}\right) \tag{4-15}$$

where D is the break size.

In the work by Morita et al. (2018), it is found that increasing inlet pressure increases the fluid pressure and density at the nozzle exit plane, leading to a larger expansion of the flow. Meanwhile, as the degree of subcooling increases, the density also becomes larger due to the delay of the flashing occurrence in the nozzle. Considering that the spreading angle for flashing jets is much larger than the steam jets, it is recommended by Morita et al. (2018) that the affected region should be a round column with diameter H_a and length z_a.

4.2.3 Distribution of Pressure within the Jet Plume

The Appendix C and Appendix D of the ANSI/ANS-58.2 (1988) describe the assumptions for defining the pressure distribution for various jet conditions. For nonexpanding jets, it assumes a uniform pressure distribution over the cross section. For an expanding jet, the Standard assumes non uniform pressure over the cross section of the jet, with a maximum value at the jet centerline. However, this assumption is only valid near the break plane. At the distances far from the break plane, the pressure distribution is quite different and outer edge peaking of the pressure can occur. As such, the Standard Review Plan (2015) argues that this could lead to nonconservative pressures away from the jet centerline.

After a literature review, it is found that the edge-peaking profiles are observed for steam jets as shown in Figure 2-17 and Figure 2-18 for free jets and impinging jets, respectively. In these plots, D is the break size and the dimensionless stagnation pressure (P^*) is defined as:

$$P^*(z,t) = \frac{P(z,t) - p_{amb}(t)}{P_0(t) - p_{amb}(t)} \tag{4-16}$$

where P^* is the dimensionless stagnation pressure, P, P_0, and p_{amb} are the stagnation pressure, vessel stagnation pressure, and ambient atmospheric pressure, respectively.

As shown in the Figure 2-17 and Figure 2-18, the edge-peaking distribution starts to show at 3.3 D for free jets and at 6.3 D for impinging jets. However, the peaking dimensionless values are generally less than 0.07. Therefore, it is believed this may not have a significant effect.

In addition, the Standard Review Plan (2015) claims that "Supersonic jet behavior can persist over distances from the break that are far longer than those estimated by the standard, extending the zone of influence of the jet and the number of SSCs that could be impacted by a supersonic jet. For example, tests in the Seimens-KWU facility in Karlstein, Germany showed that significant damage from steam jets can occur as far as 25 pipe diameters from a rupture."

This is based on statement in Sandervaag et al. (1996), where it is written that "The target materials that are hit by the steam jet core could be destroyed in a range of 25 *L/D*." Although the target materials could be destroyed, it is different from "significant damage could occur". In fact, the experimental data for saturated steam jets in large break jets (i.e., Marviken tests) indicate that the dimensionless pressure drops to almost zero at 4*D* and the small break jets data indicate that this dimensionless pressure drops to 0.07 at a distance of 4*D*.

4.2.4   Jet Dynamic Loading

Free jets, especially supersonic jets, are unsteady. Pressures and densities vary nonmonotonically with distance along the axis of a typical supersonic jet. In addition, for a typical supersonic jet, interaction with obstructions will lead to backward-propagating transient shock and expansion waves that will cause further unsteadiness in downstream shear layers. Once the dynamic jet loading on the target synchronize with the dynamic response of the neighboring structure, resonance can occur and cause further amplification of the loading. This jet dynamic loading effect has not been considered in the existing jet impingement models.

An Areva report ANP-10318NP (Areva NP Inc., 2013) discusses this dynamic loading effect on surrounding SSCs and provided a modeling approach for jet dynamic loading in nuclear power plants as reviewed in Section 2.1.3.2. The approach is to first calculate the resonance frequency of the jet and then compare with that of surrounding structures to determine the dynamic loading factor. However, there are limited experimental data to determine the frequency for jets in nuclear power plants. The existing studies in literature are for air jets in Aerospace Engineering. Alam et al. (2010) measured the pressure at the center of the target for dry air supersonic jets with two nozzle pressure ratios (P_0/p_{amb}), 3.0 and 4.5, where the axial location of the target is 2.5 *D* (nozzle diameter). The time histories of the pressure on target is shown in Figure 4-17. From the plots, it can be seen that the jets are not harmonic. Meanwhile the frequency of jets is high (~10 kHz).

In addition, Alam et al. (2010) investigated the effects of moisture (supersaturation *S,* or liquid droplet content) in air impinging jets on surface pressure at targets. It is found that with increasing the moisture, the amplitudes of the surface pressure oscillation (i.e., difference between the maximum and minimum pressure during one cycle of flow field oscillation) keep decreasing as shown in Figure 4-18. Meanwhile, the jet frequency does change significantly.

Based on these results in Alam et al. (2010), Kauffman et al. (2019) evaluates the potential for jet dynamic loading in nuclear power plants and provides justification for why dynamic amplification and resonance of impinging downstream structures and components would not occur. As shown by the data in Alam et al. (2010), the measured pressure at targets for the supersonic air jets has a high frequency. The saturated steam jets in nuclear power plants are also supersonic and they might be in the high frequency range. This frequency range is more than 100 times the first mode of any structures or components in nuclear power plants. As such, the jets cannot excite a plant target structure or component. The first mode of large SSCs in nuclear power plants is generally less than 20 Hz, with most others less than 75 Hz, although very rigid piping may be up as high as 150 Hz (Kauffman et al., 2019). For target frequency, Yano et al. (1984) approximated the lowest natural frequency of the target to be ~50 Hz, and that of the pipe to be ~100 Hz, respectively ,which is in the same order of magnitude with Kauffman et al. (2019)'s approximation. The frequency of jets is high (above 10 kHz) and unlikely to be harmonic, making it incapable of exciting an SSC. Even assume it to be harmonic, the dynamic amplification factor (or dynamic loading factor) would be negligible:

$$\text{Dynamic Loading Factor} = \frac{1}{\sqrt{\left(1-\frac{\omega^2}{\omega_n^2}\right)+\left(\frac{2\zeta\omega}{\omega_n}\right)^2}} \tag{4-17}$$

where ω is the jet forcing frequency, ω_n is the natural frequency of the impacted target, and ζ is the damping coefficient. If $\omega/\omega_n \gg 1$, the dynamic loading factor becomes very small, yielding very little displacement response.

It needs to be noted that this conclusion is consistent with the current literature review. As shown in Figure 2-3. When the ratio Ω/ω (frequency of load to the frequency of the structure) is extremely large, regardless of the damping condition, the maximum dynamic loading factor is approaching to zero.
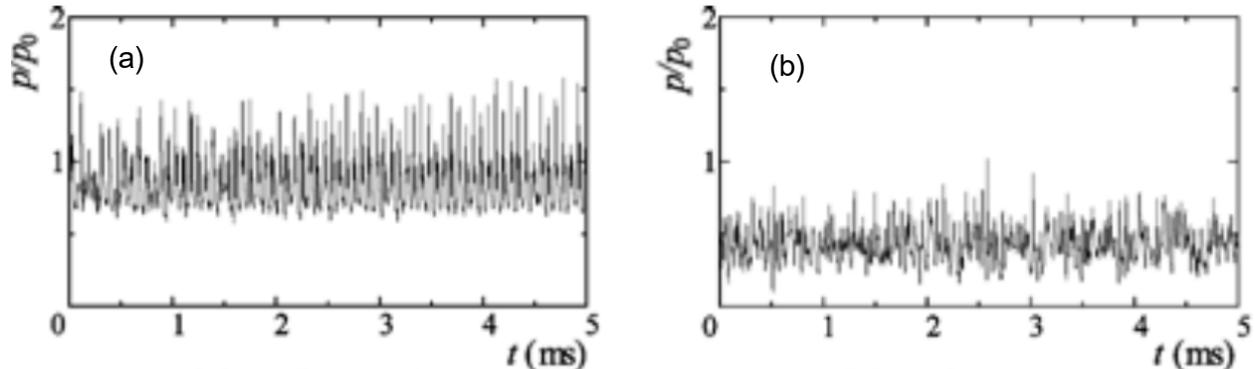

Figure 4-17 Time History of Pressure at the Center of Target for Dry Air Jets: (a) Po/p_{amb} = 3.0 and (b) Po/p_{amb} = 4.5 (Alam et al., 2010). Nozzle Size: 12.7 mm
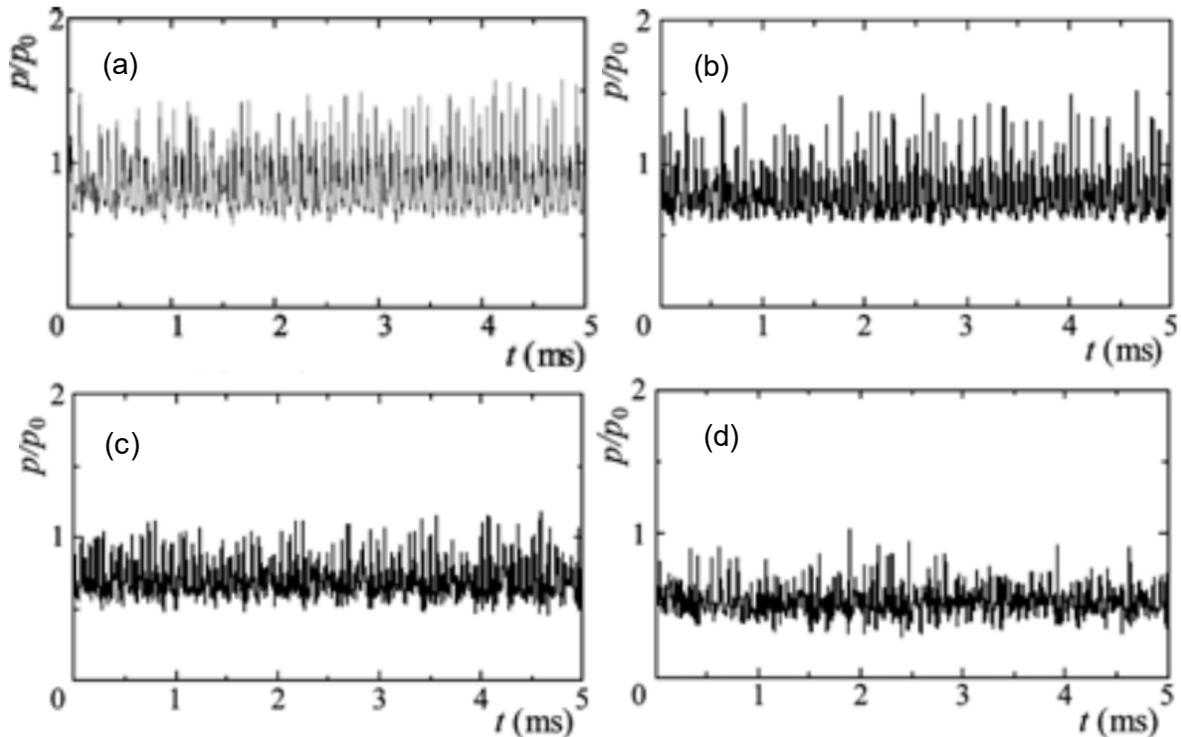
Figure 4-18 Time History of Pressure at the Center of Target for Dry Air Jets: (a) $S_0 = 0$ (Dry Air), (b) $S_0 = 0.4$, (c) $S_0 = 0.6$, and (d) $S_0 = 0.8$ (Alam et al., 2010). Nozzle Size: 12.7 mm

In addition, as demonstrated by Alam et al. (2010), the effect of moisture in air jets differs from the expansion of a dry air expansion due to "non-equilibrium condensation" or "spontaneous condensation". The pressure oscillations (not resonance) measured on targets is considerably reduced in amplitude as supersaturation level in the jet increases as shown in Figure 4-18. Kauffman et al. (2019) argued that in jet impingement in nuclear power plants, the fluid prior to pipe break is either subcooled water or saturated water in nuclear power plants. The release of high-energy fluid into near-atmospheric condition will result in phase changes that redistribute energy. In the evaluation of the potential blast wave effect in Section 3.1.3, the quality of different jets is calculated at atmospheric condition by assuming isentropic expansion. For PWR (subcooled water @ 15.5 MPa, $\Delta T = 20°C$), the quality is 0.29, while for BWR (saturated water @ 6.9 MPa), the quality is 0.30 and for saturated steam (@ 6.9 MPa) the quality is 0.75. As such, the jet in nuclear power plants will not be dry gas expansion. The liquid droplets in the jet will mitigate the resonance effect as demonstrated in previous work.

Apart from these two arguments, Kauffman et al. (2019) provides additional justifications. They are briefly summarized here.

(1) Exit geometry. A pipe break or crack in nuclear power plants is not smoothly tapered, clean-edged nozzle to produce a stable axisymmetric discharge. The irregularity of the broken pipe end prevents formation of an axisymmetric or stable flow field. It interferes with both the downstream progression of pressure fluctuations and the return of any periodic acoustic wave. Pictures in Figure 4-19 are shown that the jet will be disturbed for the break with tabs.
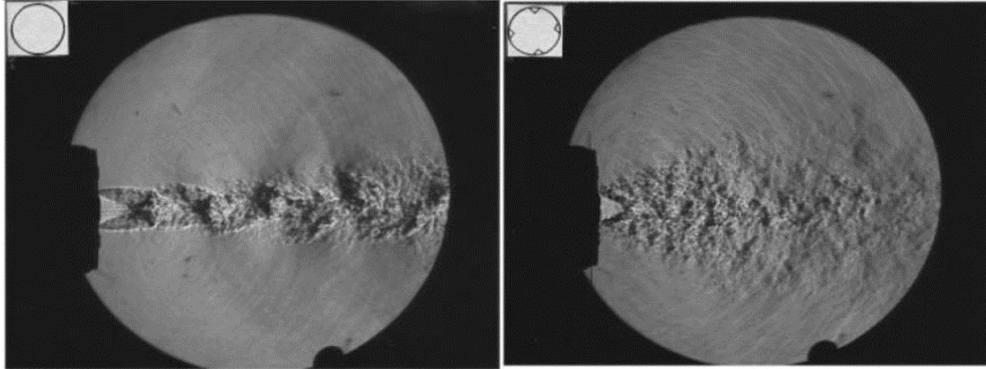
Figure 4-19 Schlieren Photographs of Jet without (Left) and with (Right) Tabs (Zaman, 1999)

(2) Alignment to Target: Observed instances where gas jet induced resonance occurs are engineered to provide a specific alignment. If the distance between the nozzle edge and impingement surface varies around the nozzle circumference, the returning acoustic waves reach the shear layer at different times. This causes excitation that is out of phase, which prevents synchronization.

(3) Discharge stability: Experiments and industrial gas jet applications are designed to prevent flutter of the discharge to ensure repeatability. However, the pipe break in nuclear power plants is subject to pipe whip and is unlikely to be sufficiently constrained to maintain spacing and orientation to a target.

(4) Jet interaction with target: For the target to be capable of establishing a feedback loop, it also must present a surface that has the following characteristics:

   a) Large enough in area that most of the expanded jet is impinged;

   b) Flat (e.g., not curved, not irregular) over the area of the jet to prevent distortion of returning acoustic waves;

   c) Hard enough not to absorb much energy;

   d) The surface, although larger than the area of the jet, must also be located such that it fully intersects the jet.

However, the arrangements of equipment inside a nuclear plant do not provide the clear line of sight pathways to large, flat, hard, smooth, perpendicular surfaces needed to form a resonance.

(5) Intersecting flow: A HELB (High Energy Line Break) deposits a large amount of high energy fluid into a relatively confined space with numerous surrounding structures. Secondary and tertiary spray reflections intersect with the shear layer of the jet, disturbing the acoustic waves. Additionally, fluid issuing from the other end of the broken pipe is likely to intersect the jet, even after pipe whip.

5   SUMMARY AND CONCLUSIONS

The jet impingement due to postulated pipe rupture is important in the design and safety analysis of nuclear power plants. While models of jet impingement have been developed to assist in designing protective systems to mitigate the damage, several potential non-conservatisms in these models have been specified following the interaction with the Advisory Committee on Reactor Safeguards (ACRS) (Appendix A of Standard Review Plan, 2015). The current work performs a comprehensive literature review and model evaluation to address the potential non-conservatisms with respect to (a) blast waves, (b) jet plume expansion and zone of influence, (c) distribution of pressure within the jet plume, and (d) jet dynamic loading. Based on the results of the literature review and model evaluation, the Standard model is revised and model guidance is developed in the current work.

Jet impingement phenomena, experimental studies, as well as modeling and CFD simulations of jet impingement are reviewed, which provide necessary information for model evaluation, model revision, and guidance development. Important phenomena are identified including pipe whip, jet expansion, jet impingement, and critical flow. Important parameters include thrust force, jet geometry, pressure distribution, jet impingement force, dynamic load factor, and critical flow rate. While most of these parameters have been modeled in ANSI/ANS-58.2 (1988), the effects of potential dynamic loading and blast wave on jet impingement are not considered. A dynamic loading factor can be employed to account for the effect of resonance on structure loading. However, the approach to determine the jet resonant frequency was developed for air jets in aerospace engineering and may not be applicable to jet impingement in nuclear power plants. In addition, there have been limited studies to investigate the effect of the potential blast wave on structure loading for jet impingement in high-energy systems as in nuclear power plants. The modeling approach for blast waves in explosions might be able to be extended to the jet impingement. In this case, the TNT (explosive trinitrotoluene) equivalent weight needs to be determined for jet impingement in nuclear power plants.

The comprehensive literature review on the experimental studies in jet impingement shows that the experimental studies were performed for different scale levels. Most of the work investigated the pressure distribution, thrust force, and impingement force. In general, the local static or stagnation pressure was measured by pressure transducers, and thrust force or impingement force was measured by load cells. The initial flow conditions, break conditions and target conditions in each experimental study are carefully reviewed, considering that jet impingement is a complicated phenomenon. Following this review, an experimental database is established for data analysis and model evaluation. The parameters including pressure, break size, and axial distance are non-dimensionalized such that the effects of initial fluid condition and break size can be investigated. The dimensionless static and stagnation pressures at the center of the free jets and the stagnation pressure at the center of the impinging jets are investigated for different inlet flow regimes (i.e., saturated steam: $x \geq 0.7$, saturated water/two-phase: $0 \leq x < 0.7$, and subcooled water). For saturated steam and saturated water/two-phase jets, it is found that the initial stagnation pressure and break size have negligible effects on the pressure within the jets except for very small breaks (D ~ 0.005 m) in saturated water/two-phase jets, but the quality has significant effects. For subcooled water jets, the degree of subcooling and the break size have significant effects on pressure distribution. Experimental data from the small and large breaks show different nondimensional pressure profiles within the jets, which may be due to the difference in the surface area to volume ratio. However, there is a lack of systematically scaled experimental data for model development. The difference between free and impinging jets are investigated by comparing the measured stagnation pressure in free and impinging jets. It is

found that the difference is small for the saturated steam and saturated-water/two-phase jets; however, the difference is significant for subcooled water jets, which requires additional investigation. For the pressure at the center of the jets, it is found that a power law can be used for the free jets, while either a power law or an exponential function can be used for the impinging jets to predict the dimensionless pressure at the center of the target.

Using the compiled experimental databank, the Standard model (ANSI/ANS-58.2, 1988) and the two-phase jet load model (NUREG/CR-2913) are evaluated. Important jet impingement parameters including stagnation pressure, jet core length, thrust coefficient, and critical mass flux are evaluated. The stagnation pressures measured in experiments are compared with those calculated by the models for saturated steam, saturated water/two-phase, and subcooled water jets. It is found that the stagnation pressure within the saturated steam jets can generally be predicted well by the Standard model except for those at far distances ($z > 3.3\ D$). However, the dimensionless stagnation pressures at these distances are less than 0.07. For saturated water/two-phase jets, the Standard model can predict the stagnation pressure well for the large-scale tests ($D > 0.28$ m), but underestimates those in the medium-scale and small-scale tests ($D < 0.15$ m). For subcooled water jets, the NUREG/CR-2913 can predict the data well for the conditions investigated using Marviken test data. The Standard model generally overestimates the data for subcooled water jets in the vicinity of the break plane, especially for conditions with a high degree of subcooling. Significant overestimation in stagnation pressure is observed for subcooled water jets with a high degree of subcooling ($\Delta T > 40$ °C), which is because the critical mass flux is overestimated using the Homogeneous Equilibrium Model (HEM). For subcooled water jets with a low degree of subcooling ($\Delta T < 20$ °C), HEM underestimates the data. Unlike HEM, Henry-Fauske model always overpredicts the experimental data, but the degree of overestimation increases as the degree of subcooling decreases. The critical mass flux for saturated steam jets and saturated water/two-phase jets can be predicted well by the isentropic expansion model and HEM, respectively. In addition to critical mass flux, the jet core length and the distance between the break plane and the asymptotic plane are also investigated, which are important parameters to define the zone of influence for jets. It is found that the Standard model can predict the jet core length well for conditions with a low degree of subcooling ($\Delta T < 30$ °C), but underestimates it for conditions with a high degree of subcooling ($\Delta T > 30$ °C). The distance between the break plane and the asymptotic plane can be predicted well for saturated steam jets, but is overpredicted with 100% difference for saturated-water/two-phase and subcooled water jets. The prediction uncertainty is due to the one-dimensional assumption of jets and the constant enthalpy assumption to determine the density at the asymptotic plane. In addition, the thrust coefficients employed in the Standard model agree well with the experimental data for different jet regimes.

Based on the results of the literature review and model evaluation, the Standard model is revised and the model guidance is developed to address the potential non-conservatisms. Newly developed correlations for the jet core length and the stagnation pressure are implemented into the revised code. It is shown that the revised code can provide improved predictions for stagnation pressure for the conditions investigated in saturated water/two-phase jets and subcooled water jets. On the potential blast wave effect, the transcript of the Advisory Committee on Reactor Safeguards (ACRS) subcommittee meeting is first reviewed. However, technical basis that can provide one to assess the conditions whether the blast wave is or is not significant could not be established. To quantify the potential blast wave effect, an approach is developed based on the equivalent weight of TNT. To employ this approach, the released energy in the equivalent of TNT needs to be determined from jet impingement. In the current work, this released energy is calculated by two approaches by employing several conservative assumptions. The static overpressure and the reflected pressure to quantify the

potential blast wave effect are calculated. For jet geometry, dynamic models to predict the jet spreading angle for saturated steam and flashing jets are reviewed. It is found that the jet spreading angle for saturated steam jets in the Standard model generally agrees with the dynamic model in literature (Morita et al., 2016) for a wide range of initial vessel stagnation pressure conditions. Regarding the pressure distribution within jets, it is confirmed that edge-peaking pressure profiles can be observed for saturated steam jets at far distances from the break plane ($z > 3.3\ D$); however, the dimensionless pressures at these locations are generally less than 0.07. Regarding the jet dynamic loading effect, justifications provided by Kauffman et al. (2019) indicate that dynamic amplification and resonance of impinged downstream structures and components might not occur for jet impingement in nuclear power plants.

6 REFERENCES

Alam, M.M.A., S. Matsuo, T. Setoguchi, "Supersonic Moist Air Jet Impingements on Flat Surfaces," Journal of Thermal Sciences, 19:51-59, 2010.

American Nuclear Society, "Design Basis for Protection of Light Water Nuclear Power Plant against the Effects of Postulated Pipe Rupture," ANSI/ANS-58.2, 1988.

Areva NP Inc., "Pipe Rupture External Loading Effects on U.S. EPR Essential Structures, Systems, and Components," ANP-10318NP, 2013, ADAMS Accession No. ML13213A037.

Baker, W.E., P.A. Cox, J.J. Kulesz, R.A. Strehlow,P.S. Westine, P.S., *Explosion Hazards and Evaluation*, Elsevier, 1983.

Biggs, J.M., *Introduction to Structural Dynamics*, McGraw-Hill, New York, 1964.

Brode, H.L., "Numerical Solutions of Spherical Blast Waves," J. Appl. Phys. 26, 766–775, 1955.

Celata, G.P., M. Cumo, F. D'Annibale, G.E. Farello, "Two-Phase Flow Models in Unbounded Two-Phase Critical Flows," Nucl. Eng. Des. 97, 211–222, 1986.

Cullis, I. G., "Blast Waves and How They Interact with Structures," BMJ Military Health 147.1, 16-26, 2001.

Cumo, M., "Unbounded Critical Flows and Jet Forces," Advances in Two-Phase Flow and Heat Transfer, Springer, Dordrecht, 555-576, 1983.

D'Auria, F., P. Vigni, "Fluid Dynamic Analysis of Steam Water Flow from a Pressure Vessel," Workshop on Jet Impingement and Pipe Whip, Genoa, Italy, June 29 - July 1, Ansaldo Impianti, SIS-81-R-06, 1981.

Fauske, H.K., "Contribution To the Theory of Two-Phase, One-Component Critical Flow," Argonne National Laboratory, ANL-6633, 1962.

Forrest, C.F., K.S. Shin, W.I. Midvidy,R.E. Pauls, Wahba, N., "Measurement of Impact Loads and Expansion of Flashing Water Jets," Nucl. Eng. Des. 99, 53–61, 1987.

Friedlander, F.G., "The Diffraction of Sound Pulses. I. Diffraction by a Semi-Infinite Plane," Proc. R. Soc. A Math. Phys. Eng. Sci. 186, 322–344, 1946.

Healzer, J.M., A. Singh, "A Simplified Model for Jet Expansion and Impingement Loads," EPRI Report NP-4418, 1986.

Henderson, B., "The Connection between Sound Production and Jet Structure of the Supersonic Impinging Jet," J. Acoust. Soc. Am. 111, 735–747, 2002.

Henry, R.E., H.K. Fauske, "The Two-Phase Critical Flow of One-Component Mixtures in Nozzles, Orifices, and Short Tubes," Journal of Heat Transfer, 93(2), 179-187, 1971.

Ho, C.-M., N.S. Nosseir, "Dynamics of an Impinging Jet. Part 1. The Feedback Phenomenon," J. Fluid Mech. 105, 119–142, 1981.

Isozaki, T., T. Yano, N. Miyazaki, R. Kato, R. Kurihara, Ueda, S., Miyazono, S., "Test Results of Jet Discharge from a 4 Inch Pipe under BWR LOCA Conditions," Nucl. Eng. Des. 79, 81–92, 1984.

Isozaki, T., S. Miyazono, "Experimental Study of Jet Discharging Test Results under BWR and PWR Loss of Coolant Accident Conditions," Nuclear Engineering Design 96, 1-9, 1986.

Kastner, W., R. Rippel, "Jet Impingement Forces on Structures - Experimental and Empirical Calculation Methods," Nucl. Eng. Des. 105, 269–284, 1988.

Kauffman, S., M. Charrouf, J.K. Yoon, S.G. Lee, T.J. Kim, "Evaluation of Potential for High Energy Line Break Jet Dynamic Loading Including Feedback Amplification and Resonance Effects," Int. Conf. Nucl. Eng. Proceedings, ICONE 2019-May, 2019.

Kawanishi, K., M. Isono, F. Masuda, T. Nakatogawa, "Experimental Study on Jets Formed under Discharges of High-Pressure Subcooled Water and Steam-Water Mixtures from Short Nozzles," Nucl. Eng. Des. 95, 243–251, 1986.

Kim, S.M., I. Mudawar, "Review of Two-Phase Critical Flow Models and Investigation of the Relationship between Choking, Premature CHF, and CHF in Micro-channel Heat Sinks," Int. J. Heat Mass Transf. 87, 497–511, 2015.

Kitade, K., T. Nakatogawa, H. Nishikawa, K. Kawanishi, C. Tsuruto, "Experimental Study of Pipe Reaction Force and Jet Impingement Load at the Pipe Break," 5th SMiRT Conference, Berlin, p. F 6/2, 1979.

Kitamura, K., E. Shima, "Towards Shock-Stable and Accurate Hypersonic Heating Computations: A New Pressure Flux for AUSM-family Schemes," Journal of Computational Physics, 245, 62–83, 2013.

Krotiuk, W.J., C. Boyd, "Analysis Report: Comparisons of Jet Calculations to Test Data," U.S. Nuclear Regulatory Commission, , ADAMS Accession No. ML121010475, 2012.

Lahey, R.T., F.J. Moody, *The Thermal Hydraulics of a Boiling Water Reactor*, ANS Monograph, 1977.

Lees, F., *Lees' Loss Prevention in the Process Industries: Hazard Identification, Assessment and Control*, Butterworth-Heinemann, 2012.

Los Alamos National Laboratory, "Knowledge Base for the Effect of Debris on Pressurized Water Reactor Emergency Core Cooling Sump Performance," LA-UR-03-0880, NUREG/CR-6808, 2003.

Luxat, J.C., "A Generalized Analytical Model of Fluid Jet Characteristics," International Topical Meeting on Nuclear Reactor Thermal Hydraulics NURETH-17, Xian, China, 2017.

Marklund, J.-E., "Evaluation of Free Jet and Jet Impingement Tests with Hot Water and Steam Part 1", Studsvik Report, SKI--84092(pt1), STUDSVIK/NR-85/54(pt1), 1985.

Marklund, J.-E., "Evaluation of Free Jet and Jet Impingement Tests with Hot Water and Steam Part 2", Studsvik Report, SKI--84092(pt2), STUDSVIK/NR-85/54(pt2), 1985.

Masuda, F., T. Nakatogawa, K. Kawanishi, M. Isono, "Experimental Study of an Impingement High-Pressure Steam Jet," Nucl. Eng. Des. 67, 273–286, 1981.

Moody, F.J., "Maximum Flow Rate of a Single Component, Two-Phase Mixture," J. Heat Transfer 87, 134, 1965.

Moody, F.J., "Maximum Two-Phase Vessel Blowdown from Pipes," J. Heat Transfer 88: 285, 1966.

Moody, F.J., "Prediction of Blowdown Thrust and Jet Forces," ASME Paper 69-HT-31, 1969.

Moody, F.J., "Fluid Reaction and Impingement Loads," Struct. Des. Nucl. Plant Facil. 219–262, 1973.

Morita, R., Y. Uchiyama, S. Watanabe, S. Takahashi, Q. Xu, N. Takamura, "Evaluation Of Jet Impact Region And Fluid Force Generated From Ruptured Pipes (1) Numerical And Experimental Evaluation Of Affected Region By Steam Jet," 2016 24th International Conference on Nuclear Engineering, ICONE 24. Charlotte, North Carolina, 2016.

Morita, R., S. Watanabe, S. Takahashi, N. Takamura, "Evaluation Of Jet Impact Region And Fluid Force Generated From Ruptured Pipes (4) Numerical Evaluation Of Affected Region By Flashing Jet Flow," 2018 26th International Conference on Nuclear Engineering, ICONE26, London, England, 2018.

Neff, M., "A Visual Model for Blast Waves and Fracture," Master of Science Thesis, University of Toronto, Toronto, Canada, 1998.

NEI, "Pressurized Water Reactor Sump Performance Evaluation Methodology, Pressurized Water Reactor Sump Performance Evaluation Methodology," NEI 04-07, Volume 1, 2004, ADAMS Accession No. ML050550138.

NEI, "Pressurized Water Reactor Sump Performance Evaluation Methodology, Safety Evaluation by the Office of Nuclear Reactor Regulation Related to NRC Generic Letter 2004-02, Revision 0, December 6, 2004," NEI 04-07, Volume 2, 2004, ADAMS Accession No. ML050550156.

Nosseir, N.S., C.-M. Ho, *On the Feedback Phenomenon of An Impinging Jet*, Los Angeles Dept. of Aerospace Engineering, 1979.

OECD Nuclear Energy Agency, Marviken Report MXD-101, The Marviken Full Scale Jet Impingement Tests, Facility Description, February, 1982.

OECD Nuclear Energy Agency, Marviken Report MXD-212, The Marviken Full Scale Jet Impingement Tests, Test 12 Results, March, 1982.

Petrovic, M.M., V.D. Stevanovic, "Two-Component Two-Phase Critical Flow," Faculty of Mechanical Engineering Transactions, Vol. 44, pp. 109-114, 2016.

Ransom, V.H., "Comments on GSI-191 Models for Debris Generation," 2004, ADAMS Accession No. ML050830341.

Russel, J.H., A.M.C. Chan, "Two-Phase Jet Reaction Forces on a Diagonally Ruptured Pipe: Experimental Measurement," Ontario Hydro Research Division Report 90-193-K, 1991.

Sandervaag, O., Serkiz, A. W., Riekert, T., Hyvärinen, J., Gisclon, J., Green, T., "Knowledge Base for Emergency Core Cooling System Recirculation Reliability," Nuclear Energy Agency, NEA/CSNI/R (95)11, 1996.

Schneider, E., D. Ballew, W. Gurecky, "Calibration and Benchmarking of Single- and Two-Phase Jet CFD Models," University of Texas at Austin, 2012, ADAMS Accession No. ML12145A438.

Shapiro, A.H., *The Dynamics and Thermodynamics of Compressible Fluid Flow*, Vol. I, Ronald Press, New York, 1953.

Smith, P., J. Hetherington, *Blast and Ballistic Loading of Structures*, CRC Press, 1994.

Takahashi, S., Q. Xu, N. Takamura, R. Morita, Y. Uchiyama, S. Watanabe, "Evaluation Of Jet Impact Region And Fluid Force Generated From Ruptured Pipes (2) Evaluation Of Fluid Force Using Computational Fluid Dynamics Analysis," 2016 24th International Conference on Nuclear Engineering, ICONE 24, 2016.

Tam, C.K.W., K.K. Ahuya, "Theoretical Model of Discrete Tone Generation by Impinging Jets," J. Fluid Mech. 214, 67–87, 1990.

Teske, M.E., A.H. Boschitsch, T.B. Curbishley, "Zone of Influence as Defined by Computational Fluid Dynamics", C.D.I. Report No. 96-01, October, 1996 (from "Utility Resolution Guide for ECCS Suction Strainer Blockage, Volume 3", NED0-32686-A, ADAMS Accession No. ML092530505.)

Todreas, N.E., Kazimi, M.S., *Nuclear Systems Volume I: Thermal Hydraulic Fundamentals*, CRC press, 2011.

Tomasko, D., G.G. Weigand, S.L. Thompson, "A model for two-phase jet loading," Workshop on Jet Impingement and Pipe Whip, Genoa, Italy, June 29 - July 1, 1981.

U.S. Department of the Army, "Structures to Resist the Effects of Accidental Explosions," UFC 3-340-02, Washington, DC, 2008.

U.S. Nuclear Regulatory Commission, "Advisory Committee on Reactor Safeguards Meeting of the Subcommittee on Thermal-Hydraulics", September 22-23, 2004, 2004 Advisory Committee on Reactor Safeguards (ACRS) Meeting Schedule and Related Documents, https://www.nrc.gov/reading-rm/doc-collections/acrs/agenda/2004.

U.S. Nuclear Regulatory Commission, "Determination of Rupture Locations and Dynamic Effects Associated with the Postulated Rupture of Piping," Standard Review Plan, Section 3.6.2, NUREG-0800, 2015, ADAMS Accession No. ML14230A035.

U.S. Nuclear Regulatory Commission, "Nuclear Regulatory Commission Conclusions Regarding Pressurized Water Reactor Owners Group Response to Request for Additional Information Dated January 25, 2010 Regarding Licensee Debris Generation Assumptions for GSI-191," ADAMS Accession No. ML100570364, 2010.

Wallis, G., "The ANSI/ANS Stanard 58.2-1988: Two-Phase Jet Model," U.S. Nuclear Regulatory Commission, 2004, ADAMS Accession No. ML050830344.

Webb, S.W., "Evaluation of Subcooled Water Thrust Forces," Nucl. Technol. 31, 48–52, 1976.

Weggel, D.C., "Blast threats and blast loading," *Blast Protection of Civil Infrastructures and Vehicles Using Composites*, Woodhead Publishing, 3-43, 2010..

Weigand, G.G., S.L. Thompson, D. Tomasko, "Two-Phase Jet Loads," U.S. Nuclear Regulatory Commission, NUREG/CR-2913, 1983, ADAMS Accession No. ML073510076.

Xu, Q., S. Takahashi, N. Takamura, R. Morita, Y. Uchiyama, S. Watanabe, "Evaluation of Jet Impact Region and Fluid Force Generated from Ruptured Pipes (3) Evaluation of Established Standards," 24th International Conference on Nuclear Engineering, ICONE 24, 2016.

Yano, T., "Void Fraction Measurement by a Gamma-Ray Densitometer under Instantaneous Pipe Rupture," Nucl. Eng. Des. 79, 101–113, 1984.

Yano, T., T. Isozaki, S. Ueda, N. Miyazaki, R. Kurihara, R. Kato, S. Miyazono, "An Experimental Study of Blowdown Thrust and Jet Forces for a Pipe under Boiling Water Reactor Loss-of-Coolant Accident Conditions," Nucl. Sci. Eng. 88, 386–395, 1984.

Yano, T., N. Miyazaki, T. Isozaki, "Transient analysis of blowdown thrust force under PWR LOCA," Nucl. Eng. Des. 75, 157–168, 1983.

Zaman, K.B.M.Q., "Spreading Characteristics of Compressible Jets from Nozzles of Various Geometries," J. Fluid Mechanics, 383, pp. 197-228, 1999.

Zerkle, D., "NRC Update #1: Prediction of Supersonic Expansions Relevant to Debris Generations", LA-UR-00-2247, A study prepared at Los Alamos National Laboratories, 2000.

Zivi, S.M., "Estimation of Steady-State Steam Void-Fraction by Means of the Principle of Minimum Entropy Production," J. Heat Transf. 86, 247–251, 1964.

APPENDIX A

OVERVIEW OF JET CODE

NRC staff developed a FORTRAN 77 code to implement the jet impingement model as defined in the appendices of the ANSI/ANS-58.2 (1988). This code is referred to as Jet11p4. Jet11p4 also includes steam tables and critical mass flux models, which are integral to the jet calculations. Jet11p4 was used for calculations of the ANSI/ANS-58.2 (1988) jet model in Chapter 3 of this NUREG. NRC updated Jet11p4 to include the recommendations in Table 4-1. This updated code is referred to as Jetrev12p0, and it was used for the calculations in Chapter 4.

Multiple activities were performed to develop confidence in Jet11p4 and Jetrev12p0. The critical mass flux models in Jet11p4 were compared to and agreed with values computed by the TRAC/RELAP Advanced Computation Engine (TRACE) and values reported in the literature. The implementation of the ANSI/ANS-58.2 (1988) jet model was investigated by comparing values calculated by Jet11p4 and Jetrev12p0 to values calculated by hand. For Jet11p4, the ANSI/ANS-58.2 (1988) jet impingement pressures were hand calculated for Marviken Test 5 conditions (see Figure B-4, t = 10 seconds) and Marviken Test 6 conditions (see Figure B-5, t = 5 seconds). Hand calculated stagnation pressures along the periphery of the jet and at the jet centerline in regions 1, 2, and 3 all agreed with output from Jet11p4. It is important to note that the hand calculated values used the diameter of the asymptotic plane calculated by the code, and this calculation was not verified other than careful visual inspection.

These calculations were repeated for Jetrev12p0. The hand calculated results agreed with the code output. Additional hand calculations were performed to target the code changes from Jet11p4 and Jetrev12p0. In particular, the Marviken Test 5 hand calculation was repeated except a break diameter of 3 inches was used instead of 11.77 inches. Marviken Test 6 was also repeated using a break diameter of 0.12 inches and ΔT_{sub} = 60°F. The values calculated using Jetrev12p0 agreed with the hand calculated values.

Last, Jet11p4 was compared to a previous NRC report (ML121010475) that investigated the ANSI/ANS-58.2 (1988) jet impingement model. The calculations in ML121010475 were performed using a different version of the FORTRAN 77 code, referred to as Jetrev10p0. Jet11p4 and jetrev10p0 were compared for Marviken Test 5 (t = 10 s) and Marviken Test 6 (t = 5 s) conditions. It was found that the values calculated by the two codes did not agree for the following reasons:

   (a) For Marviken Test 6, Jetrev10p0 used the Homogeneous Equilibrium Model (HEM) to calculate the critical mass flux, while Jet11p4 used the Henry Fauske model. The critical mass flux for Marviken Test 6 conditions at t = 5 s was 7967 lbm/ft^2/s and 9523 lbm/ft^2/s for the HEM and Henry Fauske model, respectively.

   (b) Jetrev10 calculates Equation (D-7) in ANSI/ANS-58.2 as

$$P_{oe} = F_j / A_e \tag{A-1}$$

which is incorrect. It should be

$$P_{oe} = F_j / A_{je} \tag{A-2}$$

where

$$A_{je} = C_T A_e \tag{A-3}$$

where C_T = 2 and 1.26 for subcooled and saturated conditions, respectively. As a result, Jetrev10p0 is missing a factor of 1.26 for saturated conditions and a factor of 2 for subcooled conditions in the denominator of Eq. D-7.

(c) The differences are also attributed to a combination of a few smaller code changes: (1) Jet11p4 calculates the gauge pressure for the stagnation pressure, while jetrev10 calculates the absolute pressure; (2) The local jet diameter was used in Equation (D-11) in the *if* statement for the definition of F_c in jetrev10, while D_j is used in jet11p at $z=z_c$; (3) Jetrev10 did not include the second comment in Equation (D-2) of the Standard, while it is included in Jet11p4.

APPENDIX B

EVALUATION OF THE STANDARD MODEL BY MARVIKEN TESTS

Table B-1 Test 1 Conditions in Marviken Tests for ANSI/ANS-58.2 (1988) Evaluation (D_{eff} = 0.5 m)

| Analyzed Time (s)	5	10	20	35	50	59
Input and Measured Stagnation Pressure	4,330	3,926	3,461	3,146	2,874	1,315
Fluid State	$\Delta T = 20.5°C$	$\Delta T = 14.5°C$	$\Delta T = 6.5°C$	$\alpha = 0.1$ $x = 0.0022$	$\alpha = 0.078$ $x = 0.0015$	$\alpha = 0.99$ $x = 0.91$
Measured Fluid Temperature (°C)	234.5	234.7	235.4	236.5	231.5	192.1
Calculated Fluid Temperature (°C)	234.6	234.7	235.4	236.5	231.5	192.1
Measured Containment Pressure (kPa)	287.5	308	274.1	192.9	163.3	130.7
Measured Critical Mass Flux (kg/m^{2}s)	42,724.0	35,546.0	25,860.0	16,125.0	15,130.0	1,617.9
Calculated Critical Mass Flux (kg/m^{2}s)	50,542.9 by HF	44,985.5 by HF	37,876.8 by HF	14,500.7 by HEM	13,630.2 by HEM	1,966.0 by IE
(Calculated – Measured)/Measured Mass Flux	18.3%	26.6%	46.5%	-10.1%	-9.9%	21.5%
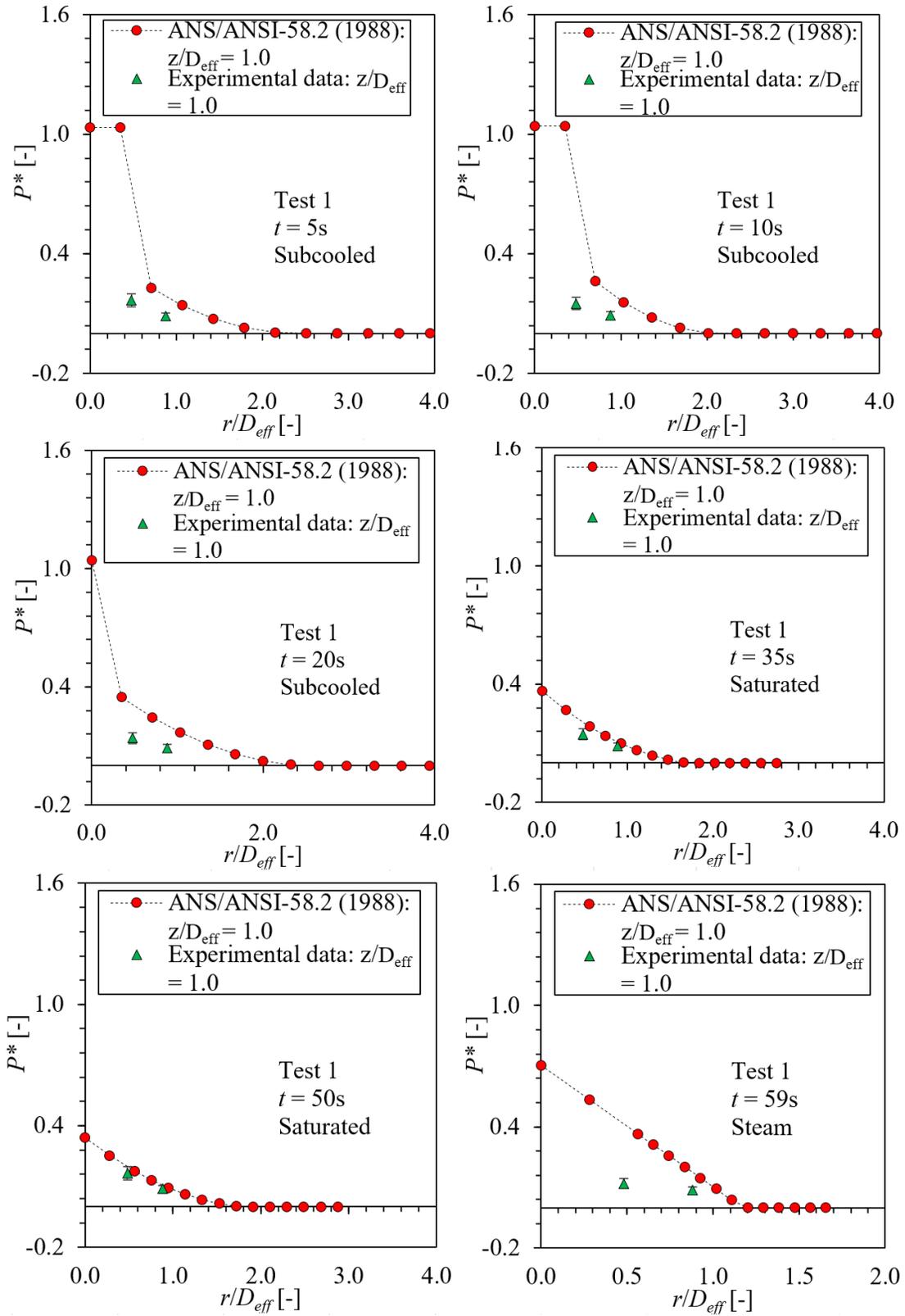
Figure B-1 Comparison between Standard Model Calculation and Experimental Data at Beam 1 in Test 1 of Marviken Tests. Error Bar: ±20%
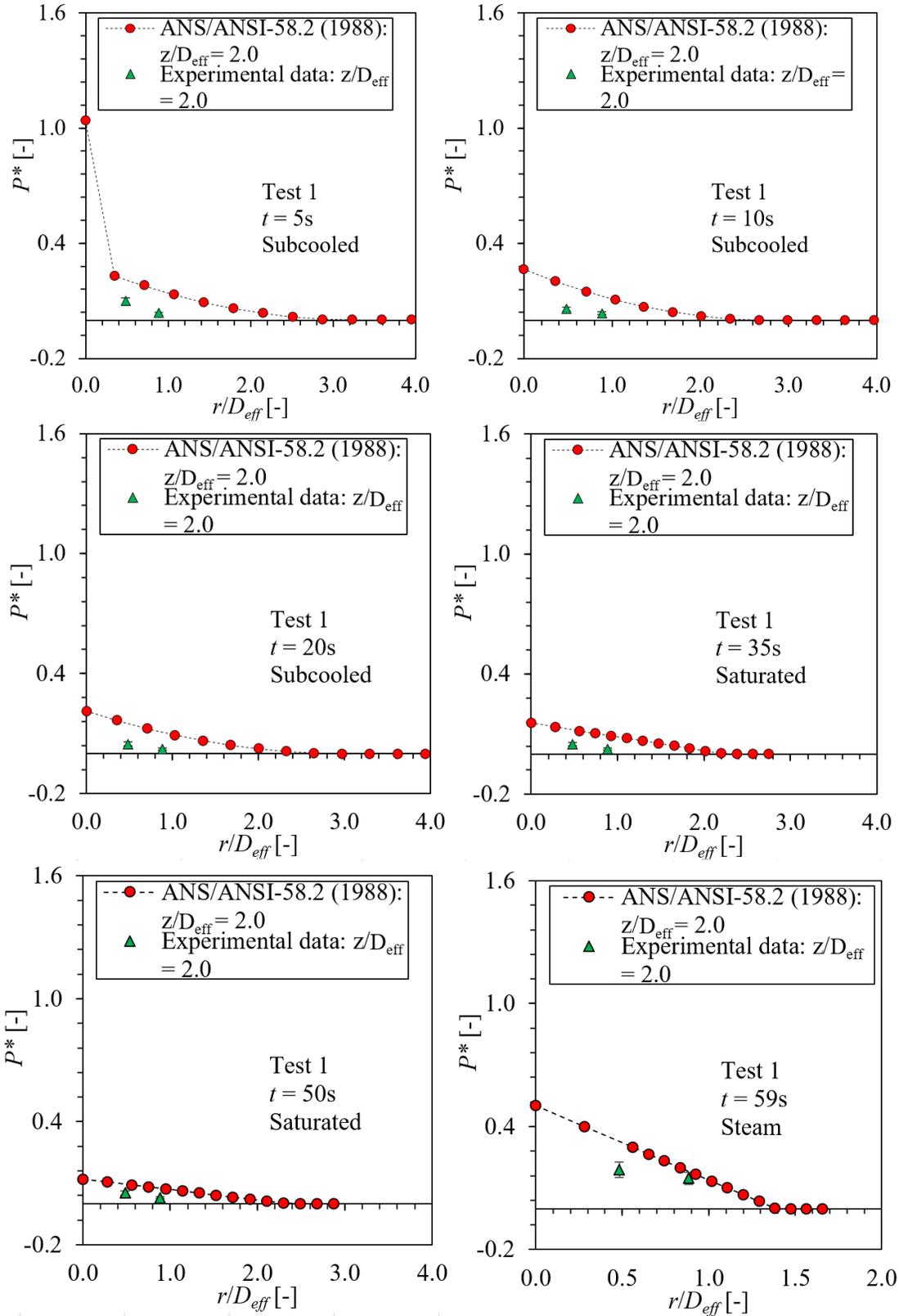
Figure B-2 Comparison between Standard Model Calculation and Experimental Data at Beam 2 in Test 1 of Marviken Tests. Error Bar: ±20%
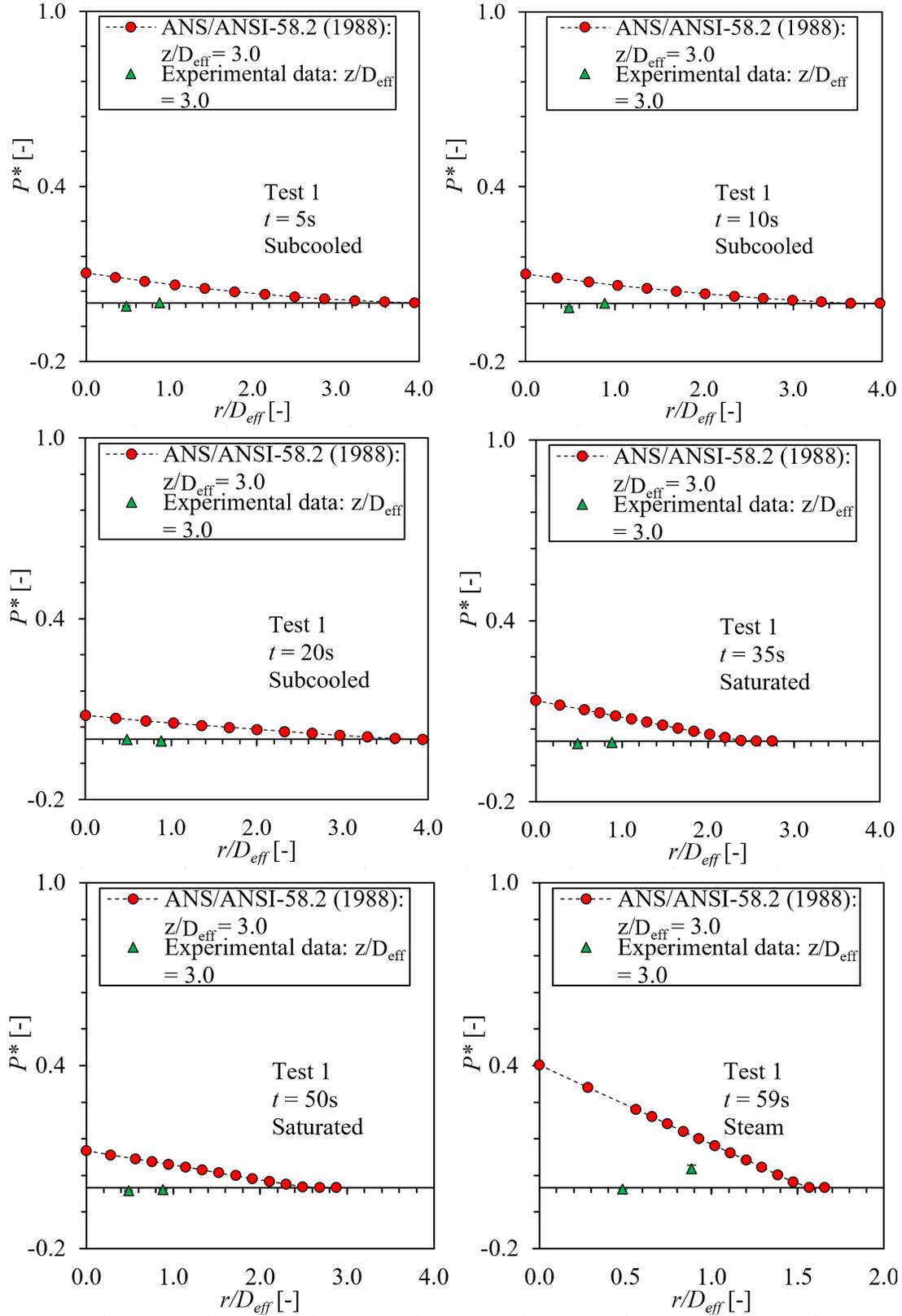
Figure B-3 Comparison between Standard Model Calculation and Experimental Data at Beam 4 in Test 1 of Marviken Tests. Error Bar: ±20%
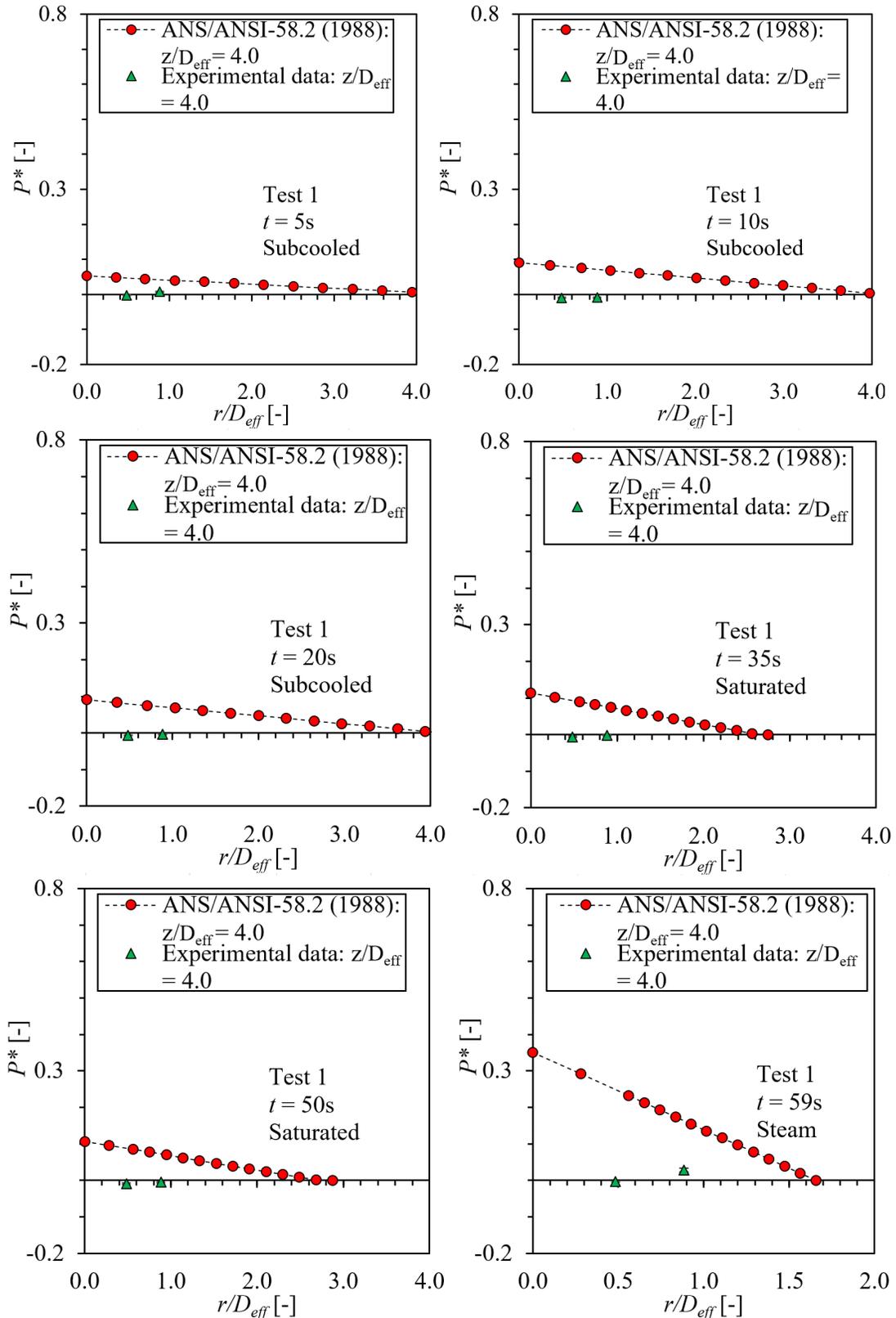
Figure B-4 Comparison between Standard Model Calculation (ANSI/ANS-58.2, 1988) and Experimental Data at Beam 6 in Test 1 of Marviken Tests. Error Bar: ±20%

Table B-2 Test 2 Conditions in Marviken Tests for ANSI/ANS-58.2 (1988) Evaluation (D_{eff} = 0.28 m)

| Analyzed Time (s)	10	20	40	50	60	80
Input and Measured Stagnation Pressure (kPa)	4,622	4,313	3,984	3,881	3,752	2,387
Fluid State	ΔT = 24.8°C	ΔT = 19.5°C	ΔT = 5.2°C	α = 0.066 x = 0.0017	α = 0.105 x = 0.0027	α = 0.996 x = 0.79
Measured Fluid Temperature (°C)	234.3	235.3	244.9	248.5	246.6	221.5
Calculated Fluid Temperature (°C)	234.3	235.3	244.9	248.5	246.6	221.5
Measured Containment Pressure (kPa)	136.4	134.3	119.4	111.7	110.1	102.5
Measured Critical Mass Flux (kg/m²s)	48,458.0	42,748.0	24,940.0	18,766.0	17,778.0	3,119.0
Calculated Critical Mass Flux (kg/m²s)	60,825.3 by HEM	49,864.3 by HF	39,655.1 by HF	16,936.2 by HEM	16,446.3 by HEM	3,996.6 by IE
(Calculated – Measured)/Measured Mass Flux	25.5%	16.6%	59.0%	-9.8%	-7.5%	28.1%
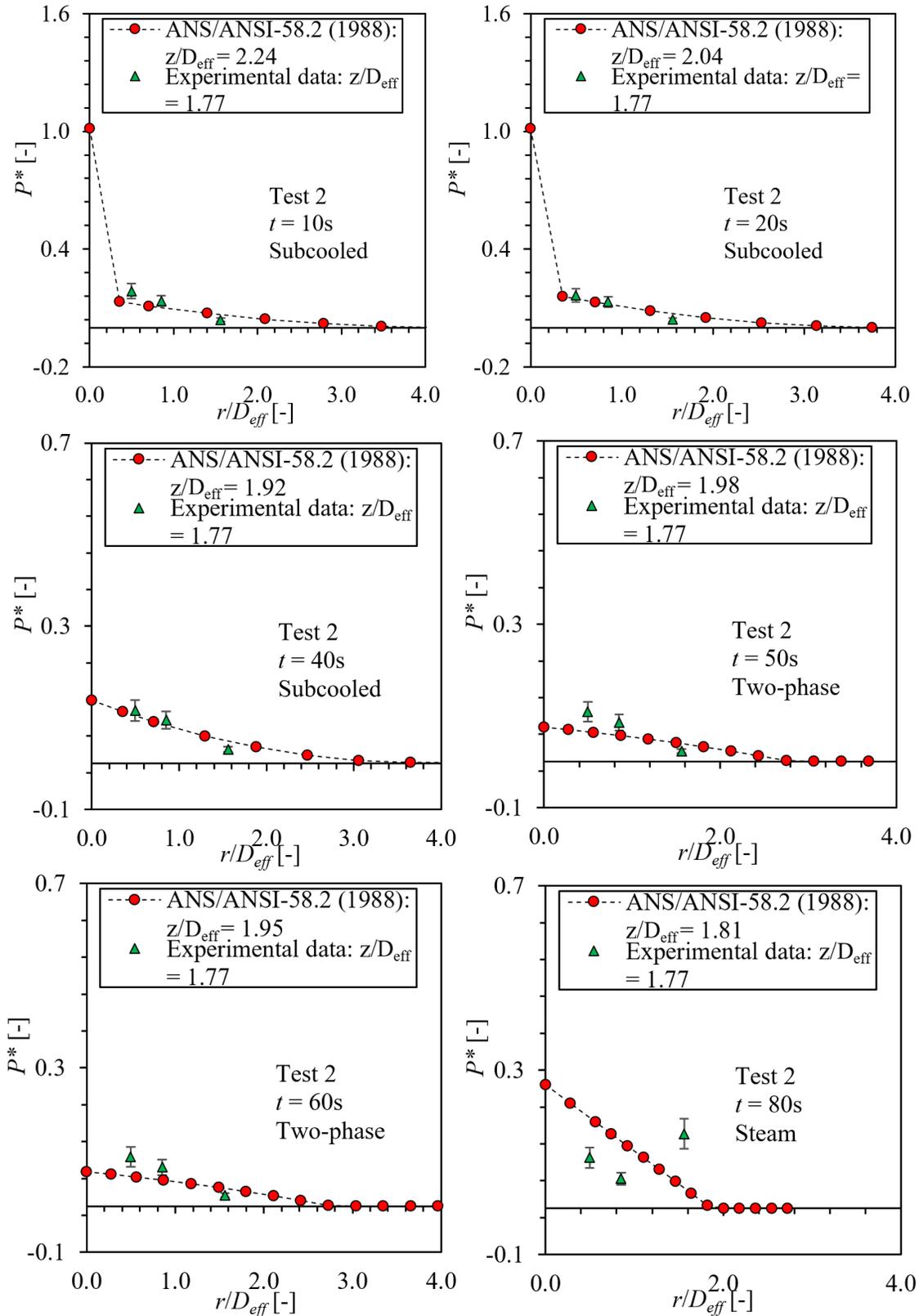
Figure B-5 Comparison between Standard Model Calculation (ANSI/ANS-58.2, 1988) and Experimental Data at Beam 1 in Test 2 of Marviken Tests. Error Bar: ±20%
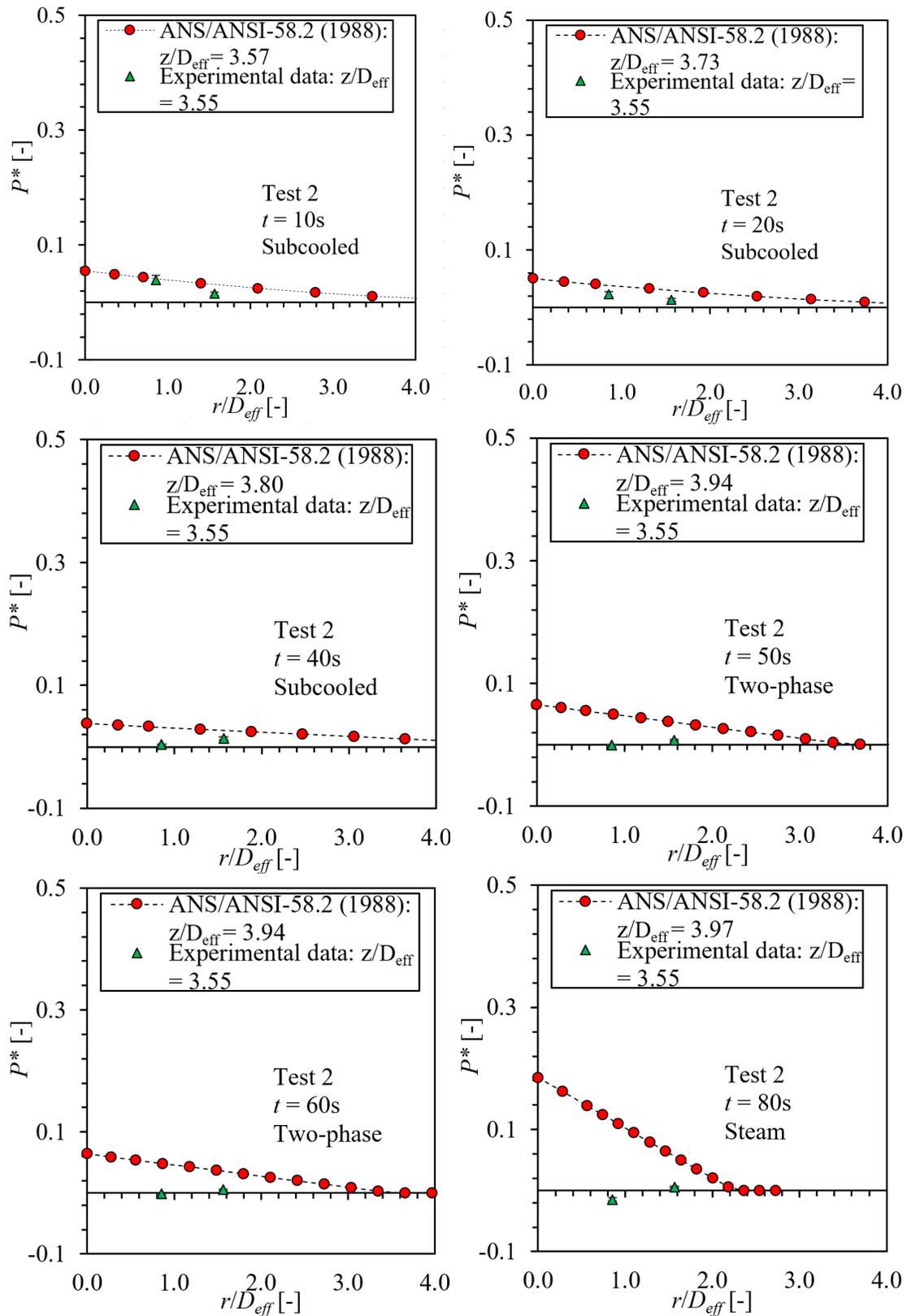
Figure B-6 Comparison between Standard Model Calculation (ANSI/ANS-58.2, 1988) and Experimental Data at Beam 2 in Test 2 of Marviken Tests. Error Bar: ±20%
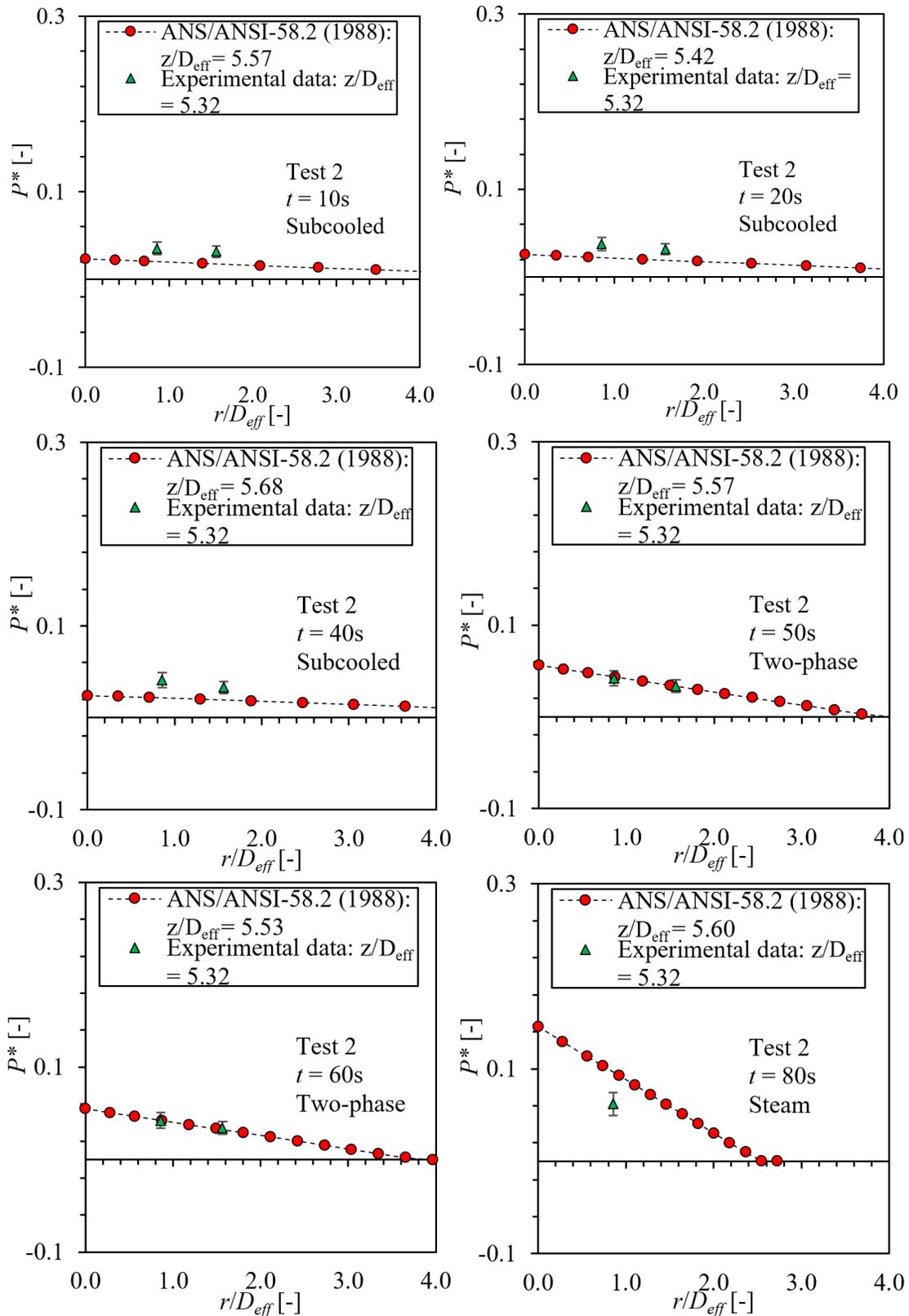
Figure B-7 Comparison between Standard Model Calculation (ANSI/ANS-58.2, 1988) and Experimental Data at Beam 4 in Test 2 of Marviken Tests. Error Bar: ±20%
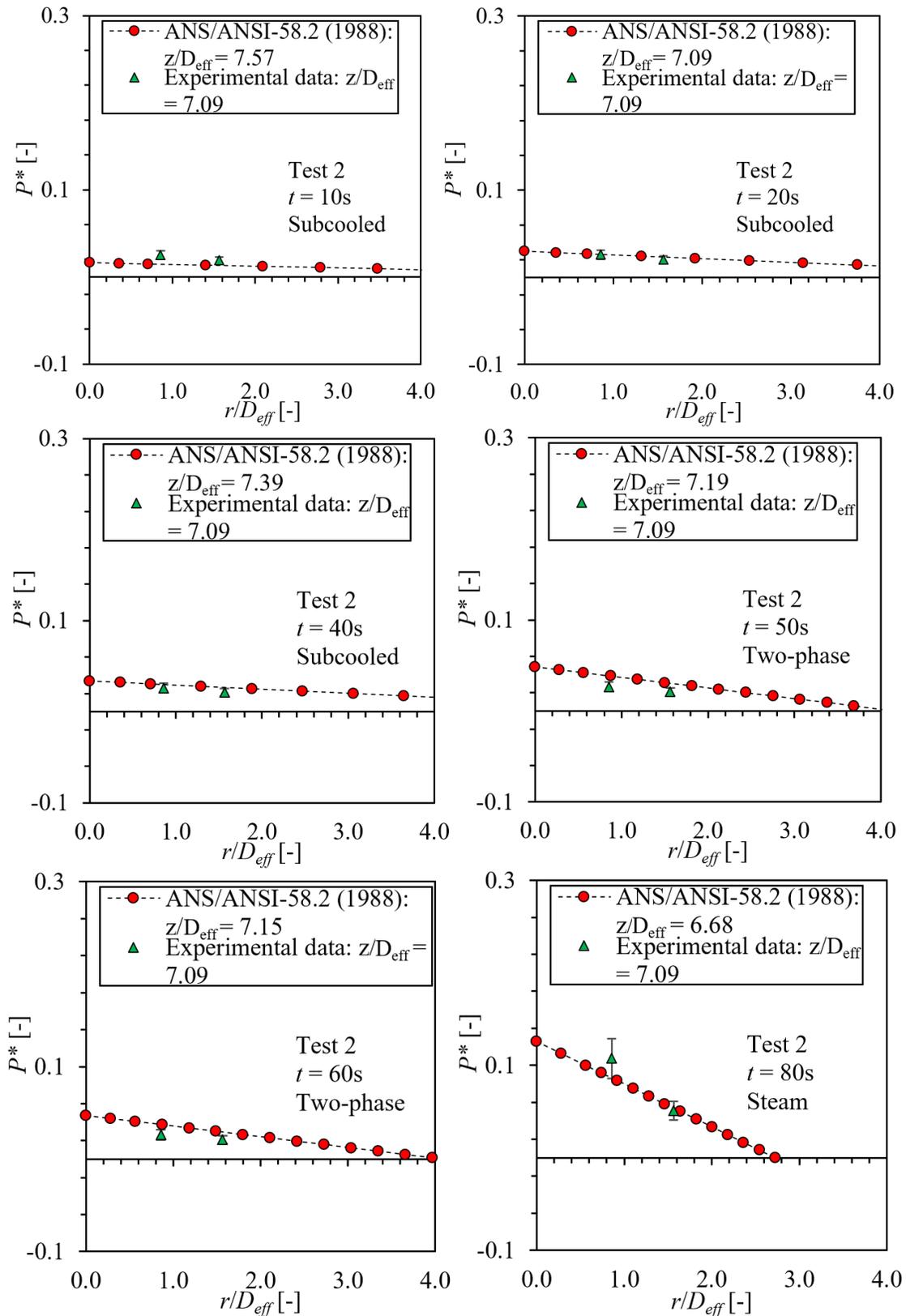
Figure B-8 Comparison between Standard Model Calculation (ANSI/ANS-58.2, 1988) and Experimental Data at Beam 6 in Test 2 of Marviken Tests. Error Bar: ±20%

Table B-3 Test 3 Conditions in Marviken Tests for ANSI/ANS-58.2 (1988) Evaluation (D_{eff} = 0.5 m)

Analyzed Time (s)	2	4	5.5
Input and Measured Stagnation Pressure (kPa)	4,604	4,390	4,161
Fluid State	$\Delta T = 45.4°C$	$\Delta T = 42.1°C$	$\Delta T = 39°C$
Measured Fluid Temperature (°C)	213.4	213.9	213.7
Calculated Fluid Temperature (°C)	213.3	213.8	213.7
Measured Containment Pressure (kPa)	221.8	260.9	277.3
Measured Critical Mass Flux ($kg/m^2 s$)	59,174.0	56,663.0	54,392.0
Calculated Critical Mass Flux ($kg/m^2 s$)	117,029.9 by HEM	108,419.3 by HEM	100,337.9 by HEM
(Calculated – Measured)/Measured Mass Flux	97.8%	91.3%	84.5%
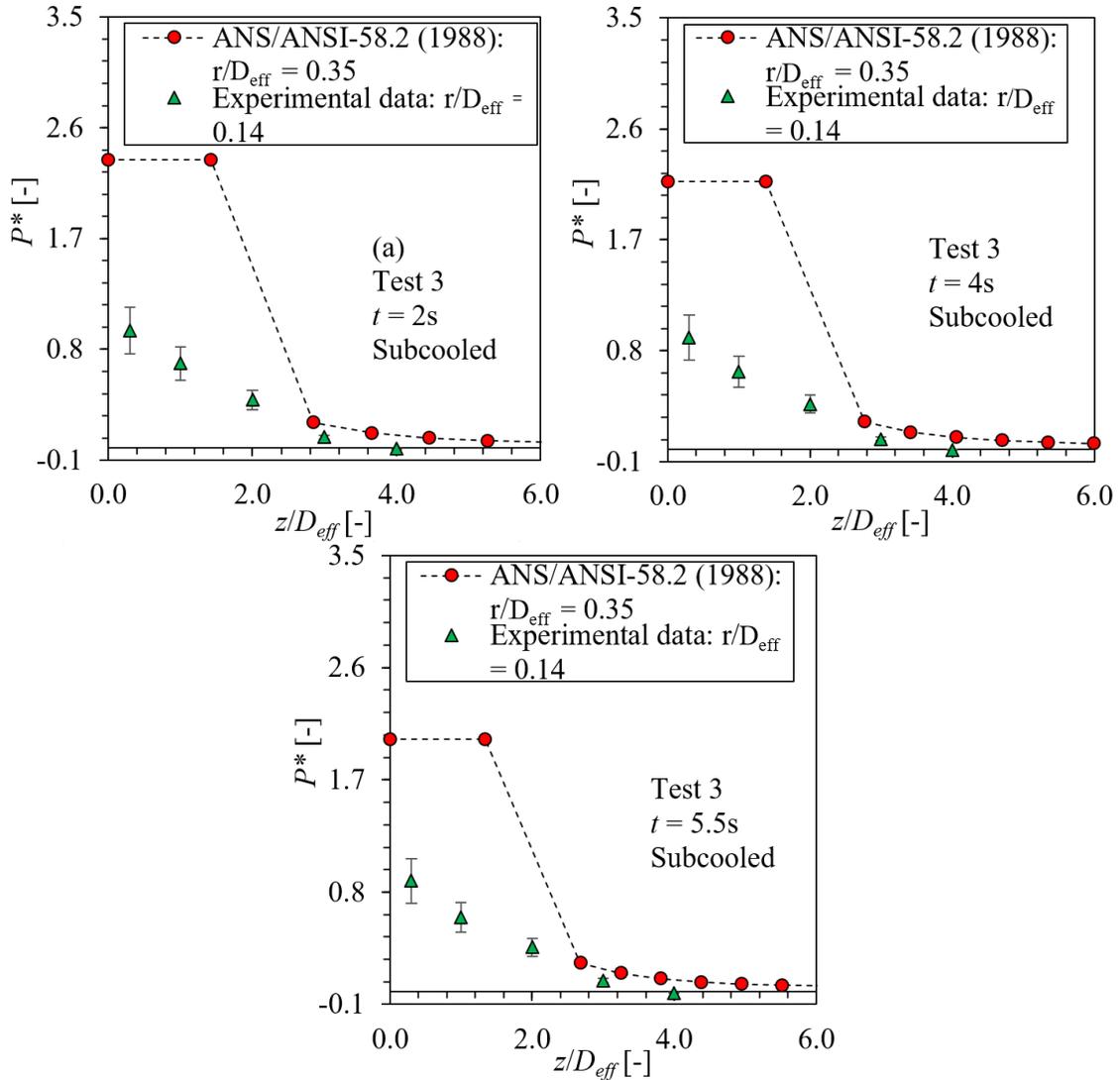
Figure B-9 Comparison between Standard Model Calculation (ANSI/ANS-58.2, 1988) and Experimental Data at the Center of Jets in Test 3 of Marviken Tests. Error Bar: ±20%
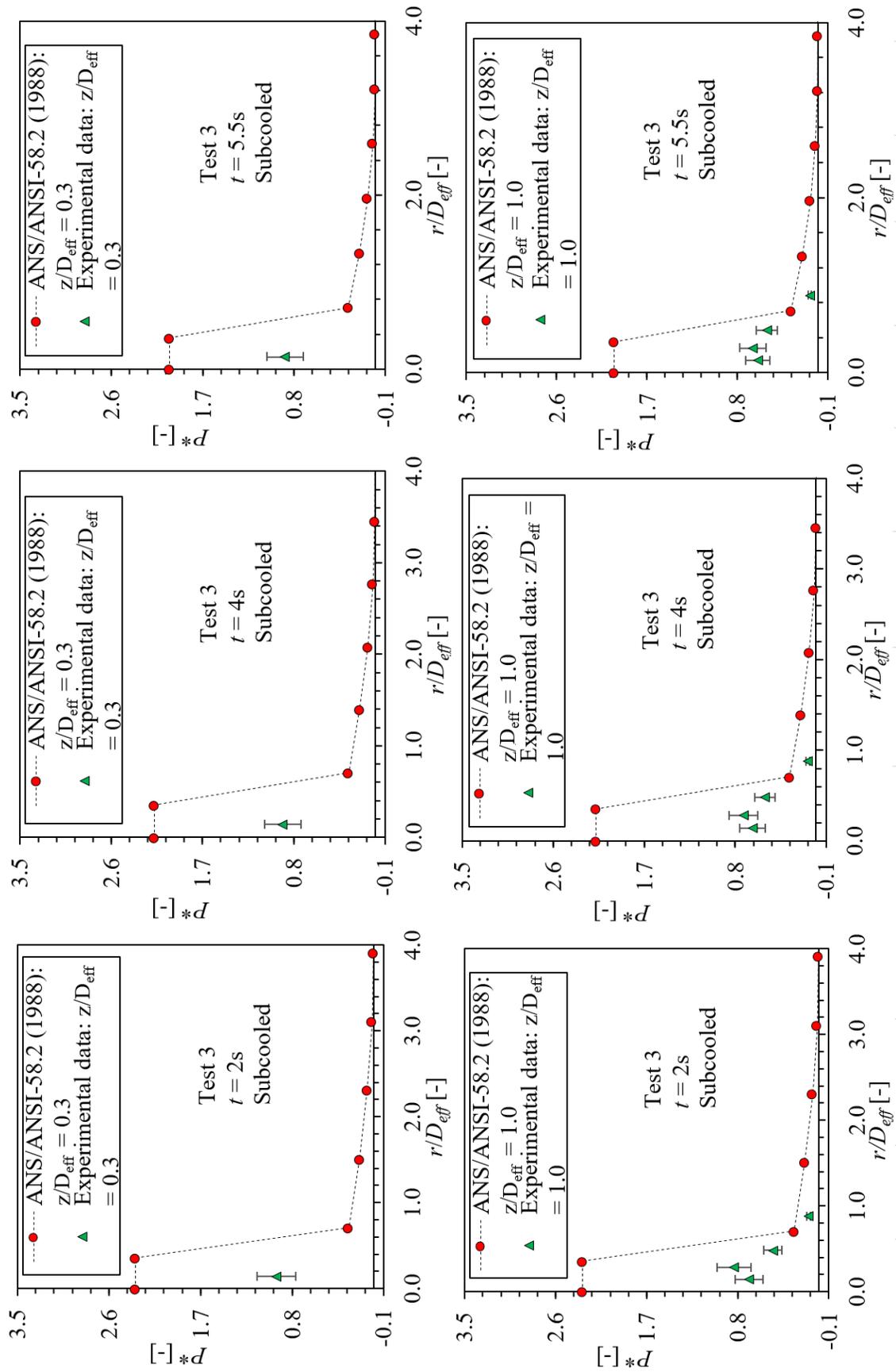
Figure B-10 Comparison between Standard Model Calculation (ANSI/ANS-58.2, 1988) and Experimental Data at Beam 0 (Upper) and Beam 1 (Lower) in Test 3 of Marviken Tests. Error Bar: ±20%
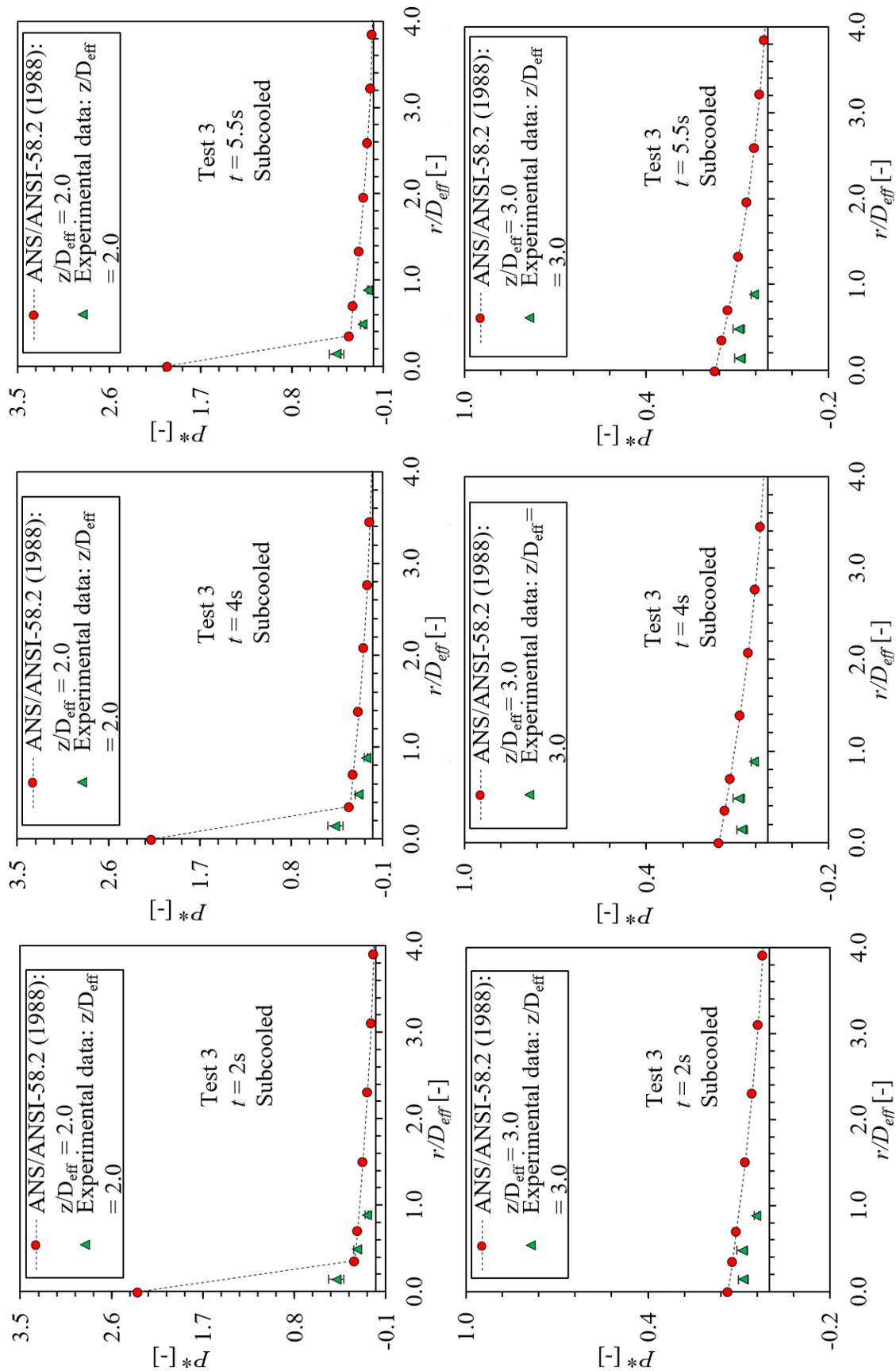
Figure B-11 Comparison between Standard Model Calculation (ANSI/ANS-58.2, 1988) and Experimental Data at Beam 2 (Upper) and Beam 4 (Lower) in Test 3 of Marviken Tests. Error Bar: ±20%
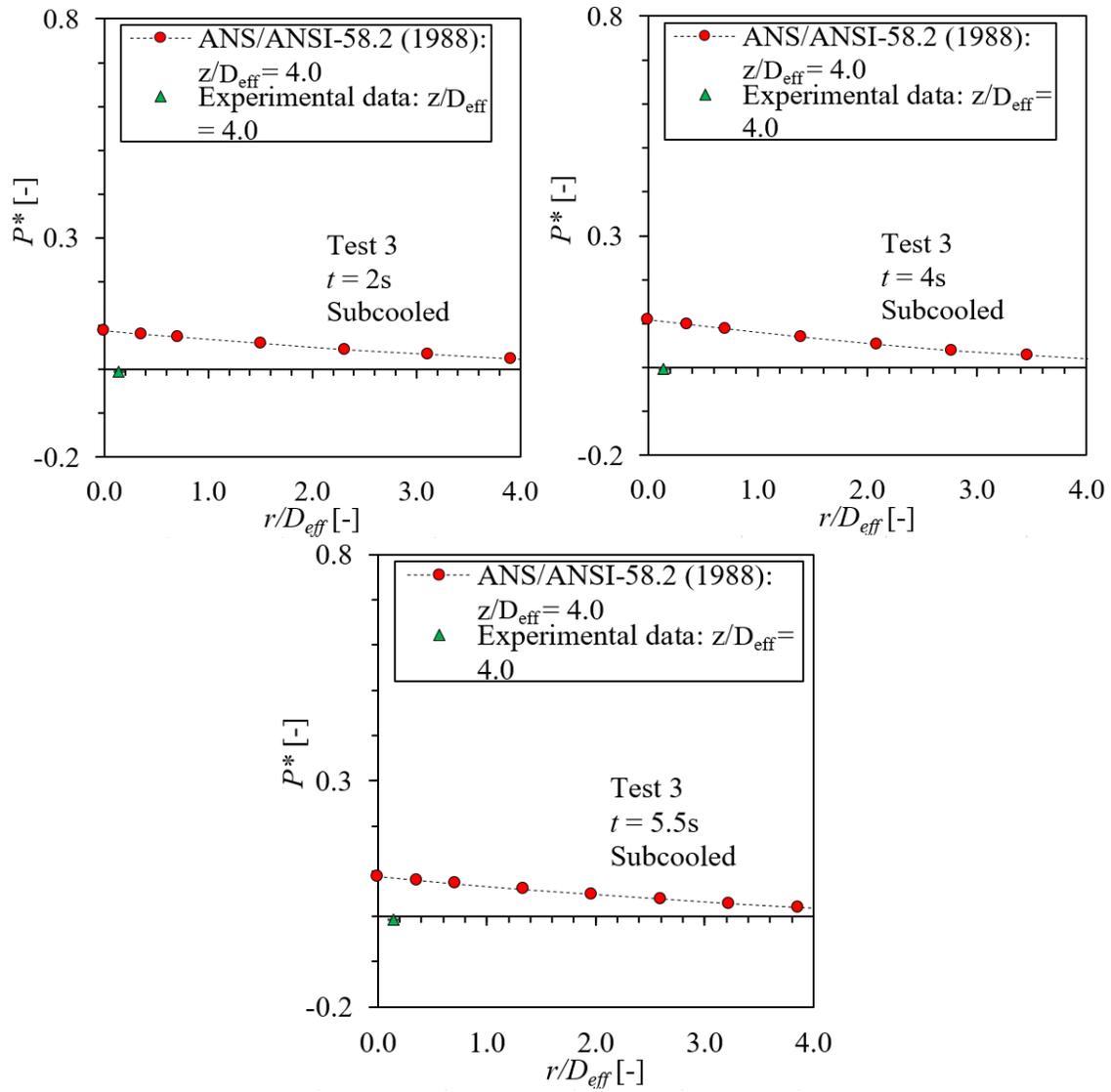
Figure B-12 Comparison between Standard Model Calculation (ANSI/ANS-58.2, 1988) and Experimental Data at Beam 5 in Test 3 of Marviken Tests. Error Bar: ±20%

Table B-4 Test 5 Conditions in Marviken Tests for ANSI/ANS-58.2 (1988) Evaluation (D_{eff} = 0.28 m)

Analyzed Time (s)	10	20	40	60	80
Input and Measured Stagnation Pressure (kPa)	4,407.65	3,859.54	3,022.26	2,414.32	1,983.91
Fluid State	α = 0.998 x = 0.97	α = 0.998 x = 0.97	α = 0.999 x = 0.99	α = 0.999 x = 0.99	α = 0.999 x = 0.97
Measured Fluid Temperature (°C)	254.8	246.6	232.4	220.5	210.0
Calculated Fluid Temperature (°C)	256.3	248.2	234.2	222.1	212.0
Measured Containment Pressure (kPa)	107	107	105	105	103
Measured Critical Mass Flux (kg/m²s)	5,812	5,084	3,868	3,059	2,343
Calculated Critical Mass Flux (kg/m²s)	6,251 by HEM	5,456 by HEM	4,277 by HEM	3,425 by HEM	2,823 by HEM
(Calculated – Measured)/Measured Mass Flux	7.6%	7.3%	10.6%	11.9%	20.4%
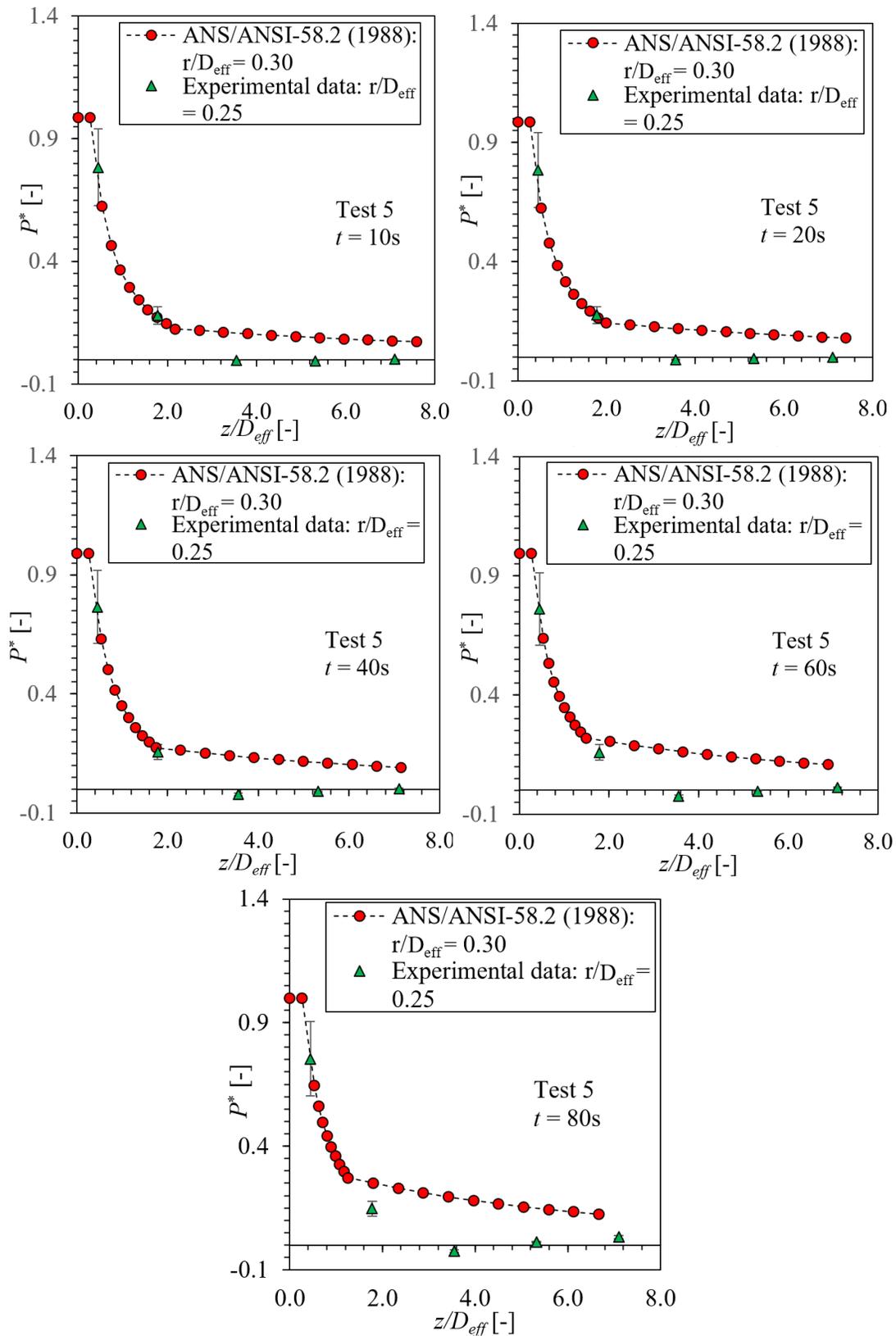
Figure B-13 Comparison between Standard Model Calculation (ANSI/ANS-58.2, 1988) and Experimental Data at the Center of Jets in Test 5 of Marviken Tests. Error Bar: ±20%
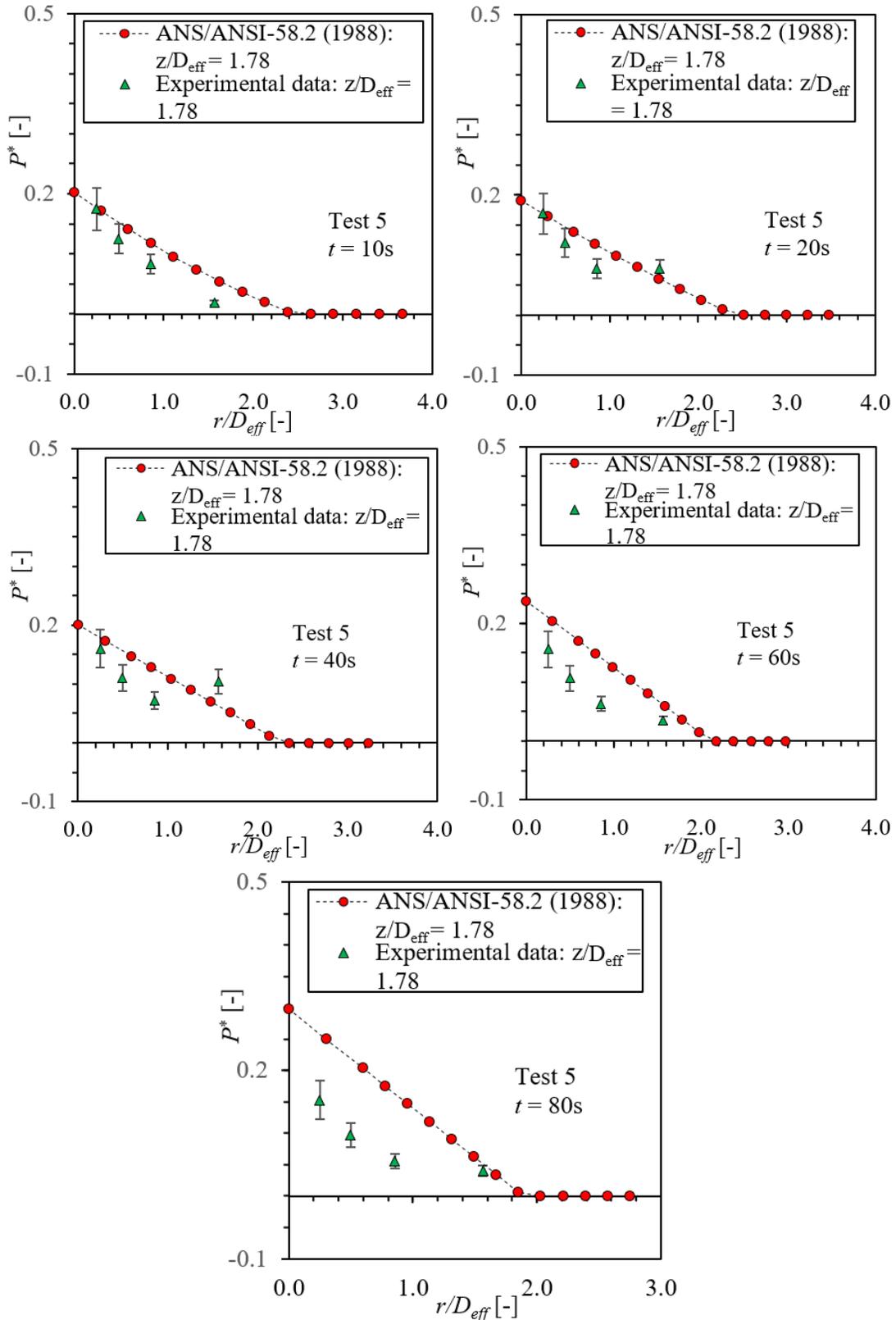
Figure B-14 Comparison between Standard Model Calculation (ANSI/ANS-58.2, 1988) and Experimental Data at Beam 1 in Test 5 of Marviken Tests. Error Bar: ±20%
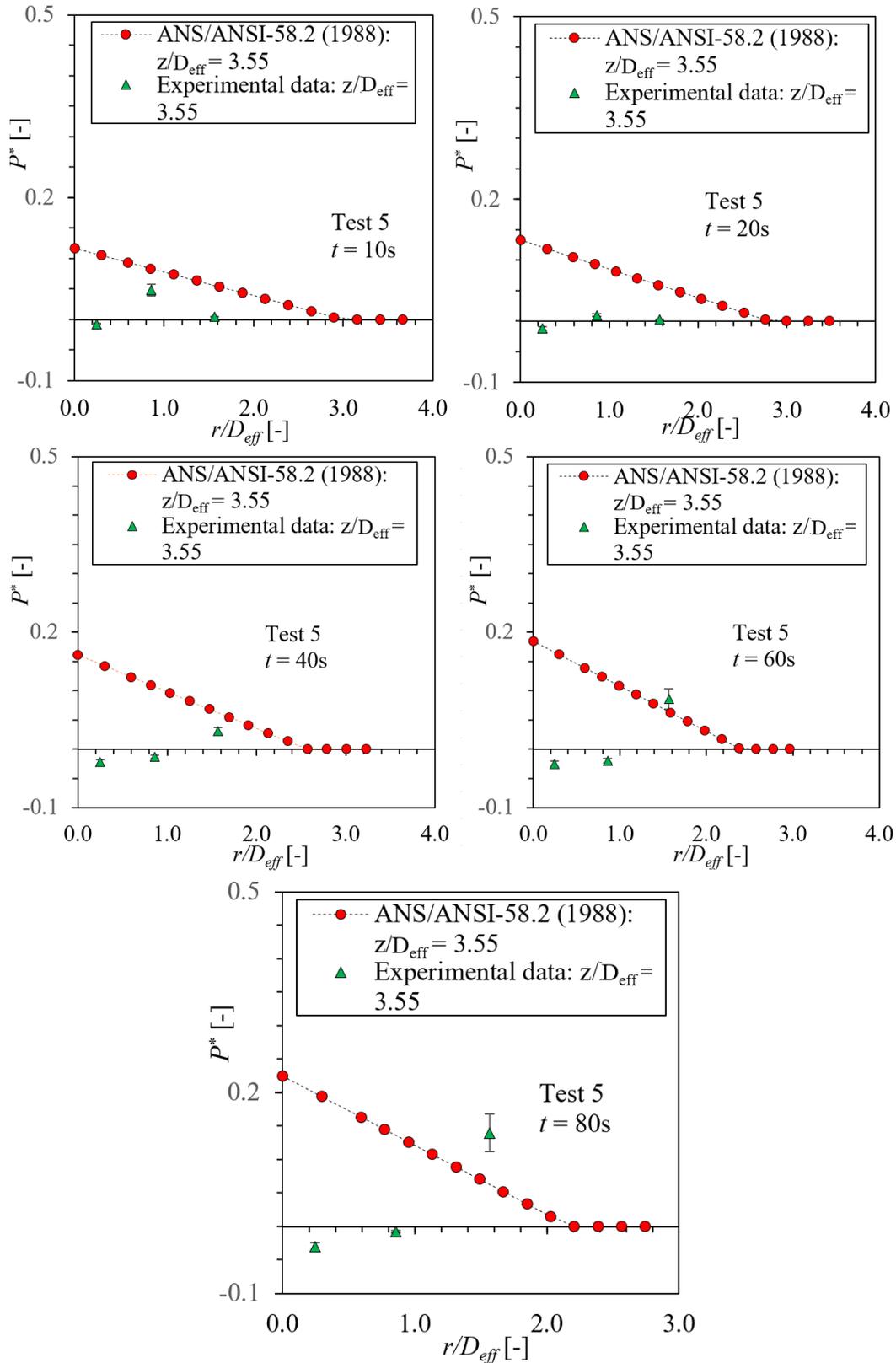
Figure B-15 Comparison between Standard Model Calculation (ANSI/ANS-58.2, 1988) and Experimental Data at Beams 2 and 3 in Test 5 of Marviken Tests. Error Bar: ±20%
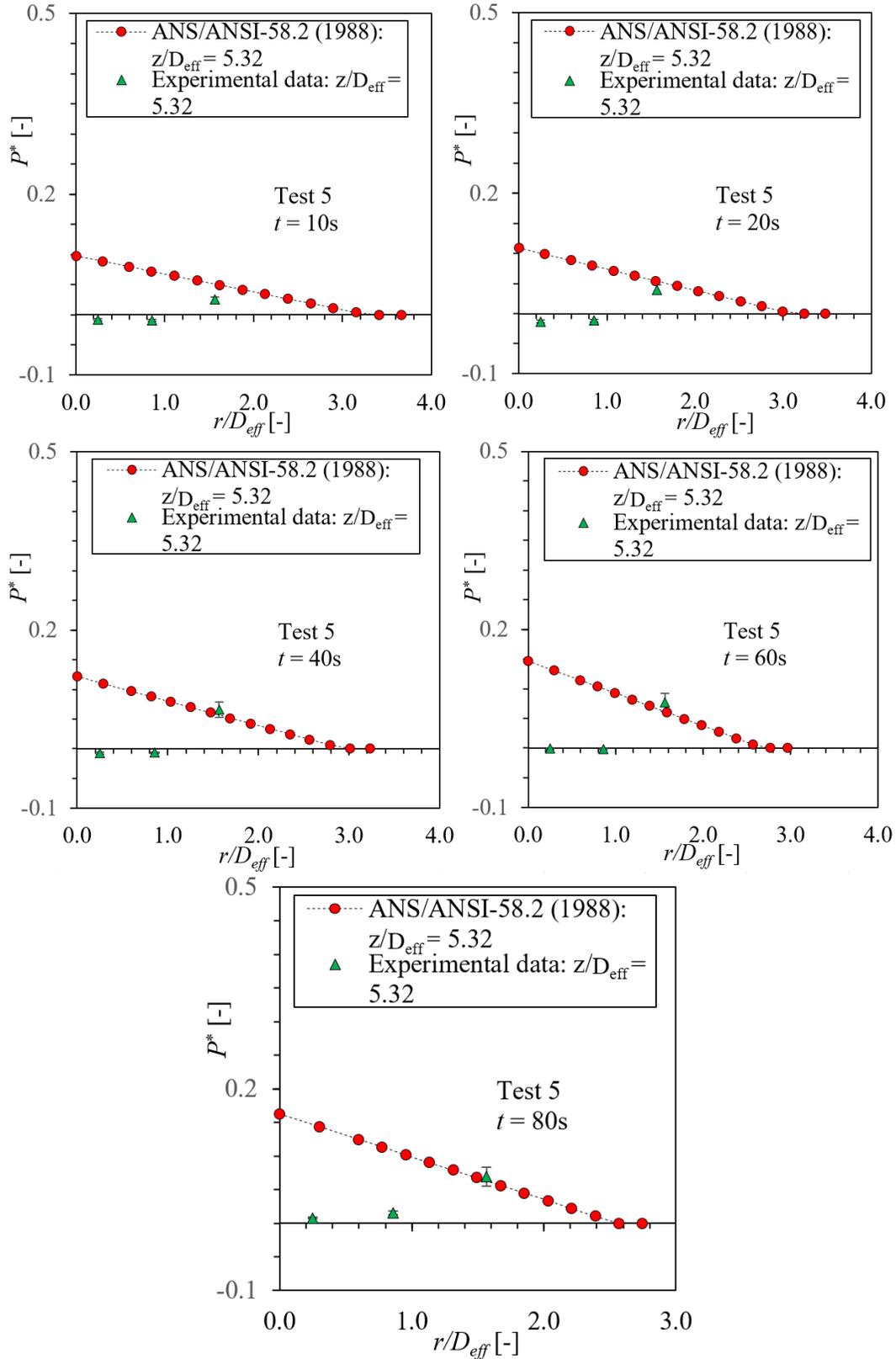
Figure B-16 Comparison between Standard Model Calculation (ANSI/ANS-58.2, 1988) and Experimental Data at Beam 4 in Test 5 of Marviken Tests. Error Bar: ±20%

Table B-5 Test 6 Conditions in Marviken Tests for ANSI/ANS-58.2 (1988) Evaluation (D_{eff} = 0.5 m)

| Analyzed Time (s)	5	10	20	45	60	75
Input and Measured Stagnation Pressure (kPa)	4,049	3,778	3,330	2,974	2,640	1,345
Fluid State	$\Delta T = 16°C$	$\Delta T = 11°C$	$\Delta T = 5°C$	$\alpha = 0.2$ $x = 0.0045$	$\alpha = 0.7$ $x = 0.04$	$\alpha = 0.995$ $x = 0.7$
Measured Fluid Temperature (°C)	233.0	233.5	234.0	232.0	226.0	189.0
Calculated Fluid Temperature (°C)	235.1	236.0	234.7	233.3	226.8	193.2
Measured Containment Pressure (kPa)	249	260	244	157	140	120
Measured Critical Mass Flux (kg/m²s)	42,000.0	35,600.0	27,000.0	17,000.0	11,000.0	2,000.0
Calculated Critical Mass Flux (kg/m²s)	46,496.6 by HF	42,140.6 by HF	36,335.1 by HF	13,741.3 by HEM	10,553.8 by HEM	2414 by IE
(Calculated – Measured)/Measured Mass Flux	10.7%	18.4%	34.6%	-19.2%	-4.0%	20.7%
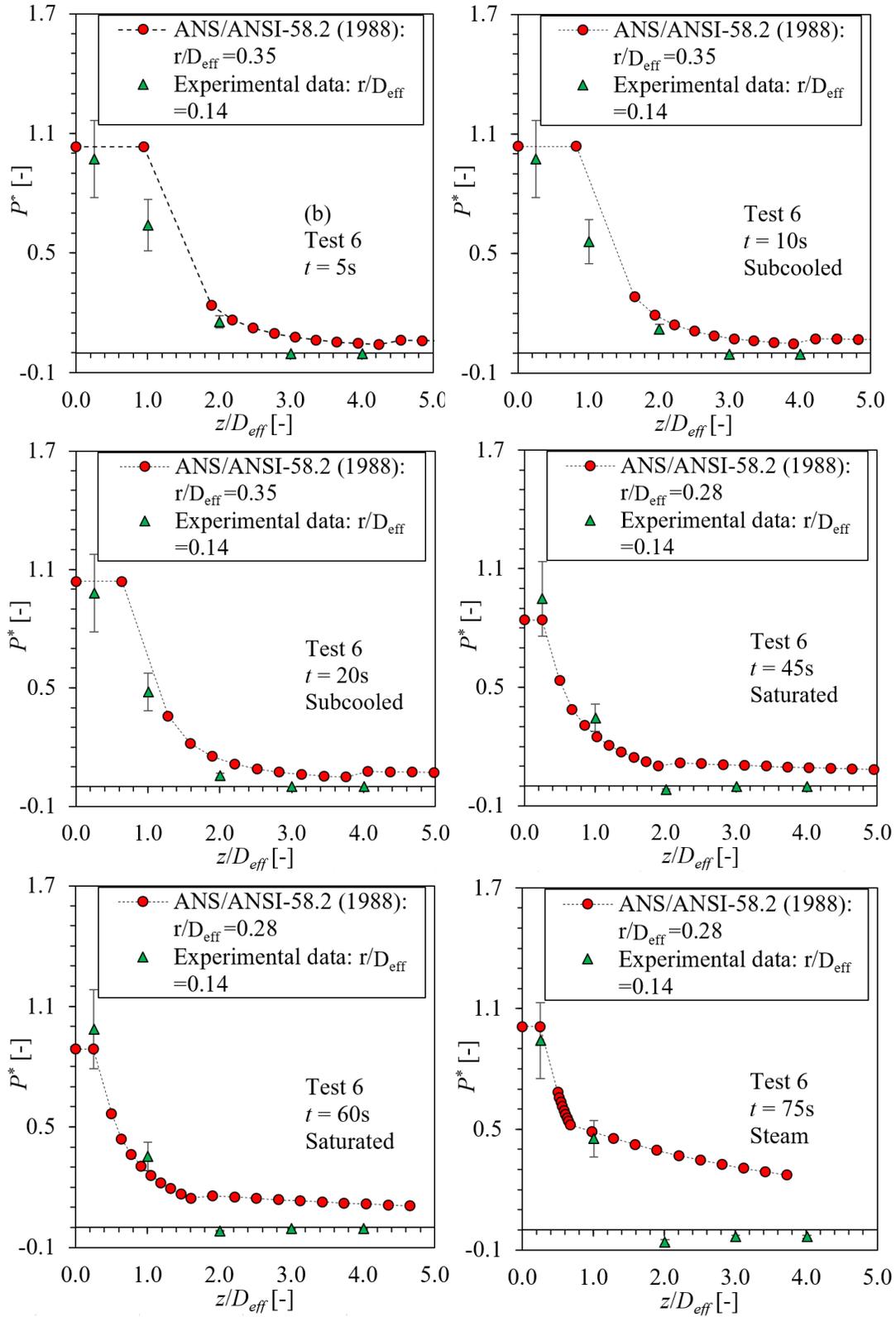
Figure B-17 Comparison between Standard Model Calculation (ANSI/ANS-58.2, 1988) and Experimental Data at the Center of Jets in Test 6 of Marviken Tests. Error Bar: ±20%
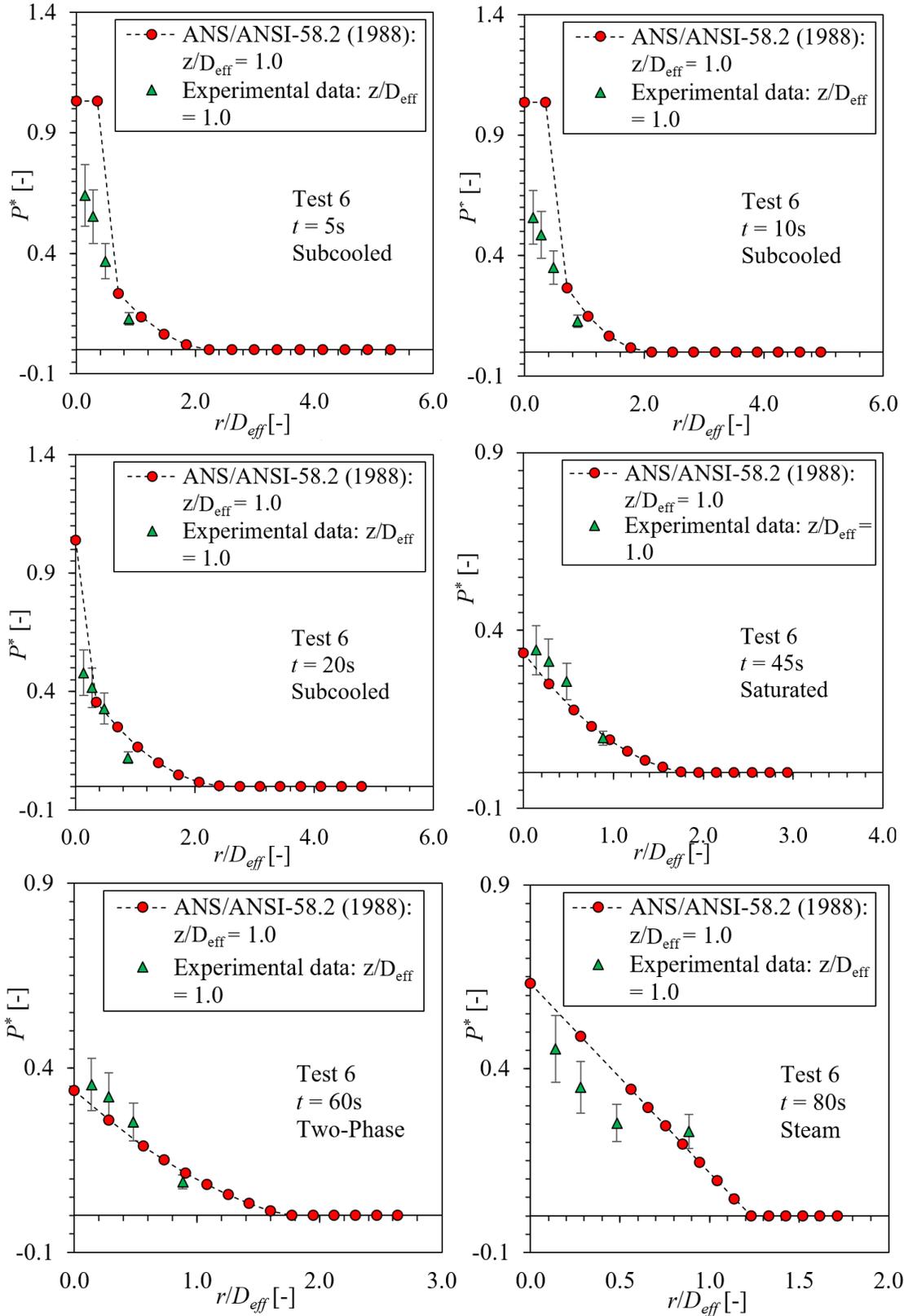
Figure B-18 Comparison between Standard Model Calculation (ANSI/ANS-58.2, 1988) and Experimental Data at Beam 1 in Test 6 of Marviken Tests. Error Bar: ±20%
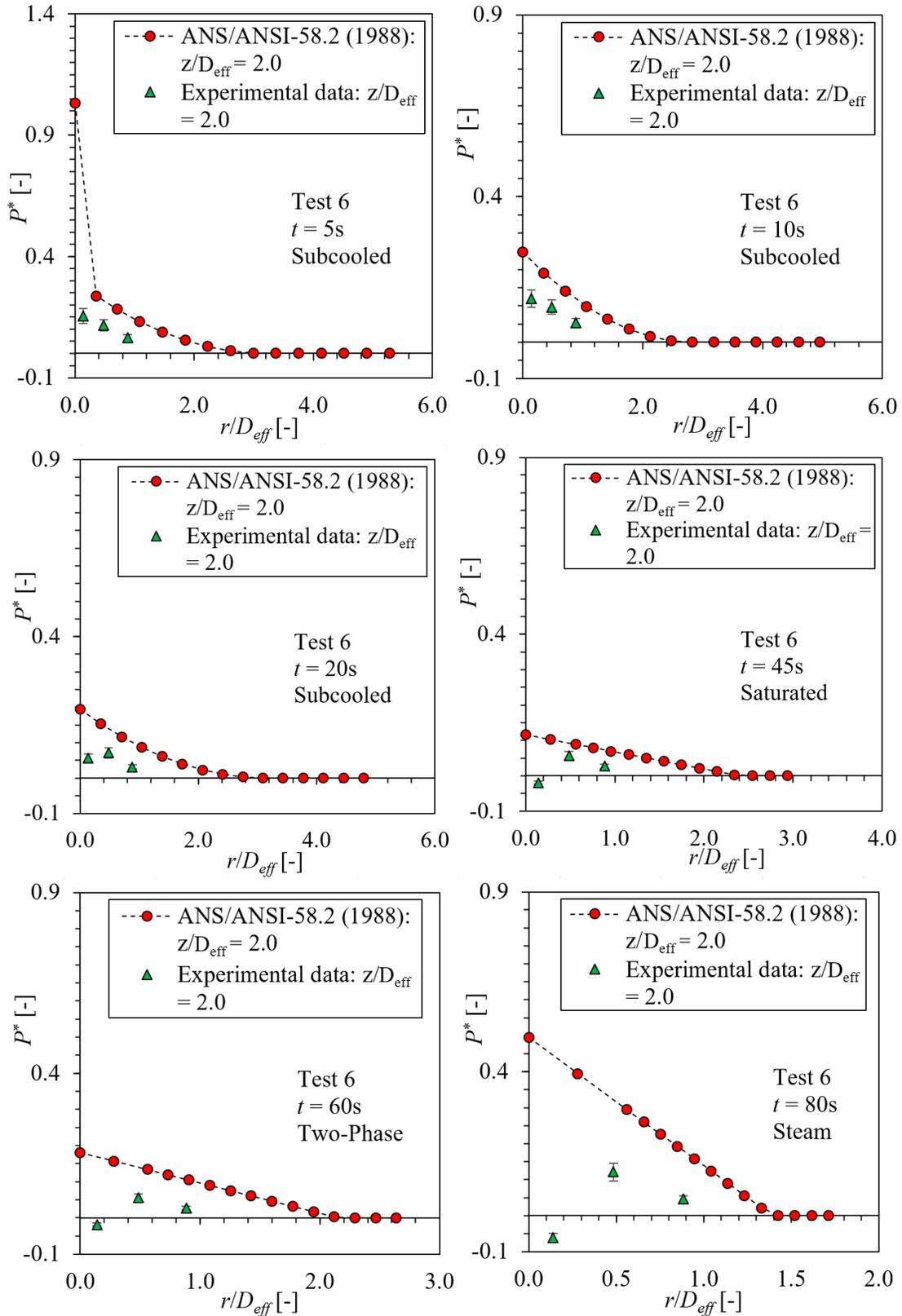
Figure B-19 Comparison between Standard Model Calculation (ANSI/ANS-58.2, 1988) and Experimental Data at Beams 2 and 3 in Test 6 of Marviken Tests. Error Bar: ±20%
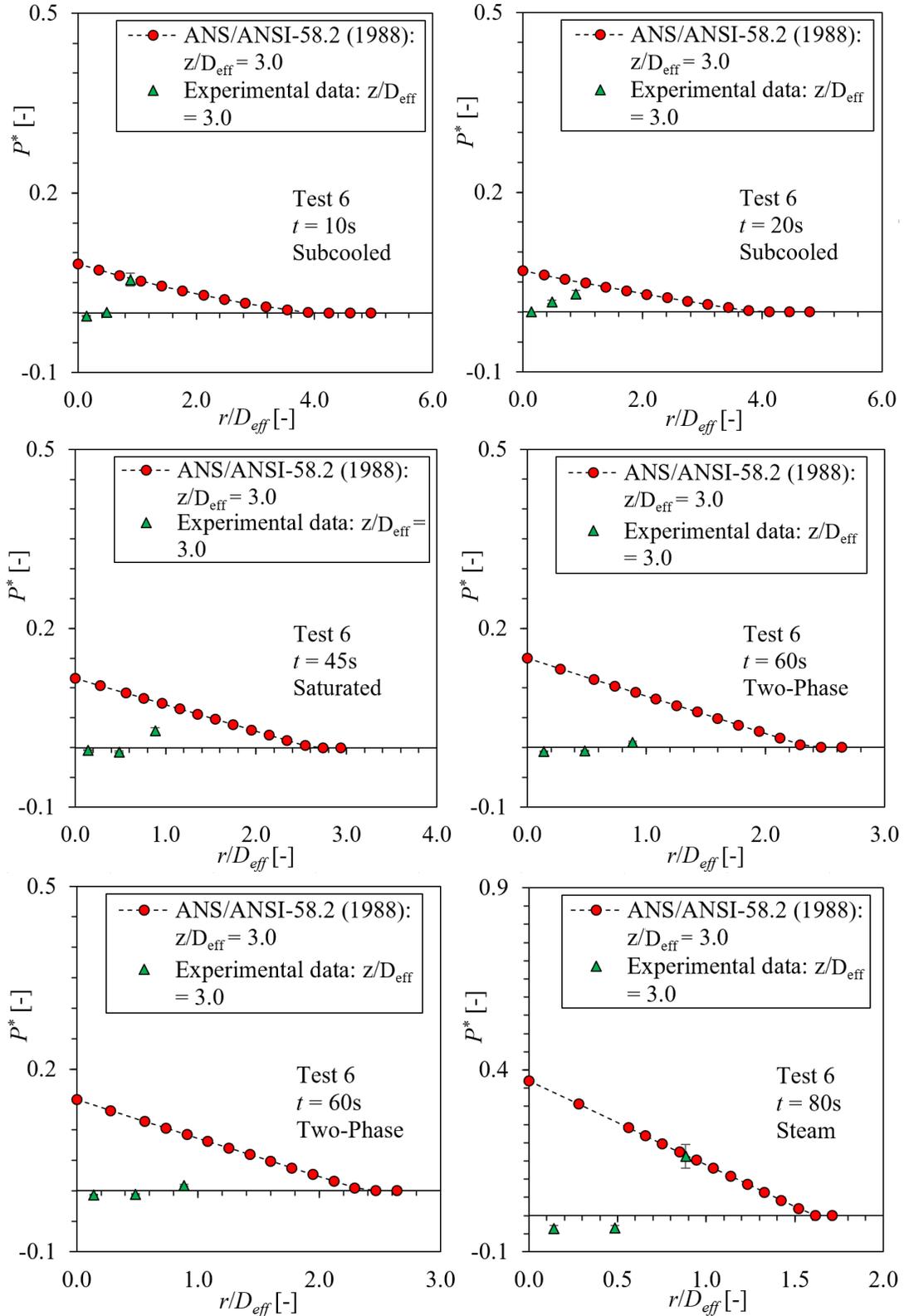
Figure B-20 Comparison between Standard Model Calculation (ANSI/ANS-58.2, 1988) and Experimental Data at Beam 4 in Test 6 of Marviken Tests. Error Bar: ±20%

Table B-6 Test 7 Conditions in Marviken Tests for ANSI/ANS-58.2 (1988) Evaluation (D = 0.5 m)

| Analyzed Time (s)	5	10	20	30	45	50
Input and Measured Stagnation Pressure (kPa)	4,318	3,784	3,234	3,003	2,489	1,615
Fluid State	ΔT = 19.2°C	ΔT = 12.5°C	ΔT = 3.3°C	α = 0.3 x = 0.005	α = 0.85 x = 0.1	α = 0.997 x = 0.7
Measured Fluid Temperature (°C)	251.9	245.5	238.6	235.3	224.4	203.7
Calculated Fluid Temperature (°C)	235.7	234.5	234.7	233.9	223.7	201.8
Measured Containment Pressure (kPa)	285.6	300.35	268.9	205.9	161	143.4
Measured Critical Mass Flux (kg/m²s)	47,625.0	39,321.9	27,149.7	17,750.3	10,077.2	3,574.9
Calculated Critical Mass Flux (kg/m²s)	49,689 by HF	43,113 by HF	34,890 by HF	13,802 by HEM	8,262 by HEM	2,917 by IE
(Calculated – Measured)/Measured Mass Flux	4.3%	9.6%	28.5%	-22.2%	-18.0%	-18.4%
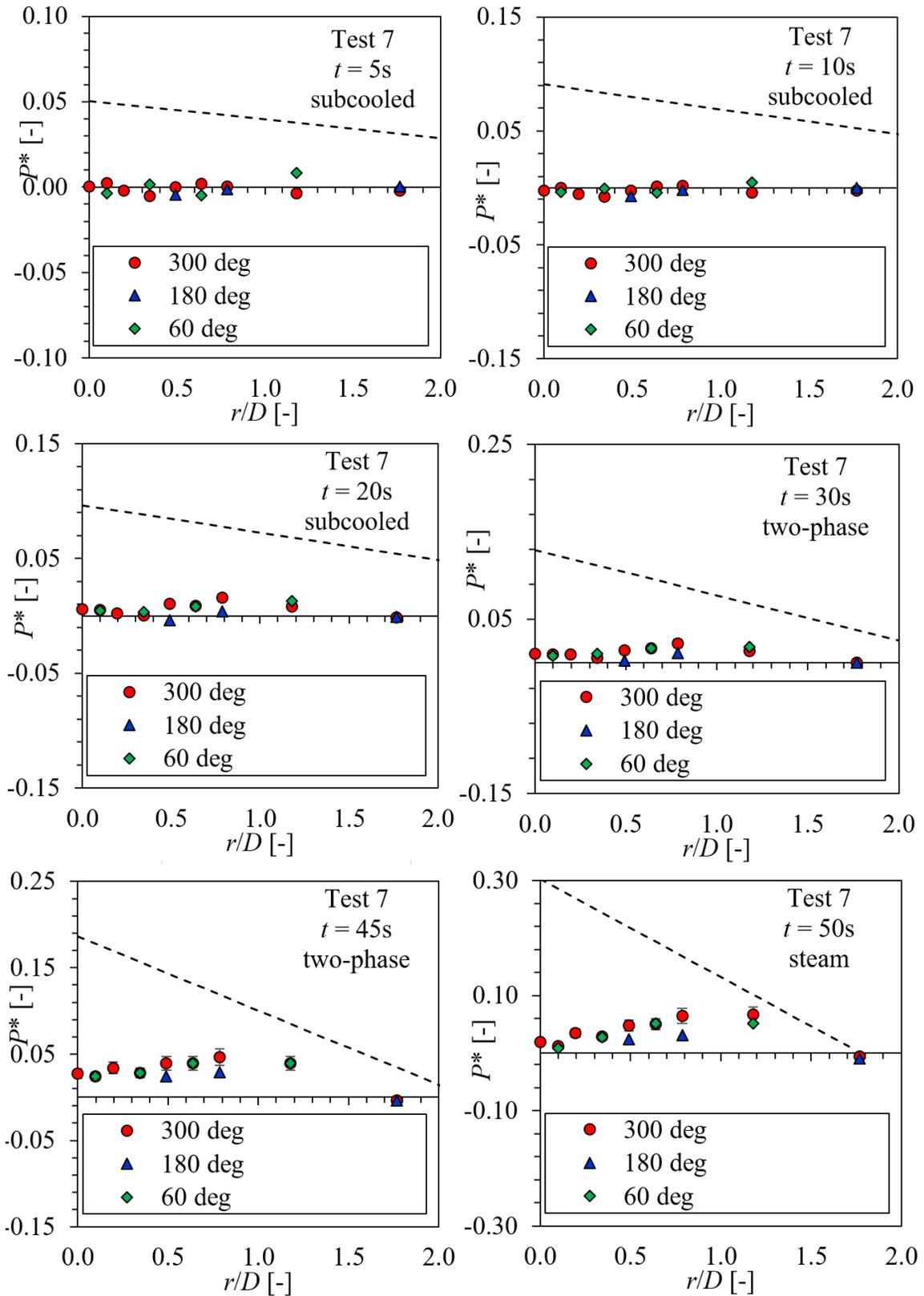
Figure B-21   Comparison between Standard Model Calculation (ANSI/ANS-58.2, 1988) and Experimental Data in Test 7 (*z*/*D* = 4.05) of Marviken Tests. Error Bar: ±20%

Table B-7 Test 8 Conditions in Marviken Tests for ANSI/ANS-58.2 (1988) Evaluation (D = 0.5 m)

| Analyzed Time (s)	5	10	20	30	45	50
Input and Measured Stagnation Pressure (kPa)	4,285	3,756	3,209	2, 995	2,580	1,845
Fluid State	ΔT = 23.6°C	ΔT = 14.7°C	ΔT = 3.6°C	α = 0.21 x = 0.005	α = 0.57 x = 0.02	α = 0.995 x = 0.7
Measured Fluid Temperature (°C)	230.9	231.9	234.0	233.8	225.6	208.3
Calculated Fluid Temperature (°C)	230.8	231.9	234.0	233.7	225.6	208.3
Measured Containment Pressure (kPa)	226.7	286.6	265.3	199.8	157.5	138.7
Measured Critical Mass Flux (kg/m²s)	47,506	39,229	28,916	17,139	12,496	4,307
Calculated Critical Mass Flux (kg/m²s)	58,200 by HEM	44,275 by HF	34,915 by HF	13,783 by HEM	11,349 by HEM	3,288 by IE
(Calculated – Measured)/Measured Mass Flux	22.5%	12.9%	20.7%	-19.6%	-9.2%	-23.7%
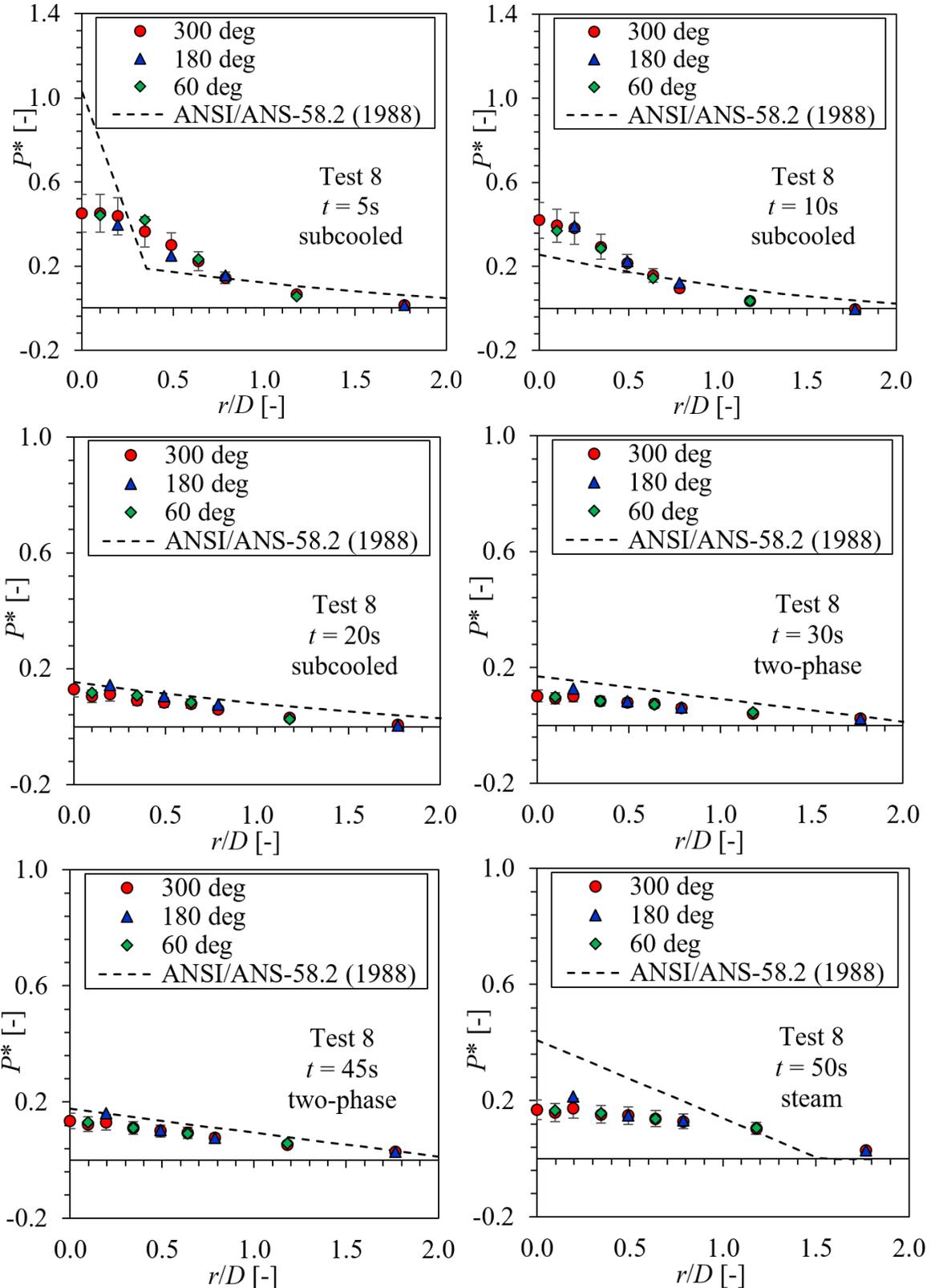
Figure B-22 Comparison between Standard Model Calculation (ANSI/ANS-58.2, 1988) and Experimental Data in Test 8 (*z/D* = 2.06) of Marviken Tests. Error Bar: ±20%

Table B-8 Test 10 Conditions in Marviken Tests for ANSI/ANS-58.2 (1988) Evaluation (D = 0.5 m)

| Analyzed Time (s)	5	10	20	30	45	50
Input and Measured Stagnation Pressure (kPa)	4,283	3,806	3,238	2,988	2,549	1,743
Fluid State	ΔT = 22.9°C	ΔT = 14.7°C	ΔT = 3.1°C	ΔT = 0.7°C	α = 0.425 x = 0.011	α = 0.982 x = 0.364
Measured Fluid Temperature (°C)	231.5	232.7	235.0	232.9	225.0	205.5
Calculated Fluid Temperature (°C)	231.5	232.7	235.0	232.9	225.0	205.5
Measured Containment Pressure (kPa)	250.3	275.3	257.3	189.75	147.1	128.5
Measured Critical Mass Flux (kg/m²s)	46,262.0	38,678.0	27,702.0	18,332.0	17,366.0	4,578.0
Calculated Critical Mass Flux (kg/m²s)	56,270.9 by HEM	44,527.3 by HF	34,786.6 by HF	32,154.5 by HF	11,784.3 by HEM	3,841.9 by HEM
(Calculated – Measured)/Measured Mass Flux	21.6%	15.1%	25.5%	75.4%	-32.1%	-16.0%
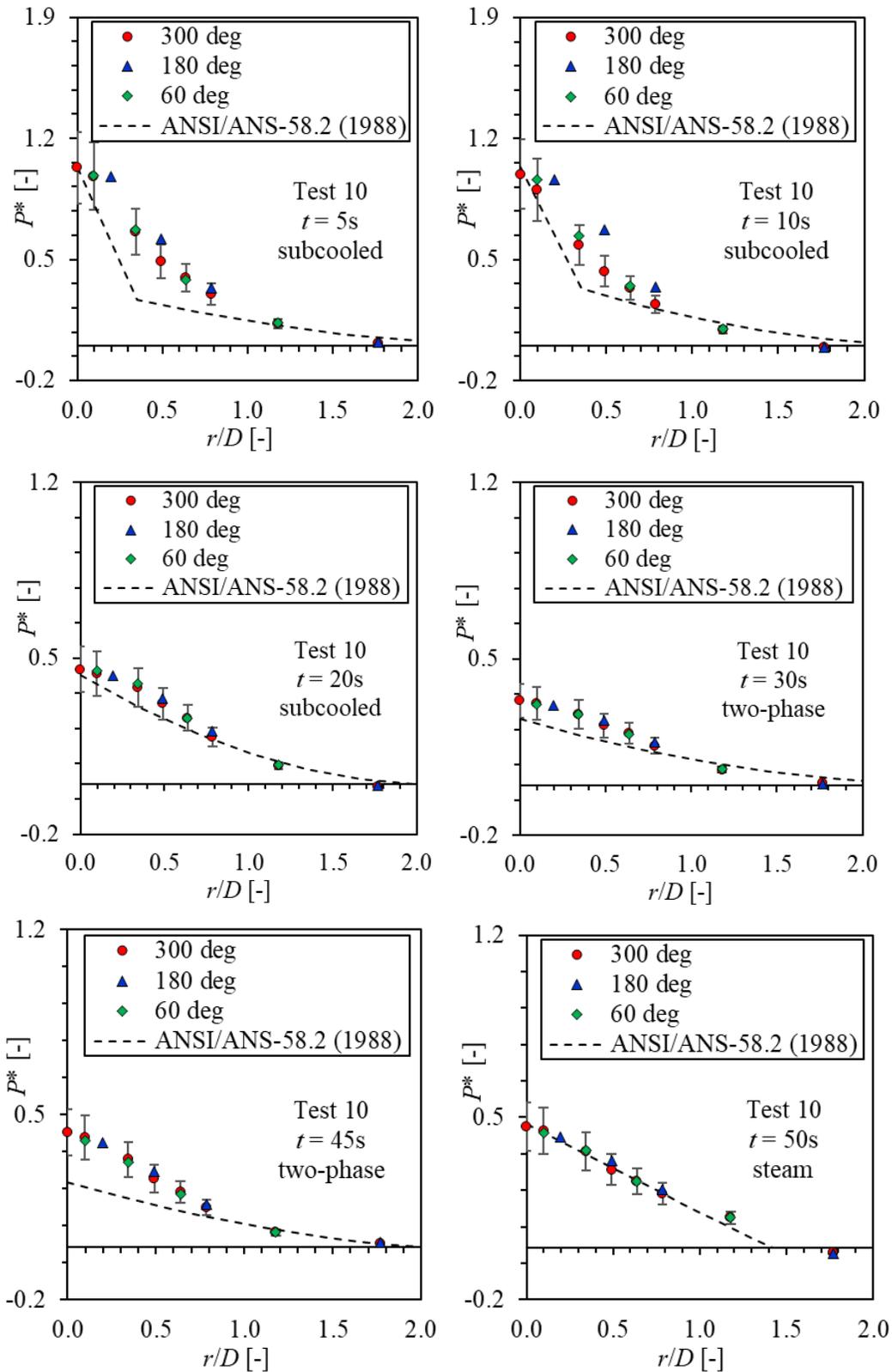
Figure B-23 Comparison between Standard Model Calculation (ANSI/ANS-58.2, 1988) and Experimental Data in Test 10 (z/D = 1.27) of Marviken Tests. Error Bar: ±20%

Table B-9 Test 11 Conditions in Marviken Tests for ANSI/ANS-58.2 (1988) Evaluation (*D* = 0.5 m)

Analyzed Time (s)	5	10	20	30	40	50	60	70
Input and Measured Stagnation Pressure (kPa)	4,467	4,155	3,627	3,178	2,796	2,468	2,191	1,952
Fluid State	α = 1.0 x = 1.0	α = 1.0 x = 1.0	α = 0.99 x = 0.7	α = 1.0 x = 0.99	α = 1.0 x = 0.99	α = 1.0 x = 0.89	α = 1.0 x = 0.99	α = 1.0 x = 0.99
Measured Fluid Temperature (°C)	257.0	252.6	244.6	237.0	230.0	223.3	217.0	211.1
Calculated Fluid Temperature (°C)	257.0	252.6	244.6	237.0	230.0	223.2	217.0	211.1
Measured Containment Pressure (kPa)	108.4	105.8	104.1	104.1	104.1	104.1	104.1	104.1
Measured Critical Mass Flux (kg/m²s)	5,618.0	5,429.0	5,654.0	4,205.0	3,525.0	3,249.0	2,841.0	2,511.0
Calculated Critical Mass Flux (kg/m²s)	6,316.2 by HEM	5,873.7 by HEM	5,979.2 by HEM	4,495.8 by HEM	3,959.7 by HEM	3,500.2 by HEM	3,112.6 by HEM	2,778.2 by HEM
(Calculated – Measured)/Measured Mass Flux	12.4%	8.2%	5.8%	6.9%	12.3%	7.7%	9.6%	10.6%
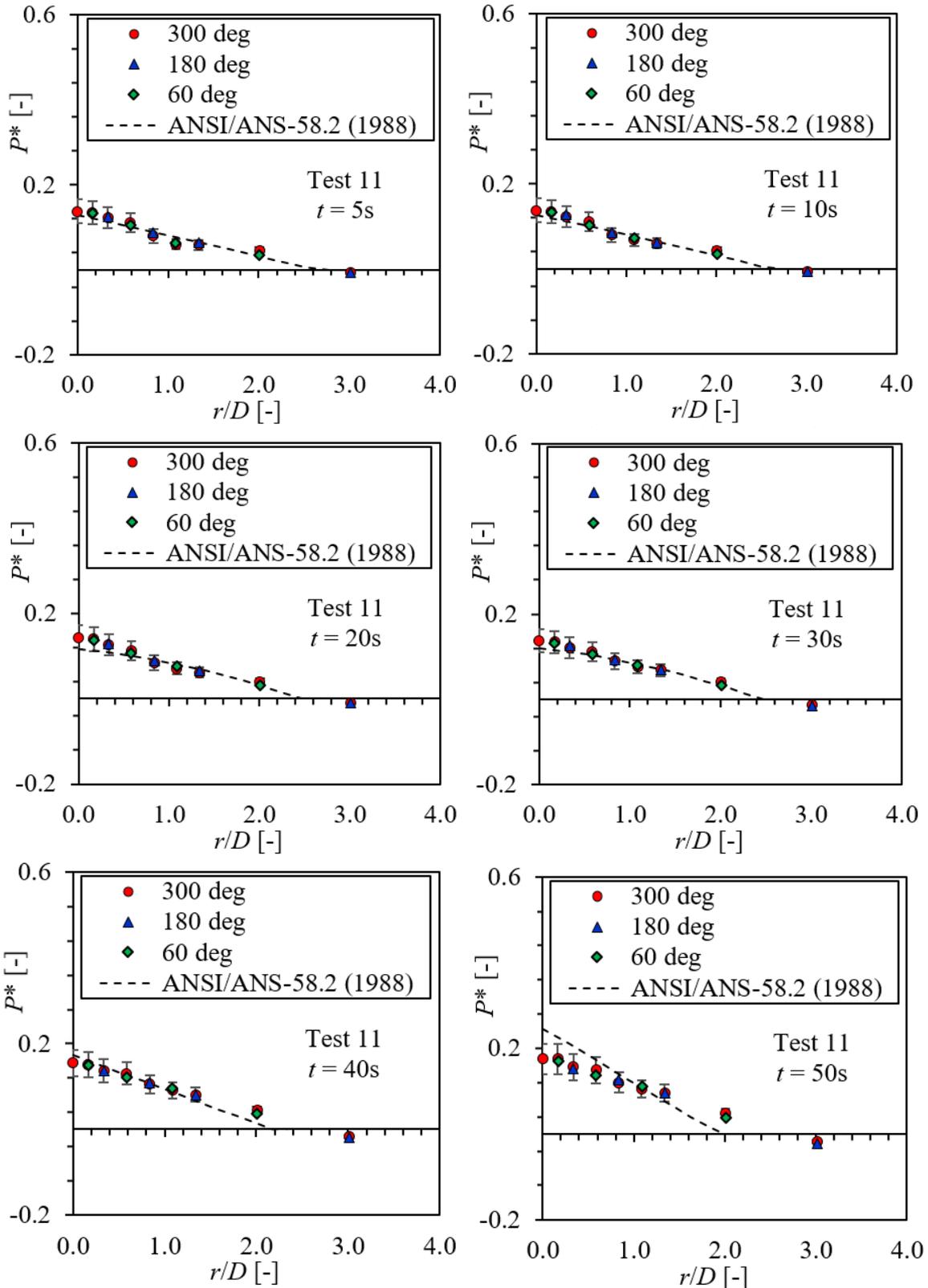
Figure B-24 Comparison between Standard Model Calculation (ANSI/ANS-58.2, 1988) and Experimental Data in Test 11 (*z*/*D* = 2.15) of Marviken Tests. Error Bar: ±20%
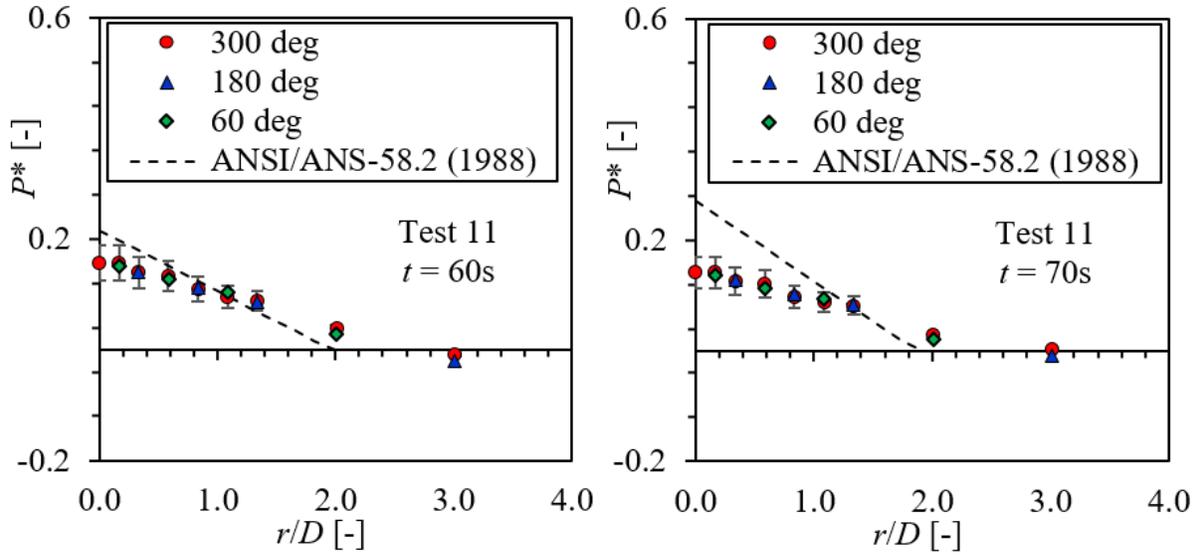
Figure B-25 Comparison between Standard Model Calculation (ANSI/ANS-58.2, 1988) and Experimental Data in Test 11 (z/D = 2.15) of Marviken Tests. Error Bar: ±20%

Table B-10 Test 12 Conditions in Marviken Tests for ANSI/ANS-58.2 (1988) Evaluation ($D =$ 0.5 m)

Analyzed Time (s)	5	10	20	30	45	55
Input and Measured Stagnation Pressure (kPa)	4,321	3,855	3,398	3,163	2,212	1,340
Fluid State	$\Delta T =$ 24.2°C	$\Delta T =$ 17°C	$\Delta T =$ 5.8°C	$\Delta T =$ 1.4°C	$\alpha = 0.961$ $x = 0.244$	$\alpha = 0.992$ $x = 0.48$
Measured Fluid Temperature (°C)	230.8	231.2	235.0	234.9	217.5	193.0
Calculated Fluid Temperature (°C)	230.7	231.1	235.1	235.4	217.5	193.0
Measured Containment Pressure (kPa)	275.5	294.2	266.4	195.6	144.4	124.3
Measured Critical Mass Flux (kg/m²s)	46,469.0	38,805.0	26,031.0	17,372.0	5,904.0	2,841.0
Calculated Critical Mass Flux (kg/m²s)	59,781.0 by HEM	46,135.6 by HF	37,133.4 by HF	33,442.8 by HF	5,611.6 by HEM	2,660.8 by HEM
(Calculated – Measured)/Measured Mass Flux	28.7%	18.9%	42.6%	92.5%	-4.9%	-6.3%
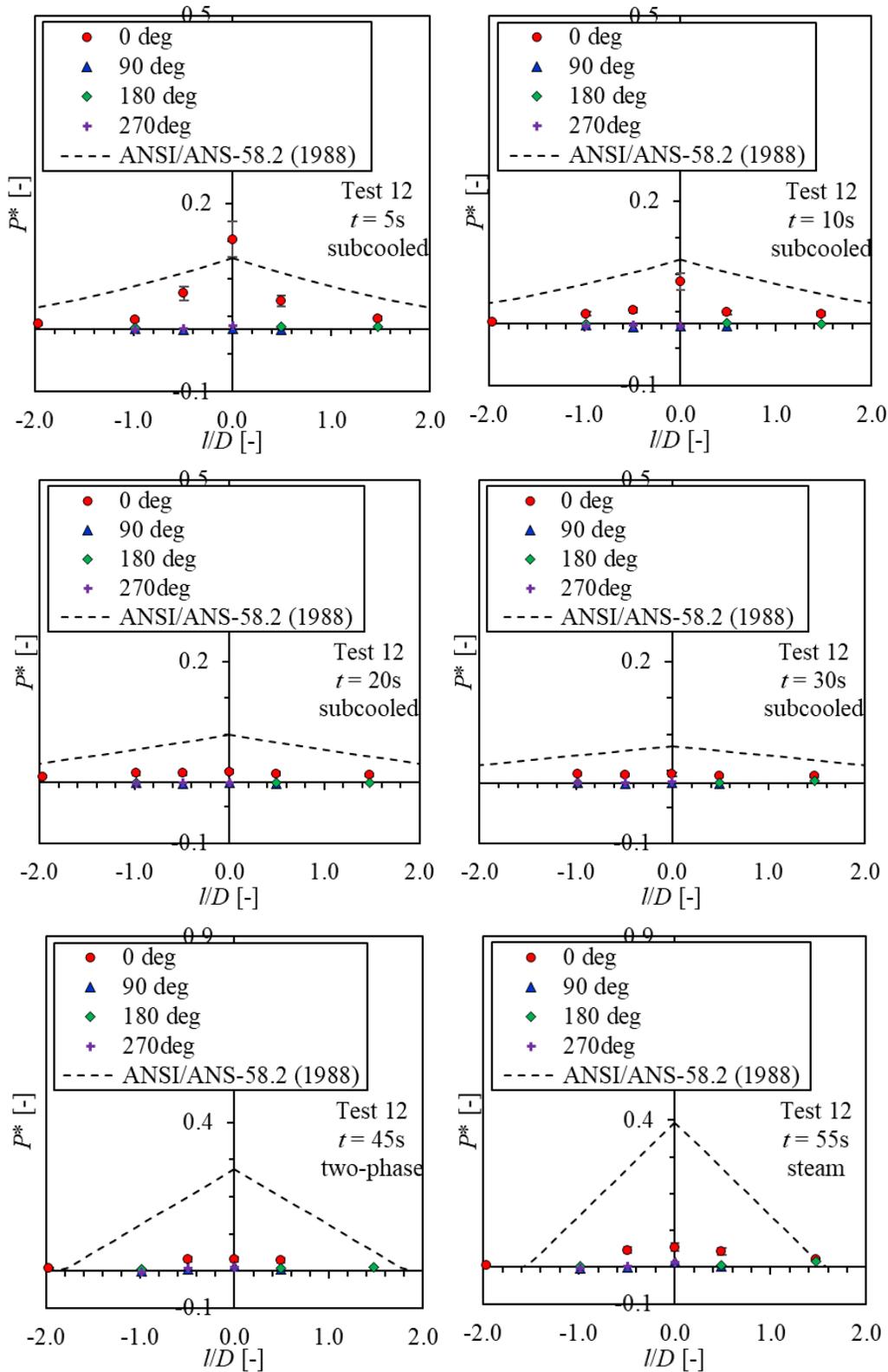
Figure B-26 Comparison between Standard Model Calculation (ANSI/ANS-58.2, 1988) and Experimental Data in Test 12 (*z*/*D* = 2.95) of Marviken Tests. Error Bar: ±20%

APPENDIX C

DISTANCE BETWEEN BREAK PLANE AND ASYMPTOTIC PLANE FROM EXPERIMENTAL DATA

In order to evaluate the model in ANSI/ANS-58.2 (1988) to calculate the axial location of the asymptotic plane, the distance between the break plane and the asymptotic plane needs to be determined first based on the experimental data. In the Marviken tests (Marklund, 1985a), the static pressure at different axial locations was measured in free jets, which provide valuable data to investigate the axial location of the asymptotic plane. In this appendix, the static pressure along the axis of the jet is plotted against the ambient pressure, to determine the axial location of the asymptotic plane. In the current report, the static pressure measured at the center of the jets are employed. All the conditions for the free jets investigated in Task 2 are included here.

Based on the definition in ANSI/ANS-58.2 (1988), the position of the asymptotic plane is where the static pressure of the jets drops to the ambient pressure. As such, it can be determined that this distance is 2 for L/D_{eff} for the condition shown in Figure C-1 (a). This dimensionless distance for all other conditions is determined in a similar way.
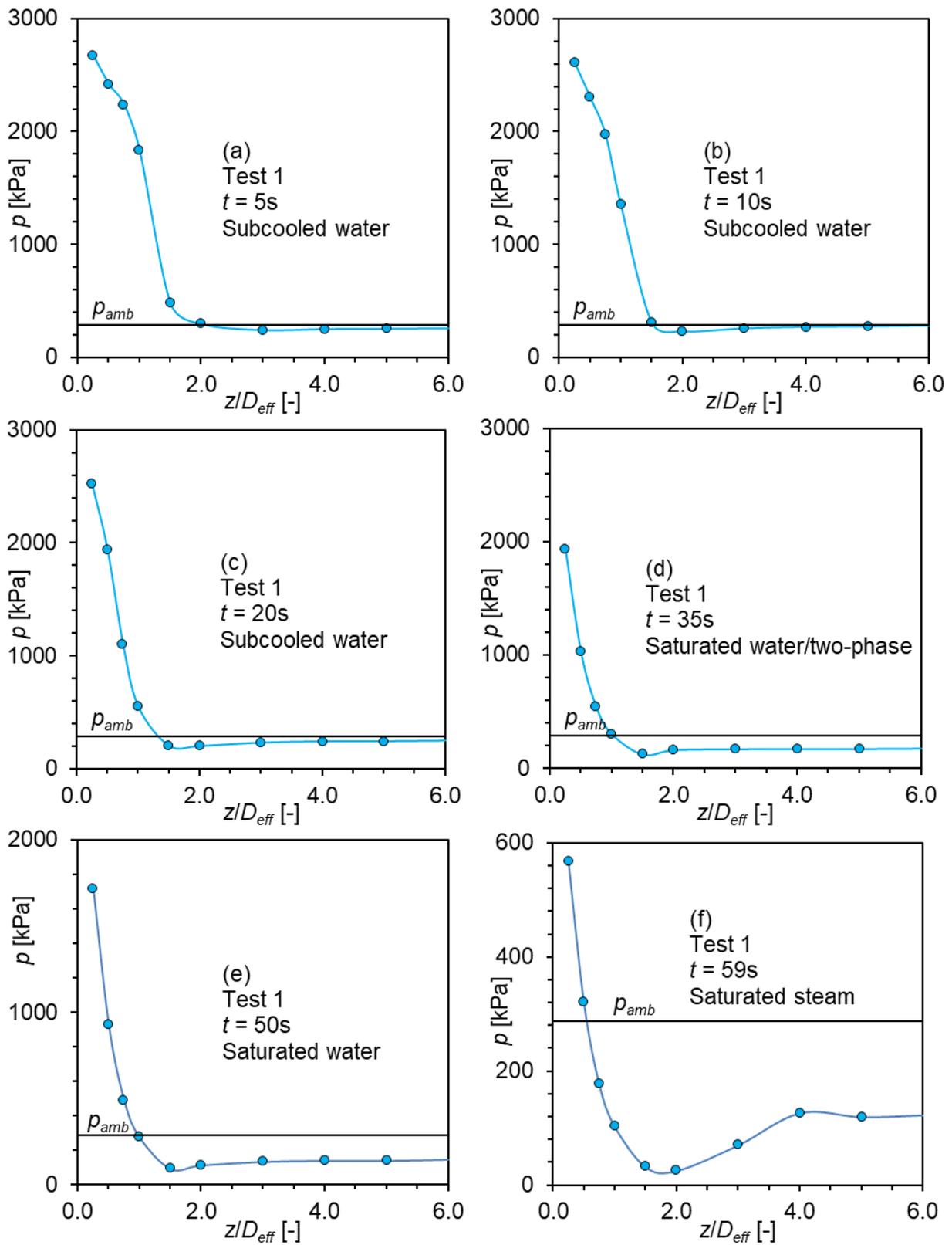
Figure C-1 Static Pressure along the Axial Direction of Jet Downstream of the Break Plane
Test 1 of the Marviken Tests
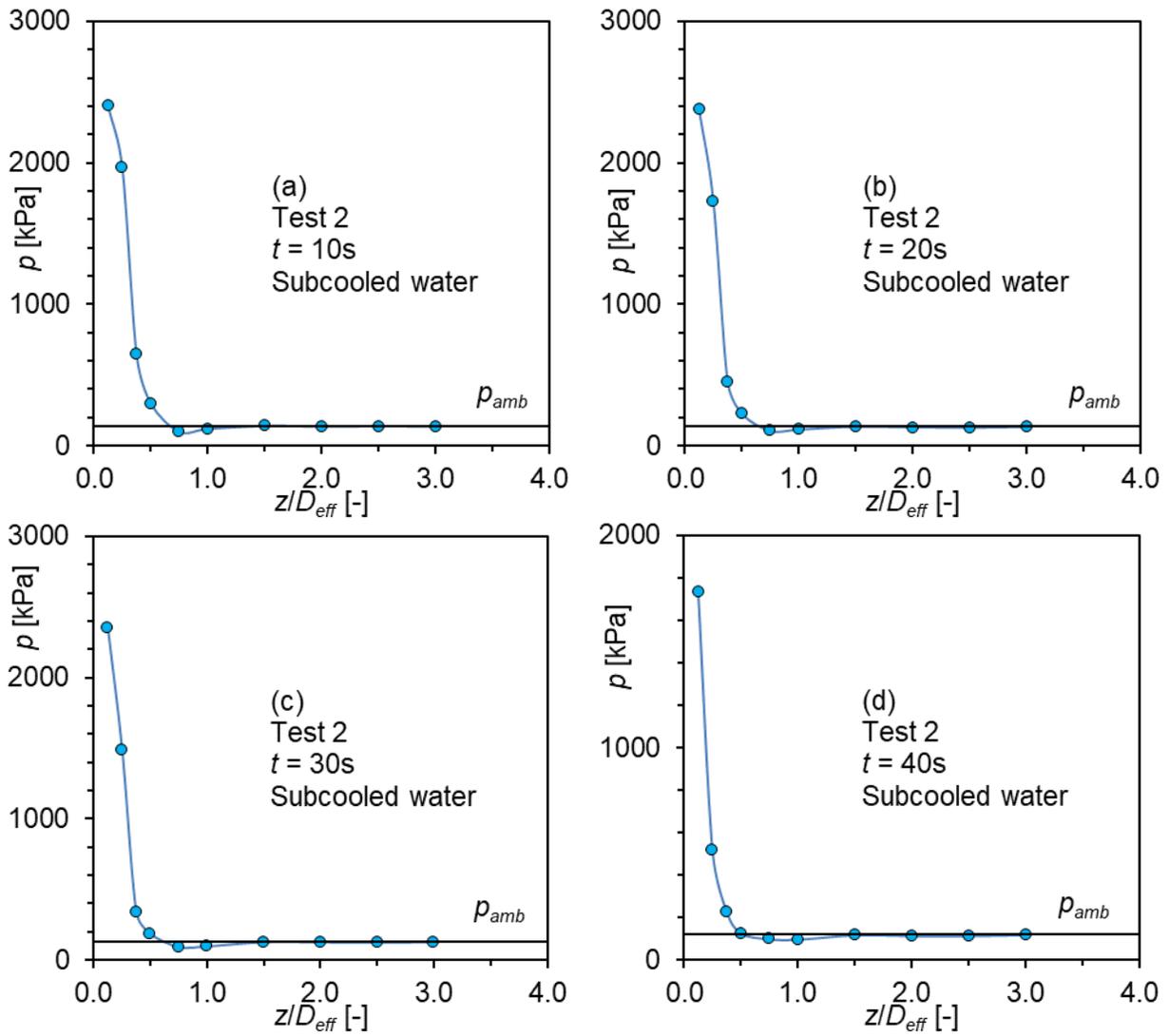
Figure C-2 Static Pressure along the Axial Direction of Jet Downstream of the Break Plane
Test 2 of the Marviken Tests
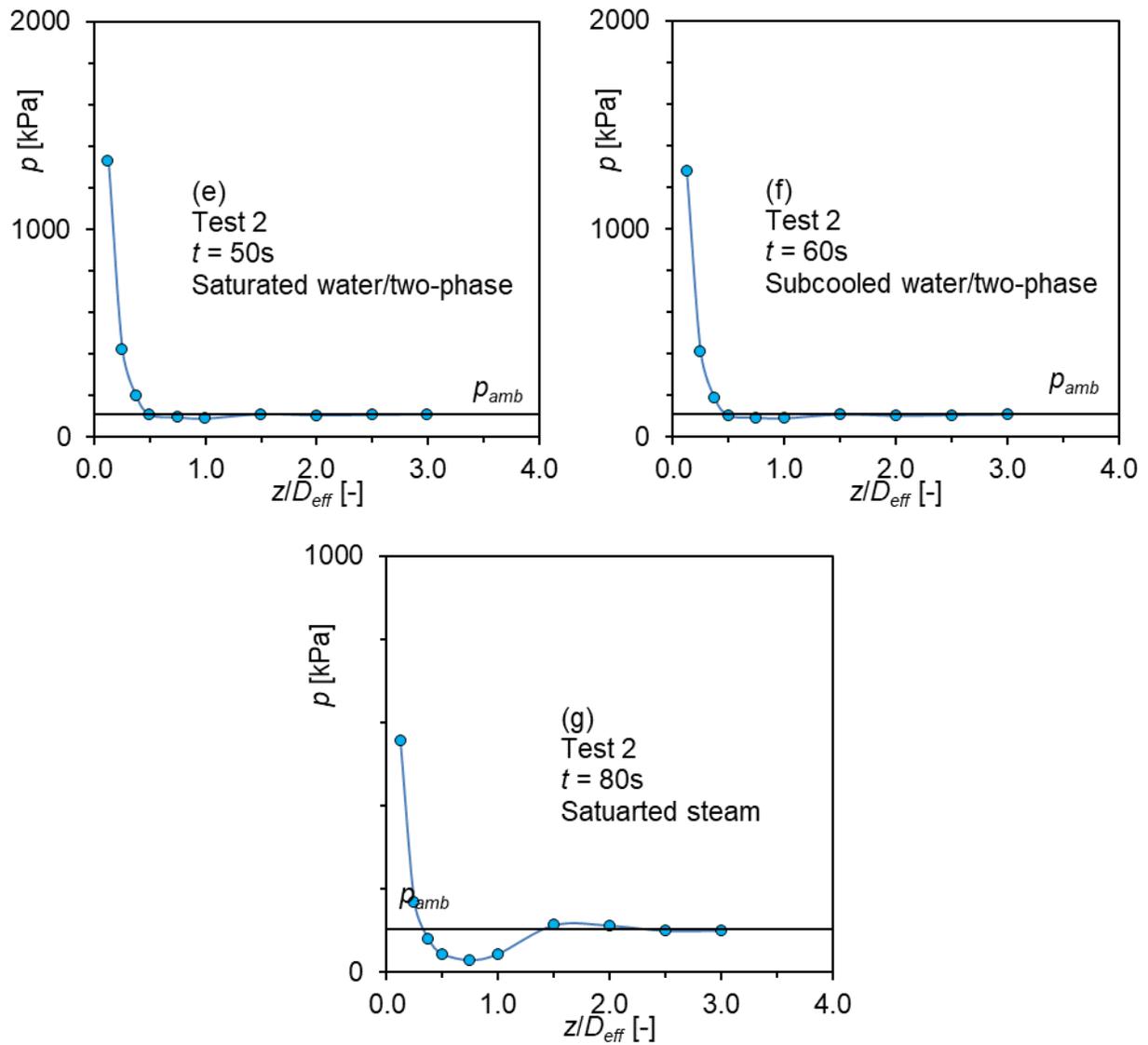
Figure C-2 Static Pressure along the Axial Direction of Jet Downstream of the Break Plane Test 2 of the Marviken Tests (cont.)
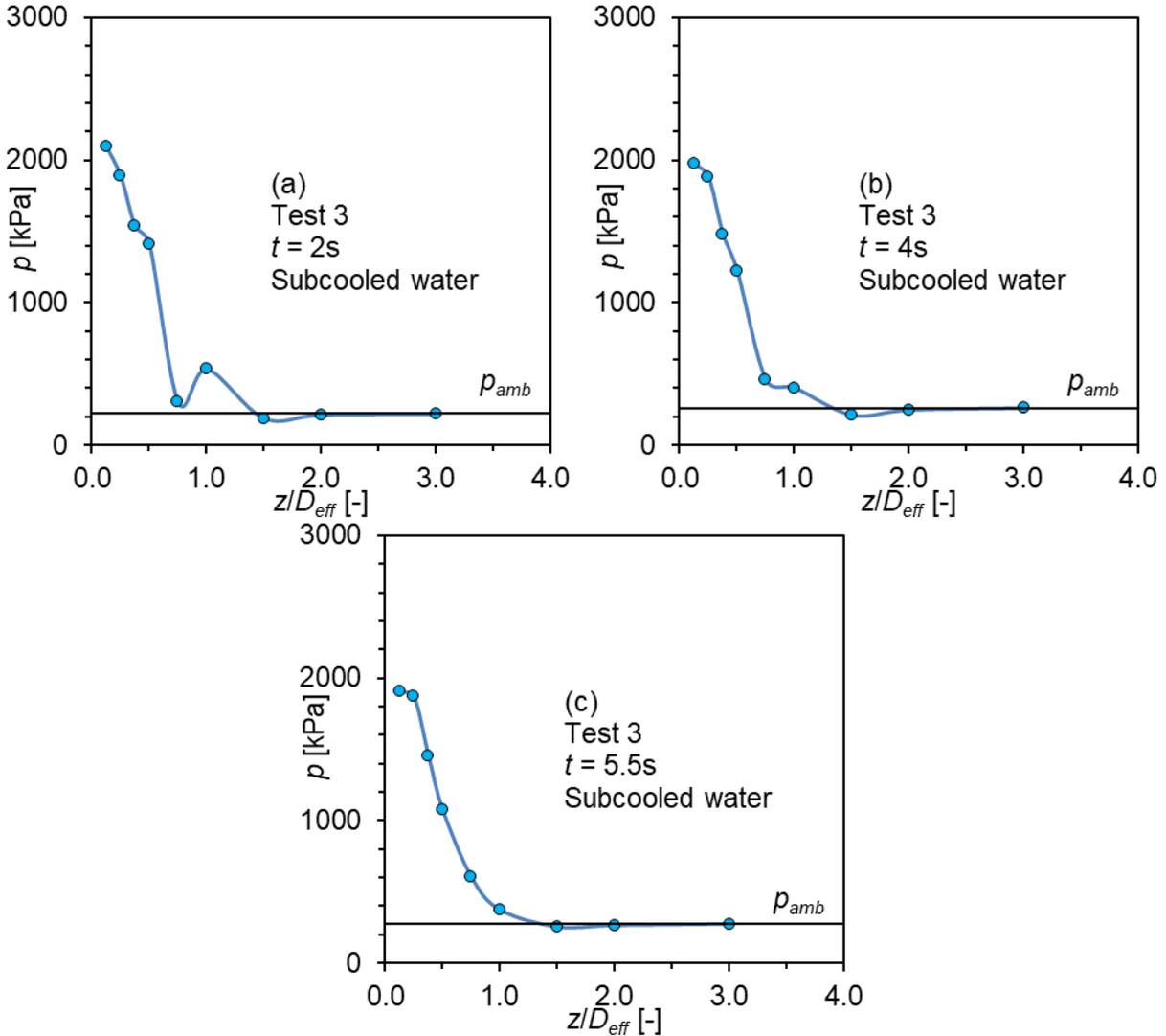
Figure C-3 Static Pressure along the Axial Direction of Jet Downstream of the Break Plane
Test 3 of the Marviken Tests
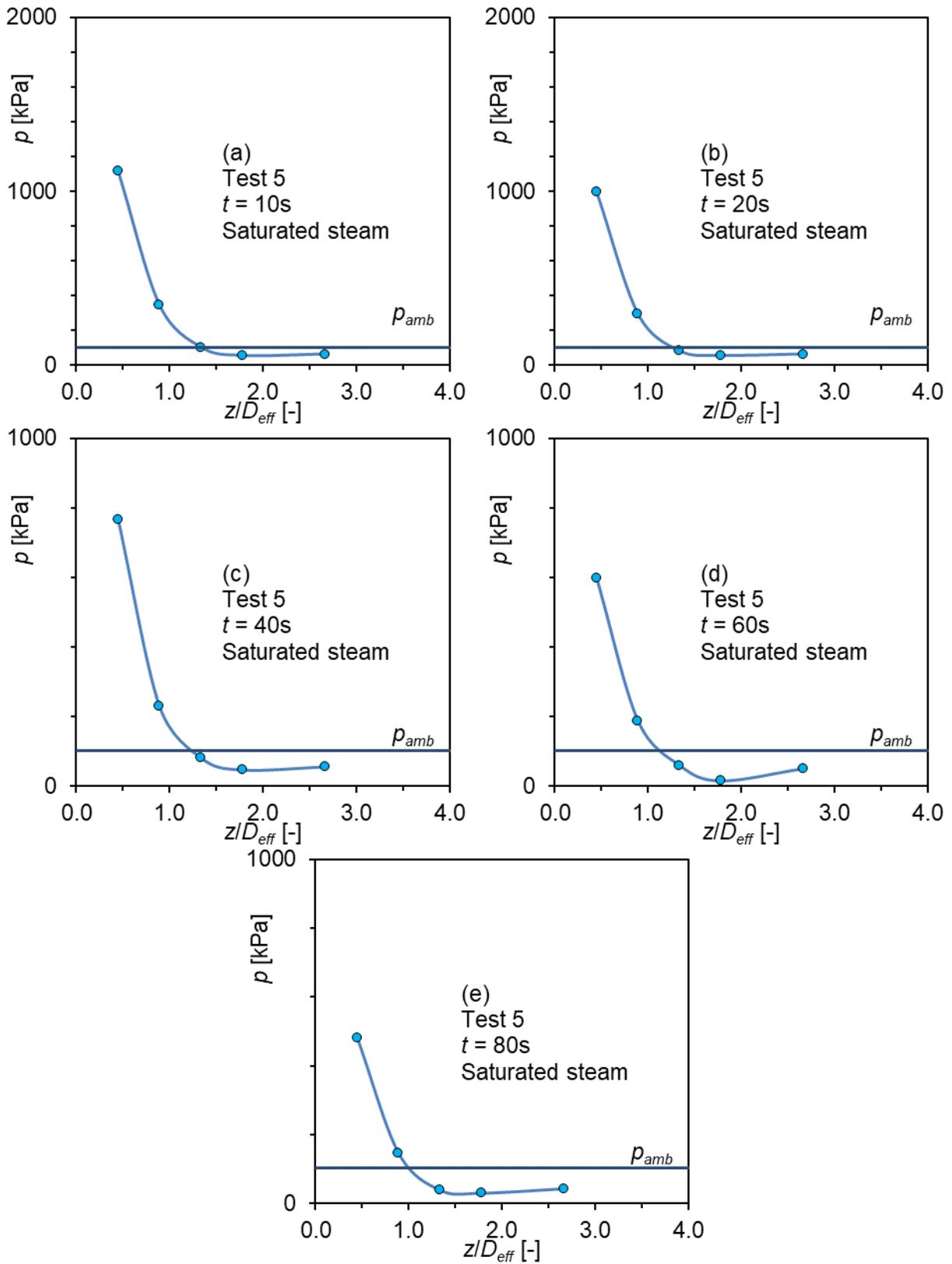
Figure C-4 Static Pressure along the Axial Direction of Jet Downstream of the Break Plane
Test 5 of the Marviken Tests
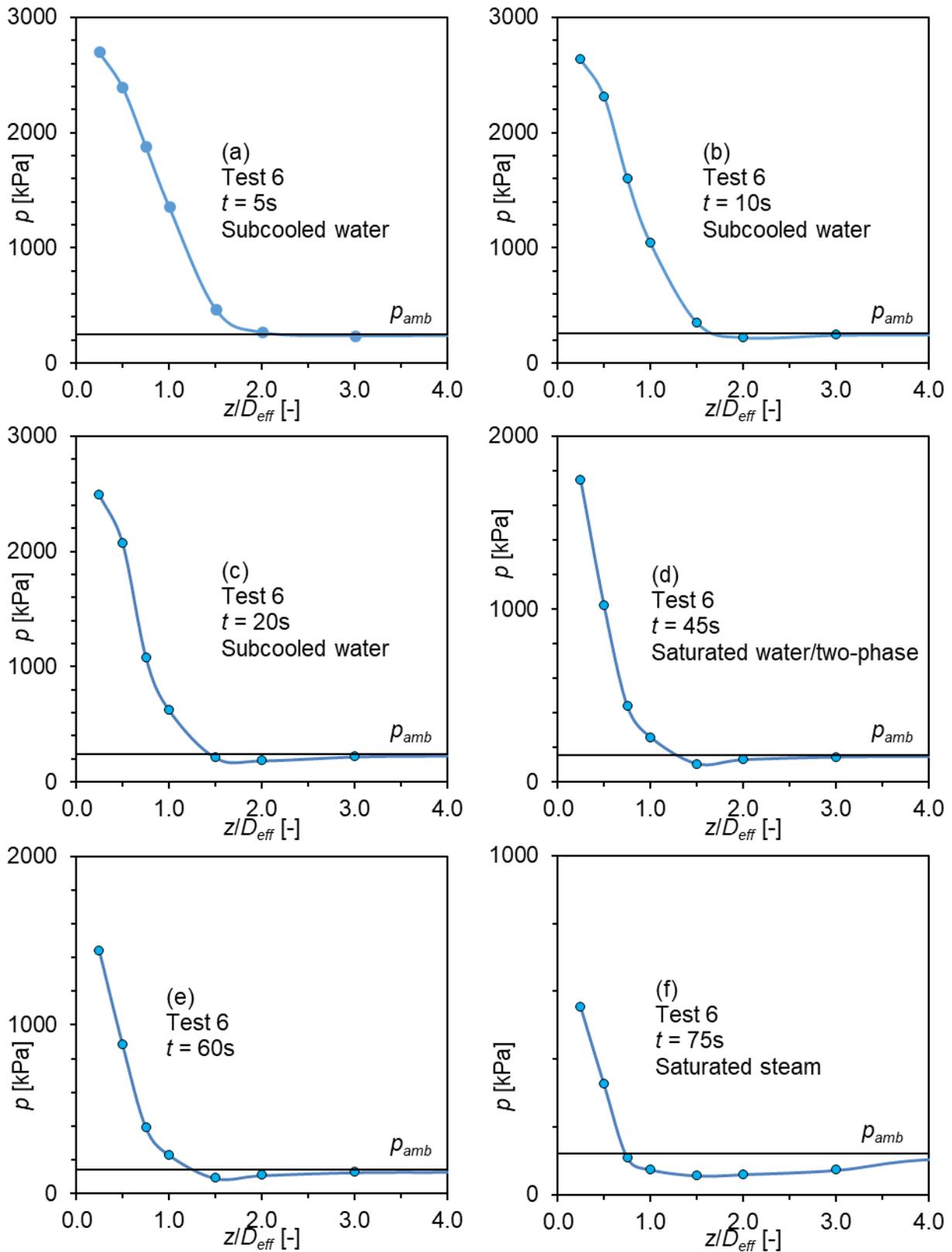
Figure C-5 Static Pressure along the Axial Direction of Jet Downstream of the Break Plane
Test 6 of the Marviken Tests

2. TITLE AND SUBTITLE	3. DATE REPORT PUBLISHED	
Jet Impingement in High-Energy Piping Systems	MONTH	YEAR
	March	2021
	4. FIN OR GRANT NUMBER	

5. AUTHOR(S)	6. TYPE OF REPORT
Dr. Seugjin Kim Dr. Mamoru Ishii Ran Kong	Technical
	7. PERIOD COVERED (Inclusive Dates)

8. PERFORMING ORGANIZATION - NAME AND ADDRESS (If NRC, provide Division, Office or Region, U. S. Nuclear Regulatory Commission, and mailing address; if contractor, provide name and mailing address.)

Thermal-hydraulics and Reactor Safety
Laboratory School of Nuclear Enginering
Purdue University
West Lafayette, IN 47907-2017

10. SUPPLEMENTARY NOTES

Performed under subcontract 31310018F0140 of NRC-HQ-25-14-E-0005, Energy Research Inc.

11. ABSTRACT (200 words or less)

Appendix A of the Standard Review Plan (U.S. Nuclear Regulatory Commission, 2015) identified several potential non- conservatisms in the existing models for jet impingement in high energy piping systems as in nuclear power plants, with respect to (a) blast wave formation, (b) jet plume expansion and zone of influence, (c) distribution of pressure within the jet plume, and (d) jet dynamic loading. The current work performs a comprehensive literature review and model evaluation to aid in addressing these potential non-conservatisms. Based on the results, the model is revised and model guidance is developed.

12. KEY WORDS/DESCRIPTORS (List words or phrases that will assist researchers in locating the report.)	13. AVAILABILITY STATEMENT
(Energy Data Base: Subject Thesaurus) jet model, impingement, expansion, nuclear power plants, blast effects, shock waves, ruptures, two-phase flow (Other) jet impingement, jet expansion, zone of influence, jet loading, pipe rupture, dynamic loading, high energy line break	unlimited
	14. SECURITY CLASSIFICATION
	(This Page) unclassified
	(This Report) unclassified
	15. NUMBER OF PAGES
	16. PRICE

NRC FORM 335 (12-2010)

Printed
on recycled
paper

Federal Recycling Program